1-1-2016

Cortical Dynamics Underlying Seizure Mapping and Control

Hank Bink
University of Pennsylvania, binkh@seas.upenn.edu

Cortical Dynamics Underlying Seizure Mapping and Control

Abstract
In one-third of epilepsy patients, antiepileptic drugs do not effectively control seizures, leaving resective surgery as the primary treatment option. In the absence of discrete focal lesions, long-term outcome after surgery is modest and often associated with side effects. In many cases, surgery cannot be performed due to the lack of a discrete region generating seizures. For these reasons, new therapeutic technologies have been developed to treat drug-resistant epilepsy with electrical stimulation. These devices are promising, but the efficacy of first-generation implants has been limited. The work in this thesis aims to advance current approaches to seizure monitoring and control by developing better hardware and building the foundational knowledge behind the cortical dynamics underlying seizure generation, propagation and neural stimulation.

In this thesis, I first develop new technologies that sample local field potentials on the cortical surface with high spatial and temporal resolutions. These devices capture complex spatiotemporal patterns of epileptiform activity that are not detected on current clinical electrodes. By adding stimulation functionalities to these arrays, we position them as an ideal candidate for responsive, therapeutic neurostimulation. Next, I explore the effect of direct electrical stimulation in the cortex by recording responses with high spatial resolution on the surface and within the cortical laminae. The findings detail the capabilities and limitations of electrical stimulation as a means of modulating seizures. Finally, I use the same three-dimensional recording paradigm in feline neocortex to investigate the genesis and propagation of epileptiform activity in an isolated, chemically-induced epilepsy model. These experiments demonstrate that important circuit elements involved in seizure propagation are found deeper in the cortex and are not reflected in surface recordings. My investigations also present potential stimulation strategies to more effectively disrupt the spread of seizures in the neocortex. It is my hope that the results of this work will inform future technologies to better detect and prevent seizures, ultimately improving the lives of drug-resistant epilepsy patients through the next generation of implantable devices.

Degree Type
Dissertation

Degree Name
Doctor of Philosophy (PhD)

Graduate Group
Bioengineering

First Advisor
Brian Litt

Subject Categories
Biomedical | Neuroscience and Neurobiology

CORTICAL DYNAMICS UNDERLYING SEIZURE MAPPING AND CONTROL

Hank Bink

A DISSERTATION

in

Bioengineering

Presented to the Faculties of the University of Pennsylvania

in

Partial Fulfillment of the Requirements for the

Degree of Doctor of Philosophy

2016

Supervisor of Dissertation	Graduate Group Chairperson
Brian Litt, M.D.	**Jason A. Burdick, Ph.D.**
Professor of Bioengineering & Neurology	Professor of Bioengineering

Dissertation Committee

Daniel K. Bogen, M.D., Ph.D. Professor of Bioengineering, Bioengineering in Medicine, and Bioengineering in Pediatrics

Diego Contreras, M.D., Ph.D. Professor of Neuroscience

Cherie Kagan, Ph.D. Stephen J. Angello Professor of Electrical and Systems Engineering and Materials Science and Engineering

Jonathan Viventi, Ph.D. Assistant Professor of Biomedical Engineering, Duke University

CORTICAL DYNAMICS UNDERLYING SEIZURE MAPPING AND CONTROL

Acknowledgements

This thesis is the culmination of six years of hard work and continuous learning. None of it would have been possible without the help of my mentors, my peers, and my friends and family. At times it seemed that I could never finish the work I set out to do, but the support of those around me kept me dedicated to seeing it through.

First, I have to thank my advisor Brian Litt for taking a chance on me fresh out of college, guiding me though the hills and valleys of graduate school, and making sure I am always looking forward. I also want to thank Cherie Kagan for opening my eyes to the world of research and for the instrumental role she played in getting me to this point from those humble REU beginnings. I must thank Diego Contreras, who was a second advisor to me and without whom the work in this thesis would not have been possible.

Next, I want to thank everyone I worked with in lab throughout the years for their scientific support and friendship. Several postdocs were vital in showing me the ropes of graduate school and helping me produce better work, including Jonathan Viventi, Duygu Kuzum, Jason Moyer, Flavia Vitale and Madineh Sarvestani. Kate Davis and Shawniqua Williams took the time to give me a better understanding of how my work applied in the clinical world. I was lucky enough to know very smart fellow graduate students during my time to bounce ideas off, get input from, and eat lunch at food trucks with. Ankit Khambhati was in the Litt Lab with me throughout nearly my whole tenure, during which we became close friends. His insightful feedback made my work significantly better. Yuming Lai taught me much about performing research well just as I was beginning graduate school. Hoameng Ung, Lohith Kini, Steve Baldassano, Preya Shah and Drausin Wulsin are just a few more of the many labmates who helped improve my work over the years and whom I am proud to consider my friends. I have to thank Carolyn Wilkinson for the innumerable number of ways she helped me and the work she continues to do to keep the lab running.

I give heartfelt thanks to everyone in my life outside of research that was there for me along the way. My friends helped keep me sane with life away from work and made my years here tons of fun. My parents instilled in me values that kept me hard at work trying to be the best I can be. They, and the rest of my family, have been pillars of support my whole life that got me to where I am today. Finally, thank you to my loving wife Kristen. She was with me every step of the way and never let me forget what I was working towards. She continues to inspire me every day and I know this is only the beginning of our lifelong journey together.

ABSTRACT

CORTICAL DYNAMICS UNDERLYING SEIZURE MAPPING AND CONTROL

Hank Bink

Brian Litt

In one-third of epilepsy patients, antiepileptic drugs do not effectively control seizures, leaving resective surgery as the primary treatment option. In the absence of discrete focal lesions, long-term outcome after surgery is modest and often associated with side effects. In many cases, surgery cannot be performed due to the lack of a discrete region generating seizures. For these reasons, new therapeutic technologies have been developed to treat drug-resistant epilepsy with electrical stimulation. These devices are promising, but the efficacy of first-generation implants has been limited. The work in this thesis aims to advance current approaches to seizure monitoring and control by developing better hardware and building the foundational knowledge behind the cortical dynamics underlying seizure generation, propagation and neural stimulation.

In this thesis, I first develop new technologies that sample local field potentials on the cortical surface with high spatial and temporal resolutions. These devices capture complex spatiotemporal patterns of epileptiform activity that are not detected on current clinical electrodes. By adding stimulation functionalities to these arrays, we position them as an ideal candidate for responsive, therapeutic neurostimulation. Next, I explore the effect of direct electrical stimulation in the cortex by recording responses with high spatial resolution on the surface and within the cortical laminae. The findings detail the capabilities and limitations of electrical stimulation as a means of modulating seizures. Finally, I use the same three-dimensional recording paradigm in feline neocortex to investigate the genesis and propagation of epileptiform activity in an isolated, chemically-induced epilepsy model. These experiments demonstrate that important circuit elements involved in seizure propagation are found deeper in the cortex and are not reflected in surface recordings. My investigations also present potential stimulation strategies to more effectively disrupt the spread of seizures in the neocortex. It is my hope that the results of this work will inform future technologies to better detect and prevent seizures, ultimately improving the lives of drug-resistant epilepsy patients through the next generation of implantable devices.

Contents

List of Tables

List of Figures

Supplementary Figures

Chapter 1 **Introduction**

Epilepsy is a neurological disorder affecting over 50 million people worldwide (World Health Organization 2005). There are a large number of physical phenomena categorized as epileptic seizures, the defining symptom of the disorder, many of which are poorly understood (Engel & Pedley 2008). Antiepileptic drugs are the primary method of treatment against seizures, though only effective in approximately 60% of cases (Kwan & Sander 2004). Traditionally in drug-resistant cases, resective surgery is the next step for treatment, in which the tissue responsible for generating seizures is localized and removed. This procedure is very invasive and stressful to the patient, with a best case probability for long-term seizure freedom of 66% in temporal lobe resections, and as low as 27% for frontal lobe resections (Téllez-Zenteno et al. 2005). There is also the risk of cognitive impairment, such as deficits in memory, sensory or motor functions, as a direct result of surgery (Berg et al. 2008). Additionally, there are many cases in which resective surgery is not an option, for instance if the seizure-generating network is too diffuse or situated in eloquent cortex.

Due to the limitations and modest long-term results associated with resective surgery, new implantable devices have been developed to treat patients with drug-resistant epilepsy. These devices modulate brain activity using electrical stimulation to prevent a seizure from occurring or inhibit its ability to spread throughout the brain. One class of devices stimulates specific peripheral or deep brain structures continuously to keep the brain out of seizure-like states, a technique similar to cardiac pacemakers or deep brain stimulation used to treat movement disorders. Clinical trials using this technology have resulted in median seizure frequency reduction of 25-40% depending on the stimulation target (Fridley et al. 2012). More recently, responsive neurostimulators have been approved that use electrodes on the cortical surface and in deeper structures to detect the onset of seizures and apply current to disrupt them. These devices have shown a long-term (3-6 years) median seizure reduction of 48-66% with significantly improved quality of life (Bergey et al. 2015). Though the outcomes are better than those from open-loop device trials, there is still much room for improvement.

The goal of this dissertation is to increase the efficacy of future neuromodulation devices for epilepsy by gaining insight on three major questions about the optimal design and implementation of the technology.

1. What is the ideal hardware for recording and stimulation to use in neuromodulation devices? Currently, responsive stimulators use surface and depth leads consisting of four contacts with over 1 mm diameter and 10 mm spacing, similar to what is used in the hospital for epilepsy monitoring (NeuroPace 2015). However, studies have shown that important epileptiform activity occurs on a submillimeter scale, including microseizures, high-frequency oscillations, and complex spatiotemporal seizure patterns, all of which cannot be seen on clinical grids (Stead et al. 2010; Viventi et al. 2011). New electrode technology must be developed and research performed to determine the optimal resolution needed to detect the onset of seizures and effectively disrupt them through stimulation.

2. How do local circuits respond to direct cortical stimulation? Epilepsy devices employ brief trains of current pulses with consistent parameters that are only adjusted during physician visits in attempts to reduce seizure frequency. This is essentially done on a trial-and-error basis, as the mechanisms that cause electrical stimulation to disrupt, or fail to disrupt, the propagation of a seizure are not well known. Further research is required to gain a better understanding of how local neuronal populations are activated by injected current, and what effect that has on epileptiform activity. Advancing this knowledge will help inform the ideal

stimulation parameters and electrode placement to more reliably terminate seizures.

3. What is the target for stimulation? One of the most difficult issues with treating drug-resistant epilepsy is its heterogeneity - that each case is somewhat unique to the patient, including the types of seizures, symptoms, and seizure onset location. Though we have an idea of how seizures occur at a cellular level, the network dynamics responsible for seizure generation, propagation and termination are still unclear. In responsive neurostimulators, detection thresholds that trigger stimulation are quite broad, resulting in 600-2000 detections per day (Sun & Morrell 2014). Developing a clearer picture of how seizures begin and spread, and what separates them from similar electrographic activity, will allow for more precise intervention. Additionally, elucidating the spatial properties of seizure propagation, both on the cortical surface and through the laminae, will inform the optimal placement of electrodes. Combining these with higher resolution recording and stimulation arrays could allow modulation paradigms to be tailored to individual patients.

An approach to answer these questions and ultimately improve next-generation neuromodulation devices for drug-resistant epilepsy is described over the following five chapters.

Chapter 2 provides the background necessary to understand the technologies developed and experiments performed as part of this thesis. It includes a look at the current field of devices used in both research and clinical settings, and the methods to diagnose and treat epilepsy. It also reviews previous work done on electrical stimulation of the brain and pertinent seizure models.

Chapter 3 details the many new recording and stimulation devices designed as part of this research and the hardware they require to run. Flexible, multiplexed, high-density ECoG arrays have the spatial resolution necessary to elucidate the complexity of seizure activity that current recording devices miss. Enabling surface stimulation on these arrays offers exciting possibilities for responsive, patterned stimulation for seizure termination. Organic-based electronics were researched as a potential low-cost, biocompatible alternative for use in multiplexed arrays. Graphene-based transparent electrodes were developed which allow the temporal resolution of electrical recording to be paired high-spatial resolution optical techniques in order to investigate network activity at the cellular level.

Chapter 4 covers experiments performed to examine the response of healthy brain to controlled visual and electrical stimuli. These experiments were performed in acute feline model using high-density ECoG grids and depth electrode probes in order to explore the relationship between data from the cortical surface and throughout the cortical lamina. Location specific visual responses were found on the surface, highlighting the importance of high spatial resolution in exploring network activity. The response to electrical stimulation in the cortex was detailed, a necessary step in improving the capabilities of seizure termination devices.

Chapter 5 consists of experiments using the same animal and recording setup as in Chapter 4. In these tests, seizures were chemically induced in an isolated part of cortex to investigate how epileptiform activity is generated and how it spreads, both on the cortical surface and through the laminae. Results from this chapter are important for several reasons. The spatiotemporal patterns revealed highlight the importance of high spatial resolution recording in mapping epileptic networks. They also serve to reveal mechanisms of seizure generation and spread from a well-controlled, focal insult to healthy cortex. Finally, the recorded depth activity shows how certain epileptic patterns on the surface are generated in the cortical lamina and give clues on how better stimulation methods can be developed to stop the spread of seizures.

Chapter 6, the conclusion of the thesis, provides a summary of the work done and its contributions to better understanding the brain and improving treatment for epilepsy. It also describes avenues for future work that can be performed using the new technologies from Chapter 3 and the experimental results from Chapters 4 and 5.

Chapter 2 **Background**

Neural Recording

The earliest known act of recording spontaneous electrical brain activity occurred in 1875, when Richard Caton used crude instrumentation to detect very low voltage signals in animals. After that, it wasn't until 1924 when the first human EEG recordings were performed by Hans Berger, who went on to lay the groundwork for the field (Bronzino 2014). Intraoperative recordings from the surface of the brain were first performed in 1935, but it wasn't until the 1950s that Wilder Penfield and Herbert Jasper truly discovered the utility of intracortical recordings. Their work at the Montreal Neurological Institute revolutionized epilepsy treatment by using ECoG to inform resective surgeries, both in removing foci and protecting eloquent cortex (Niedermeyer 1999b). Also during this time, great advancements were being made in the ability to record more locally in the brain, down to the level of single neurons. This enabled huge steps to be taken to determine the pathophysiological actions of neurons that are responsible for the mechanisms of epilepsy (Engel et al. 2005). Since then, continued advancement in the technology used to record brain activity has deepened our understanding not just of epilepsy, but also memory, cognition, sensation, movement and all other neural functions.

Current Clinical Methods

Recording electrical activity in the human brain is commonly employed to diagnose and inform treatment of epileptic patients. Once the epilepsy is determined to be drug resistant, the first step is to determine if the patient is a candidate for resection with EEG evaluation, paired with imaging methods such as MRI and magnetoencephalography (MEG). If those results reveal a clear focus causing the patient's seizures, resection is deemed a viable option for treatment. Often, to further narrow down the exact location producing seizures, a craniotomy is performed and subdural ECoG grids and/or depth electrodes are placed in the regions of interest. The patient is then monitored, often for weeks, to obtain recordings of seizures and interictal data, which is activity present between seizures. Functional mapping is also performed by stimulating from the intracranial electrodes to find areas of eloquent cortex which would cause major deficits to the patient if removed. Using all this data, the team of clinicians comes to a consensus on the portion of brain to be removed in order to give the best chance of seizure freedom.

Scalp EEG recordings represent only the largest, most synchronous neural signals since they must travel through the brain, CSF, skull and scalp before being picked up by electrodes around 10 mm in diameter. It has been shown that interictal spikes, which are often used to help determine seizure zones, need to have a source area of at least 10 cm^2 on the cortex to be seen on EEG (Tao et al. 2005). Source localization from EEG utilizes complicated mathematical models to estimate the intracerebral current sources responsible for the fields recorded at the scalp. These are typically fitted as dipoles, or paired current sources of opposite polarity, due to the nature of the flow of ions within the brain that produces electrical signals (Lopes da Silva & Van Rotterdam 1999). This is known as the inverse problem of EEG and it is impossible to determine one single solution since different source configurations can create the same field depending on the number of dipoles and their location, strength and orientation. Even with computationally-intensive algorithms, the sources modelled will never provide anatomical solutions for seizure localization. They can, however, give theoretical approximations of large areas of cortex responsible for activity, which is still very useful clinically, especially considering the noninvasiveness of the procedure (Plummer et al. 2008).

ECoG electrodes are higher resolution than EEG and are capable of picking up a wider array of signals with better quality due to their placement directly on the cortical surface. Still, they mainly sample electrical activity from the superficial layers of the cortex in an area of about 5 mm^2 (Buzsáki et al. 2012). Clinical ECoG arrays consist of platinum-

iridium or stainless steel electrodes in different configurations on a flexible plastic substrate, from single strips to large 8x8 grids. Though electrode size and spacing on the grids can vary, commonly they are around 4 mm in diameter, with 2.3 mm of exposed surface, and a 10 mm pitch between contacts (Ad-Tech Medical Instrument Corporation 2005). Figure 2.1 gives an example of an open craniotomy with subdural grids placed. Once these are implanted in areas dictated by the EEG and imaging results, patients are weaned off of any anti-epileptic drugs so they may present seizures to be recorded on the subdural grids. Epileptologists review these recordings to identify channels showing activity representative of seizure onset. This is an imperfect science, however, since seizures can arise from more than one location and not all spikes indicate epileptogenic regions (Lesser et al. 2010). Often, depth electrodes will also be placed in instances where the seizure focus is believed to be coming from deeper structures, most often the hippocampus.

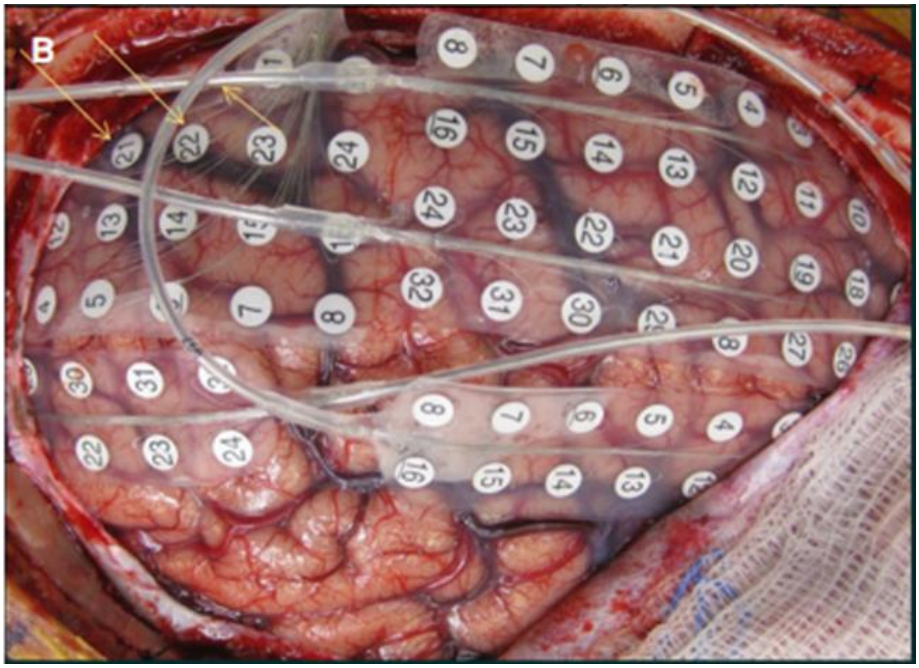

Figure 2.1 Clinical ECoG Grids Multiple clinical ECoG grids, with electrodes spaced 1 cm apart, are shown here placed in a craniotomy over the right hemisphere of a patient with drug resistant epilepsy (Greiner et al. 2016).

Current Research Methods

EEG and ECoG grids are the main modalities used clinically to record brain signals due to their large area coverage and less-invasive nature compared to electrodes that penetrate the brain, which can cause damage both upon insertion and while they are implanted (Polikov et al. 2005; Griffith & Humphrey 2006). In research applications, there are a variety of recording devices which can investigate brain activity at a much finer scale. At the finest resolution is intracellular recording, in which microelectrodes penetrate single neurons and record their membrane potential. These are typically limited as the recordings are difficult to acquire, spatially constrained, and only last on a cell for up to a few hours, ruling out chronic applications. Moving up the scale, multielectrode arrays (MEAs), which consist of many metal microelectrodes inserted into the brain, record extracellular data from a group of cells, which can be filtered to find individual action potentials if the electrodes are small enough. Though this type of recording does not give sub-threshold membrane potential information from neurons, it is much easier to implant and can stably record from units for months (Spira & Hai 2013).

The wide-band extracellular signal recorded on MEAs, known as a local field potential (LFP), is a superposition of all ionic processes happening near the electrode. The dominant contributors to LFP are thought to be synaptic currents, as they are synchronized and relatively long in duration, though other ionic and cellular mechanisms appear to play a role in shaping the field as well (Buzsáki et al. 2012). LFPs have been shown to correlate very well with intracellular recordings of nearby neurons in both fast and slow spontaneous cortical activity and even in induced seizures (Steriade et al. 1996; Contreras & Steriade 1995; Steriade et al. 1998). The spatial extent over which the LFP samples is debated, with estimates ranging from 250 μm from the electrode up to several millimeters (Katzner et al. 2009; Kajikawa et al. 2011). The main reason for estimates on the far end is the effect of volume conduction on recordings in the brain.

Volume conduction refers to the propagation of an electrical charge through the medium in which it lies. Since the brain is filled with different types of charged ions, any electric field produced will have an effect on the surrounding tissue. In the example shown in Figure 2.2a, an excitatory synapse on a dendrite causes depolarization as positive ions flow into the postsynaptic neuron. The influx of positivity is called a current sink, and it creates a negative potential in the nearby extracellular area. Since cells strive for electroneutrality, positive ions farther from the synapse flow out of the cell, resulting in a positive potential in the surrounding extracellular space, known as a current source (Lopes da Silva & Van Rotterdam 1999). A paired current sink and source create a

current dipole, which was mentioned previously as the theoretical generators used in EEG source localization model. Obviously, EEG does not record synaptic activity from a single cell, but rather from synchronized groups firing together to create larger current flows. The source-sink configuration is not always a dipole, as higher order n-poles can be formed. This configuration, along with the local properties of the tissue, can affect the extent of volume conduction and thus the distance at which LFP signals can be picked up by an electrode (Buzsáki et al. 2012). To further complicate the issue, the same dipole created by an excitatory synapse on the dendrite can also be created by an inhibitory synapse closer to the soma, as shown in Figure 2.2b. When the postsynaptic neuron is hyperpolarized, the extracellular space becomes more positive, resulting in a source near the cell body, and a corresponding sink above due to volume conduction. On a higher level, such as ECoG or EEG, this can make the interpretation of current generators very difficult.

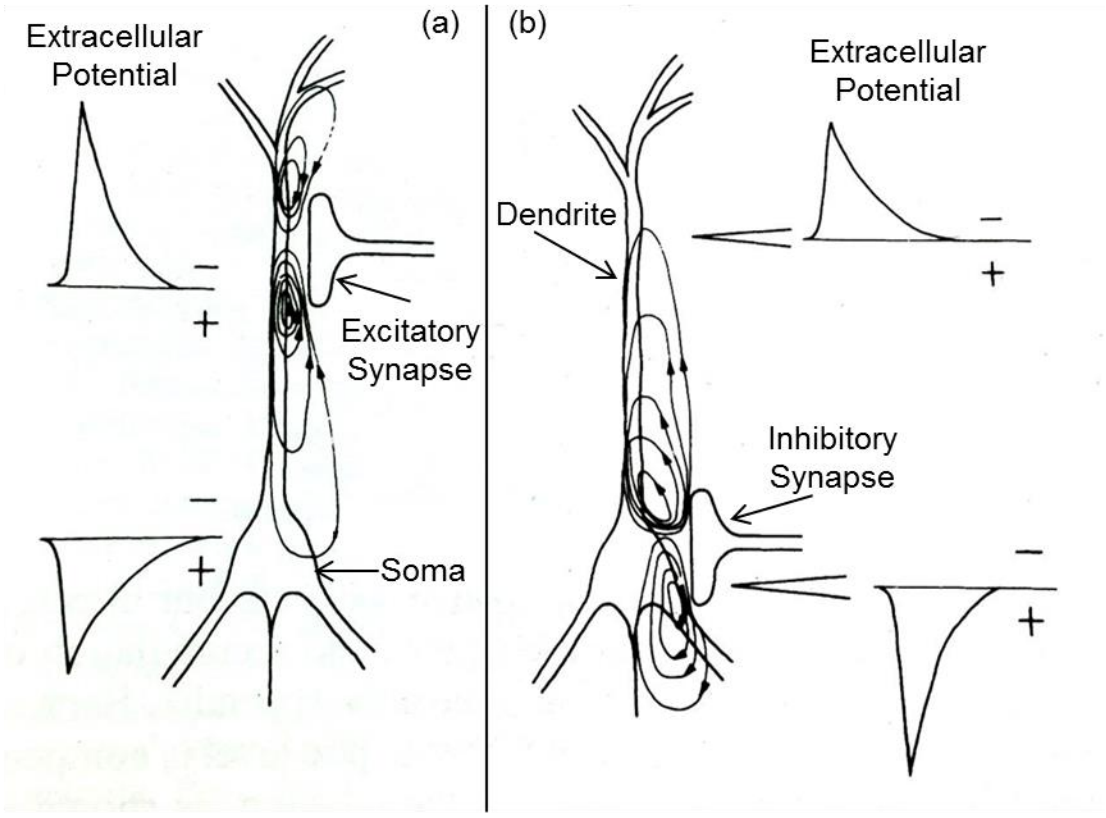

Figure 2.2 Generation of Current Dipoles The two illustrations show the generation of the same current dipole profile from synaptic activity of idealized neurons. (a) An excitatory synapse at the apical dendrite causes a local sink (negative extracellular potential) and passive source (positive extracellular potential) near the soma. (b) An inhibitory synapse near the cell body causes a local source and passive sink at the dendrite level, resulting in the same extracellular field potential profile. Adapted from (Lopes da Silva & Van Rotterdam 1999).

Current sinks and sources are typically obtained from LFP recordings using a method called current source density (CSD) analysis. The CSD is a scalar quantity that represents the volume average in extracellular space of individual membrane currents and is equivalent to the divergence of the extracellular current density. Using Ohm's law, which relates electric field to current density, and the fact that the electric field is equal to the negative gradient of the scalar potential, the CSD (I_m) can be related to the field (φ) and the conductivity of the medium (σ), as shown in Equation 2.1 (Nicholson & Freeman 1975).

$$I_m = -\nabla\sigma \cdot \nabla\varphi \tag{2.1}$$

In order to utilize this method in actual LFP recordings, this equation must be simplified by making a few assumptions. In order to apply Ohm's law in the first place, the medium must be ohmic, meaning the conductivity does not change with potential. By assuming the conductivity is homogenous and isotropic throughout the tissue recorded, it becomes a constant in the equation. Since LFPs for this purpose are typically recorded perpendicularly through the layers, the dimensionality can be reduced by assuming that the field in that area only changes in one direction. These assumptions allow us to simplify down to Equation 2.2, equating CSD to the second spatial derivative of the field in the direction of recording (z) (Mitzdorf 1985).

$$I_m = -\sigma_z \cdot \frac{\partial^2\varphi}{\partial z^2} \tag{2.2}$$

The spatial derivative of the field can easily be discretized using the finite difference approximation so that it can be applied to recorded data.

Even though CSD is very useful in overcoming volume conduction issues in LFP and deciphering sources and sinks, it is not without its issues. First, as was shown in Figure 2.2, the CSD alone cannot distinguish between dipoles created by (1) an excitatory synapse causing an active sink and passive source and (2) an inhibitory synapse causing an active source and passive sink (Lindén et al. 2010). Next, experiments have shown that the extracellular medium may be neither isotropic nor homogenous, especially through the entire depth of cortex (Buzsáki et al. 2012). Finally, performing CSD only along one dimension may be insufficient as current flow is usually three-dimensional, giving an incomplete picture of the source/sink distribution (Nicholson & Freeman 1975). Despite these drawbacks and potential issues, CSD is successfully employed in evoked and spontaneous paradigms, in different animal models and brain regions, and consistently matches expected profiles based on the known anatomy so closely that it is

often used to guide electrode placement (Buzsáki et al. 2012; Mitzdorf & Singer 1978; Blanche et al. 2005; Maier et al. 2010; Tahon et al. 2011).

Neural Interrogation

Recording spontaneous activity is useful to monitor for seizures in epilepsy. However, in order to study specific systems in the brain, the recording paradigms must be more controlled and precise. In order to achieve this, researchers look at evoked potentials, which are the neural responses to specific stimuli presented to the subject. Ideally, these responses are very consistent to the same stimulus, allowing for signals to be averaged giving a high signal-to-noise ratio (SNR) and more powerful results. They are applied to many different systems in the body, including the auditory, visual, somatosensory and motor systems. The evoked potentials from two different types of stimuli will be discussed here: visual and electrical.

Visual System

The visual system is incredibly complex as it requires the quick processing of large amounts of heterogeneous data. This makes it a great system for investigating evoked potentials, since many different types of stimuli can be used to detect different outputs. The primary flow of visual information begins with the retina, which senses light in the environment and sends the bulk of the information to the lateral geniculate nucleus (LGN) of the thalamus. From there, the main target is the primary visual cortex (V1), which is well organized and does a large amount of processing to determine attributes such as form, color and distance of the perceived image (Wurtz & Kandel 2000). In the early part of the 20th century, this general flow of information was known based mainly on anatomical and behavioral studies with little physiological data outside of the retina. In the 1940s, spatial field maps of the visual cortex were developed in cats using surface electrodes, though it did not shed much light on neuronal processing (Wurtz 2009). It wasn't until the late 1950s when David Hubel and Torsten Wiesel used novel microelectrodes to study the responses of individual cortical cells and began to elucidate the neural basis for visual perception.

One of the major initial findings by Hubel and Wiesel was that neurons in V1 are selectively tuned to stimuli of a specific form, size, position and orientation, as well as direction of movement (Hubel & Wiesel 1959). They later went on to show that neurons tuned to specific orientations are arranged in columns perpendicular to the cortical layers, and the arrangement varies in different parts of the cortex (Hubel & Wiesel 1963). Future

studies used optical properties of the brain to more fully map these columns, an example of which is shown in Figure 2.3(b) (Bonhoeffer & Grinvald 1991; Bonhoeffer & Grinvald 1993; Maldonado 1997). These columns are not completely ordered though, as orientation scatter increases with depth and the specific tuning properties of neurons depend on their location in the column (Maldonado 1997; Schummers et al. 2007). These orientation tuning experiments typically use a sinusoidal dark/light drifting grating to elicit responses, as shown in Figure 2.3(c), and properties of this grating other than orientation can have an effect on neurons. It has also been shown that orientation tuning can be performed using LFP responses, typically by using the power in the gamma band as a substitute for firing rate (Gray & Singer 1989; Berens et al. 2008). Some applications of visual evoked potentials do not seek to differentiate between responses to different stimuli like orientation tuning, but rather to match a known pattern. These are often used in clinical settings to help diagnose different diseases.

Most vision research done since the 1950's has been performed in cats due to their similarity to human vision, so the anatomy and physiology of their visual system is quite well known. Two important areas in the cat visual system are the primary and secondary visual cortices, or V1 and V2, which are depicted in Figure 2.3(a). It was shown that neurons in V1 responded more to gratings with a higher spatial frequency and lower temporal frequency than neurons in V2. This was thought to be the result of fibers from different sources in the LGN innervating each area (X- and Y-cells to V1 and V2, respectively), and may be the basis for the pattern and movement detecting mechanisms in V1 and V2, respectively (Movshon et al. 1978). There is also a transition zone between these two areas which shows properties of both as it has inputs from X- and Y-cells of the LGN (Humphrey et al. 1985). Along with thalamocortical connections, there are also many intracortical connections both within and between V1 and V2. In fact, the bulk of synapses in the cat visual cortex arise not from the LGN but from other parts of the cortex (Girardin & Martin 2009). Most horizontal connections are excitatory and typically synapse locally, though they can be up to 8 mm in length. Inhibitory connections are typically less than 3 mm, with location and layer playing a large role in the properties (Schmidt & Lowel 2002; Hirsch & Gilbert 1991). Though they are fewer in number, anatomical evidence has suggested that a single inhibitory connection can have a greater impact on its postsynaptic target than a single excitatory one (Hirsch & Gilbert 1991).

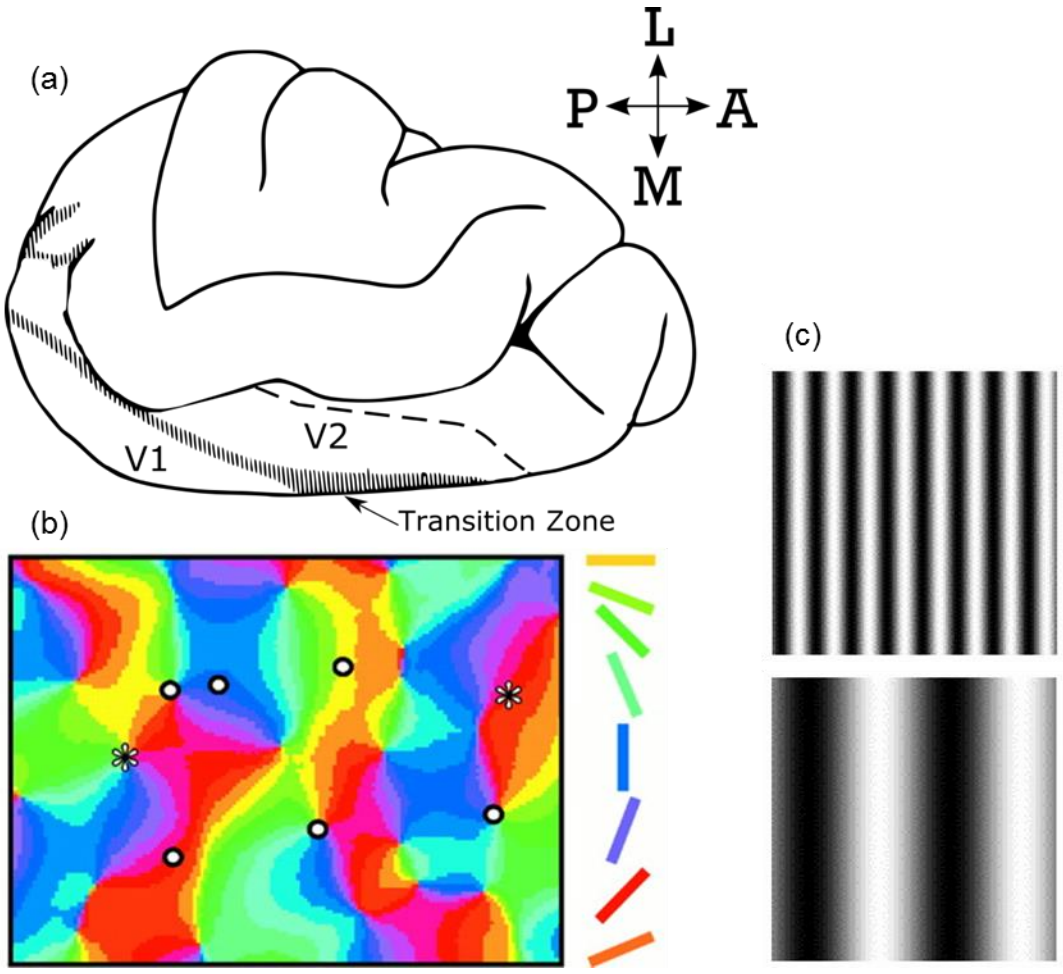

Figure 2.3 Cat Visual Cortex Orientation Tuning Map The illustration in (a) depicts the right hemisphere of the feline brain, with directions noted. The areas of interest are the primary visual cortex (V1) and secondary visual cortex (V2), which are separated by a transition zone. The image in (b) is an orientation map obtained by optical imaging, covering a cortical area approximately 4x3 mm containing portions of V1 and V2. The color on the map denotes areas that respond to a drifting grating with the angle of the bar of corresponding color on the right. Examples of sinusoidal drifting gratings are shown in (c), with the upper box showing a grating with a higher spatial frequency than that in the lower, and both at the same orientation. (a) adapted from (Payne & Peters 2002). (b) from (Maldonado 1997).

Electrical Stimulation

Another means of evoking a response from the brain is through direct electrical stimulation of the cortex. Since electrical stimulation activates neuronal elements independent of their function, the results are not predictable like those from sensory stimulation. The advantage of electrical stimulation is that it can target small areas or the brain with a controlled amount of current. Clinically, stimulation is done on patients undergoing resective surgery, either for epilepsy or tumor removal, in order to identify areas of cortex directly related to motor, sensory, language and cognitive function that could cause unwanted deficits if removed (Szelényi et al. 2010). In epilepsy cases, stimulation is delivered via implanted subdural grids, described previously, using a constant-current stimulator. Though stimulation protocol varies by institution, typically trains of 50 Hz biphasic square pulses with 0.3 ms duration are used for 2-5 s, while slowly increasing intensity with an upper threshold of 15mA (Ojemann et al. 1993). If stimulation is performed near the epileptogenic zone, it is possible to produce seizure-like activity, or even clinical seizures, which limits the ability to fully map those areas (Ikeda et al. 2002). ECoG stimulation can produce increased energy in surrounding tissue up to 2 cm away for up to 10 s, depending on the stimulation intensity (Gwinn et al. 2008).

Early experiments analyzing direct stimulation of the cortical surface found that it had a consistent response shape on the surface that held across different animal and even human subjects. The shape typically consisted of an initial short positivity, followed by a large negative deflection and then a longer, lower-amplitude positivity. The shape is thought to be brought about first by the depolarization of upper and middle layer cells, followed by depolarization of deeper pyramidal cells, and finally the afterhyperpolarization of apical dendrites near the surface. The stereotyped response changed depending on the depth of stimulation. These studies typically used large stimulating electrodes on the surface of the brain (Goldring et al. 1961; Chang 1951; Bishop & Clare 1953; Barth & Sutherling 1988).

Research has also been performed investigating stimulation with microelectrodes, or microstimulation, and how it activates elements in the brain. Evidence suggests that the directly activated sites on neurons are the initial segment of axons and the nodes of Ranvier, since they have the highest concentrations of sodium channels (Borchers et al. 2012). There are also now good models for the approximate distance of direct neuronal activation as a function of stimulation intensity (Tehovnik et al. 2006). This method of current spread has been elucidated by modern techniques, though the results are nowhere near conclusive. An experiment using two-photon imaging discovered that

microstimulation directly activates sparsely distributed neurons near the electrode, primarily mediated by axons, and increasing current fills out this area rather than extending the distance, which can be on the order of millimeters. It also showed that very little activation was due to synaptic activity, with most caused directly by the stimulation (Histed et al. 2009). A study using fMRI to measure spread, however, showed that transynaptic transmission by horizontal connections played a large role, even activating functionally connected areas outside of V1, and the radius of activation did increase with increasing stimulation intensity (Tolias et al. 2005). Clearly, there are still many questions about how exactly the brain responds to direct electrical stimulation.

One of the most important technologies to utilize neural electrical stimulation is deep brain stimulation (DBS). DBS uses an implanted stimulator with leads targeting the subthalamic nucleus (STN) of the brain to treat movement disorders such as Parkinson's disease, essential tremor and dystonia. It is believed to regularize neuronal patterns in the basal-ganglia thalamocortical network, thus preventing pathological oscillatory activity, though the exact mechanisms are still under debate (Miocinovic et al. 2013). One major finding was that in order to increase the effectiveness of DBS and reduce side effects, a specific volume of tissue activated (VTA) was required based on the anatomy near the STN (McIntyre et al. 2004). Subsequently, models were created to determine not only the best position of the electrode, but the shape of the contacts on the electrode, how much current was going through which contacts, and the waveform of the stimulus (Butson & McIntyre 2008; Butson & McIntyre 2006; Foutz & McIntyre 2010). The success of DBS in treating movement disorders has spurred research into its potential use for other neurological disorders such as depression, obsessive-compulsive disorder and epilepsy. The tenets of DBS have been employed in new devices that use electrical stimulation to prevent seizures, which will be explored in the next section.

Epilepsy

Epilepsy is a neurologic disorder characterized by chronic unprovoked seizures. Symptomatic epilepsy is an acquired condition in which seizures have a known root medical cause, such as head trauma, brain infection or brain tumor. Idiopathic epilepsies are thought to be genetic in nature, though the exact contributions are not well known (World Health Organization 2005). Although seizures can be patient-specific, there are some defining factors that allow them to be used to further classify the type of epilepsy. Most commonly, epileptic seizures fall under two categories: focal and generalized. Focal, or partial, seizures begin in a specific part of the brain and may or may not spread to other regions, whereas generalized seizures show activity over the whole brain at onset

(Westbrook 2000). In adults, only those with drug resistant focal epilepsy are candidates for resection, since there is ideally a focus that can be localized and removed. The general method of finding the seizure focus was described earlier in this chapter. This section will go into more detail of the electrographic patterns that guide this localization, other methods of treatment, and the models of epilepsy that have helped determine its cellular basis.

Diagnosis and Treatment

Once the general area of seizure focus has been determined by EEG and ECoG electrodes are placed in that region, it must be determined exactly which contacts show evidence of the seizure focus. There are several different zones relating to the seizure focus that clinicians have defined. In general, they look for the epileptogenic zone, or the entire theoretical area of the brain that is required for the generation of seizures. The seizure onset zone is defined in a patient as the area from which seizures appear to be generated, and is the tissue typically removed in surgery. If surgery leads to seizure freedom, it can be assumed that the seizure onset zone completely overlapped with the epileptogenic zone. The irritative zone is a larger area in which interictal spikes are seen and it includes the seizure onset zone. Only within the seizure onset zone do these spikes give rise to seizures (Rosenow & Lüders 2001). This practice is very difficult, as it is sometimes challenging to distinguish between epileptiform discharges and physiologic transients on ECoG grids (Nair et al. 2008).

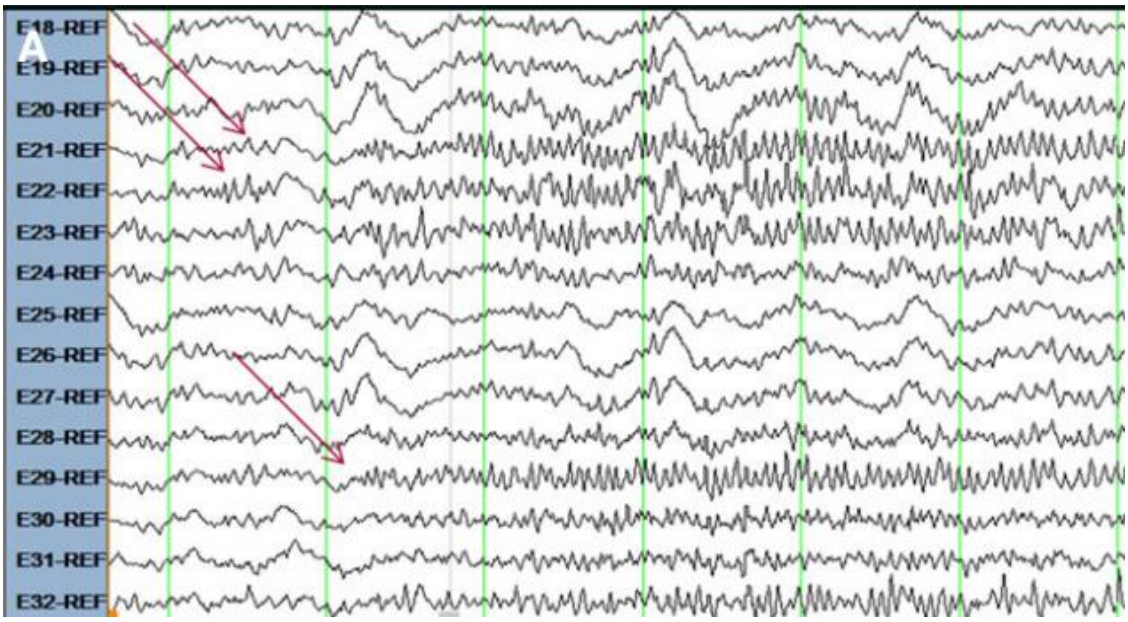

Figure 2.4 Electrographic Seizure Onset from ECoG Recording The traces in this figure show an example of a clinical seizure recorded from the grid shown in Figure 2.2. The arrows here mark the earliest signs of the seizure, with channels corresponding to the electrodes with arrows in Figure 2.2. From (Greiner et al. 2016).

Figure 2.4 shows an example of the beginning of a seizure as recorded by the implanted ECoG grid shown in Figure 2.2. The arrows in both figures mark the three contacts on which the first appearance of the seizure occurred before it spread to nearby electrodes. These three contacts were determined to be part of the seizure onset zone, with the underlying tissue later confirmed by post-resection pathology to be dysplastic (Greiner et al. 2016). A patient may have few seizures when undergoing subdural monitoring, and the locations at which they begin may not be as distinguishable as this example. For this reason, interictal periods are also monitored for non-seizure epileptiform activity, specifically interictal spikes, shown in Figure 2.5. These are brief (< 250 ms) morphologically defined events caused by synchronous discharge which can be large enough to be detected by EEG. Correlational evidence has been found linking the appearance of spikes and seizures, both spatially and temporally, but the mechanisms relating the two are unknown and their use in diagnosis is under debate (Staley & Dudek 2006; Karoly et al. 2016). Even though spikes are seen both within and outside the seizure onset zone, it has been shown that the earliest and highest amplitude spikes correspond closely to seizure onset zone, implying that spikes and seizures share a common epileptogenic generator (Hufnagel et al. 2000). A contrary theory posits that the post-spike depression actually protects against the occurrence of ictal discharges by maintaining a low level of excitation in the cortex (De Curtis & Avanzini 2001). There are many other spontaneous epileptiform events that are seen interictally on EEG and ECoG recordings. However, their etiology and relationship to seizures is even less well known than spikes.

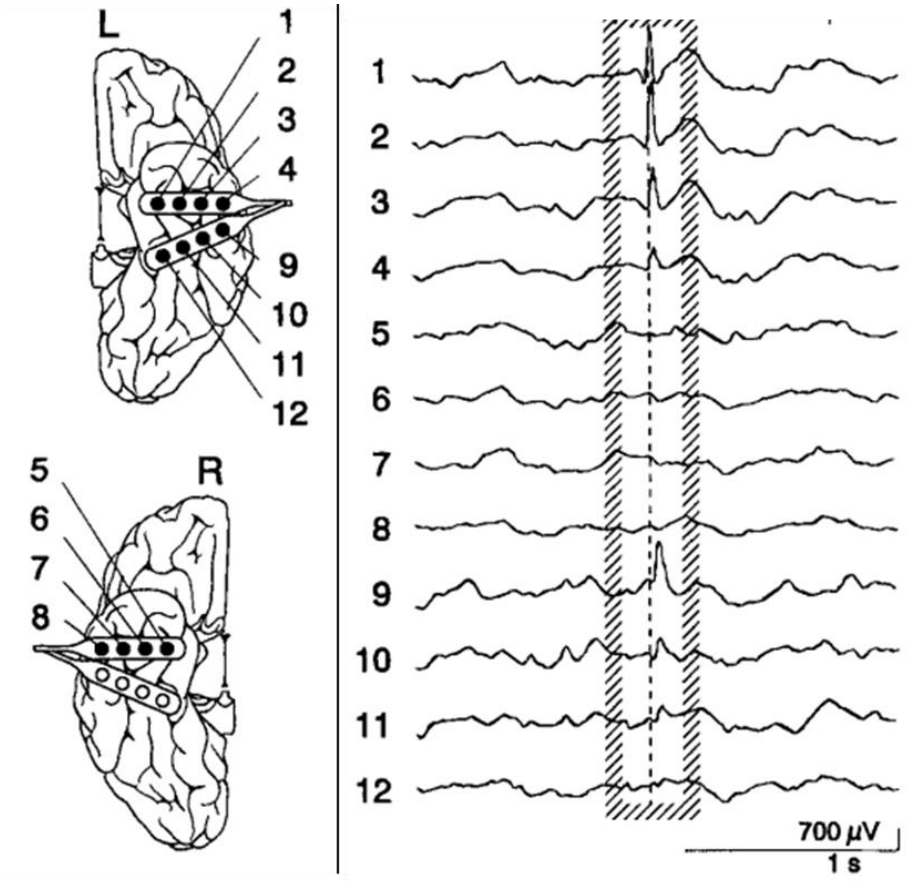

Figure 2.5 Human Interictal Spike On the right are traces recorded from the corresponding ECoG strip electrodes shown on the left, containing an interictal spike in the hatched box. From (Hufnagel et al. 2000).

After determining the seizure onset zone, surgical excision was historically the only course of action in treating drug resistant epilepsy. Recently, research into using electrical stimulation to prevent or abort seizures has led to the use of implantable devices as an alternative to traditional resective surgery. Vagus nerve stimulation (VNS) has shown benefit in open and controlled trials, though the precise mode of action is unknown (Litt 2003). DBS technology has also been utilized targeting deep brain structures for seizure termination. Open-loop stimulation of the anterior thamalic nuclei has shown promise, with around 50% reduction in seizure frequency (Fisher et al. 2010). Stimulation of deeper structures is believed to affect integral excitatory and inhibitory pathways and reduce cortical excitability or prevent the secondary generalization of seizures through these tracts (Theodore & Fisher 2004). Closed-loop systems that target the epileptic network from the depth and surface have been developed to stimulate only on the detection of seizures. In clinical trials, they have shown long-term (3-6 years) median seizure reduction of 48-66% with significantly improved quality of life (Bergey et al. 2015). Cortical stimulation also shows promise, as epileptiform afterdischarges that develop as a side effect during functional mapping were found to be significantly shortened by brief pulses of stimulation on an implanted ECoG array (Lesser et al. 1999). Overall, there are many different methods being investigated, but the science behind them and the mechanisms of action are unclear. A better understanding of the underlying physiological responses and the targeted epileptic networks is required to improve the efficacy of such devices.

Animal Models

At a cellular level, neurons within the seizure focus show a stereotyped electrical response of a large depolarization, known as the paroxysmal depolarizing shift (PDS), followed by an afterhyperpolarization, which together look like an exaggerated excitatory post-synaptic potential (EPSP). The PDS is caused mainly by activation of excitatory glutamate receptors that, in turn, trigger feedback and feedforward inhibition from interneurons mediated by γ-Aminobutyric acid (GABA) receptors, resulting in the following hyperpolarization (Westbrook 2000). A large enough group of neurons undergoing PDS and restricted by the recurrent inhibition is reflected on ECoG or EEG recordings as an interictal spike (Staley & Dudek 2006). It is believed that a comprisal of the responding inhibition is what allows longer epileptiform discharges and seizures to come about (Trevelyan & Schevon 2013). Most of what we know about epileptogenesis and seizures at this level has come from models of seizures in animals.

There are many different methods to replicate epileptic activity in animal models. Some create spontaneously occurring seizures chronically to more closely resemble human epilepsy. These can be produced using chemicals, such as kainic acid and pilocarpine, or electrical stimulation through kindling, in which repeated afterdischarges are elicited until the brain is in a permanent epileptic state. Though very useful to study, these techniques can be expensive, labor-intensive and time-consuming, mainly due to the difficulties maintaining and recording from animals chronically (Kandratavicius et al. 2014). Acute epilepsy models do not replicate the unpredictability of seizures like chronic models, but they have a distinct advantage experimentally and allow for a more in-depth exploration of the tissue. These models typically attempt to create an imbalance in the depolarizing and hyperpolarizing influences on cortical structures to produce epileptic activity. One method to achieve this imbalance is by changing the ionic concentration of the tissue, typically increasing K^+ or reducing Mg^{2+}, which is especially useful *in vitro* with slices in artificial CSF. Another technique uses drugs called chemoconvulsants. Though different types of chemoconvulsants create the depolarizing/hyperpolarizing imbalance in different ways, one commonly used type reduces the efficiency of GABAergic inhibition (Mccormick & Contreras 2001). These include drugs such as penicillin, bicuculline and picrotoxin. Picrotoxin is a $GABA_A$ receptor antagonist that effectively reduces the amplitude of the inhibitory postsynaptic currents in a concentration-dependent manner (Korshoej et al. 2010).

Experiments using these drugs have shown a very consistent response in neocortical and hippocampal preparations: large amplitude, regularly recurring spike-like discharges near the site of application, analogous to interictal spikes, as well as longer epileptiform events or seizures (Prince & Wilder 1967; Dichter & Spencer 1969a; Miles et al. 1988; Chagnac-Amitai & Connors 1989). An early experiment found that in a direct application of penicillin on cat neocortex, the majority of nearby cells exhibited large PDSs during the spike-like discharges, while cells farther away mostly showed hyperpolarization. This area distant to the focus was named the inhibitory surround. However, during longer ictal events, the neurons in the surround stopped exhibiting inhibition and instead showed the typical PDS of those in the epileptogenic focus (Prince & Wilder 1967). Further studies showed not just a focus and surround, but an intermediate zone in which cells exhibited both hyperpolarization and depolarization during the interictal spikes (Dichter & Spencer 1969a). It was posited that during these events penicillin disproportionately increased recurrent excitation in the focus while recurrent inhibition remained strong in the surround, until eventually the more prolonged action of inhibition in the focus overcame and terminated the discharge. A delay in this recurrent inhibition may have opened the window for afterdischarges and seizures (Dichter & Spencer 1969b). Experiments in

neocortical slices saw a dose-dependence of bicuculline on evoked activity, and that synchronized epileptiform activity can occur even in the presence of robust cortical inhibition (Chagnac-Amitai & Connors 1989). Recent studies have shown correlates of this inhibitory surround on MEA recordings during seizures in humans. There are instances where seizure-like activity is seen on low-frequency LFP or EEG recordings in the surround, or ictal penumbra, but the underlying neurons do not exhibit the hypersynchronous spiking of those in the ictal core, possibly due to mechanisms of inhibitory restraint similar to those in the animal models (Schevon et al. 2012).

Chapter 3 **Novel Hardware**

Summary

ECoG arrays offer higher resolution recordings than EEG and do not cause the tissue damage and gliosis seen in rigid, penetrating electrodes (Polikov et al. 2005; Griffith & Humphrey 2006). Arrays used clinically have a low spatial resolution in order to enable coverage of large areas of cortex. Higher-resolution arrays, or micro-ECoG (μECoG), can enable the use of surface recording in other applications such as brain machine interface, and with large area coverage, may provide a better tool for seizure localization (Viventi et al. 2011). μECoG devices have been developed using flexible silicon electronics to enable on-chip multiplexing, creating a conformal, dense electrode array capable of covering large areas with few connected wires. Recordings in a seizure model have shown intricate spatiotemporal patterns of epileptic activity in the cortex. Constructing these silicon devices can be a difficult and expensive process. Alternatively, organic electronics can be fabricated more easily and at lower cost than flexible silicon electronics on the same type of plastic substrates. ECoG is limited in some research applications since it is difficult to investigate the underlying neurons by other means. New graphene-based transparent electrodes offer the ability to electrically record and optically image the same area of cortex simultaneously. This allows researchers to combine the advantages of both methods and get a clearer picture of neural activity.

Results

High-Resolution Multiplexed Arrays

The μECoG arrays developed, shown in Figure 3.1, consisted of 360 platinum coated electrodes that measured 300 x 300 μm with a spacing of 500 μm, a 400 times higher spatial resolution than clinical arrays. They were fabricated on a thin polyimide substrate which allowed for maximum flexibility on the uneven surface of the brain, even capable of recording in the hemispheric fissure. At each electrode were two transistors created using silicon nanomembrane technology, which allowed them to flex without loss in performance. The electrode fed into the gate of the first transistor (QB in Figure 3.3) which was in a common drain amplifier configuration with a constant current source off-chip. This served to preserve signal quality by acting as a voltage buffer, reducing any loading from the wires to the recording equipment. The second transistor (QMUX) multiplexed the signal into a common output wire for all electrodes in the same column, controlled by an input signal common to all electrodes in the same row. These silicon transistors allowed for high-speed multiplexing under 5 μs and high sampling rate over 10 kS/s/channel. The multiplexing allowed all 360 channels to be recorded with only 39 connections off the array: 20 column lines outputting multiplexed data, 18 row lines to control the multiplexing, and one voltage supply line, VD, for the drain of the buffer transistors.

The electrodes were designed in the Litt Lab and fabricated in Rogers Lab at the University of Illinois. The fabrication was a multi-layer process. First, ribbons of doped silicon nanomembranes were transfer printed as the initial layer. Next, metal interconnects were patterned to form the contacts of the transistors, insulated by layers of polyimide. The metal contact layers were connected through offset vertical interconnect access (VIA) holes and additionally encapsulated with polymer in order to prevent electrical leakage. Finally, platinum was deposited onto the electrode surfaces to reduce their impedance. Further details on the electrode designs and fabrication process can be found in previous publications (Viventi et al. 2010; Viventi et al. 2011).

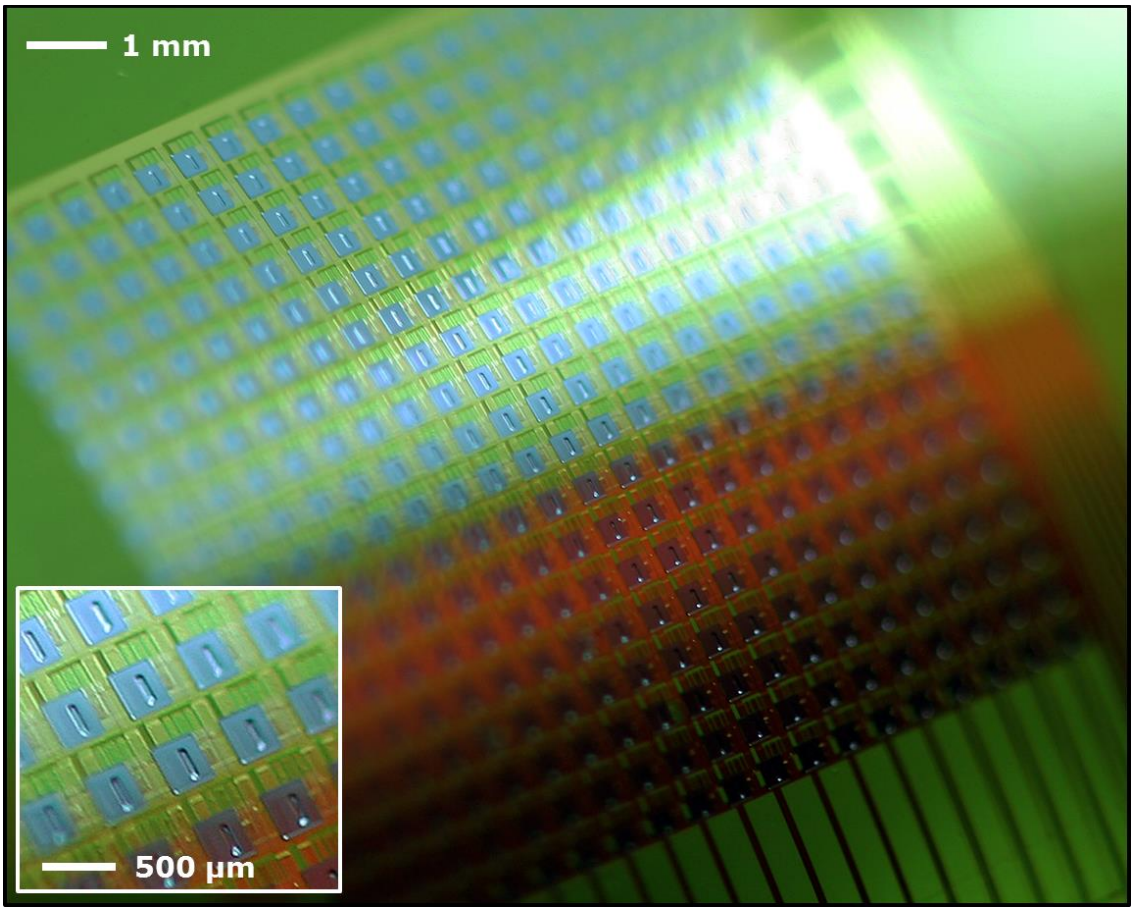

Figure 3.1 Multiplexed µECoG Array Photograph of 360-channel µECoG array with multiplexing and buffering at each electrode. Inset shows close-up of each electrode subunit with two transistors.

Recording Hardware

In order for these arrays to operate to their full extent, custom hardware and software was designed to control their operation and record the detected signal. The recording system for the µECoG arrays utilized a Data Acquisition device (DAQ) to digitize and stream the neural data and to output controls for the on-array multiplexing. The DAQ contained four National Instruments PXI-6289 cards, each with 32 analog input channels (16 differential), four analog outputs, and 48 digital I/O ports (32 clocked). These cards had 18-bit analog to digital converters capable of sampling up to 500 kS/s in aggregate, which reduced by a factor of the number of analog input channels in use. High-resolution analog-to-digital converters are required due to the presence of large offset voltage fluctuations between multiplexed channels, effectively limiting the analog pre-amplifier gain prior to digitization. These fixed voltage fluctuations were removed in a subsequent digital high-pass filtering stage after software demultiplexing.

The DAQ was connected to an acquisition computer that controlled its functions using custom-designed LabVIEW programs. Custom hardware was designed to interface between the µECoG grid and the DAQ. This hardware was comprised of two printed circuit boards: one with the circuitry to capture the analog signals of interest and another to control the row multiplexing. There were 2 sets of boards that connected to the array, each capable of 16 inputs and outputs, allowing connection to an array up to 32 columns and 32 rows. The boards could either connect to a DAQ with two cards or with four cards to obtain an increased sampling rate. Figure 3.2 shows the overall block diagram of the entire recordings system.

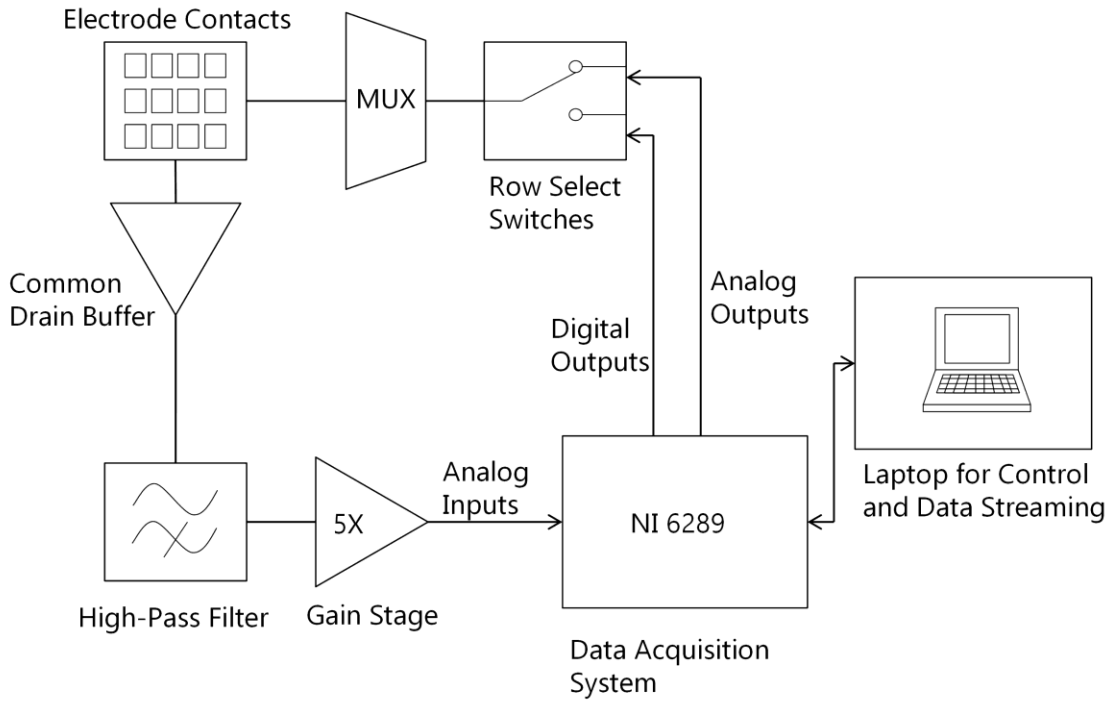

Figure 3.2 Complete Data Acquisition System Block Diagram Analog signals captured by the microelectrodes were buffered, filtered and amplified before being converted to digital data and streamed to disk. The DAQ controlled the row select switches that chose which electrodes were recording at a given time. From (Bink et al. 2013).

Figure 3.3 shows the circuit diagram of the off-chip hardware for one row and column of electrodes. On the analog side, the first stage off the array was the constant current source for the buffer transistors at each electrode. It was comprised of a low-noise op-amp with a resistor and commercial JFET transistor in its feedback path. Since the voltage was equal at both op-amp inputs, the resistor, RS, created a constant current across it to the negative supply voltage, VS, which was drawn through the transistor, QS. To keep its inputs equal, the op-amp adjusted its output voltage so the current remained fixed regardless of the voltage presented at the source of the transistor on the array, which tended to vary on different devices. The current could be adjusted by changing the input voltage to the op-amp, VSET. Often, the on-chip positive voltage supply, VD, was tied to ground or a small positive voltage in an attempt to reduce any leakage current that could have passed through the electrode to the subject.

The output of the source follower was then buffered on the board with a unity gain op-amp amplifier and fed through a 0.01 Hz high pass filter to remove the common DC signal introduced by the source follower. Finally, the output was amplified by a gain of five using a non-inverting op-amp configuration. The gain was limited to five to prevent saturating the analog to digital converter when used with electrode arrays with unusually high voltage offset fluctuations (±2 V max for ±10 V analog to digital input range). A programmable gain amplifier in the DAQ cards allowed further optimization of the overall system gain for more typical performing devices (<± 0.4 V fluctuation, ± 2 V analog input range range). The amplified signal was fed to the DAQ to be digitized and streamed to the attached computer.

On the array, when a single row select line turned on, it allowed signal from every electrode in its row to be recorded. Once a set number of samples were taken from that row, the line turned off and the next one activated, sweeping through the entire array. Because the multiplexing transistors were negatively biased in the common drain circuit on the array, digital 0-5 V outputs from the DAQ could not be directly used to control the row switching. Instead, two analog outputs were used as the high and low voltages for the row select transistors, the values of which were set in software. Digital DAQ outputs were used to control single pole, double throw switches, capable of turning each row line on or off as shown in the upper right of Figure 3.3.

Finally, an instrumentation amp was used to measure the current between the reference contact and ground. This measurement was indicative of how much current was flowing from the array to the test subject. Ideally, this value was nearly zero, but defects in the array or breakdown in encapsulation could allow unwanted contact between charged

components on the grid and the brain. The measured current was monitored in software and if it passed a set threshold, protective circuitry around the power supply was activated to shut off the system. This was the main method used to prevent damage to the brain in the event of array malfunction.

This iteration of data acquisition hardware showed great improvement in buffer gain, up to 0.97 for the best devices, which was a 13% increase over the previous design. This system still maintained a reasonable noise level of around 55 µV r.m.s. In testing using a 100 mV peak-to-peak sine wave, an SNR of 56 dB was achieved. Multiplexer cross-talk was below -65dB.

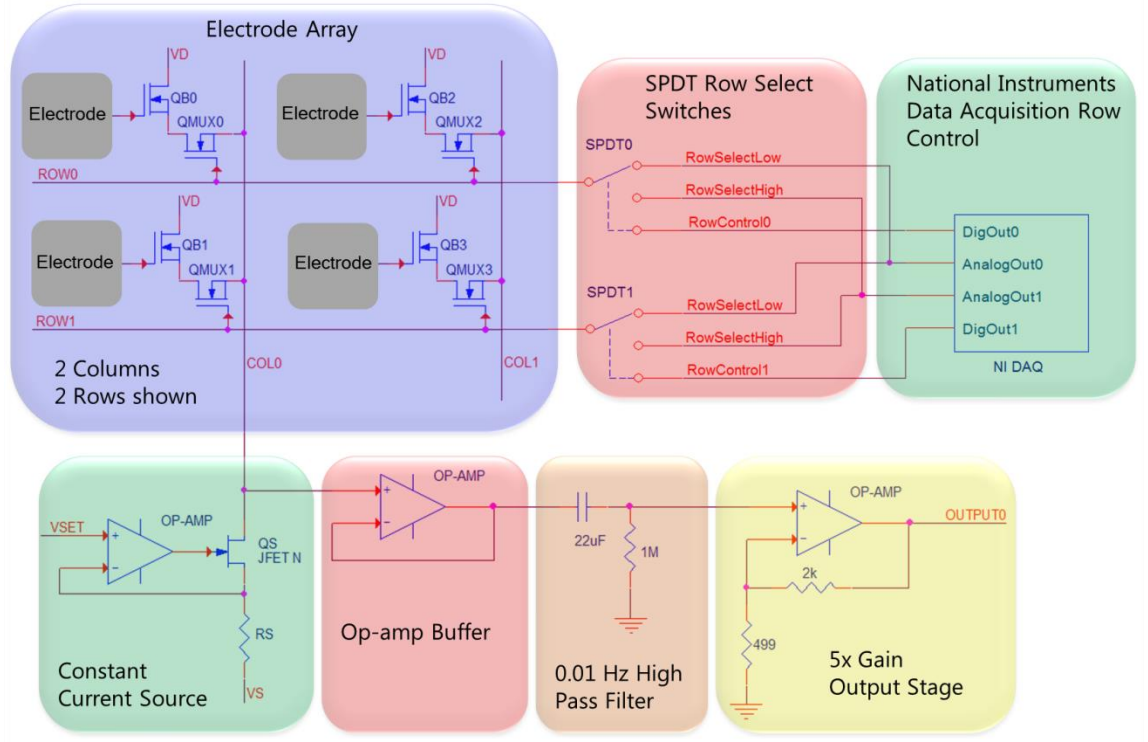

Figure 3.3 Data Acquisition Analog and Digital Subsystems Block Diagram An op-amp current source provided the load for on-array buffers. The signal was then buffered again through an op-amp before being filtered to remove the DC component and finally amplified by a factor of 5. The DAQ set the low and high row select voltages and digital control of each single pole, double throw switch. When one switch turned on, every electrode in its row began recording. Adapted from (Bink et al. 2013).

Seizure Recordings

The μECoG arrays were tested in different animal preparations including porcine heart, feline visual cortex and rat auditory cortex, covering several different iterations of array design and accompanying hardware (Viventi et al. 2011; Viventi et al. 2010; Escabi et al. 2014). In each of the experiments, the arrays successfully recorded biological signals such as cardiac rhythm, sleep spindles, visual evoked potentials and auditory evoked potentials. Additionally, picrotoxin-induced seizures were recorded in the feline model with methods similar to those described in Chapters 4 and 5. Figure 3.4 shows a small example of the epileptiform activity recorded using these arrays, then processed and analyzed using custom MATLAB code. The upper trace shows the signal from a representative channel during a seizure. The plots below it give snapshots of the entire array during the seizure, highlighting the intricate spatiotemporal patterns that are missed on lower resolution ECoG arrays.

The seizure depicted in the figure undergoes several stages that are defined by the changing spatiotemporal dynamics of the recorded spikes. The first stage, which contains only the large initial spike, shows a negative peak which enters left then turns downward, followed by a positivity that does the same. This turns into a clockwise spiral for three spikes that exhibit a similar path to the first, but completes a full circle around the array. The rest of the seizure consists of spirals in the opposite direction, as well as plane waves travelling left to right and right to left. Many different spatiotemporal patterns were found in these recordings and further work clustering them showed that some were more common in seizures than interictal spikes (Vanleer et al. 2016). The results from this work spurred the research detailed in Chapter 5 of this dissertation, aiming to provide more detail on the physiological basis of these types of patterns. They also showed the need for higher resolution devices in researching and diagnosing human epilepsy, as well as exciting possibilities for future seizure termination devices.

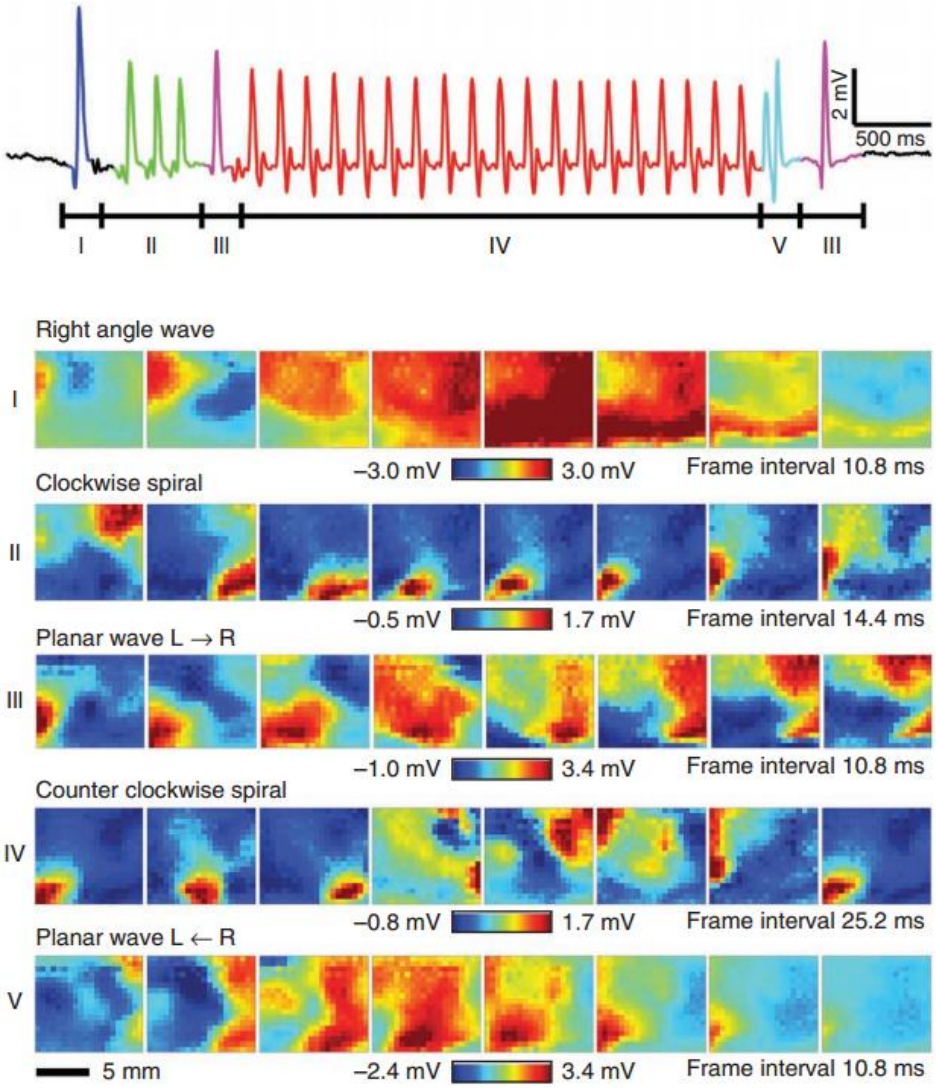

Figure 3.4 Multiplexed µECoG Array Recordings of Induced Seizures in Feline Neocortex The upper plot shows signal from a representative channel of the array, with negative up by convention. The recording is broken up into segments which correspond to the sequences below it. Each sequence contains movie frames depicting the spatiotemporal voltage pattern from all 360 channels. The time between frames and color scale for voltage are noted below each sequence. From (Viventi et al. 2011).

Stimulation Hardware

The intricate spatiotemporal seizure dynamics shown may have implications on electrical stimulation used to disrupt seizures (Anderson et al. 2007). For instance, a clockwise spiral wave, like the one seen early in the seizure in Figure 3.4, may be effectively annihilated by a counter-clockwise wave of stimulation matching its phase. Multiplexed μECoG arrays offer the perfect medium to deliver such patterned stimulation on the sub-millimeter scale. This requires the ability to simultaneously record and stimulate on the array and to individually address stimulating electrodes, delivering customizable current waveforms through them. In order to satisfy these requirements, significant changes had to be made to the system.

Since it was not possible to pass current through the gate of the buffer transistor to the electrode, a change had to be made to the array circuitry. Since the fabrication process for flexible silicon circuits was very complicated, it was important this change did not increase the complexity of the design. With this in mind, the stimulation-capable array separated recording and stimulation columns, interleaving them on the substrate. Each electrode on the stimulating columns only contained the multiplexing transistor, so no new components were added. The units on the recording columns were left the same. Figure 3.5 shows a circuit diagram of this new array. The resulting decrease in the spatial resolution of the recording in one dimension can be mitigated by reductions in electrode size and spacing in future grids.

Along with changes to the array itself, new hardware components were built to deliver stimulation to the appropriate electrodes. The desired stimulation for seizure-termination tests was constant current, biphasic pulses with adjustable frequency, amplitude, pulse width, duration, and wave shape. Another requirement was the ability to test both monopolar and bipolar regimes, with selectable returns for bipolar testing. Finally, each column had to be capable of delivering its own stimulus independent of the others. In order to fulfill all of these conditions, each stimulating column needed its own circuit that could source and sink current with varying parameters and switch between stimulating, return and open modes.

A single pole, double throw (SPDT) switch with an enable control was connected to each column so it could operate in three different facets, as seen in Figure 3.5. First, setting enable input low resulted in an open circuit for the electrodes on that column, which would serve as the state of any contact not actively stimulating or acting as a return path. When the enable was high, the switch could be connected to circuit ground or the output of the constant current circuit. Having a ground connection for the electrodes served two

needs. The first was that it acted as a bipolar return for current injected on other electrodes. Multiple contacts could be selected in different patterns to test varying bipolar configurations, within the limits of the multiplexing architecture. If monopolar stimulation was desired, no ground connections was be made, allowing the current to flow to the single reference on the animal. The second use for the ground connection was to short the contact after a pulse had been delivered to remove any excess charge that may have built up at the electrode-tissue interface. This is mostly precautionary, as there should be little residual charge due to the charge balancing of biphasic pulses (Chun et al. 2010; Constandinou & Georgiou 2008).

A Howland circuit was implemented as the constant current source for the stimulating columns. This circuit, consisting of an op-amp and four matched resistors, R1-R4 in Figure 3.5, was capable of providing both positive and negative currents with high output impedance (Texas Instruments 2008). The current provided by the circuit was controlled by an input voltage, Vcurrent, and was independent of the load impedance, an essential quality for this application since the impedance at the electrode-tissue interface can vary greatly. The analog outputs from the NI DAQ were used to set the current from the Howland pump and controlled by code in the LabView software. This granted great flexibility in controlling the parameters of the stimulation, including the shape of the waveform, amplitude, duration and frequency. By having a separate current supply on each line, the hardware could deliver different user-defined stimulus patterns that varied across the array. This would be very important in trying to determine optimal methods for delivering patterns of electrical pulses to the brain to modulate seizure activity.

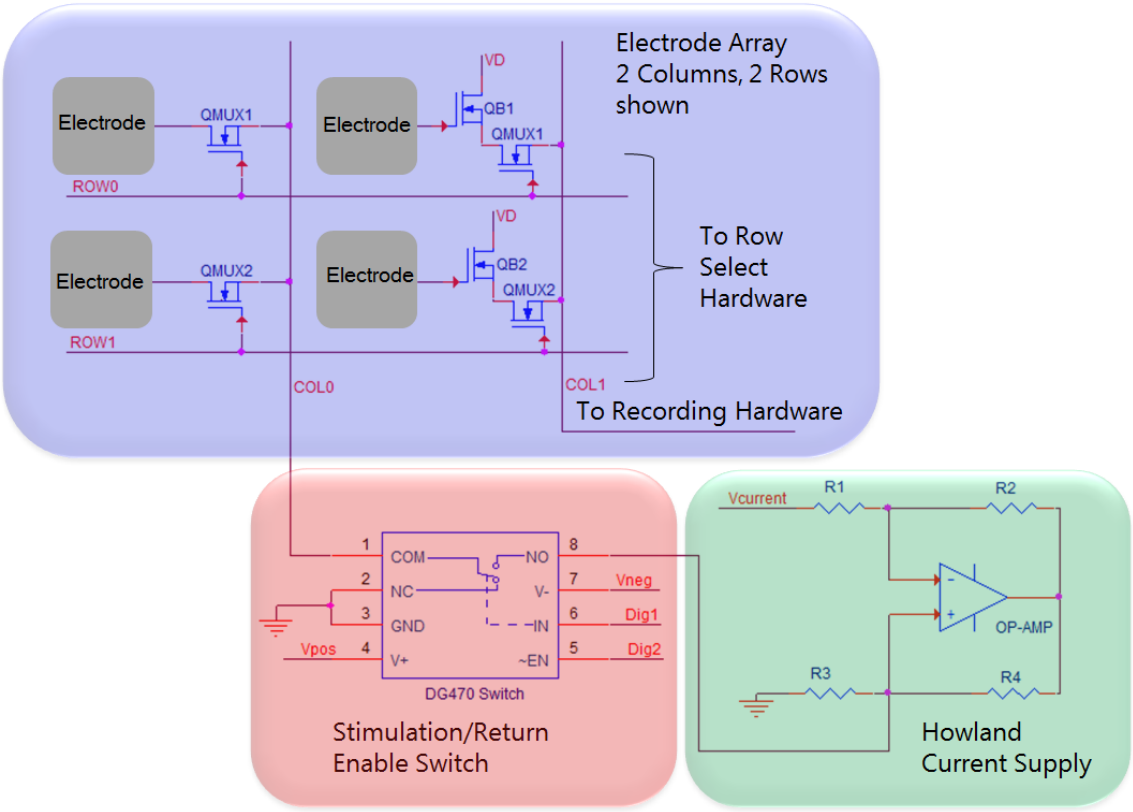

Figure 3.5 Schematic of µECoG Array with Stimulation Hardware for recording columns is the same as in Figure 3.3. Stimulating columns only have multiplexing electrodes. A Howland circuit provides constant current delivered through a switch as controlled by the DAQ.

Organic Devices

Organic materials are considered a promising candidate for flexible electronics due to the low temperatures required for fabrication. Through intensive research in the past decades, organic materials have been shown to exhibit carrier mobility comparable to or higher than amorphous silicon used in modern active-matrix liquid-crystal displays (Klauk et al. 2002). In addition, synthetic chemistry is able to tailor organic materials in a way that cannot be done with inorganics. The increased functionality of organic transistors can enable a broad array of biological signal monitoring applications.

Pentacene, among the highest performance organic thin film semiconductor materials available, is insoluble in most organic solvents. A soluble pentacene precursor can be dissolved in a chlorinated solvent, such as chloroform, and subsequently thermally converted into pentacene (Afzali et al. 2002). This production technique opens the door to large area fabrication of organic transistor circuits at low cost. These solution processable organic thin film transistors can be integrated directly into neural electrode arrays using photolithographic methods for fabrication. Combining these devices with custom circuits, common source and common drain amplifier topologies can be built with performance sufficient for recording neural signals.

Transistor Fabrication and Characterization

Pentacene thin film transistors (TFTs) with a bottom-gate, bottom-contact configuration on a Kapton® substrate were fabricated by collaborators in the Kagan lab at the University of Pennsylvania according to the method described in (Saudari et al. 2010) and (Saudari et al. 2009). A schematic of the device is illustrated in Figure 3.6a. Gold gate and source/drain contacts were patterned by photolithography with a thickness of 20 nm. A 500 nm parylene-C dielectric layer was deposited through physical vapor deposition. The pentacene precursor was applied by spin-coating and then thermally converted to pentacene to form the bottom-gate, bottom-contact configuration TFT. Figure 3.6b shows photograph of the device electrodes before spin-coating the organic semiconductor.

Representative device characteristics measured under inert nitrogen environment are shown in Figure 3.6c and Figure 3.6d. Hole accumulation can be seen in the I_{DS}-V_{DS} curve, characterized by linearity at low absolute drain-source biases and saturation at large negative biases. The saturation mobility was 0.123 ± 0.038 $cm^2/(V \cdot s)$, extracted from more than 50 transistors fabricated on different samples. The on/off current ratio was about 105, as shown in I_{DS}-V_{GS} curve (Fig. 1d).

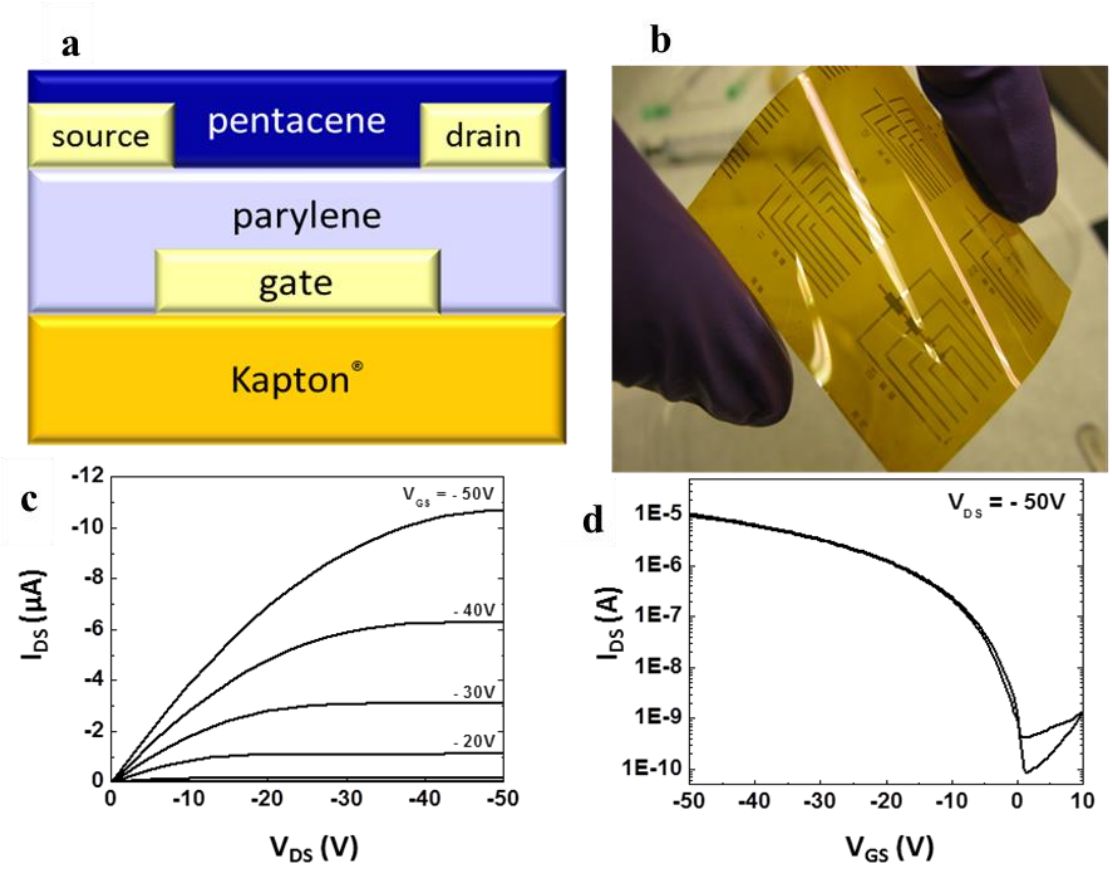

Figure 3.6 Organic Transistor Fabrication and Characterization (a) Schematic of the organic thin film transistor, a photographic example of which is seen in (b). (c) and (d) are the representative I_{DS}-V_{DS} and I_{DS}-V_{GS} properties of the devices, respectively. The channel width was 1500 µm and length was 100 µm. These properties were measured in an inert nitrogen environment. From (Bink et al. 2011).

Circuit Configuration

The pentacene TFTs were tested in both common source and common drain amplifier configurations. A circuit consisting of all elements of the amplifying configurations except the transistor was created using a custom printed circuit board (PCB), which is shown in Figure 3.7. In order to make the electrical connection between the pentacene TFTs on a flexible substrate and the PCB, the buried bottom gate had to be revealed. This was done by removing the pentacene over the electrode pads with chloroform. The parylene dielectric was then selectively etched with oxygen plasma, while keeping the active area protected. An additional small PCB with switches and finger-shaped beryllium copper contacts on the underside was designed to make mechanical contact with the flexible substrate of the transistor array. By clamping the small PCB onto the larger PCB with the flexible transistor array in between, the beryllium copper fingers were able to make solid mechanical contact with the electrodes of the transistor array, forming the electrical connection to the PCB. The pressure contact PCB is highlighted in yellow and enlarged in Figure 3.7. A short ribbon cable was used to connect the gate, source and drain of the organic transistor to their respective locations on the main PCB.

The circuit on the main PCB was designed to be used for either common source or common drain amplifying circuits. Since the source and drain of the organic transistors were interchangeable, switching between the two configurations was possible by changing power supply polarity. The schematic for this circuit is shown on the bottom of Figure 3.7. A 10 MΩ resistor was connected to the drain or source of the organic transistor depending on the desired circuit topology. This large resistance was used in order to yield higher gain. Power was supplied the organic transistor amplifier (VDD and VSS) through 0.14 Hz low-pass filters in order to reduce noise coming from voltage supply electronics. The amplifier output was directly connected to a unity-gain buffer in order to reduce loading by subsequent measurement equipment. This was then fed through a 0.16 Hz high-pass filter to remove DC bias and a second op-amp buffer to the output, Vout.

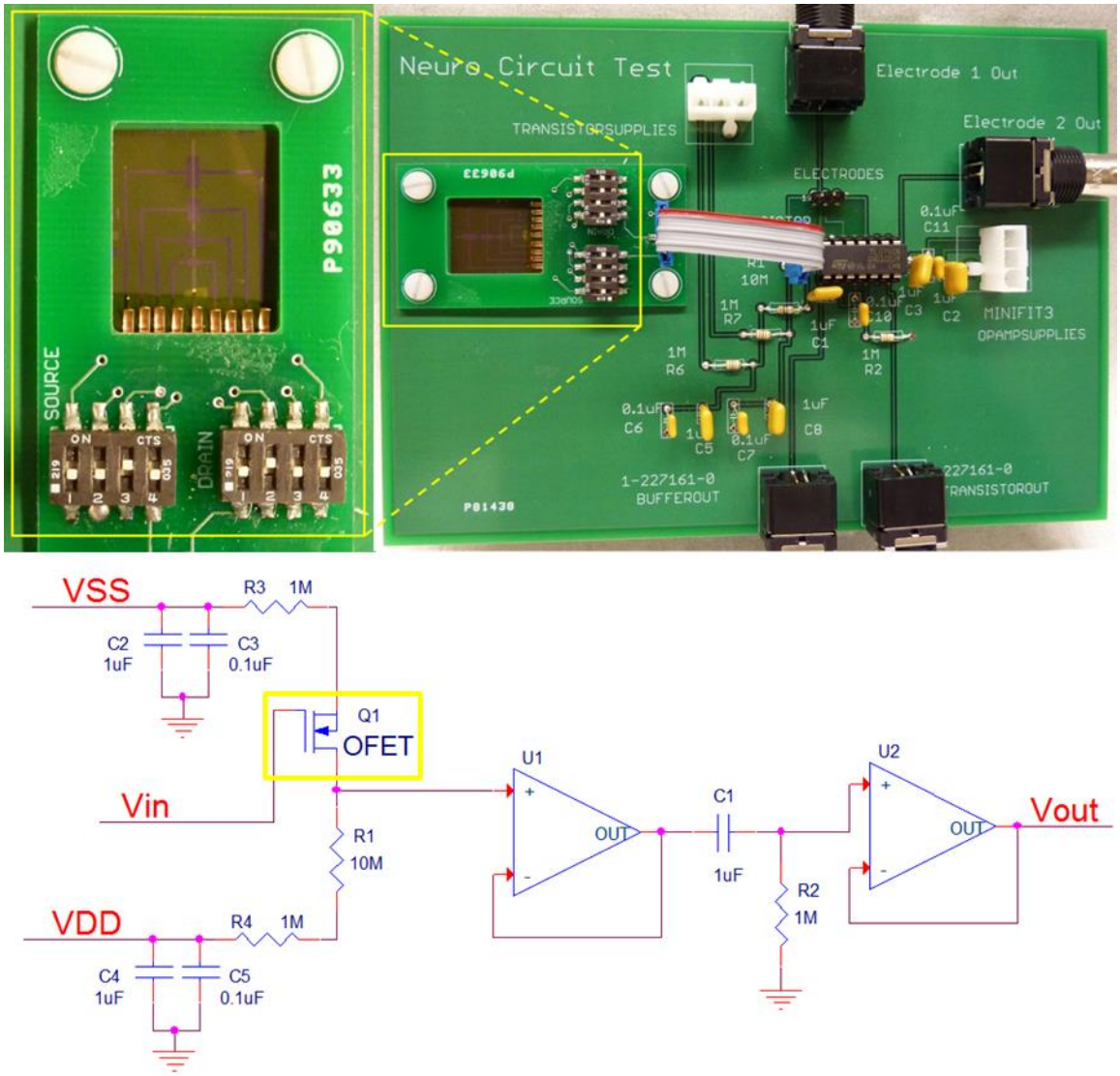

Figure 3.7 Dual PCB Board Design The large board in the upper photograph contains all elements of the circuit excluding the transistor: the amplifying resistor, lowpass power supply filters, output buffer and highpass filter, and input/output components. The ribbon cable attaches the transistor to the rest of the circuit. The enlarged image on the upper left clearly shows the copper fingers used to make pressure contact with the organic TFT underneath. From (Bink et al. 2011). The schematic on the bottom shows the circuit on the large board in the upper picture.

Amplifier Operation

The common source amplifier configuration was tested with multiple pentacene TFTs on the dual PCB setup. The source/drain transistor power supplies were kept at a difference of 50 V. The maximum gain was 5.0 dB for the highest performance device, while the average gain was 2.3 dB. Figure 3.8a shows a characteristic input/output voltage response for the best transistor with a 100µm channel. The source supply was +28 V and the drain supply was -22 V. The input was a 1 Vpp, 10 Hz sine wave. The output is inverted due to the common source topology.

The frequency response for the same organic transistor amplifier in the common source configuration is shown in Figure 3.8b. The -3 dB cutoff was observed between 700 and 850 Hz, depending on the transistor used. The square wave response rise and fall time of the amplifier was found to be 0.5 ms each. The common drain topology was tested by reversing the polarity of the TFT power supplies, effectively exchanging the source and drain. The maximum output of the device with a 1 Vpp input was 0.65 Vpp, or an attenuation of 3.7 dB. A frequency sweep revealed a -3 dB bandwidth of 2.8 kHz, much higher than the common source circuit, as expected.

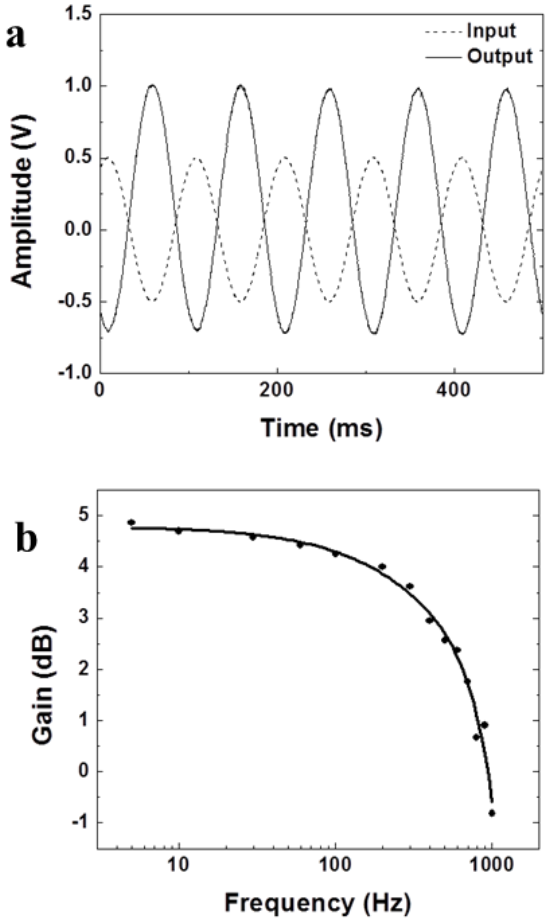

Figure 3.8 Amplifier Results (a) Representative output versus input and (b) bode plot from common source amplifier configuration using pentacene TFT. Both results shown were taken from the same 100 µm channel length device. From (Bink et al. 2011).

Transparent Graphene Electrodes

Graphene has become a very popular material in many fields due to its unique properties. It consists of a flat monolayer of carbon atoms in a two-dimensional honeycomb lattice and is the basis for all higher-dimensional graphitic materials such as graphite and carbon nanotubes (Geim & Novoselov 2007). Graphene has an incredibly high conductivity, both electrical and thermal. It is also the strongest material measured though less than 1 nm thick (Lee et al. 2008). Finally, due to its thin structure, graphene is almost completely transparent to light and incredibly flexible. These characteristics make it an ideal candidate for use in novel neural sensing electrodes.

Graphene electrodes were developed in our lab exactly for this purpose. Photolithographic methods were used to pattern the graphene and gold contact pads on a Kapton substrate, the same material used for the multiplexed μECoG arrays and organic transistors. An example electrode array is shown in Figure 3.9a. The graphene electrodes themselves could not be seen, only the metal contacts and the etched square in the encapsulation which allowed the graphene to contact the sample being recorded. In order to improve performance, the graphene was doped with nitric acid. An example of *in vivo* recording of bicuculline-induced epileptiform activity in rat model is shown in Figure 3.9b. It compares a 50 x 50 μm^2 doped graphene electrode to the same size gold electrode, both placed on the same hemisphere. The doped graphene recordings saw a nearly five times reduction in noise from the gold, with SNR values of 40.8 and 7.7, respectively. Interestingly, both materials had around the same impedance at 1 kHz, so the noise reduction seen in doped graphene was thought to be due to its large interface capacitance and small charge transfer resistance.

In addition to the low-noise electrical recordings demonstrated by the doped graphene electrodes, the transparency of the contacts allowed for even more information to be gathered about the brain simultaneously. Figure 3.9c shows the graphene electrodes used in conjunction with calcium imaging capable of providing single cell-level spatial resolution. It is clear in the figure that the electrode does not impede the fluorescence transmission in a stained hippocampal slice obtained by confocal microscopy. The electrode recording shows no light-induced artifacts, which is another advantage of the graphene electrodes. The temporal resolution of the electrical signal allows the higher frequency components of the ictal activity to be seen, which are not visible on the optical signals. However, the spatial resolution of the calcium transients captures the contribution of individual neurons to the epileptiform spiking. Combining the advantages of electrical and optical recording modalities allows us to get a clearer picture of network

activity within the brain, highlighting the impact transparent graphene electrodes can have.

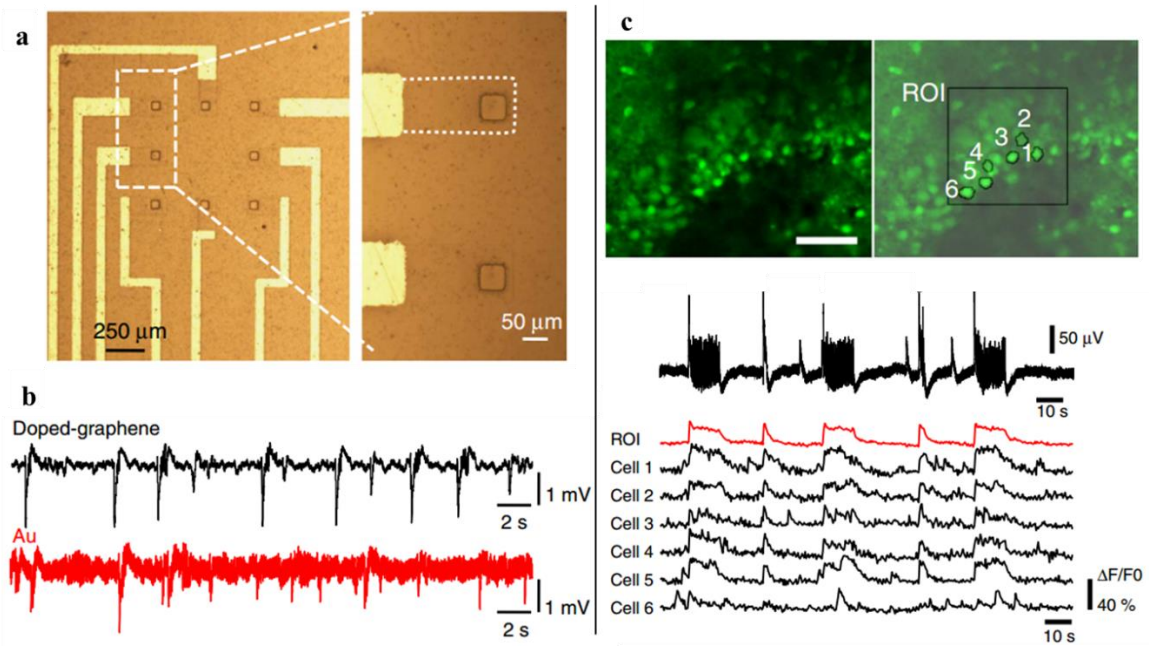

Figure 3.9 Graphene Electrodes and Recording Capabilities (a) Microscope image of an 8-electrode transparent graphene array with gold contacts and etched encapsulant visible. (b) Recording of epileptiform activity on doped graphene and gold electrodes of the same size. (c) Steady-state fluorescence (F0) image of calcium imaging on hippocampal slice obtained by confocal microscopy. The graphene electrode outline shadow is visible on the left, and six randomly selected cells within its region of interest (ROI) on the right. The top trace is graphene electrode recording, and bottom traces are calcium transients for selected cells and entire ROI in red. Adapted from (Kuzum et al. 2014).

Discussion

High-Resolution Multiplexed Arrays

The results from initial testing with high-density arrays show how much more information can be obtained from recording epileptic activity over current clinical electrodes. This could have huge impacts on seizure focus localization and resective surgery techniques. However, there are some further details that would need to be addressed for clinical use. First is the relatively limited coverage of the devices shown here. The arrays are theoretically scalable up to clinical ECoG grid sizes (8 x 8 cm) with 25,600 electrodes while maintaining high temporal resolution. This would require a dramatic increase in the accompanying hardware and an upgrade in the capabilities of the DAQ, which is feasible. The biggest issue that would affect such a scaling is in the fabrication, which caused problems even in the 360 channel devices. The process of making silicon nanomembrane transistors on a flexible substrate was very difficult, resulting in a low yield for usable devices. Having active elements directly on the array meant one of the primary causes of breakdown was current leaking through the encapsulation. In experiments, any appreciable current could be detrimental to the subject, which was a reason that a circuit was implemented in hardware to automatically detect leakage and cut power. If leakage was only an issue on specific rows or columns, they could be disabled and the rest of the array would work correctly. Most of the recordings were performed without 100% of the rows and columns active.

The grids for the epileptic recording were placed in the feline neocortex, near V1/V2, and picrotoxin was applied topically to induce seizures. This preparation was nearly identical to the experiments performed in Chapter 5. However, such intricate patterns were not seen in those recordings. Part of that may be due to the lower spatial resolution of the grids used in those tests, which had a 1 mm pitch as opposed to 0.5 mm. Another possible reason is the difference in application of picrotoxin. The Chapter 5 experiments that used a surface application used less of the drug in a more confined region of cortex. This produced a more well-defined seizure focus where spikes originated, so the waves were more consistent in their spatiotemporal spread. The more diffuse application in the multiplexed array recordings allowed for a larger focus, or multiple foci, which resulted in spikes starting in different locations, affecting how they travelled.

Organic Devices

The gain of the common source amplifier using pentacene TFTs (between 2.3 and 5 dB) was promising for use in neural amplifiers. Integrating any level of gain directly at the electrode could improve the overall system performance. The attenuation seen in the organic transistor in common drain configuration, 3.7 dB, would decrease the overall system performance, but would still be acceptable for many neural signal acquisition tasks.

One tradeoff for increased gain was decreased bandwidth: ~800 Hz for the common source configuration versus ~2.8 kHz for the common drain configuration. Given that the majority of clinically relevant, cortical surface brain activity occurs below 500 Hz (Worrell et al. 2008), a bandwidth of 800 Hz would be sufficient for most applications. However, developing multiplexed electrode arrays may be difficult, given the low frequency response of the transistors.

A cause of this low bandwidth is the high output impedance of the TFTs. Due to an Early voltage of around 150 V and a relatively low drain current, the output impedance seen at the drain of the could be up to 100 MΩ. Similarly, a low transconductance led to not only low gain, but high impedance at the source of up to 10 MΩ. Since the load resistor value used was high (10 MΩ) to increase gain, the overall output impedance of both common source and common drain topologies was also be large, around 10 MΩ and 5 MΩ, respectively. This would not only lower the bandwidth, but increase the noise picked up at the output of the device.

One of the challenges faced while testing the amplifiers was the performance reduction of the pentacene TFTs in ambient atmosphere. Devices were initially characterized directly after fabrication, while still immersed in a pure nitrogen environment. The devices were subsequently retested after being exposed to open air. Carrier mobility, and likewise drain current, both continuously decreased as a result of exposure to moisture and oxygen. Several different encapsulating materials were applied to the TFTs in preliminary attempts to prevent this degradation. None of the materials investigated effectively protected the devices from reduction in their performance while exposed to air.

There are several items remaining to be addressed before organic transistors can be used to develop large arrays of multiplexed electrodes. First, the noise performance of the organic transistor amplifiers must be evaluated to insure sufficient signal to noise levels in the final system, while measuring neural signals of 1 mV amplitude or less. This would need to be tested in experimental settings where long runs of wires come off the grid to see the effect of high output impedance on noise susceptibility. Second, the ability to pattern hundreds of organic transistors on a single flexible substrate needs to be developed. Prototypes of such devices have been fabricated, utilizing etching and

deposition processes to create vertical integration access (VIA) holes to connect individual transistors using multiple metal layers. Finally, a new encapsulation system needs to be developed to fully protect the transistors from exposure to air and biological fluids. New fabrication procedures and encapsulation materials have been evaluated for their long term reliability.

Transparent Graphene Electrodes

The graphene electrodes developed showed incredible promise for research by combining the temporal resolution of electrical recordings with the spatial resolution of optical techniques. One of the problems encountered when combining electrical recordings with optical techniques was a lower transmittance, not due to the graphene but due to the polyimide substrate. An increase in laser power about four times above normal was required to view fluorescence samples in the confocal microscopy experiments. A power increase was not required in two-photon imaging because it uses light transmittance at 840 nm, which is transmitted better through the Kapton substrate than 488 nm, used for the confocal microscope. A thinner substrate could mitigate the occlusion of light, or using a different substrate whose transmission spectrum matches better with the type of imaging being used.

Chapter 4 **Cortical Stimulation Responses**

Summary

Advanced techniques for treating patients with medically refractory epilepsy are being developed and implemented, but many fundamental questions that could improve them remain unanswered. Neuromodulation devices are becoming a popular alternative to resective surgery, and new μECoG electrodes have been developed that are capable of high-resolution patterned stimulation on the cortical surface. The ability to effectively use these advanced technologies, however, is limited by our understanding of how the cortex responds to direct electrical stimulation. Current devices grew out of the success of deep brain stimulation for movement disorders and used similar techniques to show early positive results in seizure reduction. The mechanisms through which the injected current disrupts seizure propagation are still unclear, as evidenced by the wide range of devices (open-loop vs. responsive, peripheral vs. subcortical vs. cortical stimulation targets) that have shown similar efficacy in clinical trials. This chapter aims to elucidate the effect of electrical stimulation on local circuits within the cortex in order to better understand how to best implement them in future neuromodulation devices.

To investigate the capabilities and limitations of electrical stimulation, experiments were performed in the visual cortex of healthy cats using high spatial resolution μECoG surface grids and linear depth arrays to record responses to direct current injection with varying parameters. First, visual stimulation trials showed that the high density surface contacts were able to pick up spatially-confined biological signals. These included visual evoked potentials that changed across functional areas and orientation tuning columns on a limited number of electrodes. Electrical microstimulation was performed at varying depths and intensities, revealing complex laminar patterns that were very dependent on the physiology of the local network. Increasing intensity resulted in stronger responses, but there was a limit to the radius of activation independent of stimulus depth or intensity. Recordings on surface and depth electrodes distant to the site of stimulation exhibited stereotypical LFP responses even though underlying CSD showed no local current activity. This result suggests that much of the recorded LFP reflected volume conduction and not local synaptic activity. These findings have great potential impact on seizure localization, as recorded signals may not accurately reflect the activity in underlying tissue. Additionally, the limited spatial effect of stimulation and its dependence on the surrounding physiology has implications on the design of neurostimulation devices.

Methods

Animal Protocol

Experiments were conducted according to the guidelines of the National Institutes of Health and with the approval of the Institutional Animal Care and Use Committee of the University of Pennsylvania. Adult male cats (2.5–3.5 kg) were anesthetized with an intraperitoneal injection of Nembutal (25 mg/kg) followed by supplemental isoflurane (2–4% in 70% N_2O and 30% O_2). The animal was paralyzed with gallamine triethiodide (Flaxedil) and artificially ventilated (end tidal CO_2 held at 3.8–4.0%). Anesthesia was maintained by continuous infusion of propofol, fentanyl and dexmedetomidine throughout the experiment (12–16 h). Heart rate, blood pressure, and electroencephalogram were continuously monitored. Rectal temperature was maintained at 37−38°C.

Recording Details

The two types of recording arrays used in these experiments were both commercially available passive electrodes from NeuroNexus Technologies, Inc. Commercial arrays were chosen over the multiplexed μECoG grids (discussed in Chapter 3) because the fabrication of those devices was very difficult and the technology very new, which would have added unnecessary complexity to the experiments. The surface grids (Model Number E32-1000-30-200) had 32 platinum-coated recording sites fabricated on a flexible polyimide substrate. Individual electrodes were 200 μm in diameter with a spacing of 1mm, arranged over 4 rows and 8 columns, giving a total size of 7.14 x 3.7 mm, large enough to cover most of the feline primary visual cortex (Tusa et al. 1978). There were also 21 holes in the substrate between the electrodes through which depth arrays were placed. Rigid penetrating probes (Model Number A1x16-5mm-150-703) consisted of 16 vertically arranged, iridium-coated contacts with a diameter of 30 μm. The total shank length was 5 mm with electrodes arranged over 2.25 mm, enough distance to cover the thickness of cat neocortical layers in V1 (Payne & Peters 2002). Grid layouts and relative placements of depth arrays can be seen in Figure 4.1 for the electrical stimulation experiments performed.

Experiments were recorded using a Neuralynx digital data acquisition system. The sampling rate was 32 kHz for all experiments, with a 300 Hz online low-pass filter and high-pass filter at 0.3 Hz or 1 Hz. Data was downsampled to 2 kHz and analyzed using MATLAB software. Reference and animal grounds were tested in many different

locations and placed in such a way to minimize noise contamination in the recordings. References were placed either on a bone screw rostral to the recording site or in moist gauze between the skull and skin. Grounds were typically placed on the neck muscle or the retractors opening the skin to expose the cranium. It was very important to keep all the references and grounds in separate locations to reduce line noise on the recordings. The experiments took place in a Faraday-caged room as well in attempts to keep out extraneous electrical noise. The biggest artifact seen was low-frequency drift in the signals, but since it was non-continuous and only on a small percentage of channels, the overall fidelity of the recordings was not compromised by its presence.

Visual Stimulation

For visual experiments, the pupils were dilated with 1% ophthalmic atropine and the nictitating membranes retracted with phenylephrine. Contact lenses were used to protect the corneas and spectacle lenses chosen to optimize the focus of stimuli on the retina. Visual stimuli were presented on a spatially adjustable monochrome monitor (Image Systems model M09LV) situated 30 cm from the lenses. The monitor had a spatial resolution of 1024 x 786 pixels and a mean luminance of 47 cd/m^2, operating at 125 frames per second.

Electrical Stimulation

The recording arrangement for electrical stimulation experiments was the same as for visual stimulation. Current was delivered via a bipolar stimulating electrode composed of a pair of insulated tungsten wires 50 μm in diameter with tips exposed. It was inserted just next to the surface array, or through one of the holes in it, using a stereotaxic micromanipulator to control positioning. The current supplies used were an FHC Pulsar with a Grass constant current isolation unit or an A-M Systems Model 2100 Isolated Pulse Stimulator. The stimulation waveforms were square waves with 100 μs duration per phase. Stimulating electrode depth and current intensity were swept in experiments to see the effect of these parameters on the cortical response. Multiple trials were performed for each setting and averaged to obtain an evoked response at every recording site. Six stimulation experiments were performed in total. Figure 4.1 shows the locations of the depth electrode arrays and stimulating electrodes relative to the surface ECoG grid for each experiment.

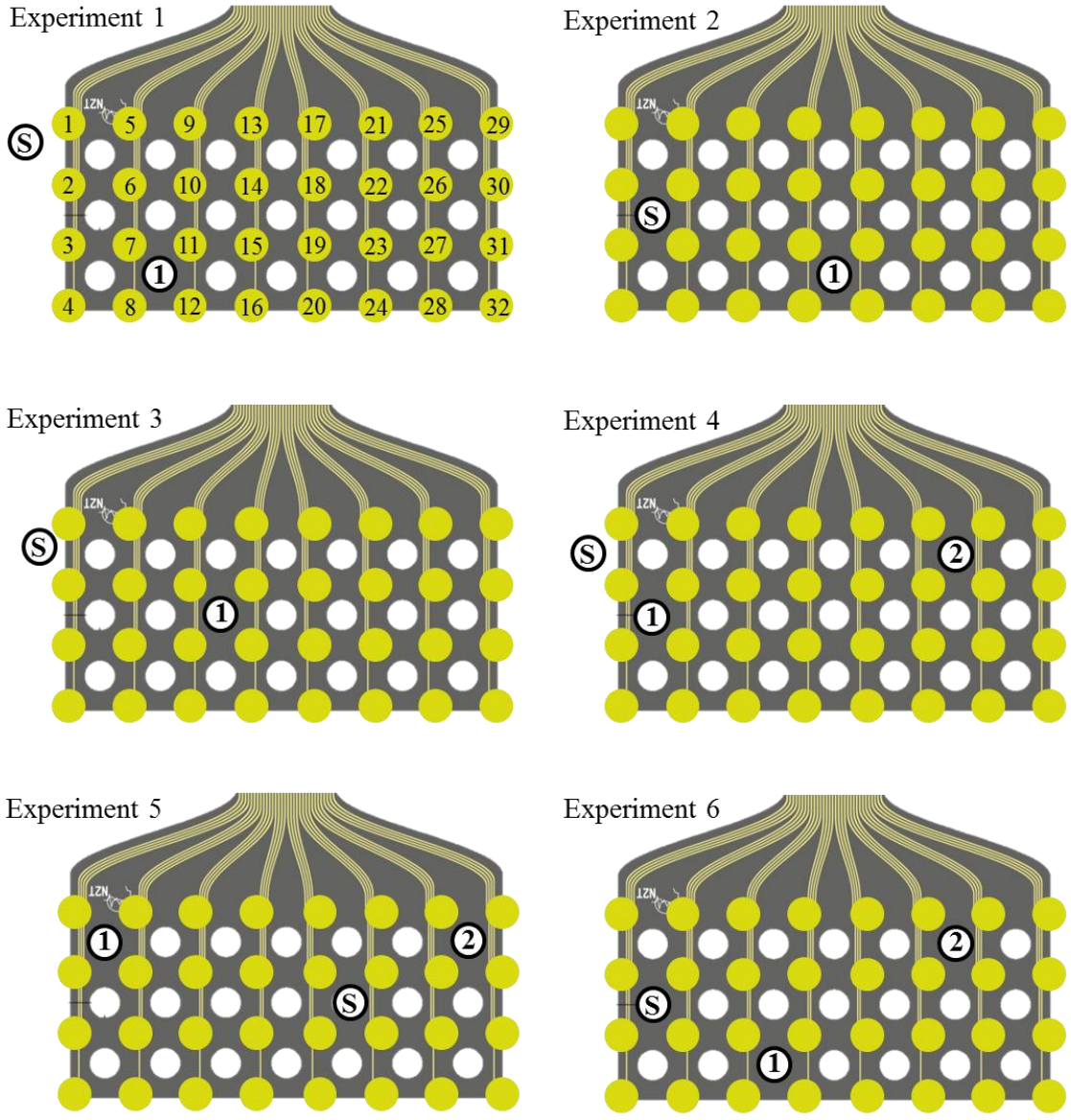

Figure 4.1 Electrode Arrangements The surface array is shown for each experiment, with gold circles representing electrodes and white circles the holes in the substrate. The electrode numbering convention is shown in the experiment one example. The illustration orientation is looking down from above the arrays as they would appear in the craniotomy, such that the exposed contacts underneath are touching the cortex. The positions of the depth shanks and stimulating electrodes are noted relative to the ECoG grid.

Results

Visual Stimulation

The impetus behind using visual stimuli was to elicit a natural, known response in the cortex to validate the LFP recordings and determine the capabilities of high-resolution arrays. Drifting gratings were chosen as the primary stimulus because of the arrangement of orientation-specific columns in visual cortex. The ability to adjust the temporal and spatial frequency of the grating was another advantage in order to discriminate between V1 and V2. Additionally, the immediate response in the cortex to the beginning of each stimulus presentation was consistent and independent of orientation or frequency. These evoked responses could be averaged to obtain a high enough SNR to perform CSD in the depth and look for a known pattern of propagation through the layers to verify the shank electrode recordings.

Orientation Tuning

The visual stimuli consisted of full-field drifting gratings of 100% contrast presented for 1 s over eight different orientations with 45° separation. Spatial frequencies were varied between 0.2 and 1.3 cycles/degree and temporal frequencies from 1 to 5 Hz, as detailed in Table 4.1. The different spatial and temporal frequencies used were intended to elicit responses more strongly in V1 or V2.

Orientation columns in the cat visual cortex have diameters ranging from around 200 μm to 1 mm (Stepanyants et al. 2009). The optically generated orientation map from cat V1 (Figure 2.3 in Chapter 2) shows how much the shape and size of these areas change and overlap. It must be noted that the image was created by subtracting the responses to different stimuli from the average, so it really shows relative orientation selectivity. Regardless, the sizes and separation of the columns led to a reasonable hypothesis that at least some of the 200 μm diameter surface electrodes could discriminate between individual orientation responses.

There were no previous studies found that attempted to use surface ECoG electrodes to perform orientation tuning. It has been shown that gamma band LFP power shows a greater increase above baseline than higher or lower bands in response to increasing stimulus contrast (Henrie & Shapley 2005). Studies using LFP specifically for orientation tuning saw an increased power above baseline in the 25–70 Hz range for any stimulus, often greater for one orientation. However, the tuning calculated from the LFP did not always match up with that found from multi-unit recordings of nearby neurons, showing

only a weak correlation (Gray & Singer 1989; Berens et al. 2008). Additionally, the LFPs in these studies were recorded using electrodes nearly ten times smaller than those on the surface array, so it's possible that a larger sampling area would decrease the likelihood of capturing tuning to a specific orientation.

There were four experiments performed, ORT1–4 in Table 4.1, some with different tests varying spatial and temporal resolutions. In every experiment, each of the grating angles was presented at least 16 times, up to 50 times in some experiments. Based on the evidence from previous studies, the average power in the frequency range 20–80 Hz was calculated from the spectral density estimate for each presentation. The log of the gamma power was taken in order to normalize the distribution and the mean was calculated over the repeated presentations of each angle. Finally, the minimum value over the 8 orientations was subtracted from all the responses within a test to set the baseline at zero. The resulting value served as the response, $R(\theta_k)$, to a given angle of the presented grating, θ_k. In order to quantify the orientation selectivity of each electrode, a metric called circular variance optimized for orientation tuning, Equation 4.1, was recommended (Mazurek et al. 2014).

$$1 - OriCirVar = \left| \frac{\sum_k R(\theta_k) \exp(2i\theta_k)}{\sum_k R(\theta_k)} \right| \tag{4.1}$$

The equation essentially assigned opposite signs to the responses to perpendicular angles before summing, so a 1-OriCirVar of 0 was not tuned and 1 was perfectly tuned. The factor of 2 in the exponential term treated parallel orientations as the same angle, thus basing the calculation on orientation rather than direction of movement.

Figure 4.2 gives tuning examples from two close electrodes in the experiment ORT1. The power spectral density for the electrode on the bottom row exhibited no difference in the response over stimulus orientations. This was further shown in the broad, low magnitude polar plot of the log gamma power (inset). The other example electrode shown had a much higher power response to stimuli at 0° and 180°, especially compared to perpendicular angles, 90° and 270°, further evidenced by the sharply tuned polar plot.

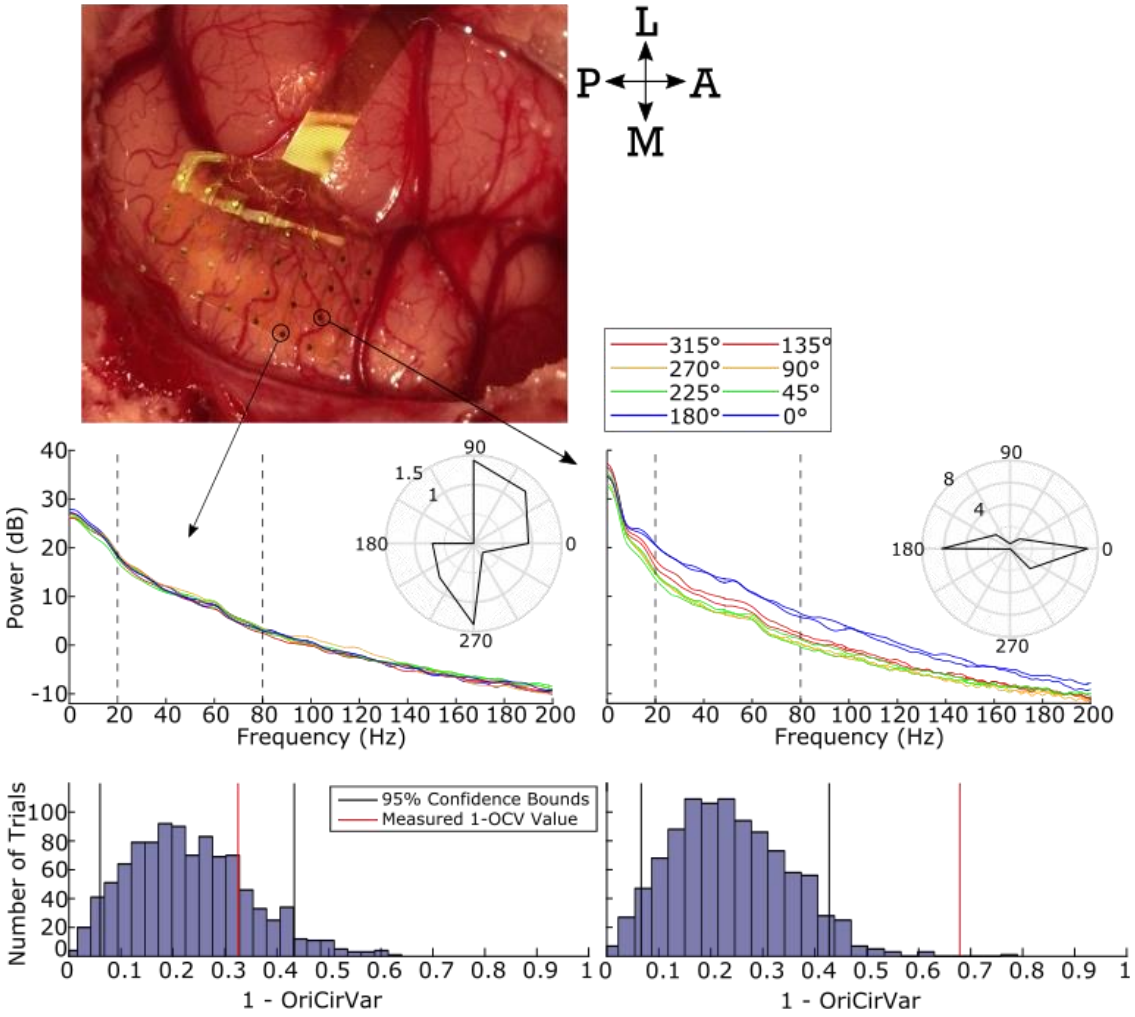

Figure 4.2 Orientation Tuning Examples Two electrodes form experiment ORT1 separated by 1.4 mm on the visual cortex. Upper plots are the power spectral density averaged over presentations of the same stimulus grating orientation, with clear angle preference seen on the right. The inset is a polar plot showing the log average gamma power (20-80 Hz) against orientation. Note the scaling difference between the tuned and untuned electrodes. The lower plots are the 1-OriCirVar values for each electrode against the permuted null distribution.

The 1-OriCirVar values for the examples in Figure 4.2 were 0.33 for the more medial electrode and 0.68 for the more lateral. The contact that showed a more orientation-selective power spectrum was closer to 1, but there is no set threshold of 1-OriCirVar to say whether or not the response from a given electrode was tuned or not. A permutation test was applied to each electrode by randomly ordering the orientations to which each response belonged 1000 times and re-computing circular variance. If the real tuning value was greater than the 95^{th} percentile of the shuffled null results, it was considered tuned. This can be seen for the two examples in Figure 4.2, as the lateral electrode's higher 1-OriCirVar value of 0.68 is significantly tuned, whereas the more medial electrode's tuning response falls near the middle of the null distribution.

The results over all experiments are summarized in Table 4.1, for both surface and depth electrodes. The majority of electrodes were not tuned, with the highest proportion of the surface array showing orientation selectivity at 50% for one test. In ORT3 and ORT4, there was only some overlap in tuned electrodes between the tests with different stimulus parameters. Additionally, the changes in spatial and temporal frequency that were intended to specifically target V1 and V2 did not result in a tuning preference for either of those presumed areas on the surface. Very few depth electrodes were tuned.

Experiment	Spatial Frequency (c/d)	Temporal Frequency (Hz)	Number of Tuned Electrodes	
			Surface (of 32)	Depth (of 16)
ORT1	0.2	2	9	0
ORT2	0.2	2	3	0
ORT3	0.75	2	10	-
	0.2	2	2	-
ORT4	1.3	1	4	0
	0.9	2	7	4
	0.6	4	16	3
	0.2	5	4	0

Table 4.1 Orientation Tuning Results The number of electrodes on the surface and depth arrays that exhibited orientation tuning based on their 1-OriCirVar value against a permuted distribution. Four experiments were performed, two of which had multiple tests varying spatial and/or temporal frequency.

Visual Evoked Potential

The beginning of each grating presentation elicited a common shape in a given electrode within an experiment. The shape was not dependent on orientation suggesting that it was a general visual response to a high-contrast stimulus. An example is shown in Figure 4.3a, averaged over all presentations independent of orientation. This electrode was not tuned, but many that were exhibited the same consistency in visual evoked potential (VEP) across stimulus angles. Figure 4.3b shows the first 300 ms of response averaged over all trials and orientations, with one example from each of the four visual experiments. These responses all came from the most anterolateral electrode on the array and exhibited a positive peak around 50-75 ms after the stimulus was presented. The activity after the peak varied between experiments but was consistently lower amplitude.

Figure 4.3c shows the average depth profile of the VEP across orientations from one text in ORT4. The shank was located on the posteromedial portion of the array, closer to the surface electrode used in (a) than (b). The LFPs all looked very similar throughout the depth, so the CSD was used in order to find the sources of local synaptic activity. CSD was calculated by taking the negative second spatial derivative of the averaged depth VEPs, with the top and bottom traces duplicated to obtain CSD spanning the entire recorded depth. Further details of CSD analysis can be found in Chapter 2. There were two major sinks, one superficial from the surface down to about 0.5 mm and another that was concentrated around 1.2–1.5 mm. There was a current source directly between the two sinks. All of the local activity occurred between about 50–120 ms after the stimulus was presented, though the LFP continued presumably due to volume conduction. This type of CSD profile was seen through all the parameter tests in ORT4 and similar to that from ORT1 and ORT2, though they were less clear. ORT3 had no depth recordings.

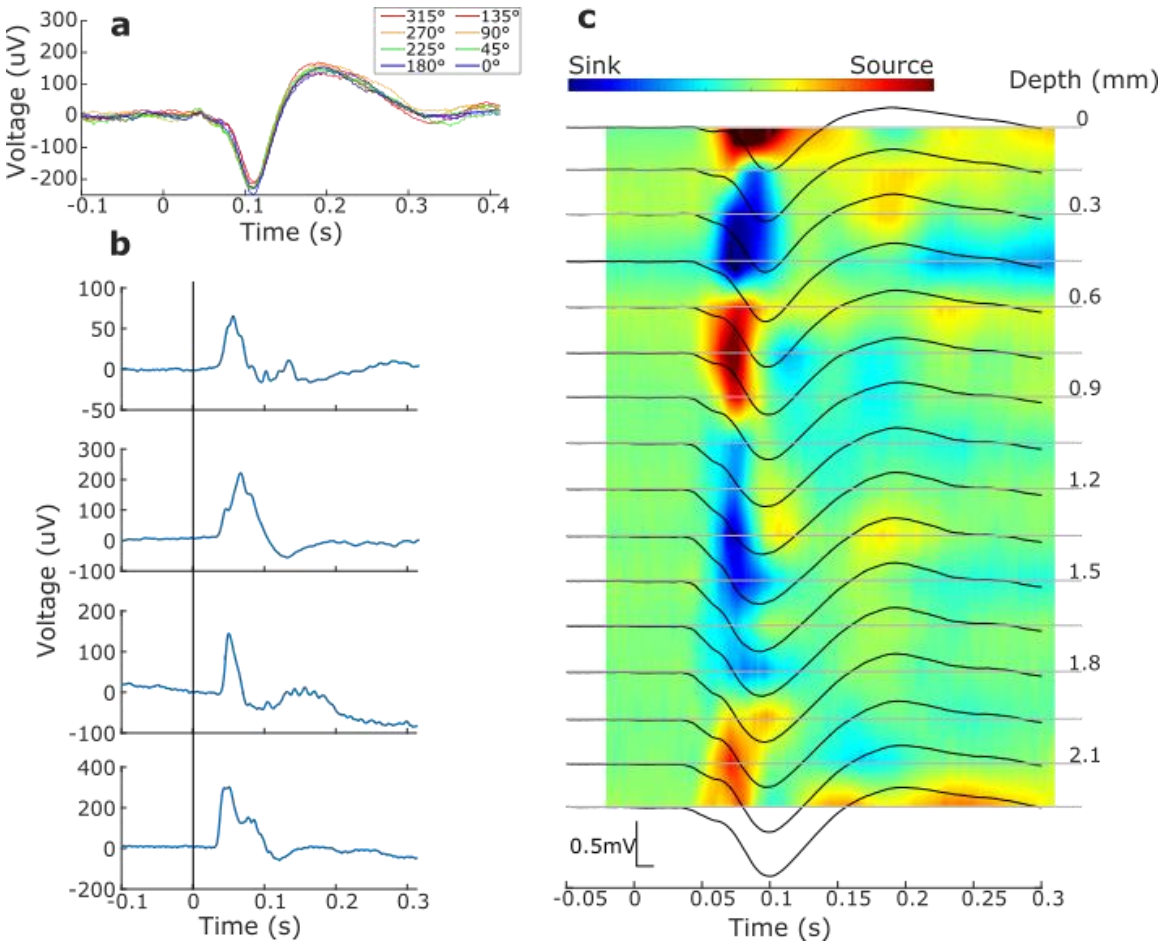

Figure 4.3 Visual Evoked Potential Examples (a) The first 400 ms after stimulus presentation shows nearly identical responses across orientations, seen in both tuned and untuned electrodes. (b) Example evoked potentials from the most anterolateral electrode on the surface array averaged over orientations for all four experiments show a similar shape, notably a positive peak around 50-75 ms. (c) Depth LFPs and calculated CSD profile from one test in ORT4 averaged over orientations. A consistent depth response was seen with a superficial and deeper sink separated by a source. Depths indicate distance between electrodes on the array, not necessarily depth in the cortical layers.

The two examples shown in Figure 4.3a and b came from different parts of the array and showed distinct responses. There was a clear spatial dependence on the VEP shape, visible to some degree in all of the experiments. Figure 4.4 shows an example of this from one of the tests in ORT4. Most of the electrodes had an initial negative spike followed by a smaller, longer positivity, with some variation between them. In the most anterolateral electrodes, however, the stimulus evoked a strong, early positive peak followed by a return to baseline or long, low amplitude negativity. The figure shows the approximate location on the cortex where the array was placed, and the known functional boundary between V1 and V2 lined up with the change in response shape. There are electrodes between the two that have a smaller initial positivity and a quick negativity, which could be evidence that they were over the transition zone between V1 and V2. All of the experiments showed a difference in shape between the posteromedial and anterolateral portions of the array, and all were placed in similar areas on the visual cortex, though none were as clear as those from ORT4.

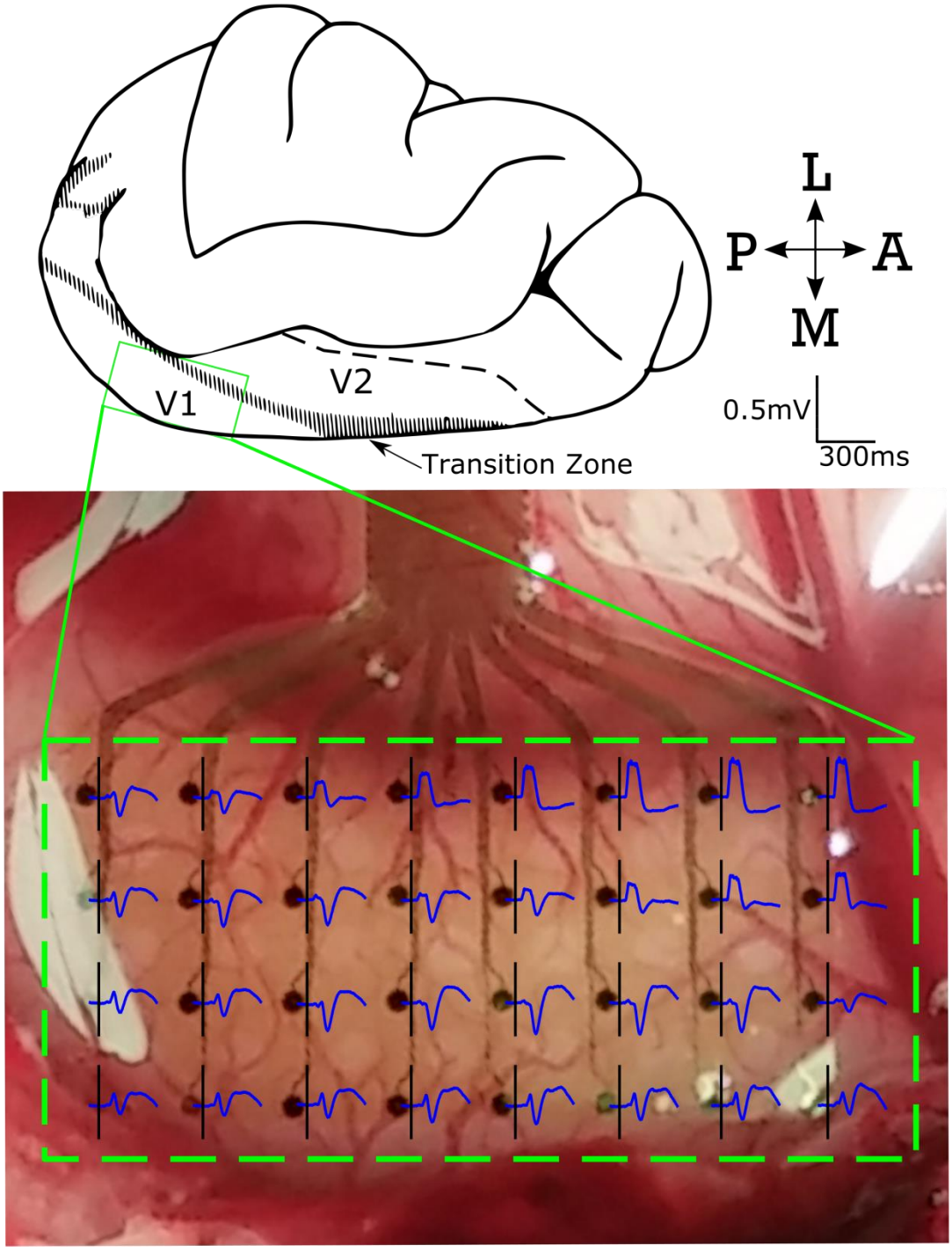

Figure 4.4 Spatial Dependence of Visual Evoked Potential The first 300 ms averaged over orientations from one of the ORT4 tests. The most anterolateral electrodes show a much different response from the rest of the array, which anatomically matches with the functional border between V1 and V2.

Electrical Stimulation

Unlike visual stimulation, responses to direct electrical stimulation do not follow prescribed functional pathways; rather, the injected current indiscriminately activates elements close to the electrode. Though the processes that result from such activation can be unpredictable, a major advantage of electrical stimulation is that specific areas of cortex can be targeted. It is a method of interrogating the brain that has long been studied, but there is still much that is not known about the mechanisms behind it. With the list of clinical applications for neural stimulation growing, it is increasingly important to better understand how evoked activity spreads and how it can be easily monitored.

Evoked Response Shape

The electrically evoked response shape on the surface was overall very similar, with variations depending on the experiment, the depth and intensity of stimulation, and the distance from the stimulating electrode. The most common pattern of the signal was a negative peak followed by a longer duration positive peak. In many responses, an early positive peak appeared before the negativity, but it was often occluded by stimulation artifact. This typical pattern, seen in Figure 4.5, matches with responses to direct cortical stimulation seen in previous studies, as outlined in Chapter 2. The examples in the figure came from a surface contact about 2 mm from the stimulating electrode and give an idea of how the responses changed with stimulation intensity and depth in the upper and lower plots, respectively. The responses were averaged over multiple trials of repeated stimulation. The number of trials varied between experiments, but was typically around 30, with a minimum of 15. The trial-to-trial variability is given in Table 4.2, which was under 100 μV in every experiment.

The evoked responses were quantified by finding the amplitude of the negative and secondary positive peaks, and the time after stimulus that they occurred. An algorithm was employed to detect peaks that were at least three times greater than the standard deviation of baseline activity prior to the stimulation. These detected points were then manually reviewed and adjusted to remove extraneous or wrong detections. Not all responses contained both peaks, especially during lower amplitude or deeper stimuli and at farther electrodes. The peak amplitude and latency values were then used to explore how the responses changed with stimulation parameters.

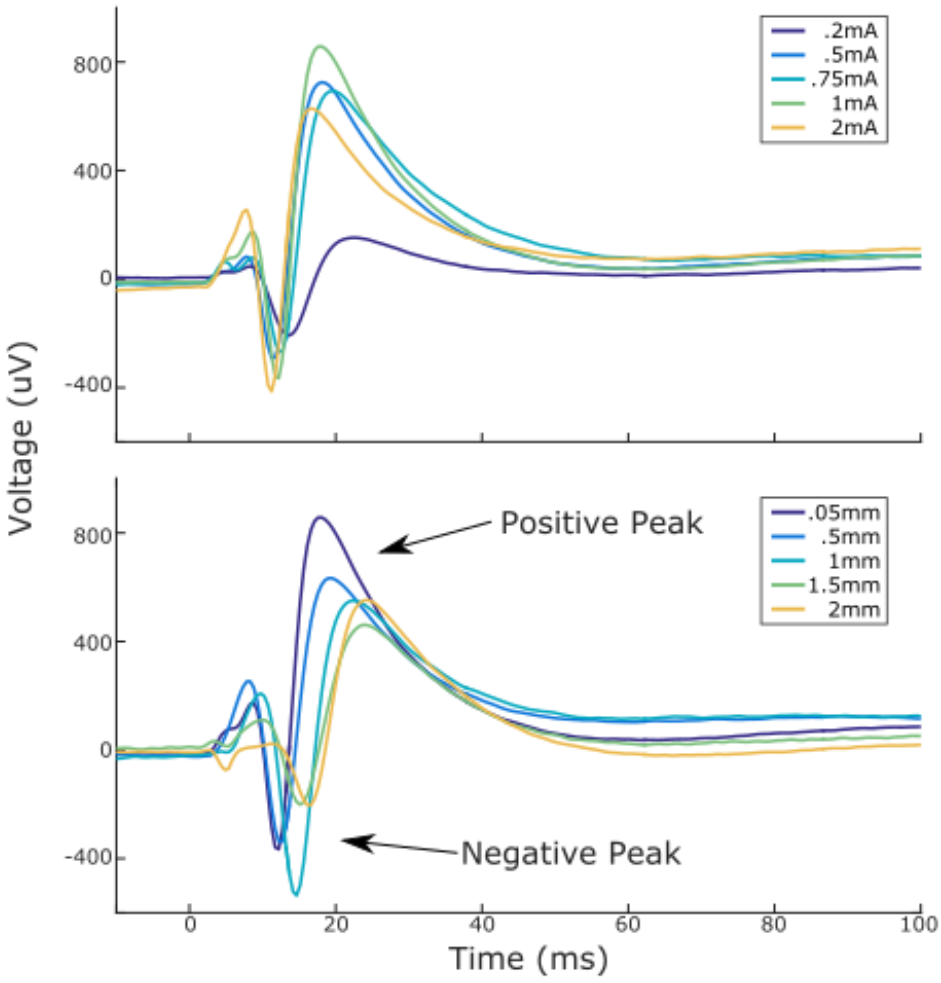

Figure 4.5 Example Electrical Stimulation Surface Responses. Both sets of traces are averaged responses from a surface electrode about 2 mm away from the stimulation site during the sixth experiment. The upper and lower plots show evoked potentials in response to varying stimulation intensity and depth, respectively.

	Stimulation Type	# Depths and Range (mm)	# Intensities and Range (mA)	Trial-to-Trial Std Deviation (uV)
Experiment 1	Monophasic	1 (0.1)	8 (0.26-1.5)	66.7
Experiment 2	Monophasic	10 (0.05-2.25)	2 (0.57-1.19)	92.7
Experiment 3	Monophasic	5 (0.1-1.9)	1 (7.24)	76.9
Experiment 4	Monophasic	4 (0.2-1.5)	1 (1.5)	82.6
Experiment 5	Biphasic	5 (0.05-2)	8 (0.05-4)	74.6
Experiment 6	Biphasic	5 (0.05-2)	5 (0.2)	63.8

Table 4.2 Stimulation Parameters and Response Variability per Experiment This table details the different depths and intensities of electrical stimulation used in each experiment and whether in was monophasic or biphasic. All experiments used pulses with 100 μs width per phase. Only experiments five and six swept more than 2 depths and intensities of stimulation. The table also gives the average trial-to-trial standard deviation of averaged responses. This was calculated by first finding the standard deviation across trials (at least 15 trials, typically around 30, depending on the experiment) at every time point in a given stimulation response. The median standard deviation was then found for a 100 ms clip starting 7.5 ms after the stimulation time to avoid artifact contamination. The value given here is the median value of those average standard deviations across stimulation depths and intensities, and across electrodes, for each experiment.

Effect of Stimulation Parameters

There was a clear effect of stimulation intensity on the responses recorded from the surface array. Figure 4.6 shows plots of the negative peak amplitude (normalized to the most negative per experiment) and latency as a function of stimulation intensity for each electrode and stimulus depth in experiments five and six. These experiments were chosen because they had the most exhaustive stimulation parameter sweeps, with five or more depths and intensities used in each, as detailed in Table 4.2.

In both experiments, the overall negative peak amplitude of responses across the ECoG grid grew stronger with increasing intensity. It showed a logarithmic response, increasing steadily at lower intensities and levelled off around 1 mA, most clearly seen on electrodes closer to the stimulating electrode. The latency of the negative peaks in both experiments decreased with increasing intensity, also reaching an asymptote around 1 mA. The response of both amplitude and latency to changing intensity varied with distance from the stimulus.

The depth of stimulation also had an effect on the response, though it was not as consistent as that of intensity. In experiment five, the amplitudes for the most superficial stimulation were typically higher than those for deeper stimuli, which had little difference between them. The latency response exhibited similar behavior, with peaks caused by the most superficial stimulation occurring earlier than those evoked by deeper stimuli. In experiment six, the latency responses were quite consistent in that each deeper location of stimulation pushed the intensity response curve slower. The amplitude response varied more with respect to depth, as many electrodes exhibited maximum peak amplitudes caused by the most superficial depth, while 1 mm deep stimulation evoked maximum response in others.

These results show that the negative peaks of surface responses to cortical microstimulation grew larger and occurred faster with increased intensity, until around 1 mA when they plateaud. The latency of the peaks consistently increased with deeper stimuli, though the effect of depth on amplitude was not as clear. The unpredictable effect of stimulation depth within and across experiments suggests the responses to stimulation are very dependent on the stimulus location relative to the underlying network.

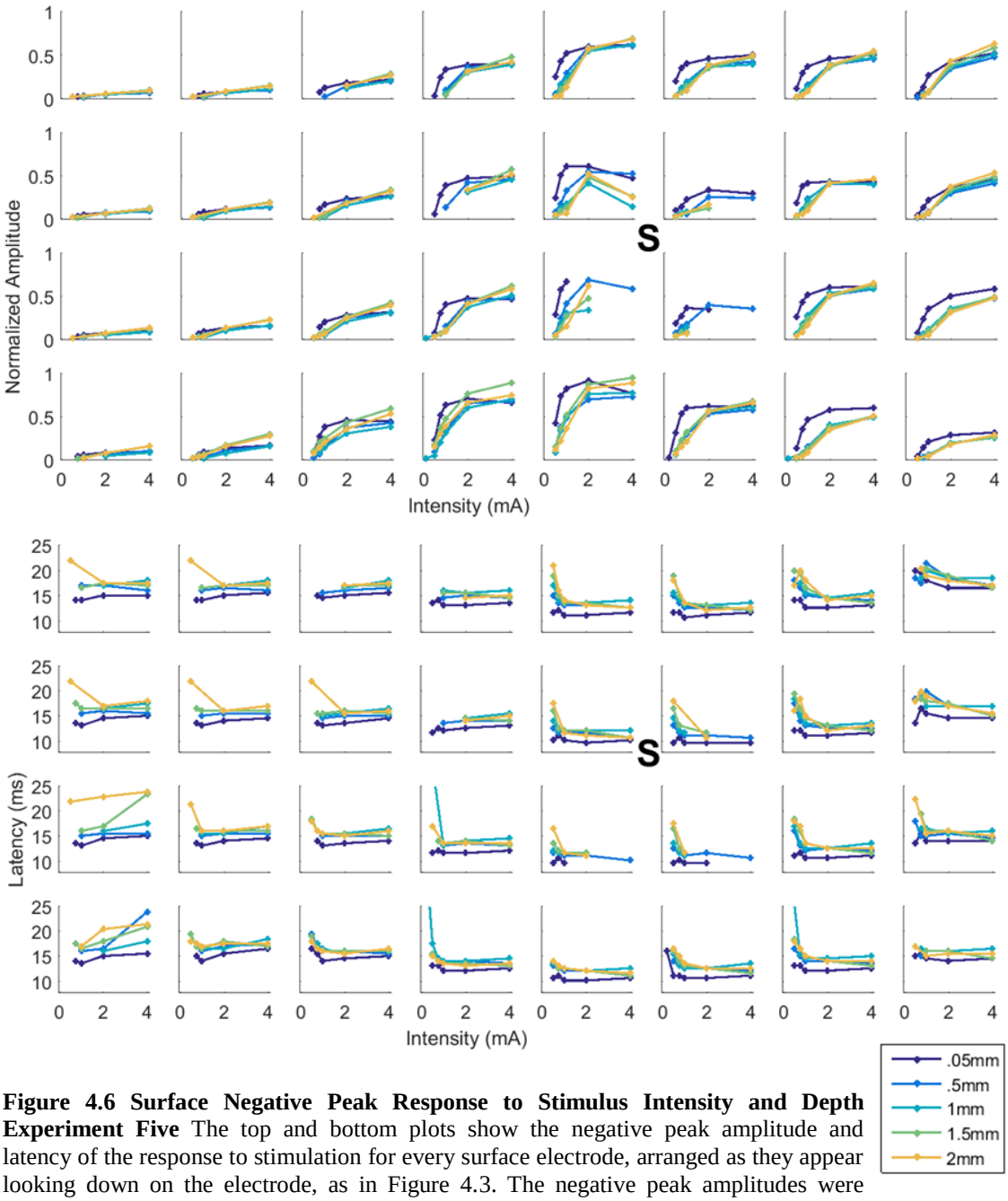

Figure 4.6 Surface Negative Peak Response to Stimulus Intensity and Depth Experiment Five The top and bottom plots show the negative peak amplitude and latency of the response to stimulation for every surface electrode, arranged as they appear looking down on the electrode, as in Figure 4.3. The negative peak amplitudes were normalized to one by dividing by the most negative value in the experiment. 'S' marks the location of the stimulating electrode, and the colors represent its depth, noted in the legend. Negative peak amplitude and latency plots from the first four experiments are in the supplementary figures chapter.

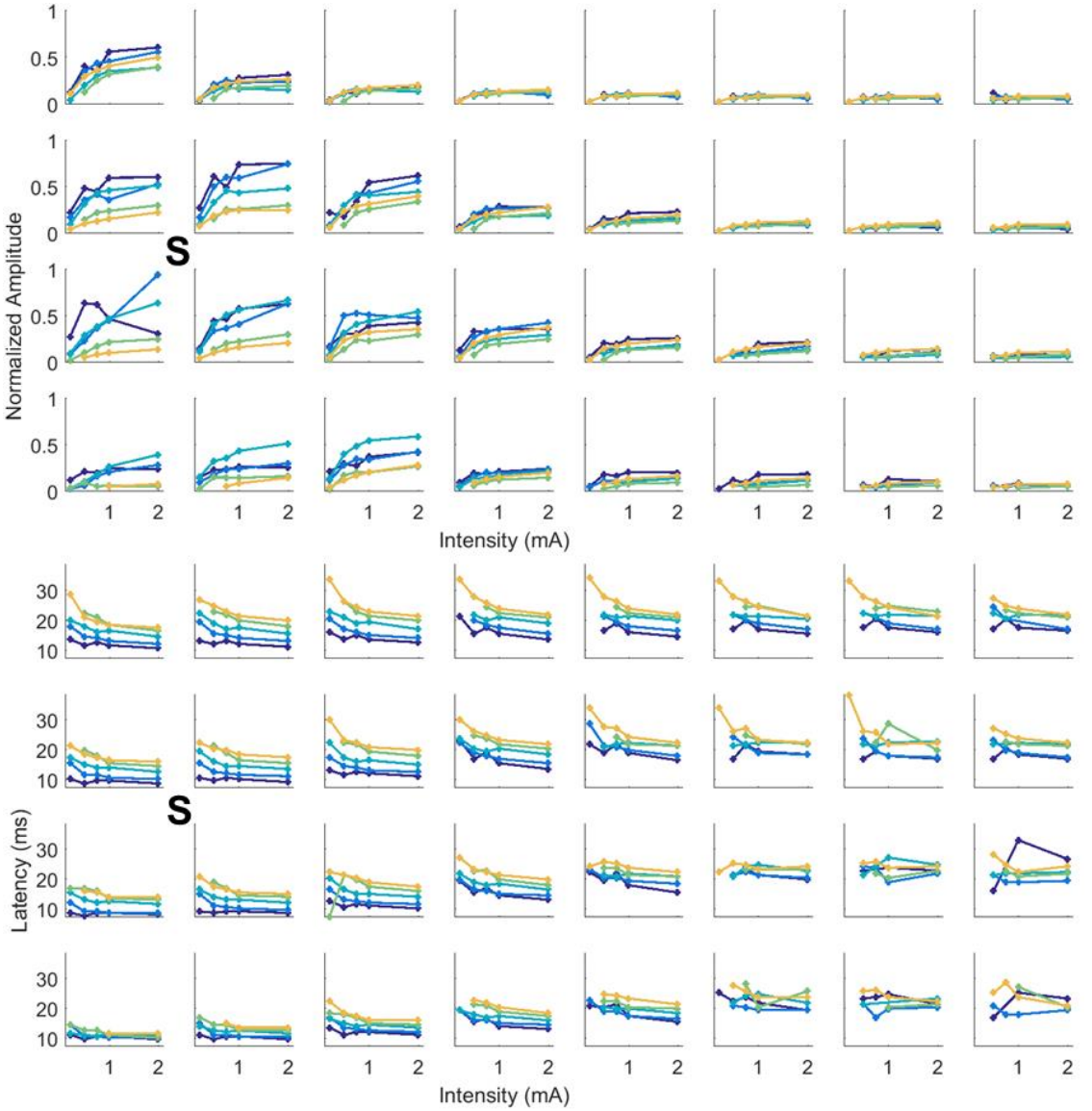

Figure 4.6 Surface Negative Peak Response to Stimulus Intensity and Depth (cont'd) Experiment Six

The plots in Figure 4.6 all showed how the negative peak of the stimulation response varied with stimulus depth and intensity. As Figure 4.5 showed, there was also a later positive peak in the typical response shape. Figure 4.7 shows the same plots as Figure 4.6, but using the quantified amplitude and latency of the positive peak to show how they responded to changing stimulus intensity and depth in the fifth and sixth experiments.

The first major difference seen between the two peak responses is that the positive peaks exhibited reduced spatial spread. Electrodes far from the stimulus site that had above-baseline negative peaks had very few positive peak detections. In positive peaks that were present on closer electrodes, the change in amplitude with respect to swept intensity was much more variable than with the negative peaks. Some electrodes showed a similar logarithmic response, though many reached a maximum around 0.5–1 mA and decreased in amplitude with higher stimulus intensities. The shape of the amplitude response was affected by the location of the surface electrode and the depth of stimulation, something not seen in the negative peaks. Overall, however, more superficial stimuli resulted in greater positive peak amplitude. The latency of the more closely resembled those of the negative peaks in the corresponding experiments, exhibiting faster responses to stronger, more superficial stimuli.

These results suggest that the positive portion of the stimulus response on the surface reflects either more local or weaker activity in the cortex. It is also more dependent on the local underlying network architecture due to the large changes in response curves in different areas of the array.

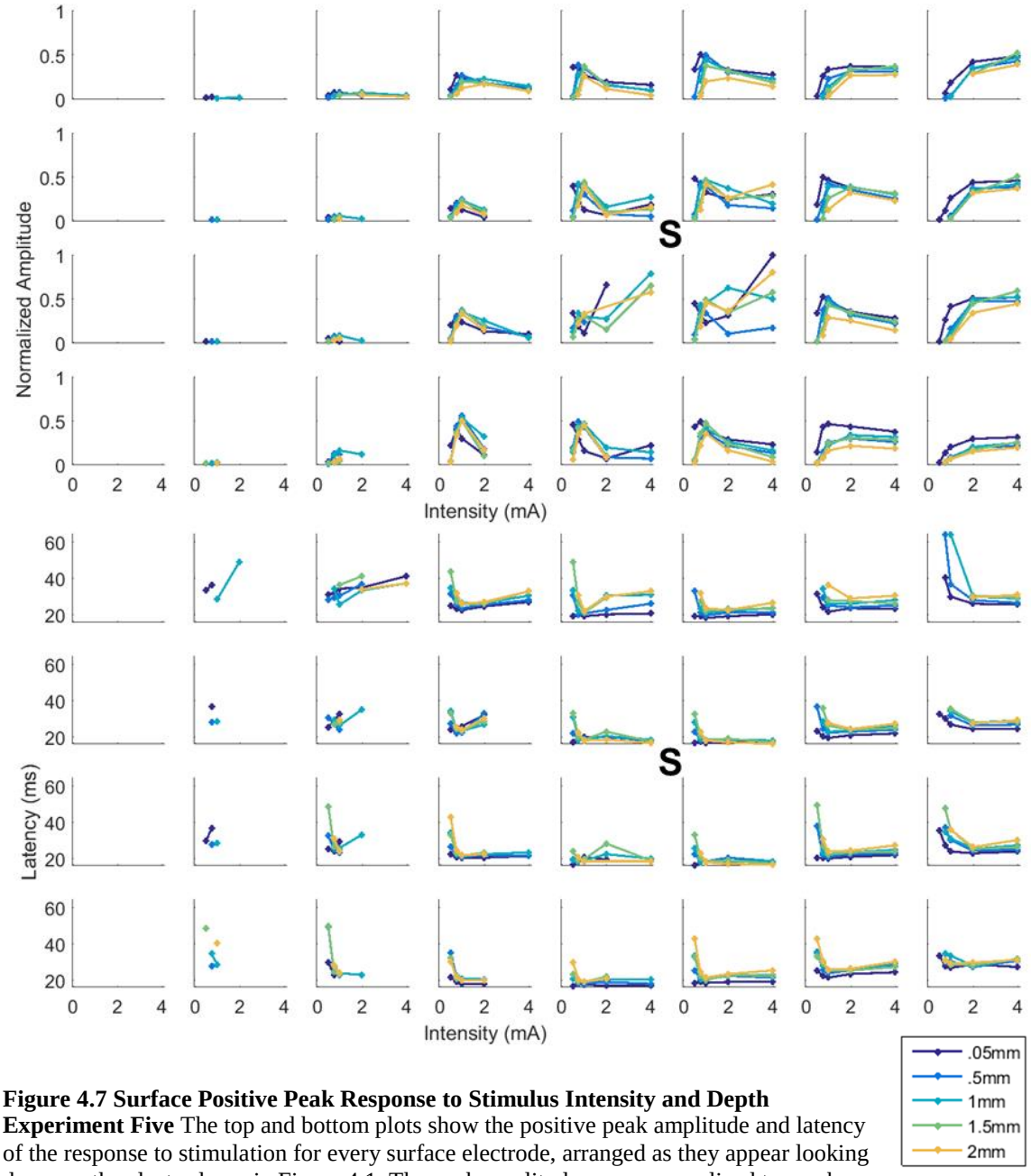

Figure 4.7 Surface Positive Peak Response to Stimulus Intensity and Depth Experiment Five The top and bottom plots show the positive peak amplitude and latency of the response to stimulation for every surface electrode, arranged as they appear looking down on the electrode, as in Figure 4.1. The peak amplitudes were normalized to one by dividing by the maximum value in the experiment. 'S' marks the location of the stimulating electrode, and the colors represent its depth, noted in the legend. Positive peak amplitude and latency plots from the first four experiments are in the supplementary figures chapter.

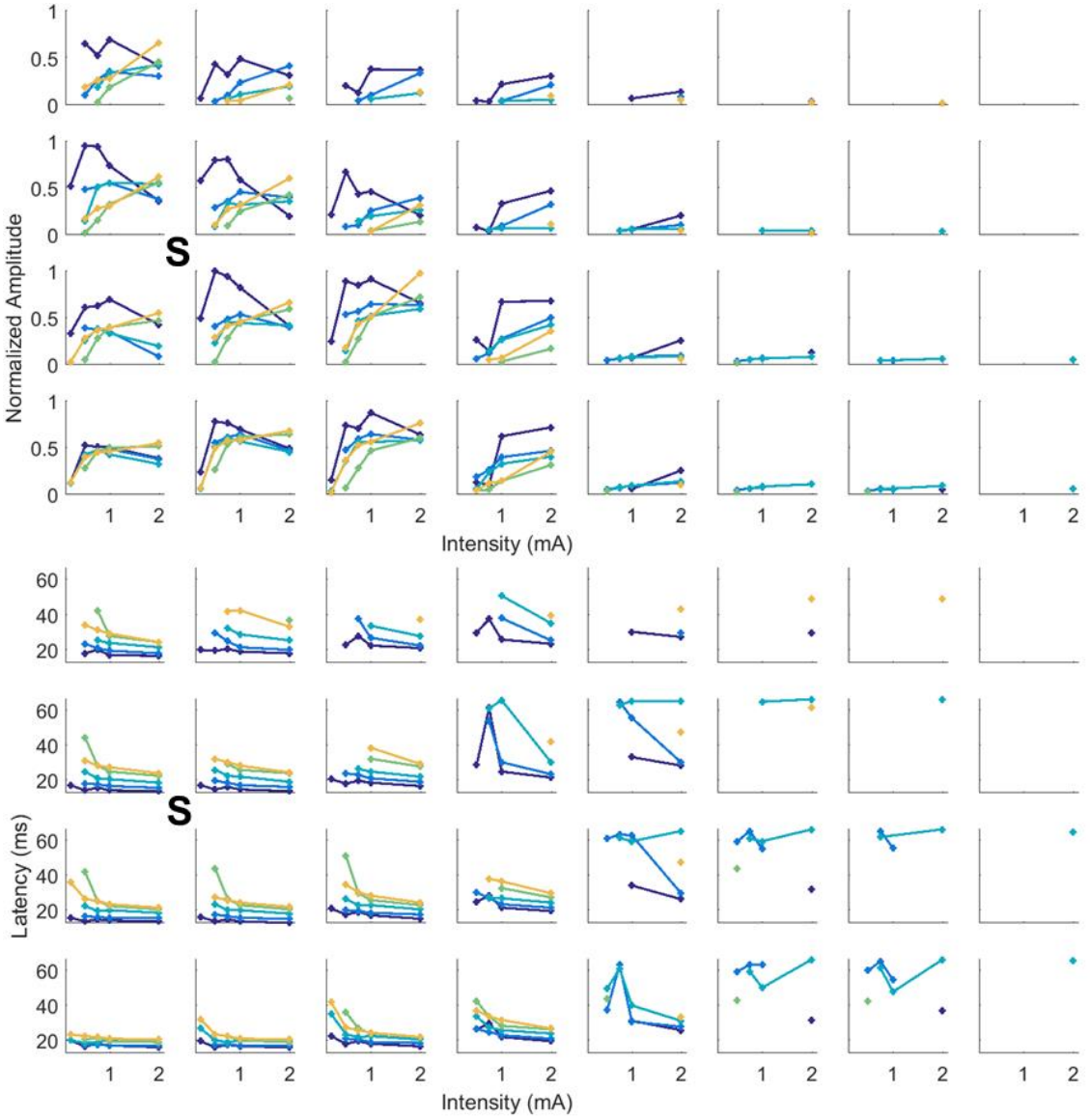

Figure 4.7 Surface Positive Peak Response to Stimulus Intensity and Depth (cont'd) Experiment Six

Spatial Spread of Response

Changes in depth and intensity of stimulation also had an effect on the spatial spread of stimulation, as shown from experiments five and six in Figure 4.8. The upper plots show the maximum radius of response versus stimulation intensity over depths, as determined by the farthest surface electrode on which a peak was detected above baseline, either negative or positive. The black line represents the distance of the farthest electrode on the array from the stimulation site. In both examples, increasing intensity elicited response from a greater surface area for all depths. In both experiments shown, all except one depth reached the maximum radius by 1mA. Over all of the experiments performed, most of the radii were between 4 and 9 mm, though the actual area covered on many of those might have been higher, extending past the edge of the surface array. In both examples, the most superficial and deeper depths tended to have a higher response radius than the intermediate depths.

It must be noted that the given depth values in millimeters represent how deep the stimulating electrode was inserted, which does not necessarily line up with the exact perpendicular dimensions of the cortical lamina and varies between experiments depending on position and angle of the electrode. For instance, the 1.5 mm depth in experiment 6, which had the smallest radius, may have been stimulating a different layer than 1.5 mm in experiment 5, which was among the largest.

The lower plots are the sums over all responding electrodes of the peak amplitude, with negative and positive peaks added separately. The values reached a maximum around 1–2 mA before plateauing and the more superficial stimuli had a higher amplitude sum in general than deeper ones.

Both these results are in accordance with the amplitude-intensity curves shown for each individual electrode in the previous section. Ultimately, they show that response amplitude is directly correlated with intensity and depth, such that stronger and more superficial stimuli elicit higher amplitude responses. The spatial spread shows this positive association with intensity, but the dependence on depth is more complicated, suggesting the elements activated in different layers govern the spread of the response.

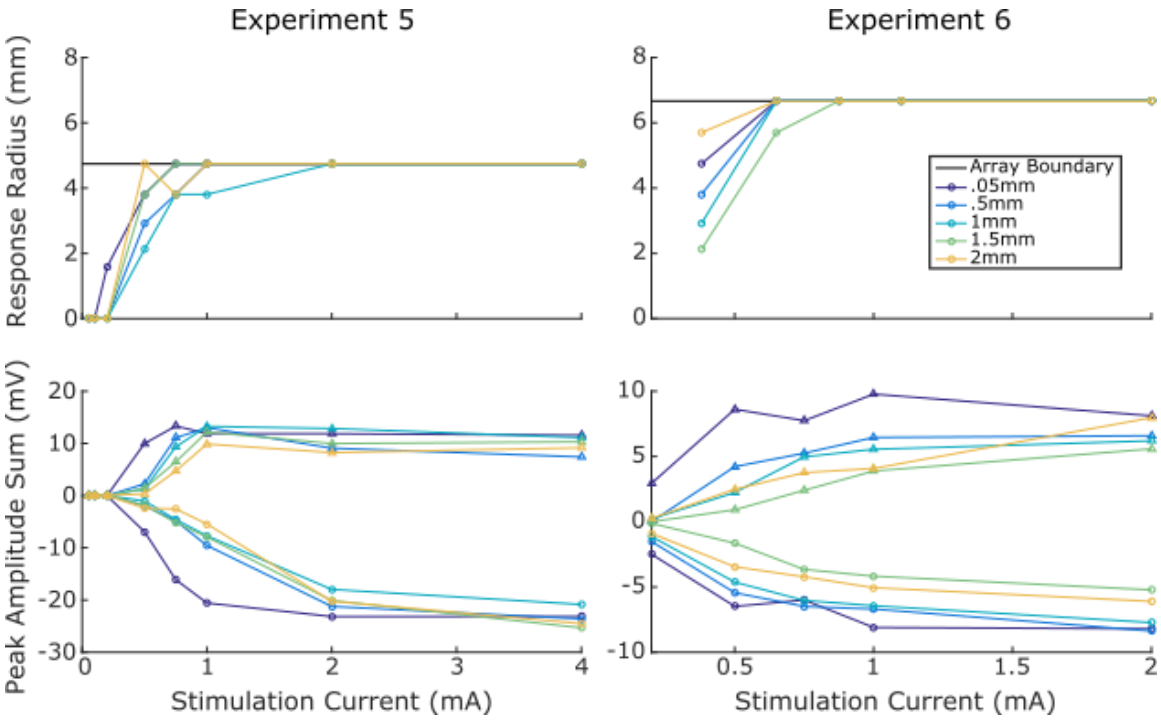

Figure 4.8 Response Distance and Amplitude Sum The plots are from the fifth (left) and sixth (right) electrical stimulation experiments. The upper plots show the response radius, or the farthest electrode from the stimulating site to have a significant peak, against stimulus intensity. The upper boundary indicated by the black line is the edge of the surface array. The lower plots are the sum of the peak amplitudes over all responding electrodes as a function of stimulus intensity. The positive values are the sums of positive peaks, represented by triangles, and the negative values are the sums of negative peaks, represented by circles. The legend matching depths to trace colors applies to all plots.

The radius and sum metrics shown in Figure 4.8 used either the farthest responding electrode or combined all contacts together to investigate the spread of the response. They did not take into account any differences between electrodes as the response propagated across the surface. Figures 4.6 and 4.7 show that the responses to varying stimulation depths and intensities were dependent on the individual electrode location relative to the stimulation site. It was clear in those examples that, in general, contacts farther from the stimulation exhibited lower amplitude peaks. To get a general idea of how response voltage fell off as a function of distance, Figure 4.9 gives plots of negative peak voltage for each electrode (normalized to the largest magnitude peak in each experiment) against distance from the tip of the stimulating electrode for each stimulation depth and intensity in experiments five and six. Note that the distance for each contact changed depending on the depth of stimulation.

Along with the scattered negative peak amplitudes, each plot in Figure 4.9 shows a simple source-field model of the scalar potential spread caused by a point current source in a uniform conducting medium of infinite extent. Formula 4.1 gives the basis for the model, where Φ is the potential caused by the point source with magnitude I_o at a distance r in a medium with conductivity σ (Malmivuo & Plonsey 1995).

$$\Phi = \frac{I_o}{4\pi\sigma r} \tag{4.1}$$

The simple model was not intended to fully explain the voltage spread, but rather serve as a known physical comparison for the experimental responses. For this reason, and since normalized voltage was used, the constant value in the formula, $\frac{I_o}{4\pi\sigma}$ was replaced by a single coefficient, k. The specific value of k was found for each depth and intensity of stimulation to minimize the error of the model to the peak amplitudes across contacts in that trial. The error was calculated for each trial and each value of k being swept by finding the Euclidean distance between the model and every contact with a detected negative peak in 2D distance-voltage space. The value of k that had the smallest mean error across electrodes was chosen for that trial as the best fit source-field model.

Figure 4.9 shows that the point source model was a reasonable approximation of the general trend of response amplitude falling off over distance. The voltage-distance relationship in experiment six was especially well fit by the k/r model, with a mean error of 0.049 across trials, compared to 0.089 in experiment five for the trials plotted. As a comparison, a null data set comprised of 32 randomly generated points with voltage-distance values in the same range gave a mean error of 0.23 over 1000 trials. A boxplot

of the resulting fit errors for the random null data, as well as the fit errors in all the experiments, is shown in Figure 4.10. No fit errors from collected data were as high as the smallest error from the random data, rejecting the null hypothesis. The median error in all experiments fell between 0.03 and 0.09, with the fifth experiment being the highest. Neither k nor the fit error changed significantly as a function of depth over the experiments, though both increased with greater stimulation intensities, as seen in Figure 4.11.

Many contacts on the array at the same distance from the site of stimulation had varying peak voltages, displaying a preference for a certain direction over others. This is indicative of a response dependence on the structure of the network directly around the site of stimulation. Figure 4.12 gives polar plots for each experiment to show directional preference of stimulation response. The points represent the detected negative peak amplitudes across all depths and intensities of stimulation, with the normalized voltage portrayed as the radial distance from the center and the direction to the contact as the angle. The points are broken down by their distance from the stimulating electrode, signified by their color according to the legend. It is important to note that in most of the experiments the stimulating electrode was not in the center of the array, so there are more points in certain directions. Experiments two and five showed a clear preference for directions along 0 and 240 degrees, respectively. Experiment six had higher voltage peaks closer to the electrode in the second and fourth quadrants, while farther electrodes exhibited larger amplitude peaks in the first and third quadrants.

Overall, these results show that the amplitude of the response to electrical stimulation is inversely proportional to the distance from the stimulus, as explained by the field model of a point current source. This points to volume conduction contributing greatly to the responses recorded on the surface. The more nuanced differences in the spread, however, vary by direction and between experiments, due to the complicated networks the electrical stimulation is activating.

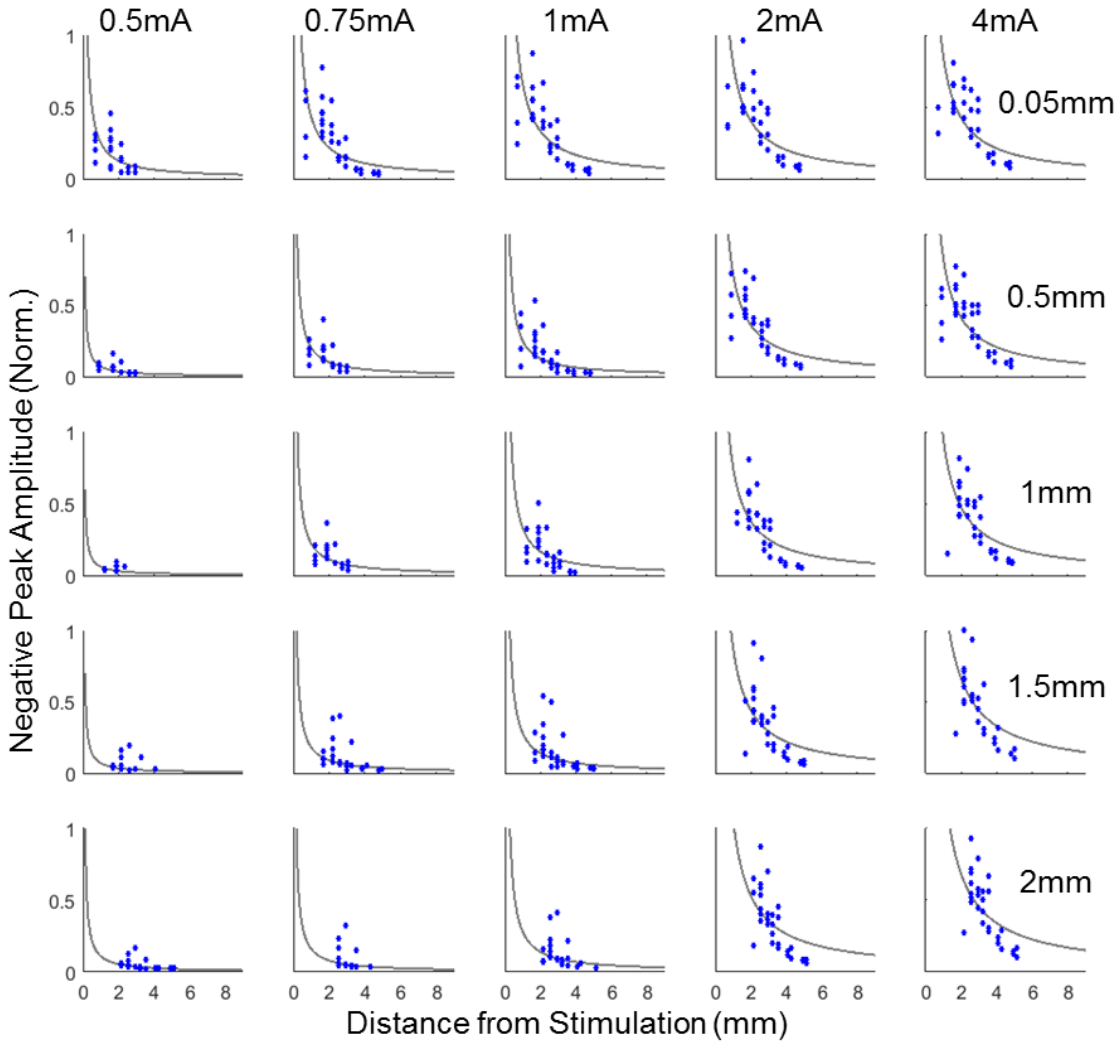

Figure 4.9 Surface Peak Voltage Change with Distance from Stimulation – Experiment Five The 5 rows and columns of plots correspond to labeled depths and intensities of stimulation, respectively. In each trial, all detectable above-baseline negative peaks were found and normalized by dividing by the largest magnitude peak in the entire experiment. These values were plotted as blue dots against the 3D distance from the ECoG electrode on which they were detected to the tip of the stimulating electrode. The gray line is the point-source model, $\Phi = k/r$, in which k was optimized to each trial by reducing a defined error metric. Plots from the first four experiments are in the supplementary figures chapter.

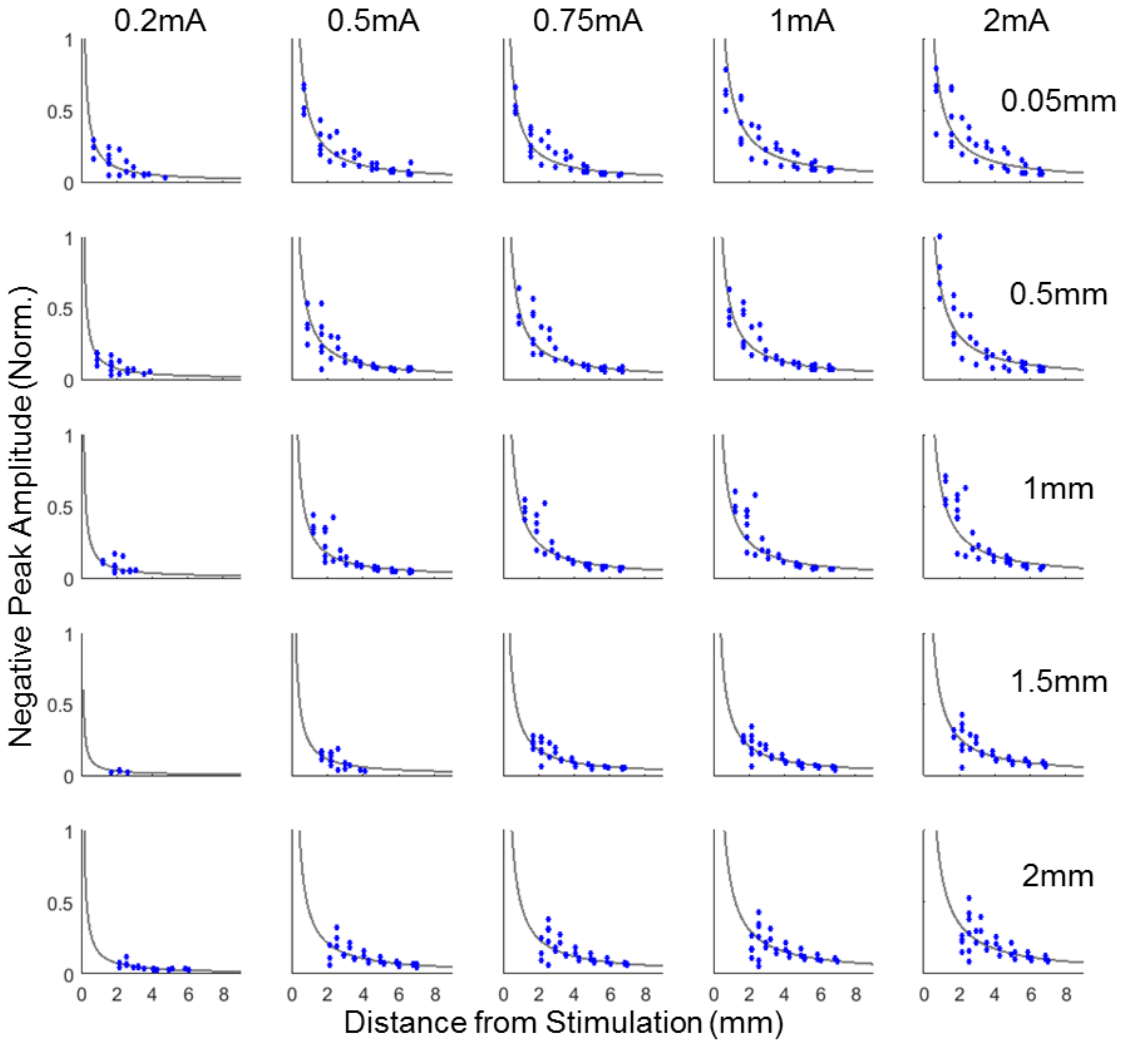

Figure 4.9 Surface Peak Voltage Change with Distance from Stimulation (cont'd) – Experiment Six

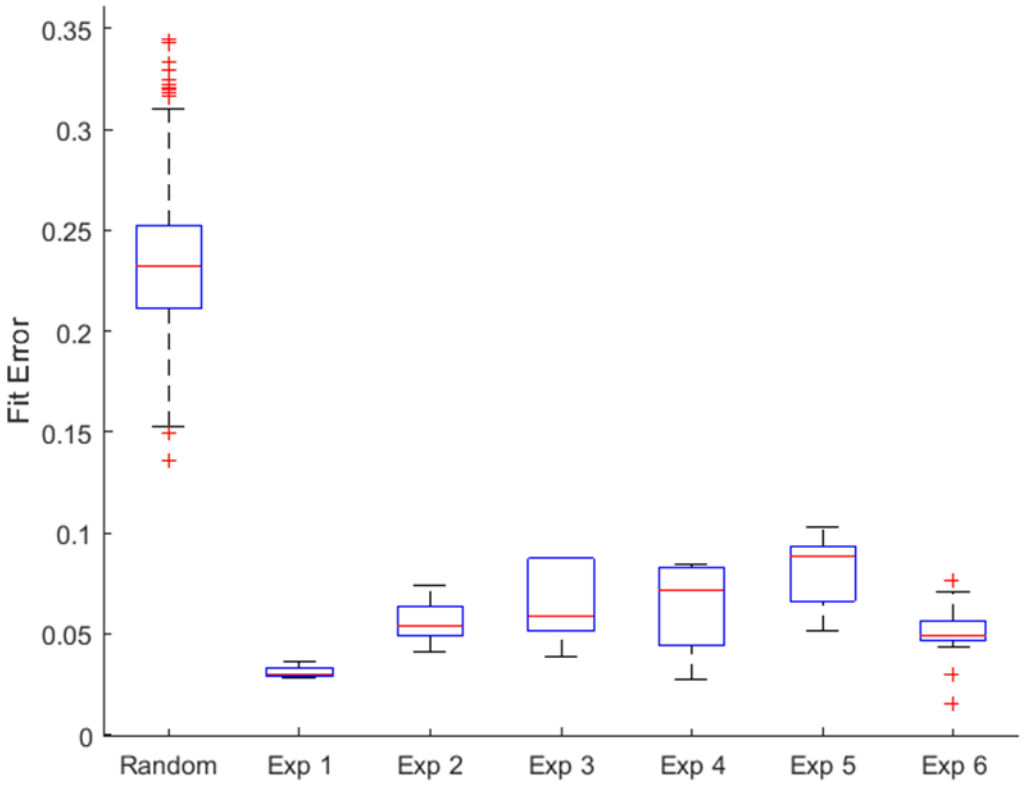

Figure 4.10 Point Source-Field Model Fit Error In every experiment, the coefficient of the point source model was optimized to minimize fit error to the peak data. The error was found by calculating the Euclidean length of each peak amplitude point to the model in distance-amplitude space and taking the median across electrodes. The error was normalized to the largest distance and space values in each trial to make them comparable across stimulation parameters and experiments. This plot shows a box plot of the fit error in every experiment, with the red line representing the median across trials and the blue box spanning the 25^{th} to 75^{th} percentiles. On the left is the same error calculated when fitting 32 random distance-amplitude data points to the source-field model, after coefficient optimization, for 1000 trials. No errors calculated on real data were above the smallest error on random data, showing that the model fit on peak amplitude data is significantly better than on a null data set.

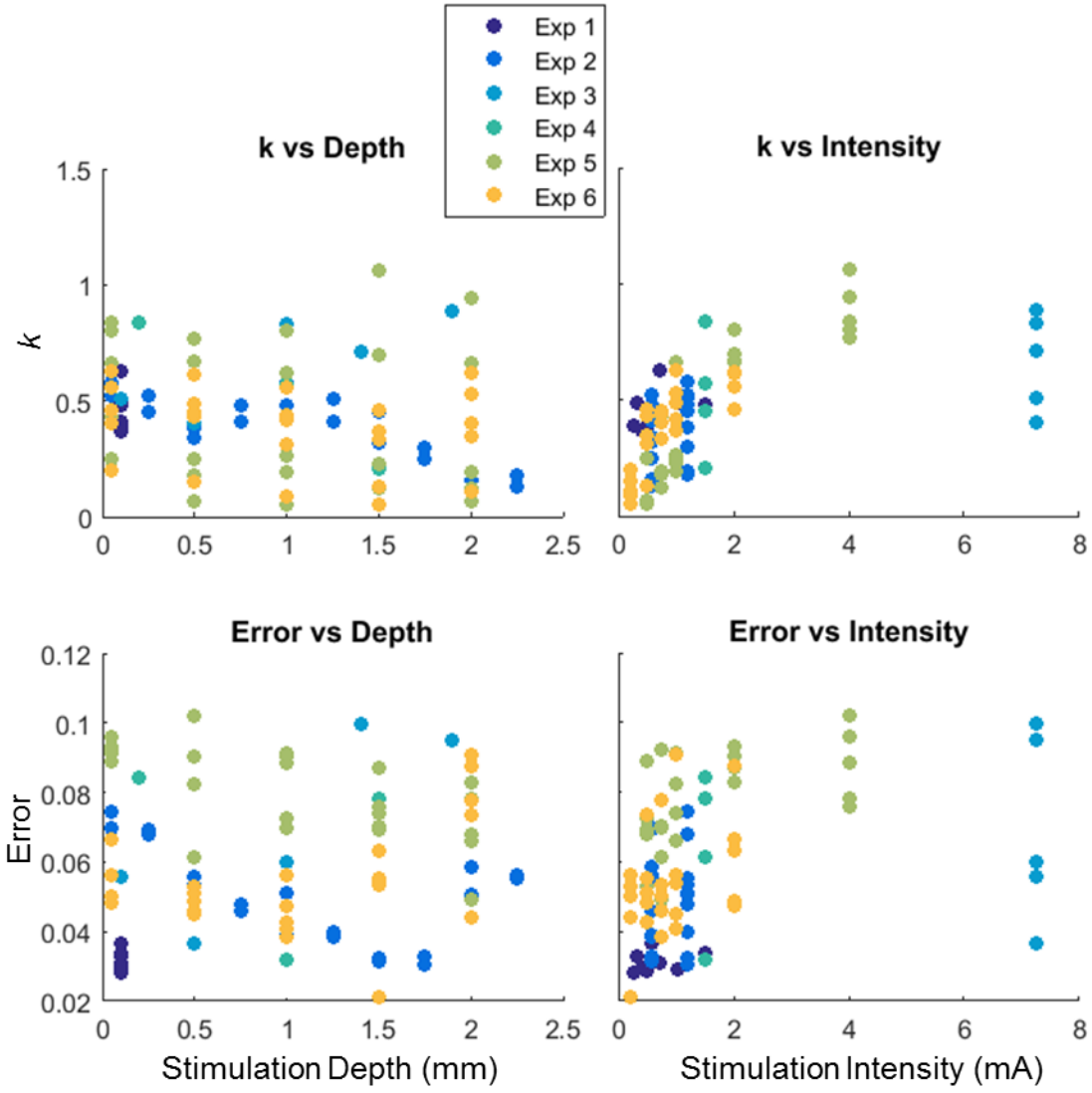

Figure 4.11 Fit Error and Coefficient of Point Source Model The source-field model of a single point source was used to approximate the relationship between response voltage and distance from stimulus. The model coefficient, *k*, and the fit error, described previously, are plotted here as a function of stimulation depth (left) and intensity (right). The colors of each point correspond to different experiments, as defined by the legend. There is an increase in both values with greater stimulation intensities, while there is no clear dependence on depth.

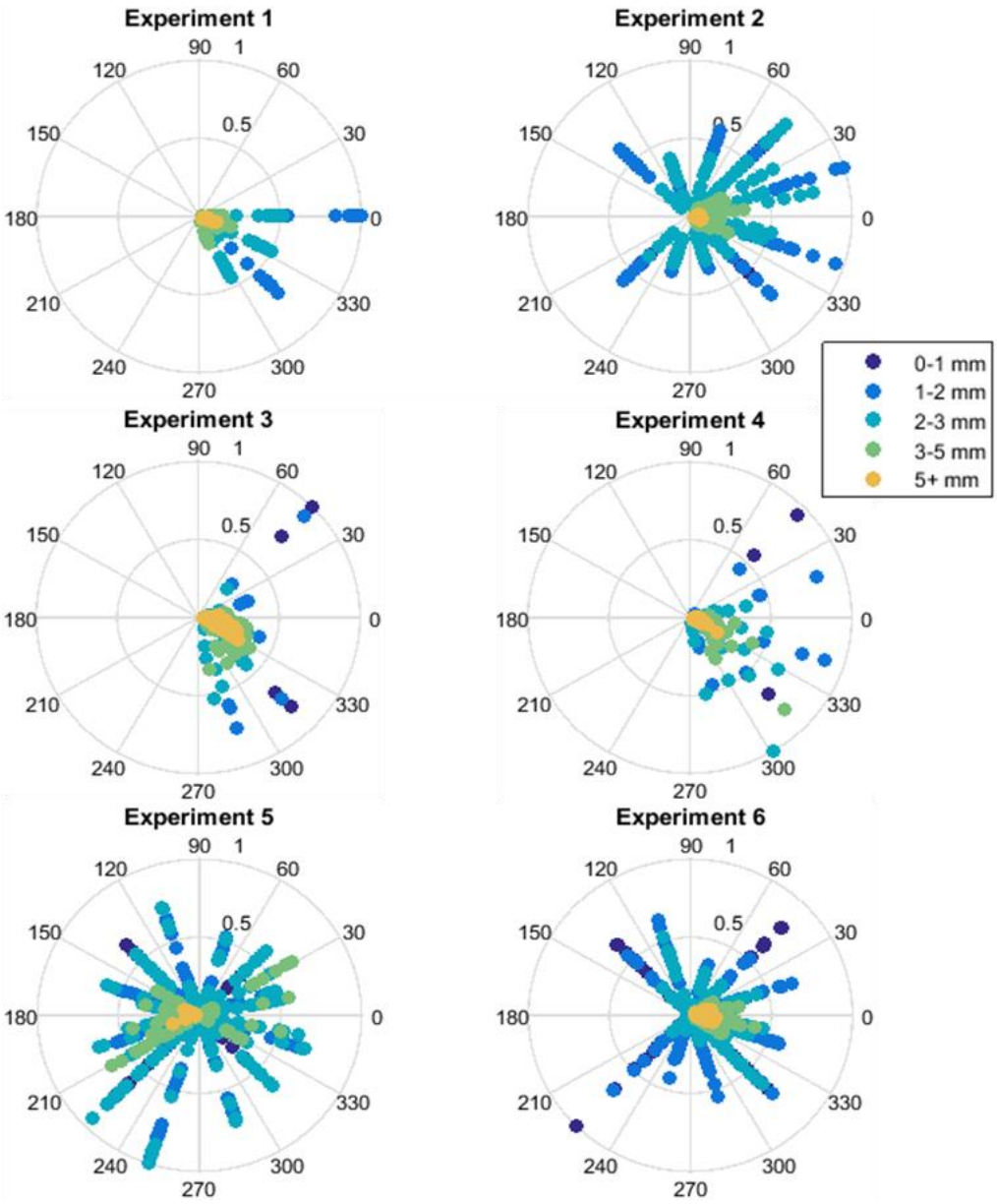

Figure 4.12 Direction of Response Amplitudes For each experiment, all detected negative peaks are plotted in a polar plot, with the normalized amplitude displayed as radial distance, and the direction of the electrode to the stimulus as the angle. The different colors correspond to different distances from the tip of the stimulating electrode, shown in the legend. Many of the experiments exhibited higher amplitude responses in certain directions over others.

Depth CSD Profiles

In all six experiments, there were one or two depth arrays inserted into the cortex through the holes in the ECoG grid. CSD analysis was performed by taking the negative second spatial derivative of the averaged depth responses for each stimulation depth and intensity, with the top and bottom traces duplicated to obtain CSD spanning the entire recorded depth. The resulting differences were divided by the square of the depth electrode pitch to obtain CSD values in units of mV/mm^2. Further details of CSD analysis can be found in Chapter 2.

Figure 4.13 shows the CSD from the eight stimulation intensities swept in the first experiment, all just below the surface at 0.1 mm. Blue represents current sinks and red current sources, with dotted lines encompassing 7.5 ms after stimulation during which artifact contaminated the signal. It is clear that a nearly identical pattern of response took place as a result of each stimulus. Increasing intensity served to increase the strength of the sinks and sources, though it had little effect on the spatiotemporal arrangement. A dominant superficial dipole was seen in all trials, while much weaker elements appeared deeper in the cortex at intensities of at least 0.4 mA. The depth array was 3.5 mm from the stimulating electrode, so the CSD is showing only local activity distant to stimulus. The increasing source and sink amplitude with stronger currents matches the trend seen on the surface.

Figure 4.14 shows the CSD profile for ten different stimulation depths spanning the cortex from experiment two, all at 1.2 mA. The depth array was 3.2 mm from the stimulus site, about the same distance as the first experiment. There was a common arrangement of sinks and sources across stimulus depths deep in the cortex, below 1.7 mm. A dipole near the surface was also elicited, though only visible at some stimulation depths. Interestingly, both elements were strong with superficial stimulation, decreased in amplitude until about 1 mm when they grew stronger, and then again dropped in amplitude below 1.5 mm. The fact that there were two separate depth ranges that caused the strongest CSD response suggests that injecting current at different layers in V1 results in broader activation.

The results here agree with those found using the surface LFPs; namely, higher intensity stimuli generate stronger responses, while stimulus depth has a more complicated relationship with response based on the physiology. Also, neither variable has much effect on the spatiotemporal pattern of the evoked CSD, just as the surface response shapes remained relatively consistent within experiments.

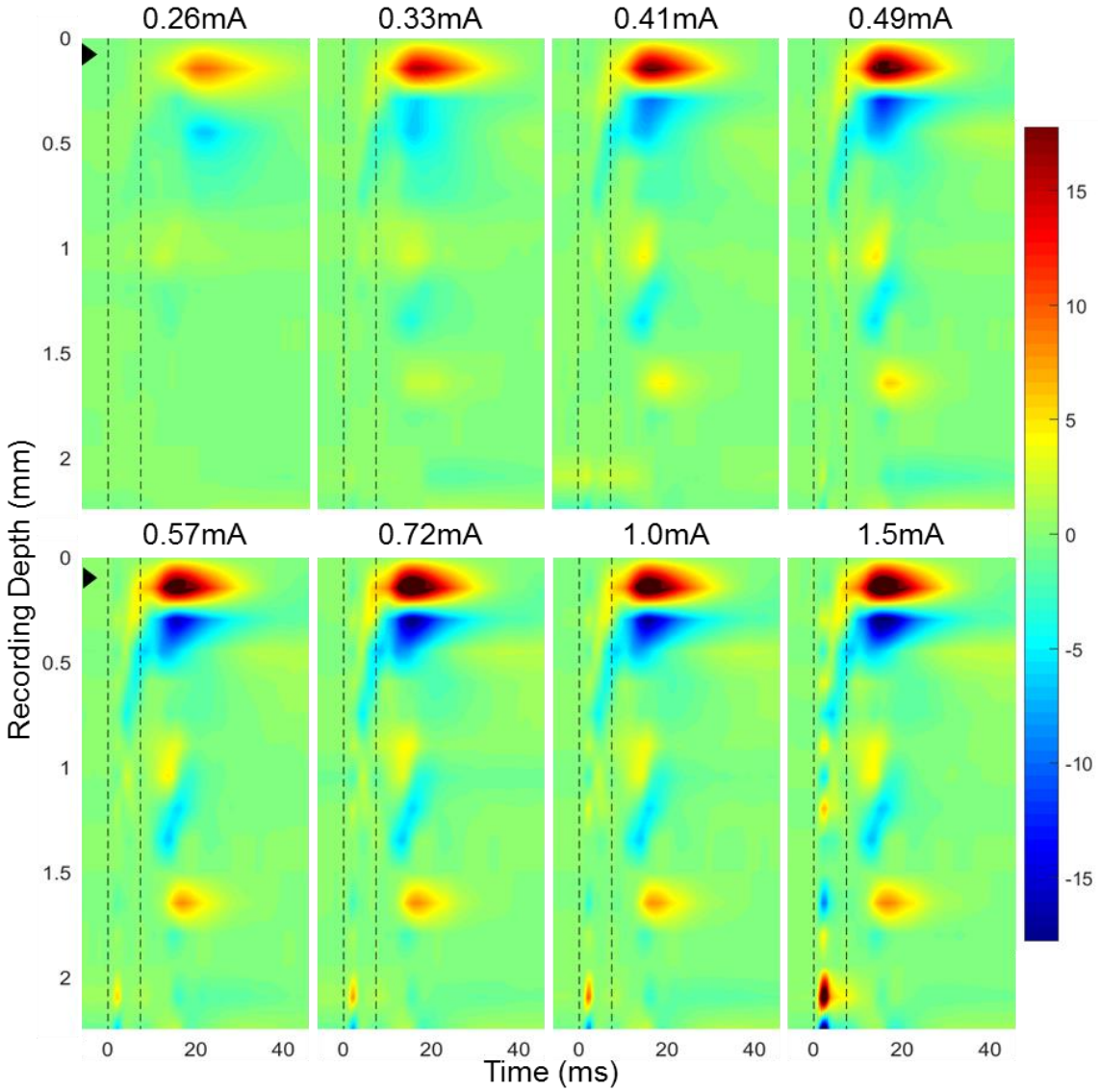

Figure 4.13 CSD Changes with Stimulation Intensity – Experiment One Each plot is the CSD profile calculated from the depth array LFP signals at the stimulation intensity marked above it. The profile covers the entire depth the electrodes spanned, 2.25 mm, and just over 40 ms response time, during which most activity was seen. All stimuli were just below the surface at 0.1 mm, as marked by the black arrow. The first dotted line in each response is at the time of stimulation (0 ms) and the second is 7.5 ms, during which the response was often contaminated by artifact. The color represents the current source density, with blue as sinks and red as sources. The color bar gives the corresponding amplitude for the colors, in mV/mm^2, with the same color limits across plots.

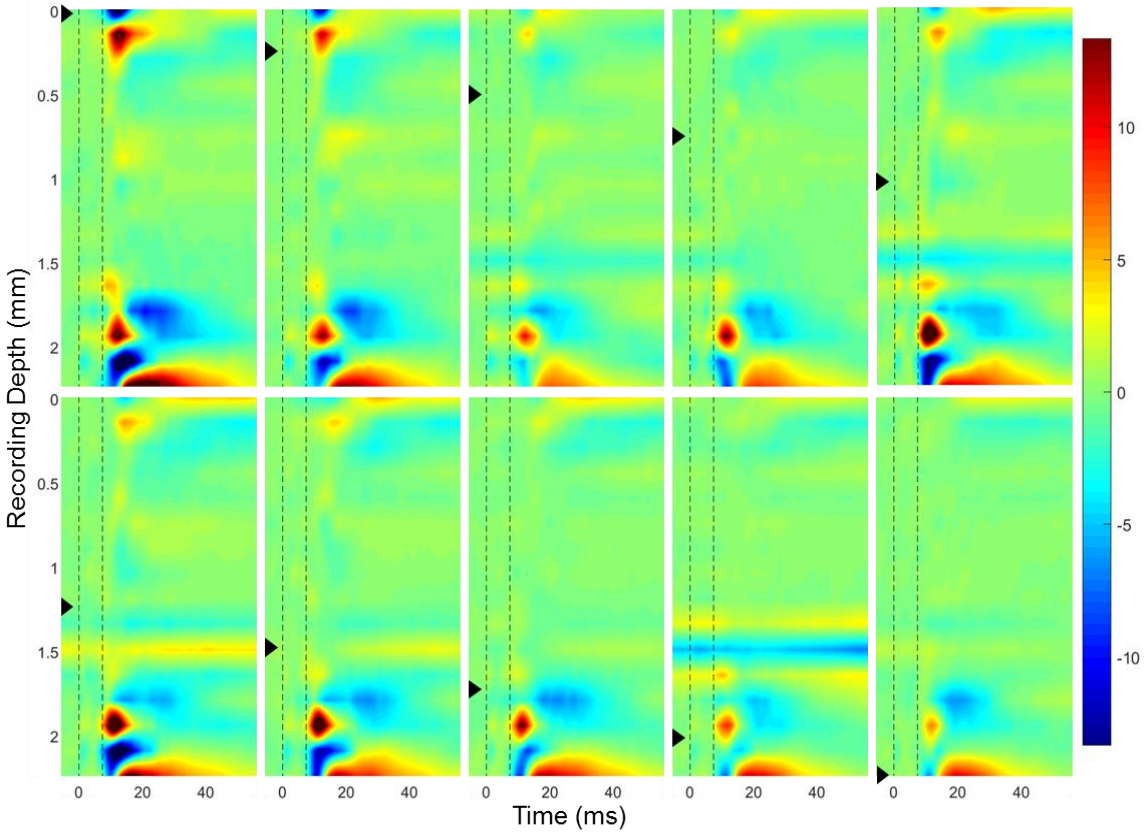

Figure 4.14 CSD Changes with Stimulation Depth – Experiment Two CSD profiles shown with the same convention as Figure 4.13. All stimuli were at 1.2 mA at varying depths, which are shown by black arrows for each trial, spanning from 0.05 to 2.25 mm. CSD changes with depth from the third and fourth experiment are in the supplementary figures chapter.

Thorough sweeps of both stimulus depth and intensity were conducted in experiments five and six. The CSD calculated from those sweeps on the depth arrays closest to the stimulating electrode (2.2 mm distance in each experiment) are shown in Figure 4.15. In experiment five, the profile was very similar across depths and intensities, dominated by a large source around 1 mm with sinks above and below that drifted slightly deeper with deeper stimuli. More superficial stimuli evoked responses at lower intensities than their deeper counterparts. Across all depths, increasing intensity resulted in stronger CSD responses with little change in the spatiotemporal pattern. Looking only at 1 mA intensity, stimulus depths of 0.5 and 1 mm elicited a dipole near the surface of the cortex that was not readily seen at other depths. At higher intensities, this dipole is apparent at all stimulation depths, suggesting that larger currents activated neurons in layers that couldn't be reached at lower intensities, or was not strong enough to elicit a response.

The stimulation sweep in experiment six exhibited many of the same characteristics. The most consistent element was a source around 1 mm that got deeper with deeper stimuli. At higher intensities, a superficial dipole was present at all depths, though at lower intensities it was only elicited by superficial and deep stimuli, not those in the middle. There was deep CSD activity around 2 mm evident at all intensities as a result of stimulation at 2 mm. At higher intensities, the activity was seen clearly up to 1 mm stimulus depth.

It is important to remember that the same depth measurement in two experiments could be in far different parts of the brain physiologically. The physical depth of each layer in cat V1 can vary between subjects and even within a subject due to the curvature of the brain and changes with functional areas. Since each experiment was a different cat and electrode placement varied, stimulation at 1 mm in the fifth experiment did not necessarily affect the same layers as 1 mm stimulation in the sixth experiment, resulting in different network responses.

The results from these sweeps match those found from the surface and the previous CSD profiles. The differences between the nearly identical experiments serve to highlight how variable responses can be between subjects and different stimulation locations. The effect that injected current has on surrounding tissue is clearly dependent on the physiological structure around it.

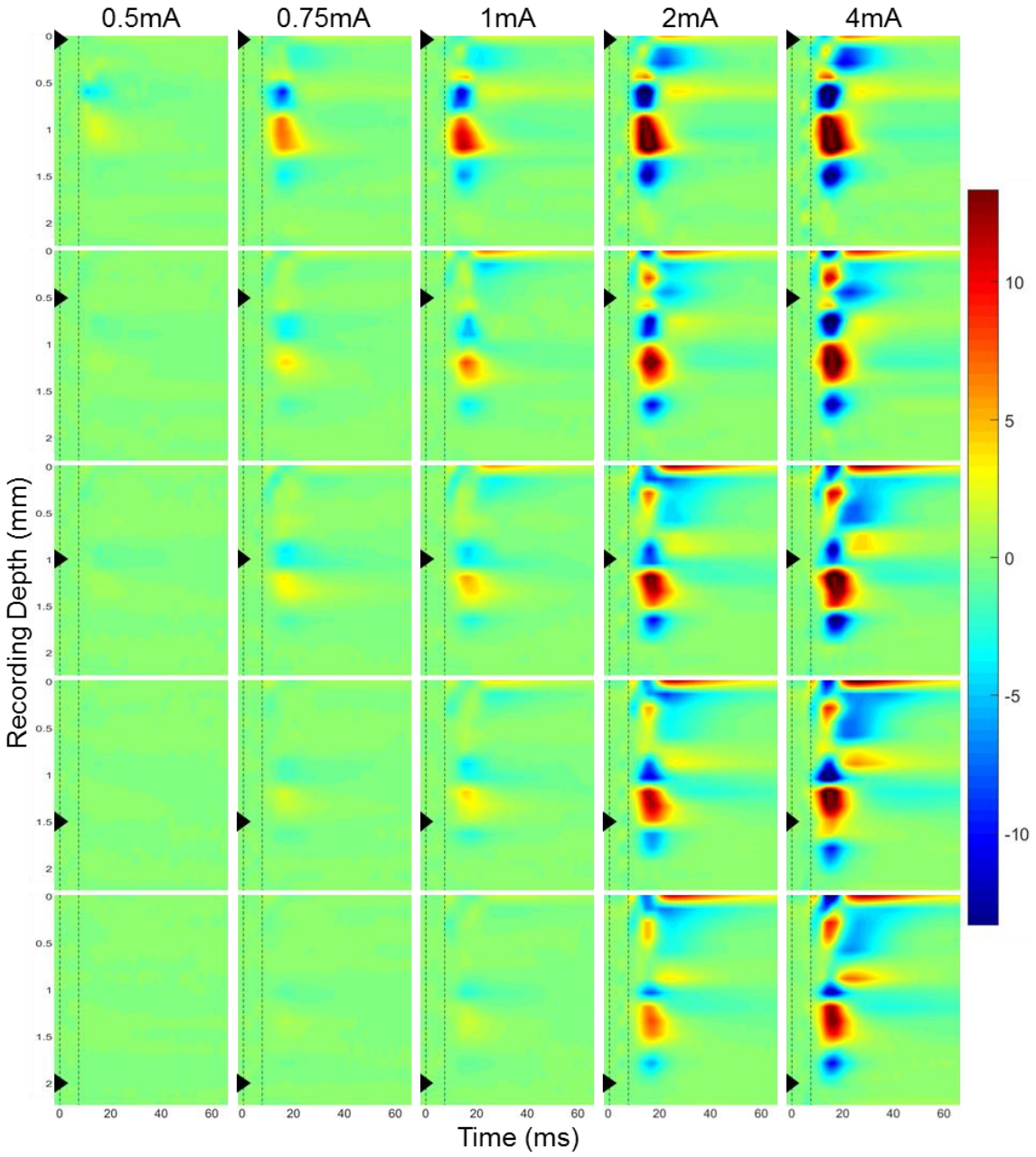

Figure 4.15 CSD Profiles from Stimulation Depth and Intensity Sweep - Experiment Five CSD profiles for every depth (rows) and intensity (columns) of stimulation in the fifth experiment. The stimulation depths are marked by black arrows, and the intensities are marked above each column. The same CSD convention from Figure 4.13 is used here.

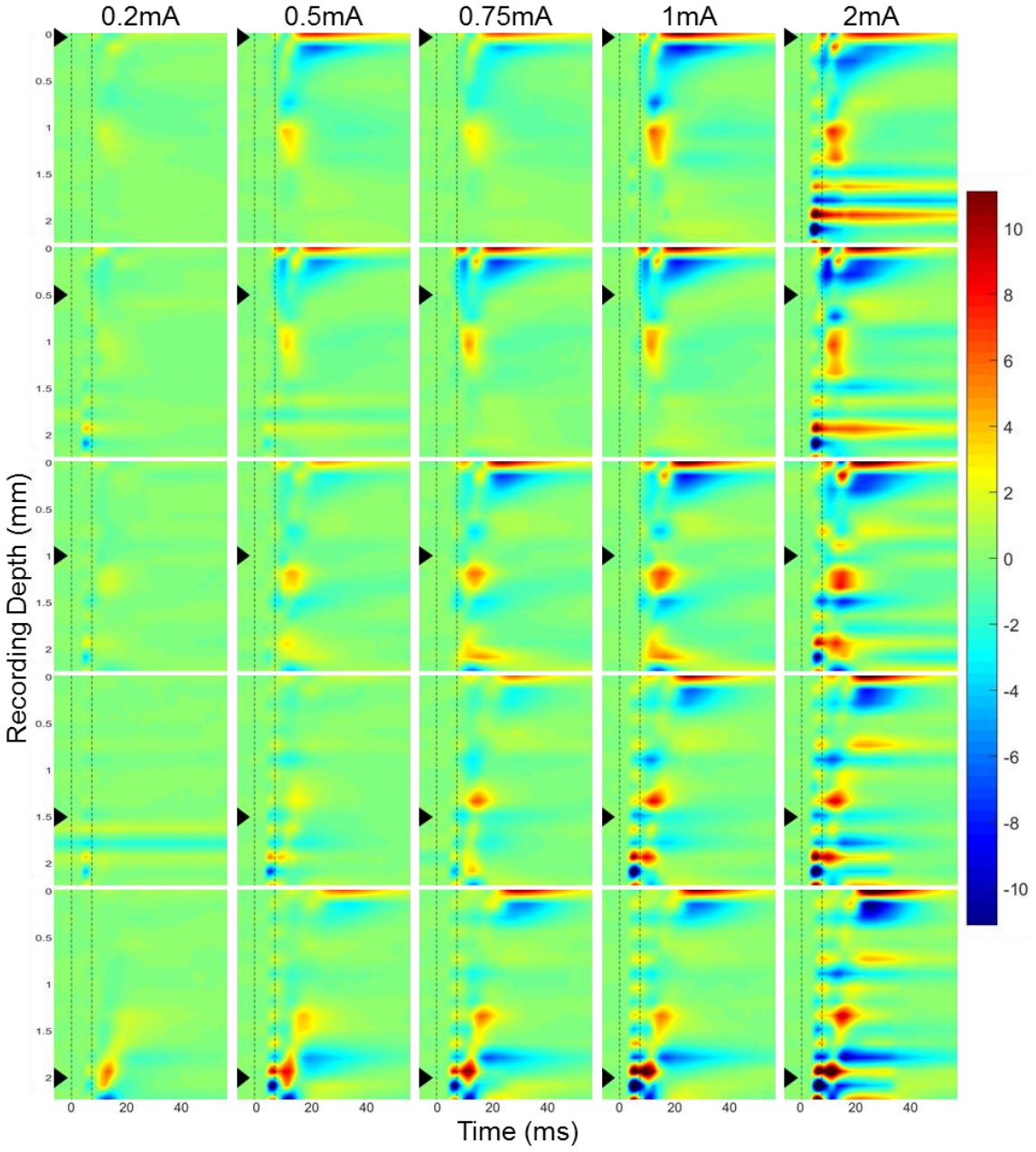

Figure 4.15 CSD Profiles from Stimulation Depth and Intensity Sweep (cont'd) - Experiment Six

Finally, both the fifth and sixth experiments had second depth arrays placed 4.1 and 5.1 mm from the stimulating electrode in each, respectively. Across all depths and intensities, there was no discernible non-artifact CSD response on either array. However, there were detected peaks on the surface electrodes around each array, and the LFPs on the depth electrodes exhibited a significant response. The fact that these were not accompanied by any sources or sinks suggests that the responses at that distance were due to volume conduction and not local synaptic activity. This can also help explain why the surface peak amplitude versus distance results so closely match the model of a point source in a conducting medium.

Propagation Velocity

The propagation velocity for every depth and intensity of stimulation across all six experiments was found. First, the response latency at each electrode was determined using a -0.2 mV threshold crossing within a 17 ms window of time following stimulation artifact for each trial. A negative threshold was used because the negative peak was the most consistent element of the stimulation response across the surface. Next, within each trial, the median latencies for contacts the same distance on the surface from the stimulating electrode were calculated. The distance between each pair of consecutive radii was then divided by the difference between their average latencies. Any latency differences below 0.1 ms were discarded to obtain only outward propagating activity. Finally, the median velocity over all radius pairs was calculated as an estimate for the propagation velocity in that trial.

The calculated propagation velocities are plotted in the top part of Figure 4.16. Over all trials and experiments, the median velocity was 0.48 m/s, with 25^{th} and 75^{th} percentiles of 0.37 and 0.64 m/s, respectively. Experiments five and six had more variability between trials, possibly due to the use of biphasic current pulses or more extensive depth/intensity sweeps. To investigate the effect of stimulation parameters, the lower plots of Figure 4.16 show the velocity of every trial against the respective stimulation depth (left) and intensity (right), with a linear fit for each. The slopes of the best-fit lines were -0.0014 (m/s)/mm and 0.0034 (m/s)/mA, showing that, independently, neither variable had a strong effect on velocity.

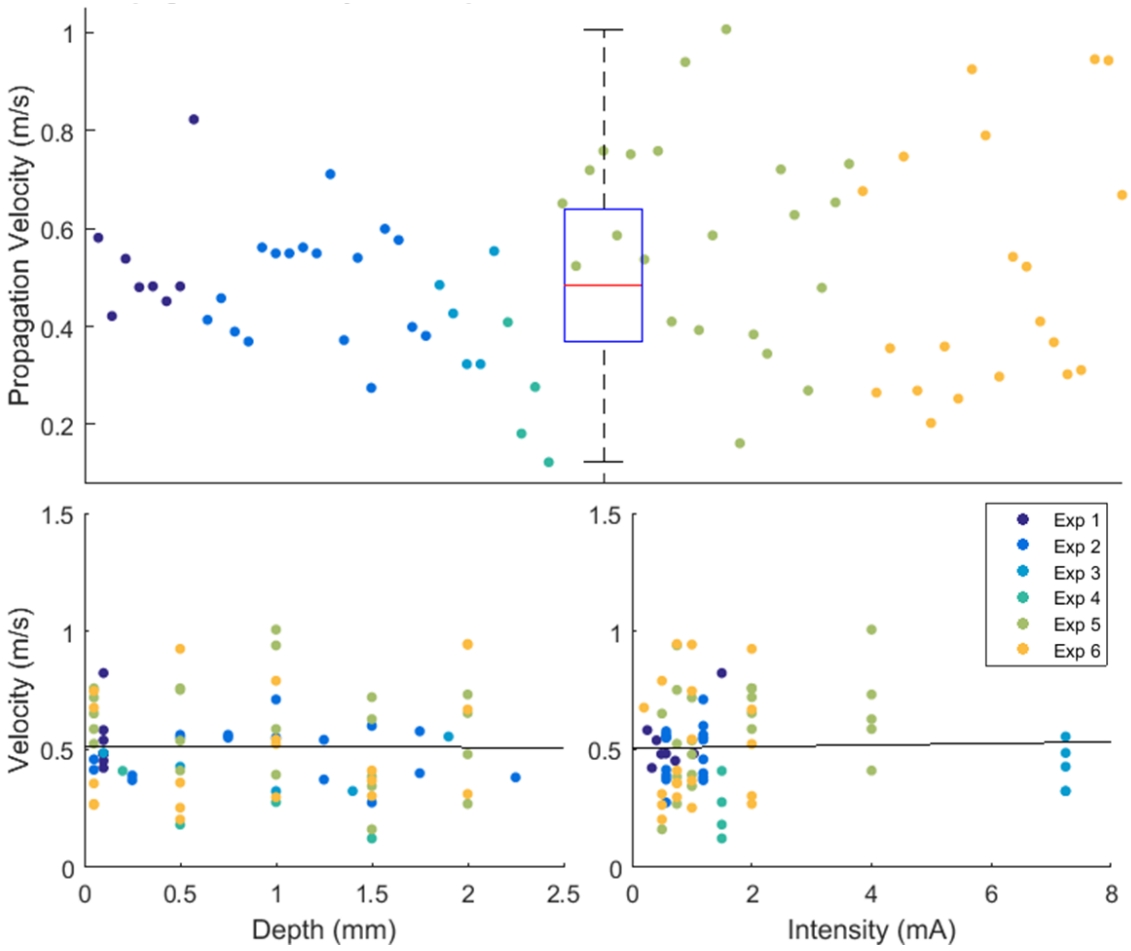

Figure 4.16 Stimulation Response Propagation Velocity The top plot shows the calculated propagation velocity for every stimulation depth and intensity across all experiments, which are broken up by color, according to the legend. The box plot shows the median velocity was 0.48 m/s, with 25th and 75th percentiles of 0.37 and 0.64 m/s, respectively. The lower plots scatter the same velocity data but as a function of stimulus depth on the left and intensity on the right. Linear fits for each are shown, with slopes -0.0014 (m/s)/mm for depth and 0.0034 (m/s)/mA for intensity, indicating velocity was not strongly dependent on either variable.

Discussion

Orientation Tuning

Some electrodes showed a clear preference for specific orientations based on their LFP power in the gamma band, as has been shown in previous studies. Just as those studies found issues relating the LFP tuning to that of the surrounding neurons, many of the tuned electrodes here did not follow patterns found in neuronal orientation tuning research. In two of the experiments, the spatial and/or temporal frequencies were varied in order to target V1 and V2. However, there was not a clear trend showing an increased tuning in the expected area. In ORT3, the low spatial frequency test revealed 10 tuned electrodes mainly near the center of the array, many possibly over the transition zone. When the spatial frequency was increased, only two electrodes were tuned, one of which was tuned at the lower frequency value as well. Similarly in ORT4, there was no trend of tuning going from V1 to V2 as the spatial frequency was decreased and temporal frequency increased. One of the possible issues was picking spatial and temporal frequencies that did not best suit finding tuning in V1 and V2, or, in the case of ORT4, changing both parameters simultaneously. In fact, spatial tuning columns are seen throughout the visual cortex, as well as differences in preference between cortical layers, which could further confuse the results of this testing (Payne & Peters 2002). Also, orientation tuning might not be the right metric to use in delineating functional boundary responses, but something like contrast sensitivity instead.

It is possible that the surface electrodes were too big and the recorded LFP sampled too large an area to consistently show orientation tuning. As Figure 2.3 showed, there are many boundaries between orientation domains, as well as pinwheels where several domains meet at one point. This could also limit the ability of the depth electrodes to parse out tuning, even though they are much smaller. Additionally, it has been shown that the heterogeneity of preferred orientation increases with depth (Maldonado 1997). Since discrepancies between LFP and neuronal tuning have been seen before, even with smaller microelectrodes, the inconsistent tuning could have a different root cause. LFP in the gamma range may not be a reliable indicator of tuning, either because the orientation selective cells do not always fire in rhythm, or because the oscillations in that range are caused or influenced by other populations of cells (Gray & Singer 1989). Also, LFP is typically comprised of synaptic activity, whereas unit-based tuning calculations use action potential firing rate as a response metric, which could cause discrepancy between the two methods of tuning (Berens et al. 2008). More specific experiments would need to

be set up to determine the relationship between the orientation preference of some LFP responses and the underlying columns.

Visual Evoked Potential

The evoked potential of the average response over orientations appeared to be a better indicator of the functional boundary between V1 and V2 than orientation tuning. Typically, in research and clinical settings, VEPs are recorded with EEG, and the few studies that looked at surface LFP response were from one location in V1 and varied between animals and between different visual stimuli (Padnick & Linsenmeier 1999; Schroeder et al. 1991). It has been shown that V1 and V2 exhibit different CSD profiles when presented with visual stimuli due to the differences in how they are enervated (Mitzdorf 1985). The hallmark of the VEP response in what is presumed to be V2 of this study was a very early large and short positive spike, often starting less than 50 ms after stimulus presentation. The speed and brevity of these signals agree with the physiology that V2 mainly receives Y-cell afferents from the LGN, which have rapidly conducting axons and evoke shorter latency effects on target neurons. V1, on the other hand, is dominated by X-cells which are slower and longer sustaining (Payne & Peters 2002; Movshon et al. 1978). This is reflected by many of the VEPs in that area which began later and lasted longer.

The positive V2 peak that occurred less than 100 ms after presentation was the only consistent element across experiments, as was shown in Figure 4.2b. V1 responses outside of ORT4 were small and varied, which may have been due to the low spatial frequency (0.2 c/d) used in most experiments. In ORT4, the VEP shape in V1 was a negative peak around 100 ms followed by a longer positivity, though the positivity disappeared in the final test that had a spatial frequency of 0.2 c/d. The CSD from V1 in that experiment, shown in Figure 4.3c, could shed some insight on the underlying activity causing the response. The profile matches what was seen in (Padnick & Linsenmeier 1999), where they concluded that the early deeper sink must have been caused by thalamocortical afferents to layer IV. Though the depth of layer IV in cat V1 typically spans about 500–1000 μm, it was argued that the electrode was not exactly perpendicular to the lamina. This is certainly possible in these experiments, and the upper sink is too superficial to be layer IV, so it is a reasonable conclusion. The more superficial sink must then lie in layers II/III, which is the target of polysynaptic intracortical connections (Mitzdorf 1985). No VEP depth responses in V2 were recorded to see the CSD profiles there, though it is known that V2 and V1 physiology and connections are significantly different.

Electrical Stimulation

Cellular Mechanisms

The surface response seen across experiments, characterized by a large negative peak and a following broader positive peak, matches with the direct cortical response seen in previous studies. Figure 4.17 shows the average CSD response across intensities from the most superficial stimulation in the fifth and sixth experiments. Above each CSD profile is the response seen on the four surrounding ECoG electrodes, averaged over the electrodes and intensities. This shows the general relationship in those experiments between the surface recordings and underlying activity as a result of superficial stimulation. It is clear the ECoG reflects the current sinks and sources in the most superficial layers, matching the results from previous work (Buzsáki et al. 2012).

Barth et al. used CSD analysis to investigate the laminar activity caused by stimulation directly on the cortical surface (Barth & Sutherling 1988). They postulated that the initial positivity seen on the surface response was caused by the depolarization of the soma and proximal apical dendrites of surface cells, creating a surface source. An early superficial source can be seen in experiment six profile in Figure 4.17. As mentioned before, the early positivity was not prominent on the surface across experiments and was often occluded by artifact. Next, the large negative peak was thought to be caused by depolarization at the distal ends of apical dendrites of surface and deep cells, along with additional hyperpolarization of deep cell somas, causing a superficial sink and deeper source. Both elements are clearly seen in the figure occurring at the time of the negative peak, around 15–20 ms after stimulation. This pattern, especially the mid-layer source, was the most consistent element in those experiments, just as the negative peak was the most consistent surface response. The appearance of the middle source across all depths of stimulation could be evidence that it was the location of pyramidal cells that received many afferent connections from different distal layers. The propagation velocity of the negative peak, 0.5 m/s, is on the order of what was seen previously with surface stimulation (1 m/s) and attributed to the relatively slow conduction in apical dendrites of deep pyramidal cells (Chang 1951). Finally, the late positivity on the surface was seen with a large surface source and a distributed sink below it, caused by deep soma hyperpolarization and repolarization of distal apical dendrites. The late superficial dipole was also common at all depths of stimulation concomitant with the positive peak.

The response to superficial stimulation in the first two experiments, which was shown in Figures 4.13 and 4.14, had different CSD profiles than those of experiments five and six.

Experiment one had almost no negative peak on the surrounding ECoG electrodes but a large positive one, corresponding to only a large source in the upper layers of the CSD. Experiment two had a negative peak, but instead of middle-layer activity, it saw very deep sinks and sources. These differences could be attributable to the fact that the depth arrays were 1 mm farther from the stimulating electrode than in the later experiments. Also, the stimuli were monophasic, as opposed to the biphasic pulse used in five and six. Finally, the angle and location of the depth electrode varied between experiments, which causes issues comparing the depths of sources and sinks.

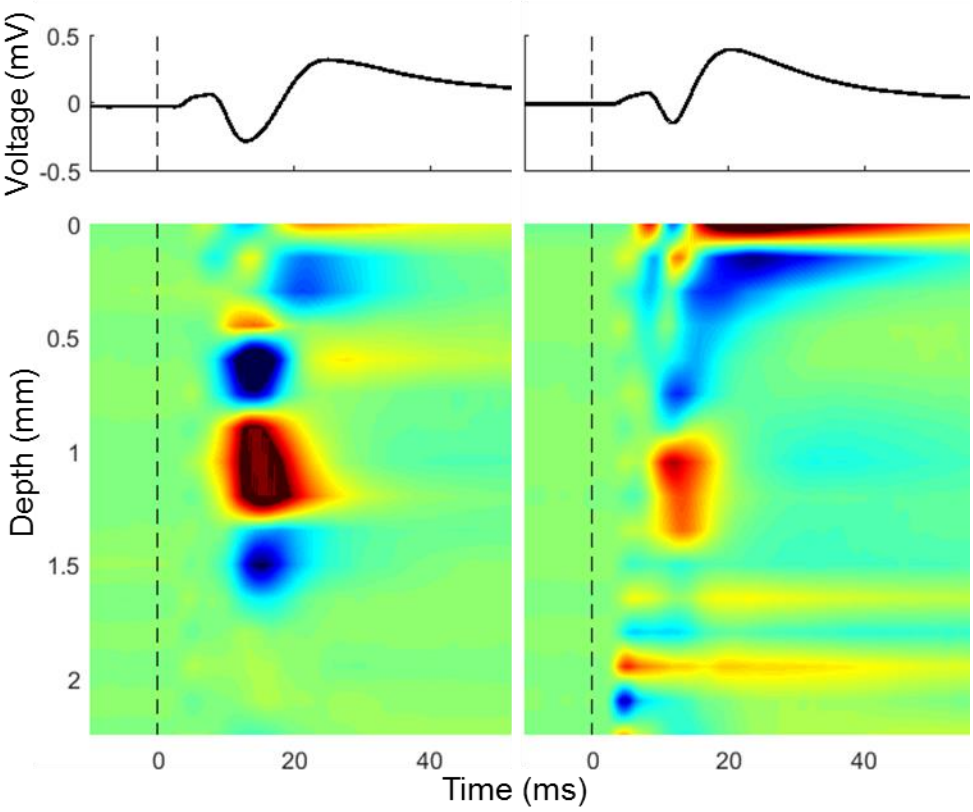

Figure 4.17 Average Superficial Stimulation Response The CSD plots are the average response over intensities to stimulation at 0.05 mm in experiments five (left) and six (right). The upper traces are the average of the four surrounding surface electrodes over all intensities. A superficial sink is aligned with the negative surface peak, followed by a superficial source during the positive peak. The CSD profiles generally agree with previously theorized mechanisms of activation resulting from surface stimulation.

Spread of Activation

Previous work has shown that there is an area around the tip of a stimulating electrode in which neurons are reliably activated. The radius of that area is proportional to the intensity of stimulation in the following manner:

$$r = \left(\frac{I}{K}\right)^{\frac{1}{2}} \tag{4.2}$$

where *r* is the radius of activation, *I* is the current level and *K* is the excitability constant of the tissue (Tehovnik et al. 2006). To see how this activation area relates to the spread exhibited in these experiments, Figure 4.18 shows a plot of response radius, or the distance from the stimulation electrode to the farthest ECoG contact with a detectable peak, for every trial across experiments as a function of stimulation intensity. Red circles denote a radius calculated from an electrode that was on the edge of the array, so the actual response radius might have been higher. The solid black line is the equation for the activation radius (Equation 4.2), using 1,292 μA/mm^2 as an excitability constant, per (Tehovnik et al. 2006). The dashed black line is the equation with *K* optimized to fit the data using the method least squares. This was done to determine if the spread captured by the negative peaks on the ECoG array was proportional to the activation radius. The fitted line had an R^2 value of -0.47. The negative value indicates that the fit is worse than that of a horizontal line at the mean distance. Clearly, the response spread calculated in these experiments does not follow the same model.

There are a few possible reasons for the difference between the response radius and activation radius. First, the values that come from the edge of the array may be smaller than the actual spread, bringing down the overall trend. Also, stimuli with the same intensity at different depths gave much different values, making it difficult to model the response. The changes with depth suggest that the spread on the surface is very dependent on what neuronal elements are within the area of activation. For instance, at low intensities in experiment six, the response radius values were highest for the most superficial and deepest stimuli. Assuming the same activation radius for all depths of stimulation, more neurons, or more well-connected neurons, must have been activated at those two depths than the others. Additionally, high intensity stimuli evoked similar CSD responses independent of depth, indicating that the areas of activation were large enough to activate elements throughout the laminae.

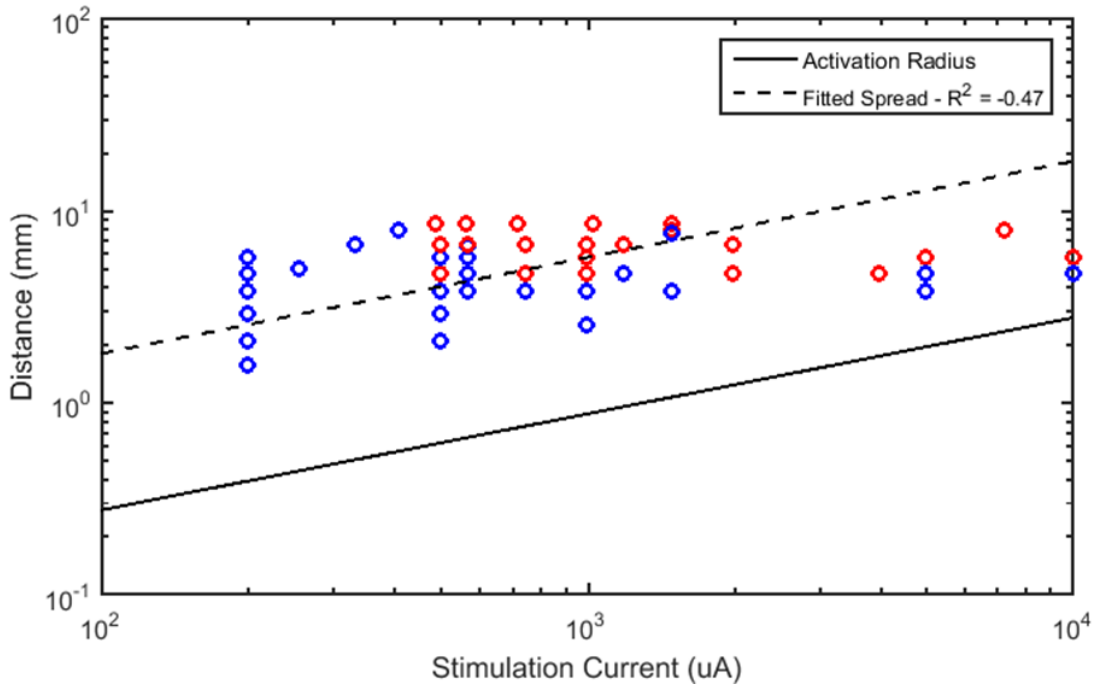

Figure 4.18 Response Distance vs Activation Distance The scatter plot shows the response radius values for all responding trials across experiments. The red circles represent values taken from electrodes on the edge of the array, indicating the response radius may have been greater. The black line is the activation area model from Equation 4.2, with 1,292 $\mu A/mm^2$ as the excitability constant. The dashed line used least squares to find the coefficient that best fit the data to the model. The R^2 of the line was -0.47, indicating a worse fit than using the mean distance value across all intensities.

Implications for Seizure Treatment

The results point toward the idea that much of what was recorded on the surface was due to volume conduction. The peak amplitude values fit well with the point current source model in a conducting medium. Many of the values that fit best were those far from the stimulating electrode with small amplitudes. CSD profiles near those distant electrodes, however, showed no consistent sources or sinks, indicating a lack of local activity below the surface response. In experiments four through six, two depth arrays were used, with the closer ones at 1.4, 2.2 and 2.2 mm, respectively, and the farther ones at 6, 4.1 and 5.1 mm, respectively. Consistent CSD profiles were found on the closer arrays starting at low intensities, but the farther ones did not see any detectable pattern across the entire intensity sweep. The experiments with only one depth array all had distances less than 4 mm and all saw CSD responses, suggesting that the evoked activity is limited to a set distance and does not necessarily scale with intensity. This matches with the theory that microstimulation directly activates sparsely distributed neurons near the electrode and increasing current fills out this area rather than extending the distance, with little synaptic activation (Histed et al. 2009).

These conclusions have implications for the treatment of medically refractory epilepsy. First, in both clinical macroelectrodes and μECoG, the sampling of volume conducted signal would misrepresent underlying cortex as being engaged in epileptic activity. This could lead to incorrect localization of the seizure focus or the unnecessary removal of healthy tissue. Studies using macroelectrodes and multielectrode arrays simultaneously to record seizures in humans found that the low frequency clinical ECoG often shows early, hypersynchronous activity in areas where the underlying tissue is not actually recruited into the seizure, giving misleading information for localization (Schevon et al. 2012).

In addition to localization, the findings could also impact how neurostimulation devices are designed. The limited spatial range of activation would require the stimulation to be in close proximity to the intended target. If the focus is believed to be diffuse, this may require more electrodes to effectively activate the disruptive tissue. The volume conduction of signals could misrepresent the extent of cortex on which stimulation actually has an impact. Finally, it was seen that the response patterns varied depending on the underlying physiology. Modelling the network around the suspected focus could enable stimulation guided to the intended target.

Chapter 5 **Cortical Ictogenesis Model**

Summary

The advancement of seizure treatment technologies, such as μECoG recording grids and responsive neurostimulation devices, necessitates a better understanding of how we map epileptic networks on the surface and in the depth, and how to effectively modulate them to disrupt seizure propagation. *In vivo* experiments were performed in which a seizure focus was chemically induced in an isolated portion of healthy feline visual cortex and the ensuing epileptic activity was recorded with high density surface and depth electrodes. Using a custom algorithm, epileptic events were detected and quantified. A consistent evolution was seen across subjects starting with single spikes leading to polyspike events and eventually seizures. The spatial spread of these events on the surface was examined, revealing a slight growth of seizure focus over time and a strong inhibitory surround, though not present in all experiments. CSD profiles revealed complex patterns of activity through the cortical laminae not represented on the surface recordings. The spread of the seizure focus was marked by the appearance of deep activity on the CSD, suggesting that the recruitment of healthy tissue requires engagement of deep horizontal connections. There were similarities between the induced events and what is seen in human epilepsy. The findings here could have significant impact on clinical localization methods and potential targets for stimulation devices to terminate seizures.

Methods

The methods for animal preparation and data recording are detailed in Chapter 4. Portions of recordings that had large amounts of noise across multiple electrodes were discarded. Periods of electrical stimulation were present during three of the seizure experiments. When the stimulation was constant or high-frequency, the recordings were discarded. If it was intermittent, there was little effect on seizure activity and it was left in for analysis.

Seizure Model

Picrotoxin was applied to the cortex of five cats. In the first three experiments, 5-15 mg was placed in a confined area on the surface of the cortex. In the remaining two experiments, picrotoxin in solution with saline (5-10 mM) was injected 1 mm deep in the cortex with a Hamilton syringe. 100 μL and 10 μL of solution was injected in experiments four and five, respectively, with the latter spread over multiple injections. Figure 5.1 shows the location of the depth electrodes and picrotoxin application relative to the surface array in each experiment. Figure 5.2 is a photograph of the surface array over the left posterior lateral gyrus with two depth electrodes and one Hamilton syringe inserted through the holes in the ECoG array.

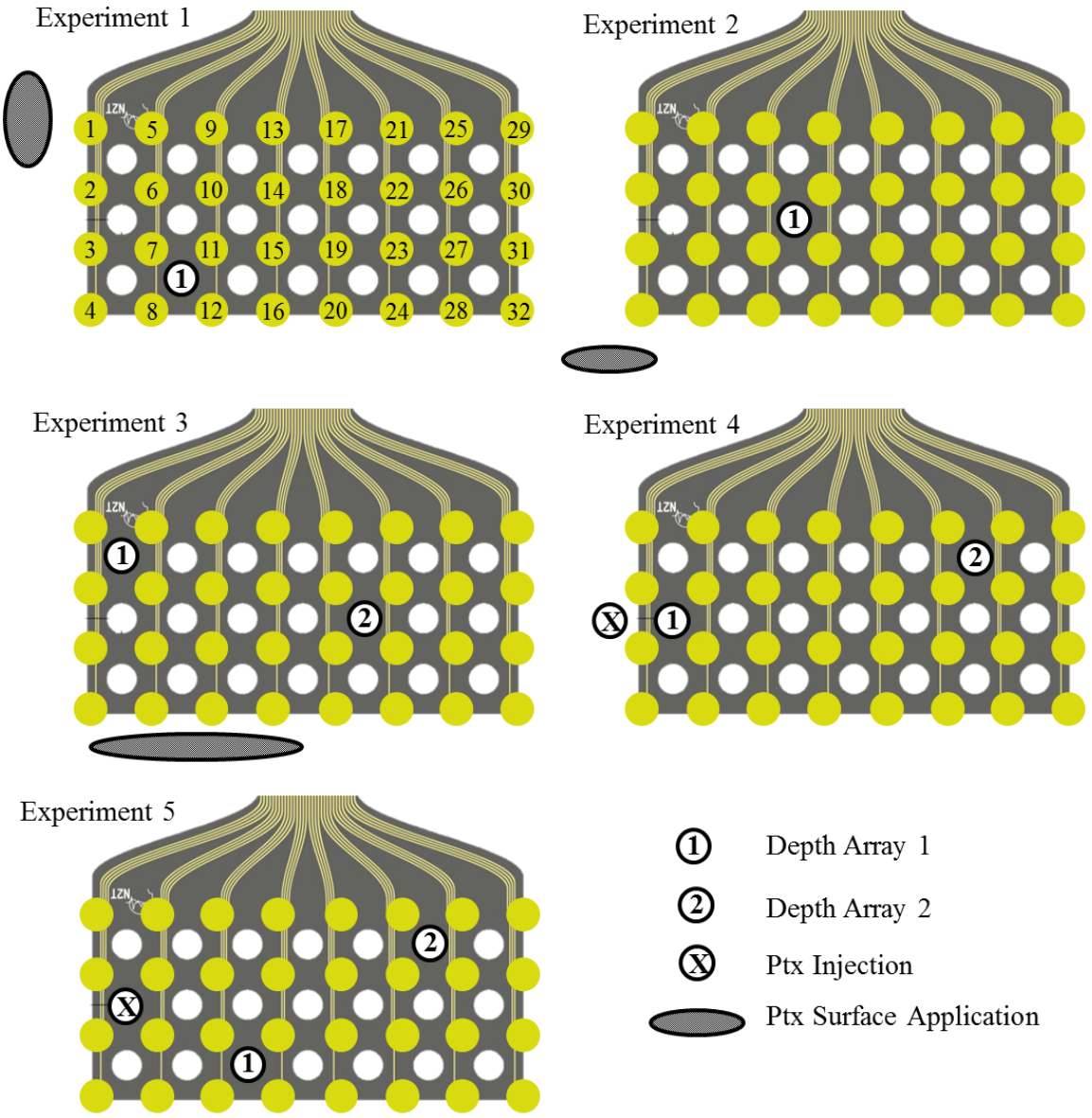

Figure 5.1 Experimental Arrangements The surface array is shown for each experiment, with gold circles representing electrodes and white circles the holes in the substrate. The electrode numbering convention is shown in the experiment one example. The illustration orientation is looking down from above the arrays as they would appear in the craniotomy, such that the exposed contacts underneath are touching the cortex. The positions of the depth shanks and areas of picrotoxin application are noted relative to the ECoG grid.

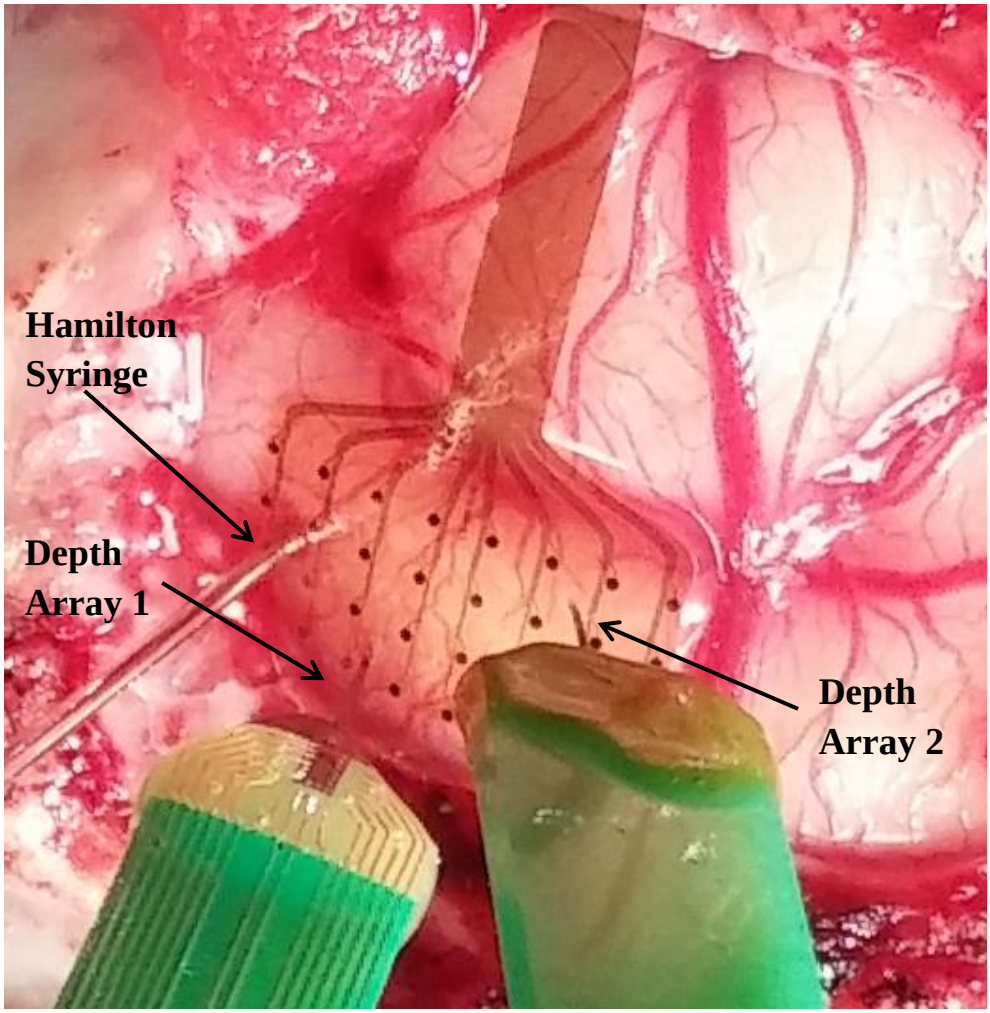

Figure 5.2 Preparation Picture An example from the fifth experiment showing the surface array on V1 with two depth arrays and a Hamilton syringe (left) placed through the holes.

Epileptic Event Detection

Spontaneous epileptic events appeared on the surface and depth recordings of otherwise normal background EEG within minutes of adding picrotoxin. There were three main types of events: (i) isolated, high amplitude single spikes, (ii) polyspike complexes with an initial large spike followed by a small number (<15) of lower amplitude, shorter duration spikes, and (iii) seizures, consisting of longer periods of repetitive spikes with variable frequency. Hundreds to thousands of these events were recorded in each experiment. An automated detector was developed in order to capture the events for further analysis. It was run on one surface electrode with high amplitude, consistent spiking activity and low noise, typically close to the picrotoxin application. For the experiments 1-5, the electrodes chosen were 4, 3, 3, 3, and 6.

The detector consisted of a sliding window 400 ms in length with a 300 ms overlap to capture spikes occurring close in time as a single event. The standard deviation of the recorded signal was calculated in each window. A threshold was determined by eye to separate the standard deviation values of baseline and epileptic activity in each experiment. The thresholds were 130, 275, 300, 300 and 200 μV for the five experiments. The positive-going and negative-going standard deviation threshold crossings marked the beginning and end points of events, respectively. Each end point was extended by one window length to capture small, typically positive activity that followed a spike. Figure 5.3 shows example detections of single spike and polyspike events. The event starting point for the single spike in the top trace was well before the spike occurred, due to the length of the sliding window. The second trace shows two spikes detected as a single polyspike event due to their close proximity in time. The bottom trace shows the ability of the detector to pick out individual polyspikes.

Seizures in this model typically exhibited a reduction in spike frequency within each event. Late in seizures, discharges had long intervals between them and were detected as separate polyspike events using the detector as described. This can be seen in the examples in Figure 5.4, where the magenta trace represents the standard deviation detector that drops below threshold before the end of the seizure. A memory component was added to the detector in order to capture entire seizure events. If 15 consecutive windows (1.5 s) were above threshold, then the value of the next window was the standard deviation calculated in the normal fashion plus one-half of the mean standard deviation values from the previous 15 windows. The detector then stayed well above threshold until the end of the seizure before returning to baseline levels. The blue trace in Figure 5.4 shows this modified detector, and the event start and stop points (green and

red lines) found when it crossed threshold, encompassing the entire seizure in all three examples.

The detector had very few false negatives due to the large amplitude of the spikes. False positives were also rare, typically resulting from noise artifact detections. There were events that were clearly misclassified by the detector. The bottom trace in in Figure 5.5 shows a single seizure from experiment 4 in which the beginning was classified as polyspikes due to the low-amplitude interval that occurred before the memory component was engaged. In other cases it was difficult to tell if the event detections were correct due to abnormal spiking activity. The top three traces are clips from experiment 3 that show long runs of spiking activity that were detected as seizures or multiple polyspikes. These detected seizures did not share the same pattern common in the other experiments, especially the top example, which may in fact show status epilepticus. Outside of the third experiment and parts of the fourth, there were very few misclassifications.

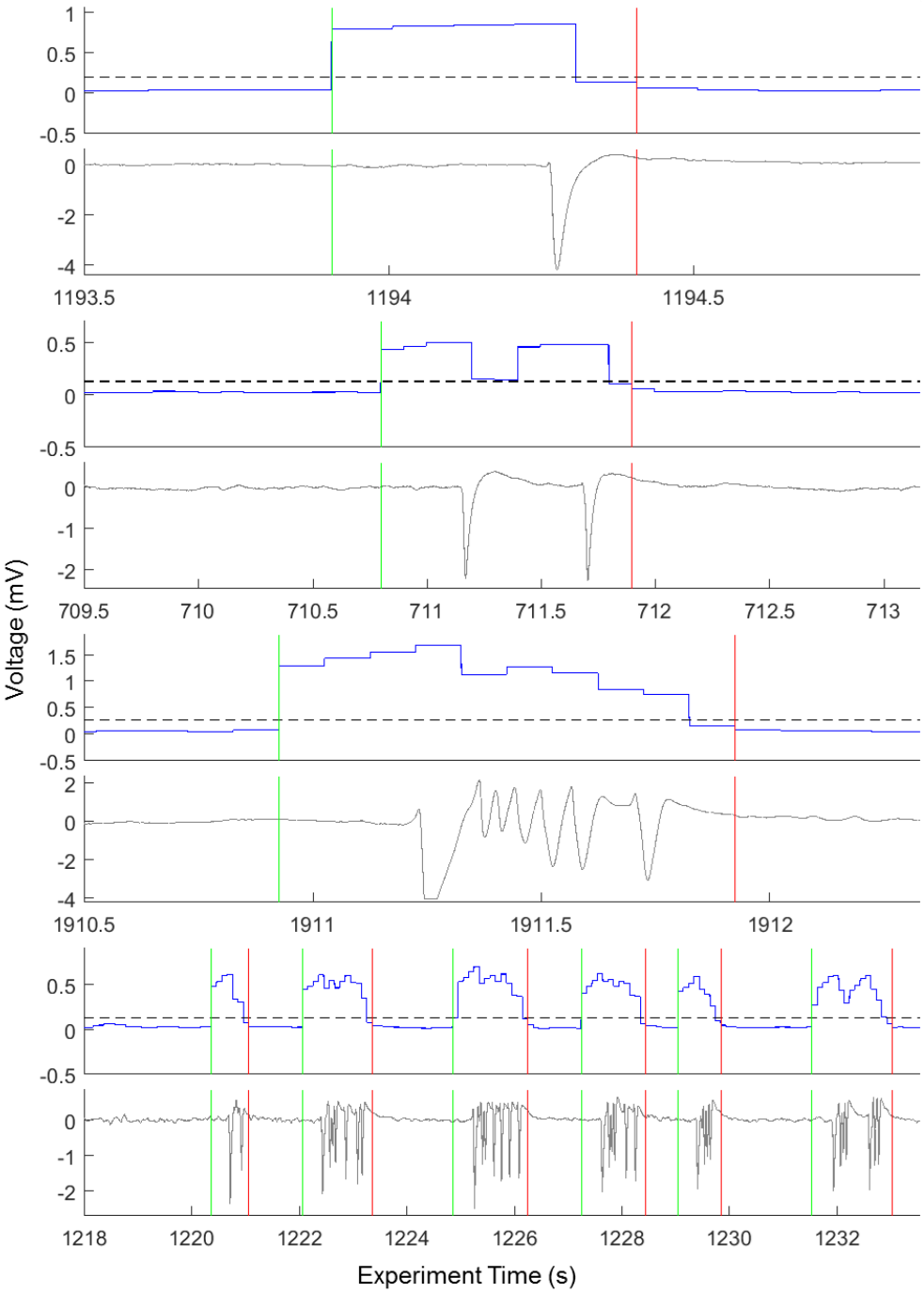

Figure 5.3 Single/Polyspike Event Detections Example detections of single/polyspikes from three different experiments (5, 1, 2 and 1 from top to bottom). The gray traces are the recorded events and the blue traces are the standard deviation detector whose threshold for detection is represented by the dashed black lines. The horizontal green and red lines mark the start and end points of each event detection.

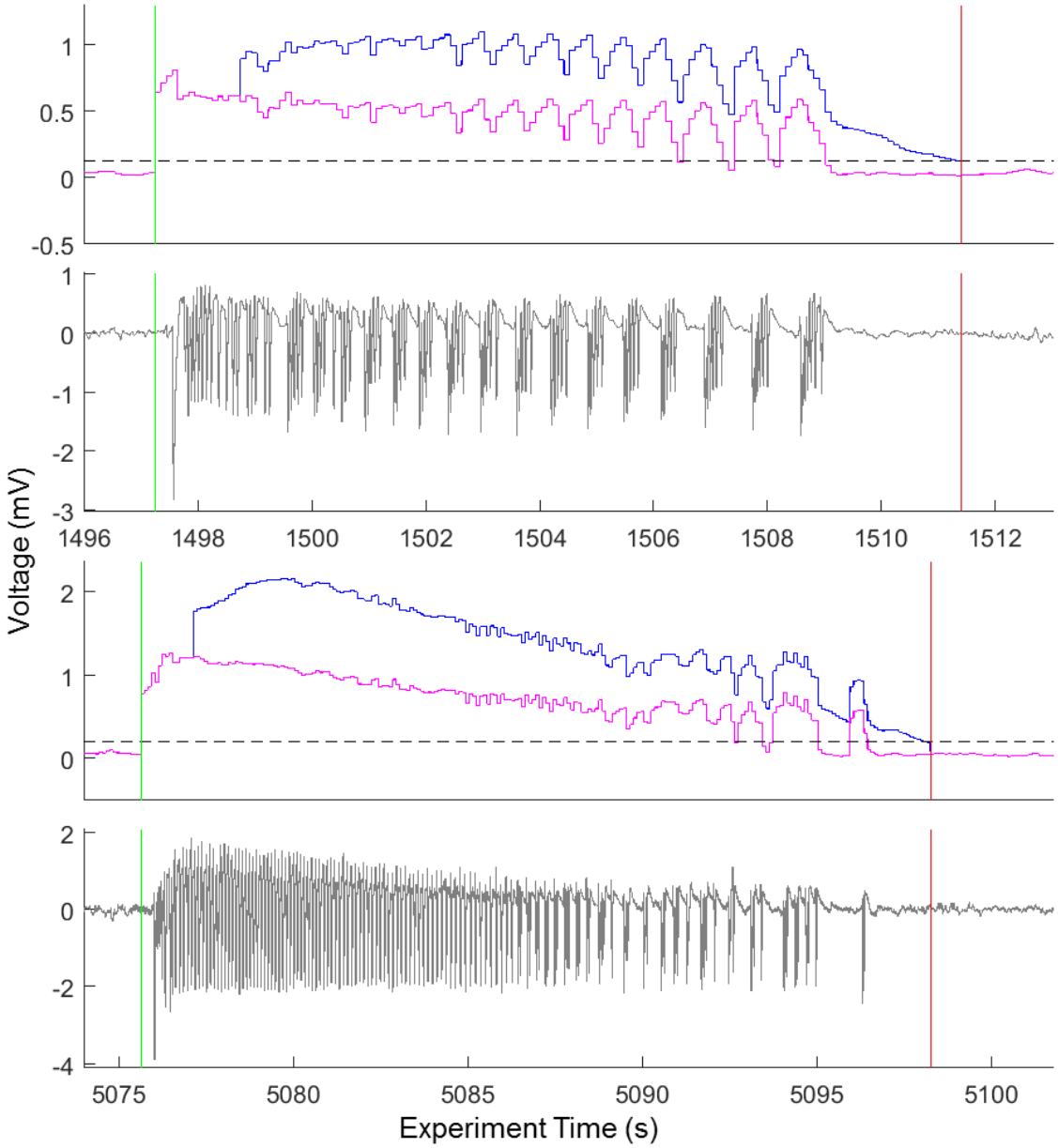

Figure 5.4 Seizure Detection with Memory Component Seizures detected in two different experiments showing how the detector with an added memory component (blue) improved seizure detection over the standard detector (magenta).

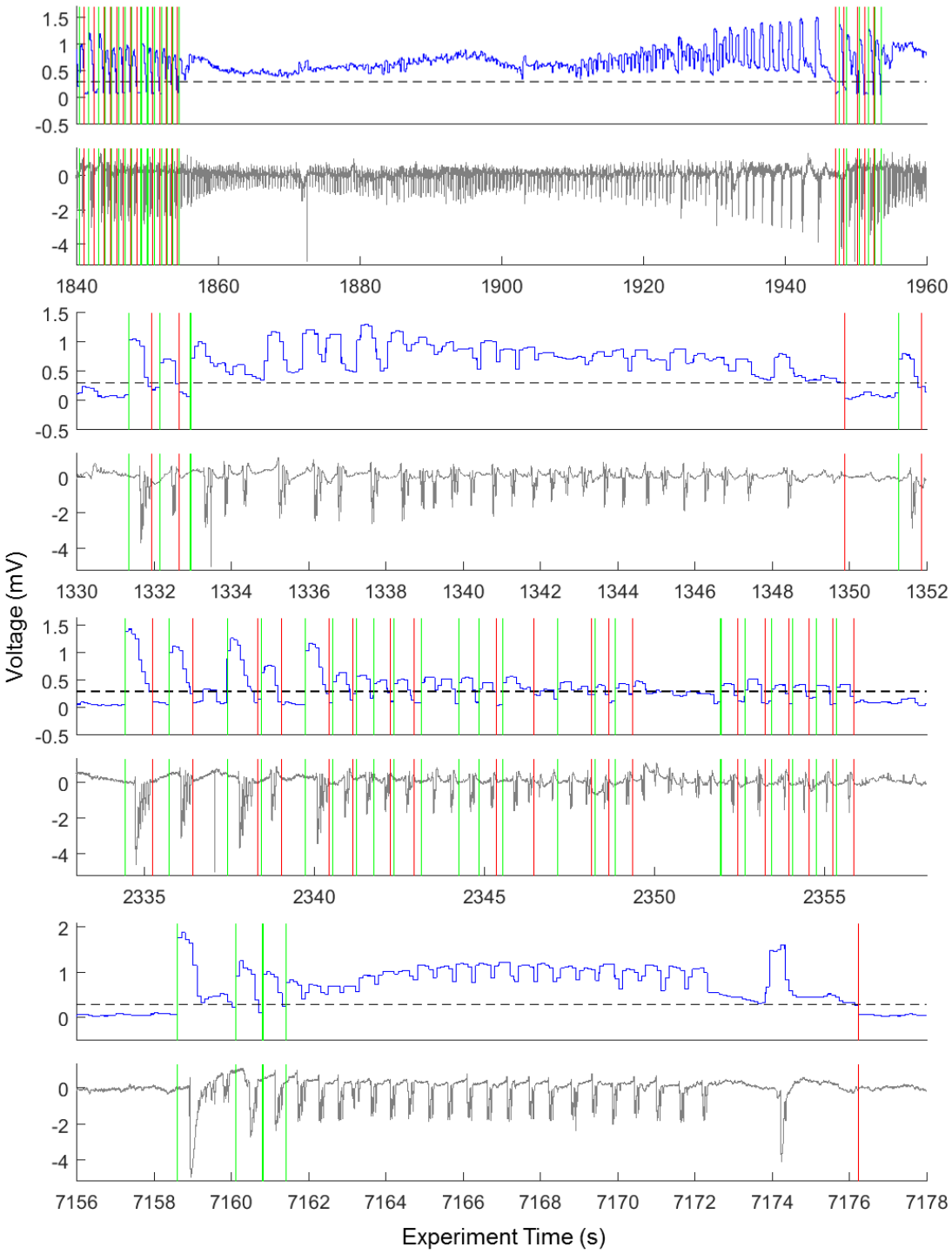

Figure 5.5 Event Detector Issues Problems in detecting events mainly arose in experiment three (top three) due to its unique activity, making it difficult to delineate seizures from polyspikes. Experiment four (bottom) saw similar issues with slow activity at the beginning of seizures.

Finally, the spikes within each event were found. To get a measure for baseline voltage, the pooled standard deviation of all sub-threshold detector windows within each experiment was calculated. A voltage threshold was set at six times this baseline value to be well outside of non-epileptic activity but still able to catch many smaller spikes. It was only applied to negative spikes since they were the predominant type seen on the chosen electrodes. All threshold crossings of the recorded traces were then found. Any crossing separated from the previous by 10 samples or fewer (~ 5 ms) was discarded, as it was either noisy activity close to threshold or an artifact due to stimulation or environmental noise. If the first detection in an event did not cross a larger threshold of ten times the baseline pooled standard deviation, it was discarded and the next spike was made the first. This was done to remove any early spurious near-threshold detections that were not spikes. After applying these criteria, events that did not contain any spikes were removed and the remaining negative-going crossings were saved as the spike starting points and the following positive-going crossings as the end points.

Figure 5.6 shows examples of detected spikes for events from different experiments. The green and red asterisks mark the start and end points of each spike, respectively, and the dashed black line is the spike threshold voltage specific to each experiment. Examples from the first and fifth experiment (a, b, f) show detections within polyspikes of varying lengths. All of the spikes of these events were well detected, which was the case throughout most of these experiments. The example in (c) is a polyspike from experiment two, in which the large spikes were detected, but smaller spikes riding on the positivity after the first spike did not reach the threshold. This was seen in many events that had a large positive deflection following the initial spikes. The opposite case is seen in (e) from experiment four. Since the second spike occurred as the first spike was still returning to baseline, it was too negative to reach threshold and grouped as part of the first spike. These two cases typically only involved a small number of spikes within each event and did not dramatically affect the spike counts. Finally, the example in (d) shows an anomalous event whose baseline began near threshold, so all of the spikes that occurred were counted as a single event.

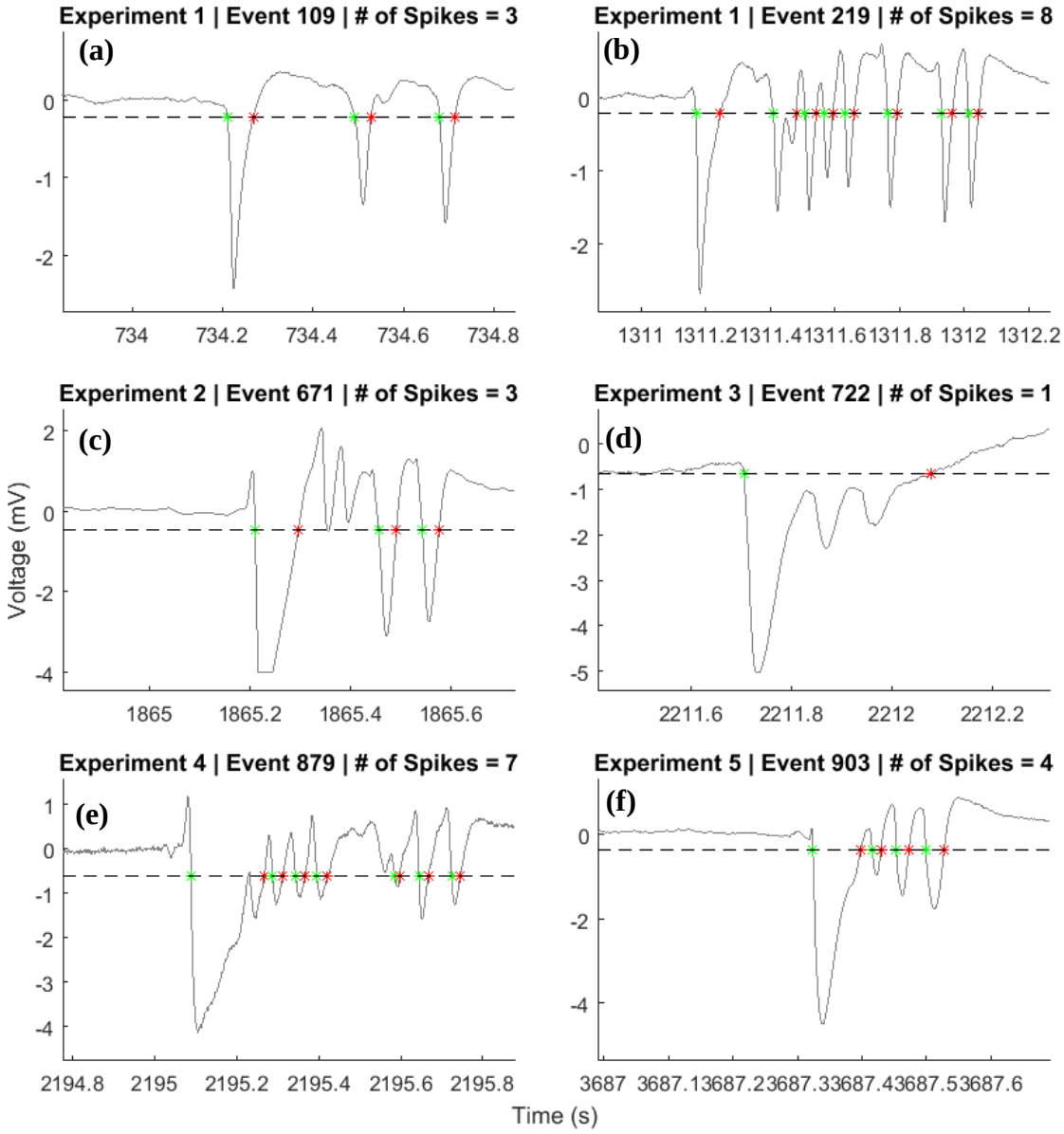

Figure 5.6 Detecting Spikes within Events Examples from every experiment of individual spike detections within polyspikes. Green and red asterisks mark the start and stop times of each detected spike in the event.

Results

Properties of Epileptic Focus Responses on the Surface

Quantification and Distribution of Event Types

The first step after detecting events was determining how to quantitatively classify them into single spikes, polyspikes and seizures. The histogram in Figure 5.7 shows the distribution of events grouped by the number of spikes each contained over all five experiments. Most events had 10 or fewer spikes and single spikes were the most prevalent. Event occurrence decreased with increasing number of spikes until 20 spikes. The inset shows a second grouping of longer events with a peak near 70, representing the detected seizures over all experiments. Since the polyspike and seizure distributions were distinct with little overlap, a threshold of 20 spikes per event, the minimum point between the two, was chosen to separate them. Of 6153 total detected events, there were 2363 single spikes (38.4%), 3541 polyspikes (57.6%) and 249 seizures (4%). The median number of spikes per event for polyspikes and seizures were 3 and 71, respectively.

Within each experiment, the event distributions differed slightly from that of the overall population, as seen in Figure 5.8 and Table 5.1. In experiments 2 and 5, single spikes outnumbered polyspikes in total. Experiment 4 had nearly five times as many polyspikes as single spikes, mainly consisting of events with two spikes. Experiments 3 and 5 contained a lower number of seizures than the other experiments. In the case of experiment 5, this was due to a smaller amount of picrotoxin used. In experiment 3, the seizures that were detected did not resemble those in the other experiments and could have been considered periods of status epilepticus. The number of spikes per seizure was more narrowly distributed in experiments 1 and 4, around 80 and 50, respectively, and more widely in experiment 2.

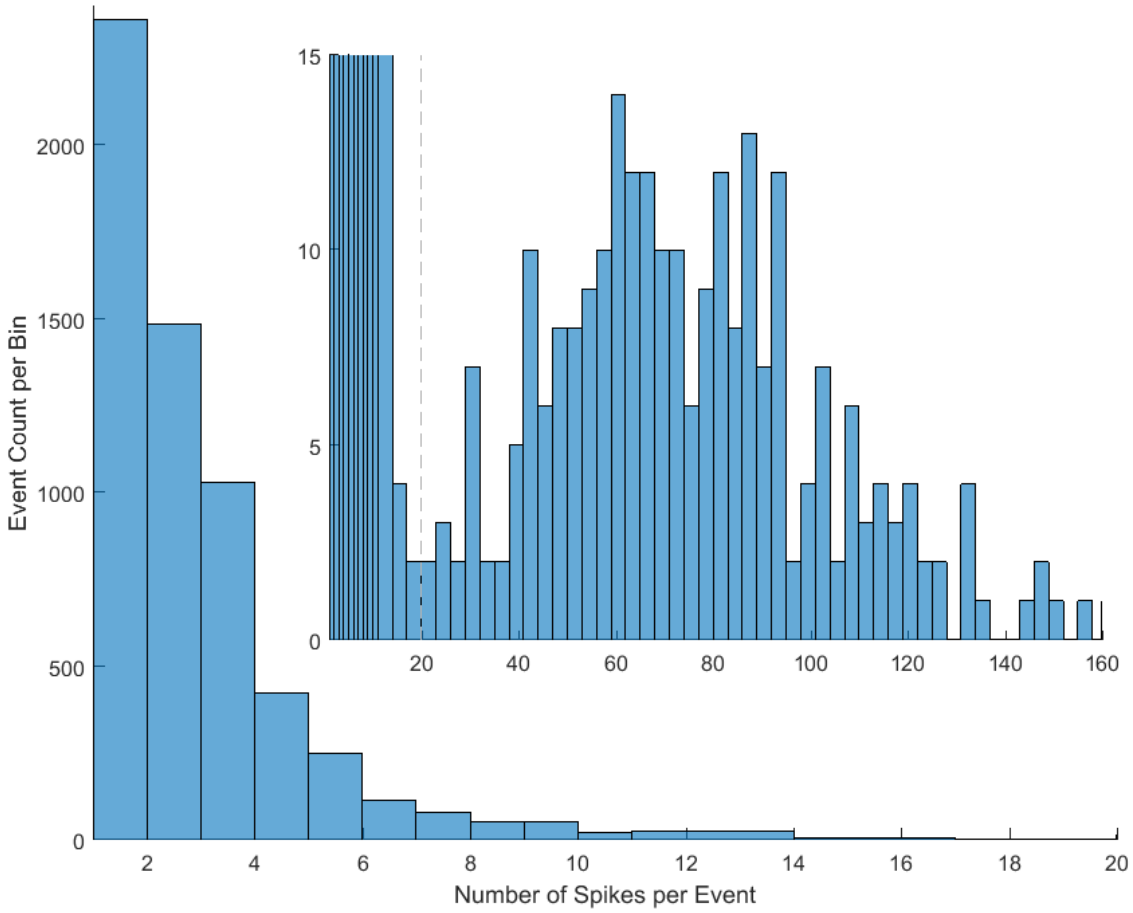

Figure 5.7 Number of Spikes per Event Histogram A bin size of 1 spike/event was used for events with 10 or fewer spikes, while a bin size of 3 spikes/event was used for longer events. The inset is the outer histogram zoomed in to see the distribution of longer events. The line at 20 spikes/event was chosen to separate polyspikes from seizures as it is the minimum between the two peaks in the distribution.

	Number of Events (Spikes/Event)		
	Single Spikes	Polyspikes	Seizures
Experiment 1	100	127 (5)	56 (82.5)
Experiment 2	638	606 (3)	94 (83.5)
Experiment 3	429	721 (2)	9 (60)
Experiment 4	317	1406 (3)	79 (51)
Experiment 5	879	681 (3)	11 (61)

Table 5.1 Event and Spike Totals The total number of events of each type is shown for each experiment, as well as the median number of spikes/event for polyspikes and seizures in parentheses.

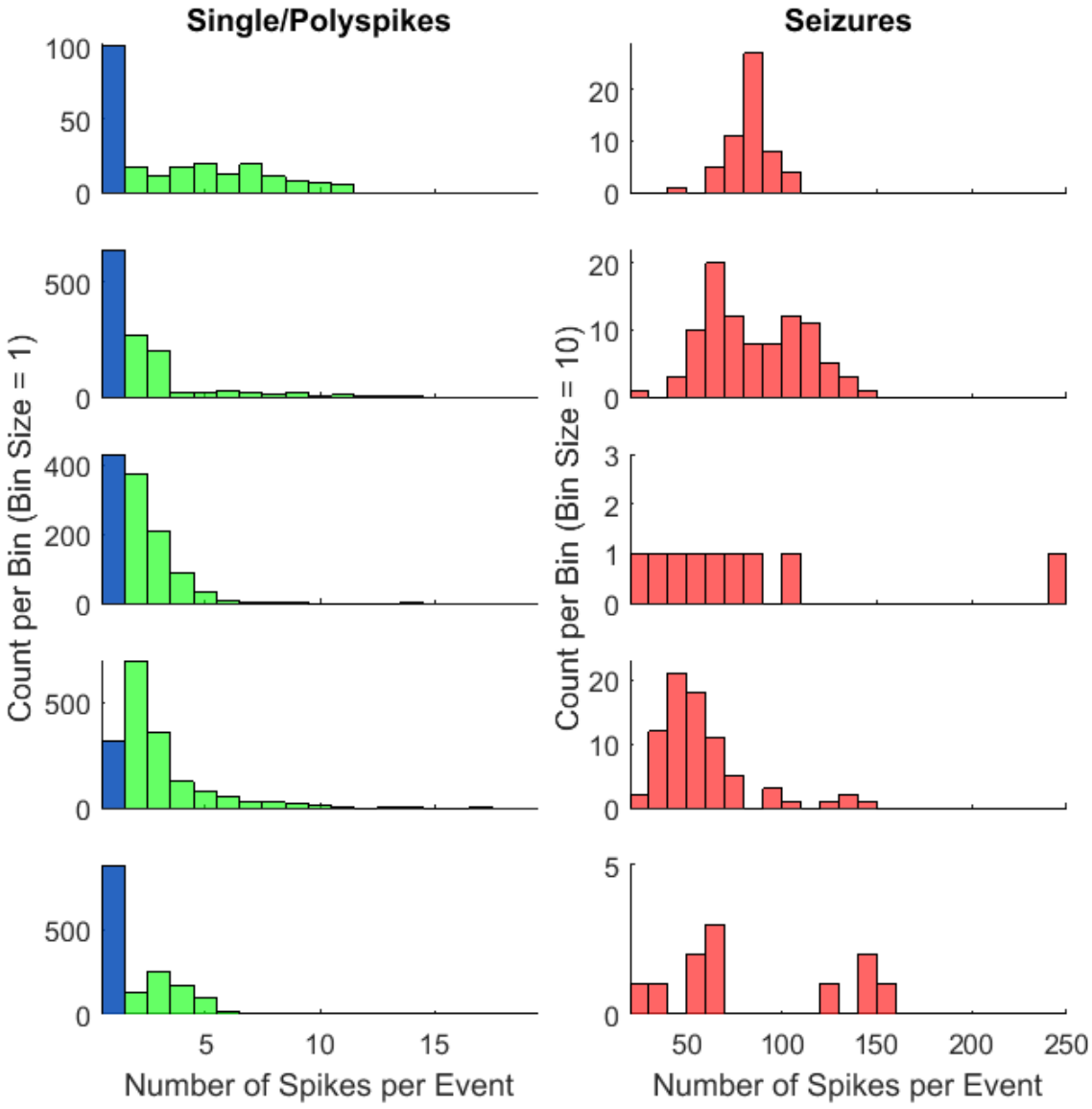

Figure 5.8 Number of Spike Histograms by Event Type Each experiment was broken down into event type using the 20 spikes/event number to separate single/polyspikes (left) and seizures (right). The rows are broken up by experiment, with one to five plotted top to bottom

Figure 5.9 shows all detected events plotted by the number of spikes in each event over the time course of all five experiments. Single spikes are colored in blue, polyspikes in green and seizures in red. There is a clear pattern of event evolution in all experiments. Initially, only single spikes were present, followed by polyspikes with an increasing number of spikes per event, and finally seizures. Polyspikes continued in the presence of seizures in most experiments, as did single spikes, though to a much smaller degree. Experiment 5 had a much longer period of single spikes and a reduced number of seizures compared to other experiments due to a smaller amount of picrotoxin used. Gaps in time are due to breaks in the recording or periods of high artifact or disruptive electrical stimulation. The effect of increased anesthesia can be seen, most notably in experiment 2 where it caused all activity to disappear then slowly return starting with single spikes.

Figure 5.10 shows how the prevalence of each event type changed during the course of the five experiments. Each experiment was broken up into 20 equal-size time bins, and a histogram of each event type was plotted to show how many events occurred per bin. Again, it is seen in each experiment that initially the majority of all events were single spikes before polyspikes took over. In most experiments, the number of events per bin in periods dominated by single spikes and polyspikes were similar. Seizure frequency was about one order of magnitude below the other events, since seizures were much longer duration and occurred less often. There were very few time bins that had similar counts of each event type within the bin, especially between single and polyspikes.

Table 5.2 gives the amount of time that elapsed after applying picrotoxin until the first event of each type appeared. The time for polyspikes and seizures to appear in experiment 5 was longer than the others because of the much smaller amount of picrotoxin used. Outside of that, there was no clear dependence between the amount of picrotoxin and the timing of event occurrence. In experiments 1, 2 and 5, the time from application to single spike, and from single spike to polyspike, were similar and much shorter than the amount of time needed to go from polyspike to seizure. Experiment 3 had slightly different timing, possibly due to the abnormal nature of its seizures.

These results show that there was a clear, consistent pattern to the ictogenesis across experiments, despite varying amounts of picrotoxin used and different delivery methods. This suggests that there is an ordered response from the underlying network to an insult of this kind.

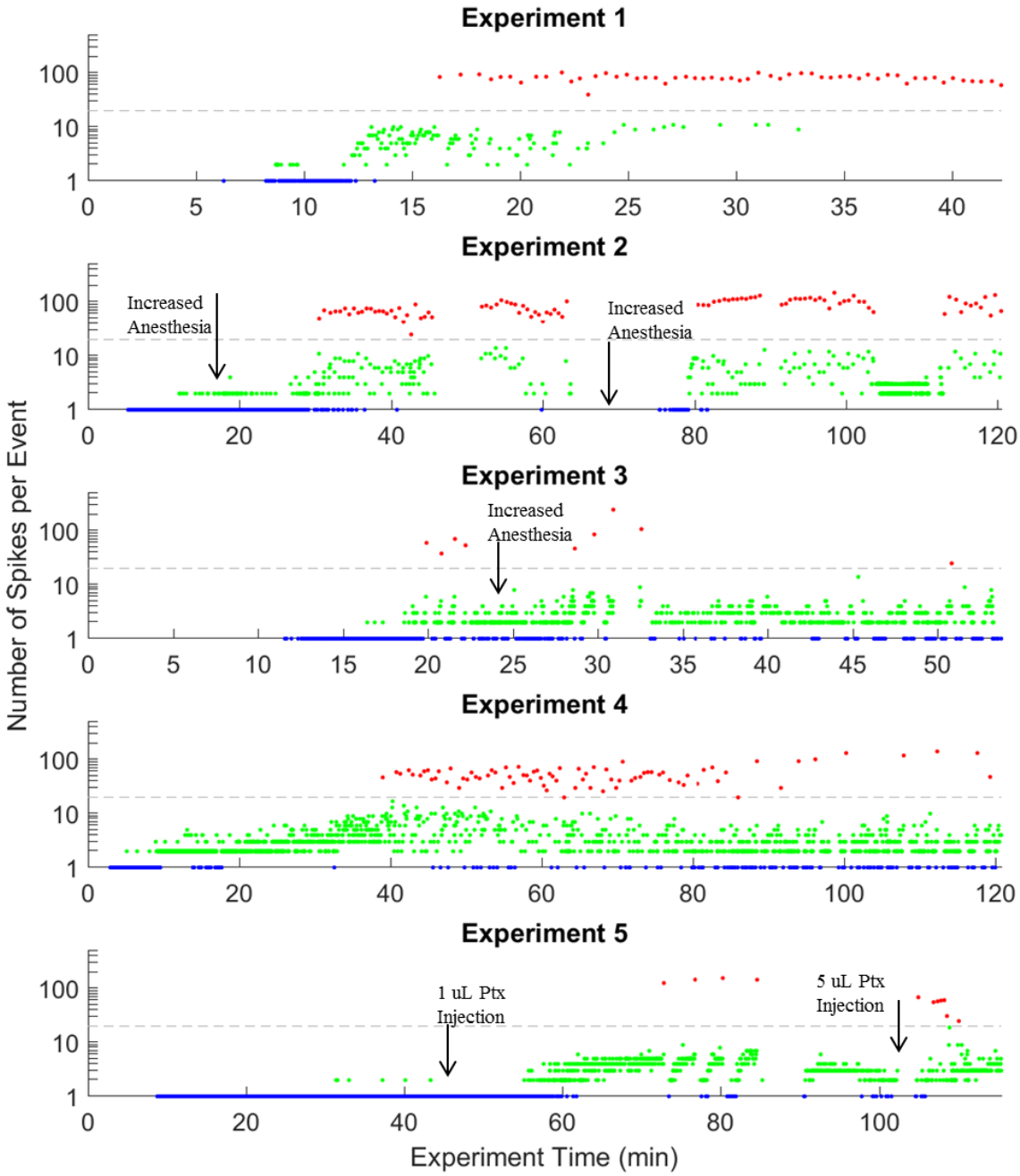

Figure 5.9 Number of Spikes per Event over Experiment Time Blue, green and red points mark the start time of each single spike, polyspike and seizure event, respectively, using the 20 spikes/event cutoff to separate polyspikes and seizures (represented by the gray dashed line). The y-value of each point is the number of spikes detected in that event. Annotations indicate when additional anesthesia or convulsant was added, which often had a noticeable effect on the responses.

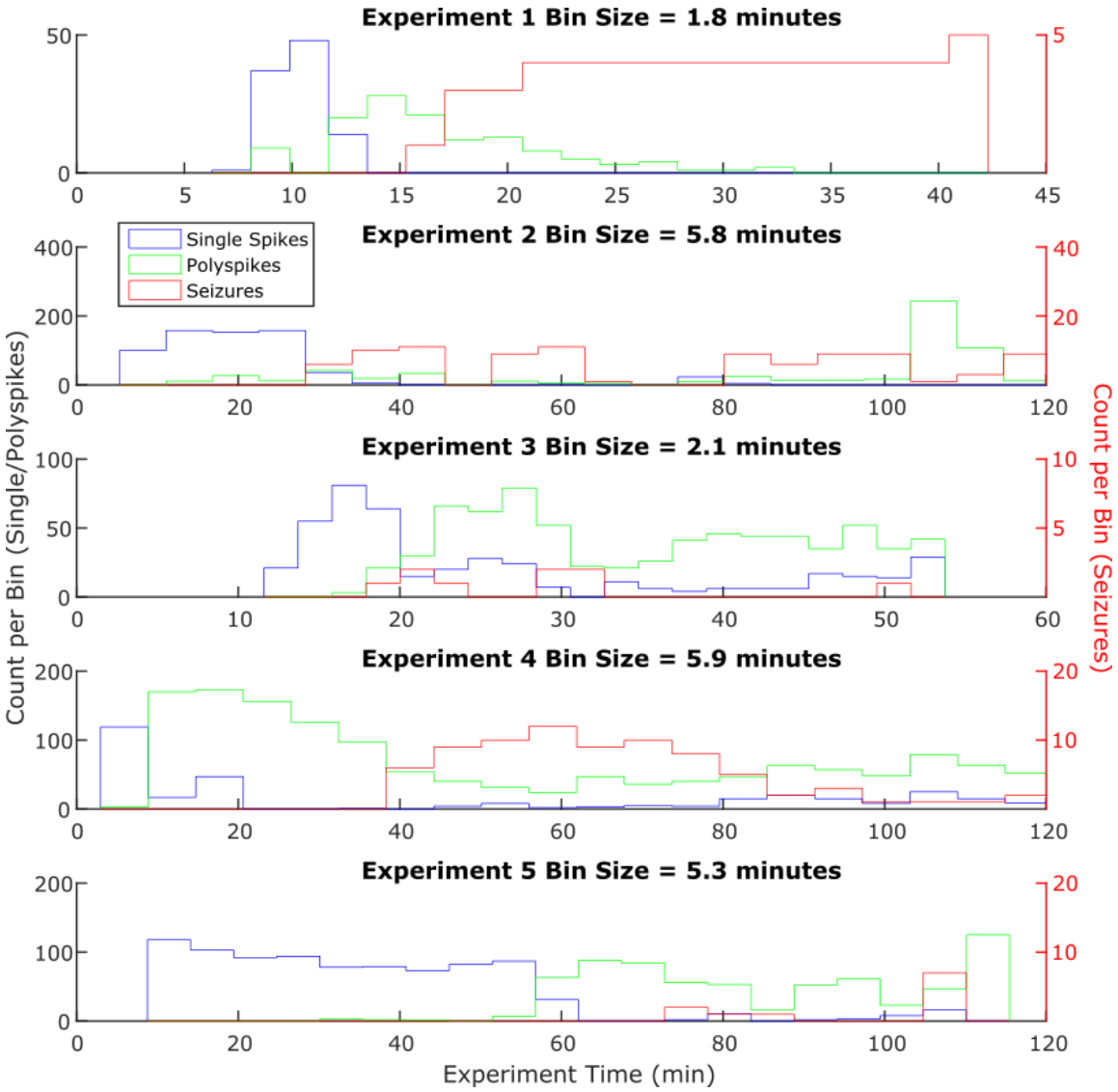

Figure 5.10 Event Start Time Histograms Each experiment time was separated into 20 bins and the number of events of each type with a start time in the bin was counted. Every experiment started with only single spikes before polyspikes took over. Note the seizure histograms are scaled up one order of magnitude on the right axis.

	Amount of Picrotoxin Added (mg)	Time to First Event (min)		
		Single Spikes	Polyspikes	Seizures
Experiment 1	~10-15 (Surface)	6.3	8.7	16.3
Experiment 2	~5-10 (Surface)	5.3	12.0	30.5
Experiment 3	~5-10 (Surface)	11.6	16.4	19.9
Experiment 4	~0.5 (Injection)	3.0	5.1	39.0
Experiment 5	~0.05 (Injection)	8.8	31.4	72.8

Table 5.2 Time to First Events Time from the application of picrotoxin until the first single spike, polyspike and seizure appeared in each experiment

Temporal Properties of Events

The next analysis consisted of exploring the properties of each event to see if there were observable differences between them and validate the method of classification used. The first property investigated was the duration of events, defined as the time from the start of the first spike to the end of the last spike in each event. Figure 5.11 shows that there was a clear relationship between the number of spikes and the duration of events, which differed slightly between single/polyspikes and seizures. A linear fit on each group gave R^2 values of 0.72 and 0.5 for single/polyspikes and seizures, respectively. Other fits, including quadratic and power equations, were calculated, though none offered any marked improvement in R^2 over a first-order polynomial. The slopes of the two groups were 0.1 and 0.14 s/spike.

The increased duration per spike in seizures suggests that they are overall lower frequency events than polyspikes. Figure 5.12 shows that the distributions of spike frequency for the two event types were significantly different, with a Wilcoxon rank sum p-value < 0.001. Seizures, defined as events with 20 or more spikes, had a median frequency of 6.4 spikes/s, and polyspikes had a median frequency of 13 spikes/s. The spike frequency decrease is due to the slower late phase that was only present in seizures.

In addition to lower frequency, seizures had a longer post-event delay than polyspikes, which was the time after a given event before the next event began. Figure 5.13 shows that, on average, the post-event delay for seizures was 9.9 s and only 2.3 s for single/polyspikes. The two distributions were significantly different according to a Wilcoxon rank sum p-value < 0.001. This post-ictal quieting is seen in human epilepsy and other seizure models, though the cause is not well known.

The significant differences in frequency and post-event delay suggest that there are mechanistic differences between seizures and polyspikes, and validates the method used to separate the two event types.

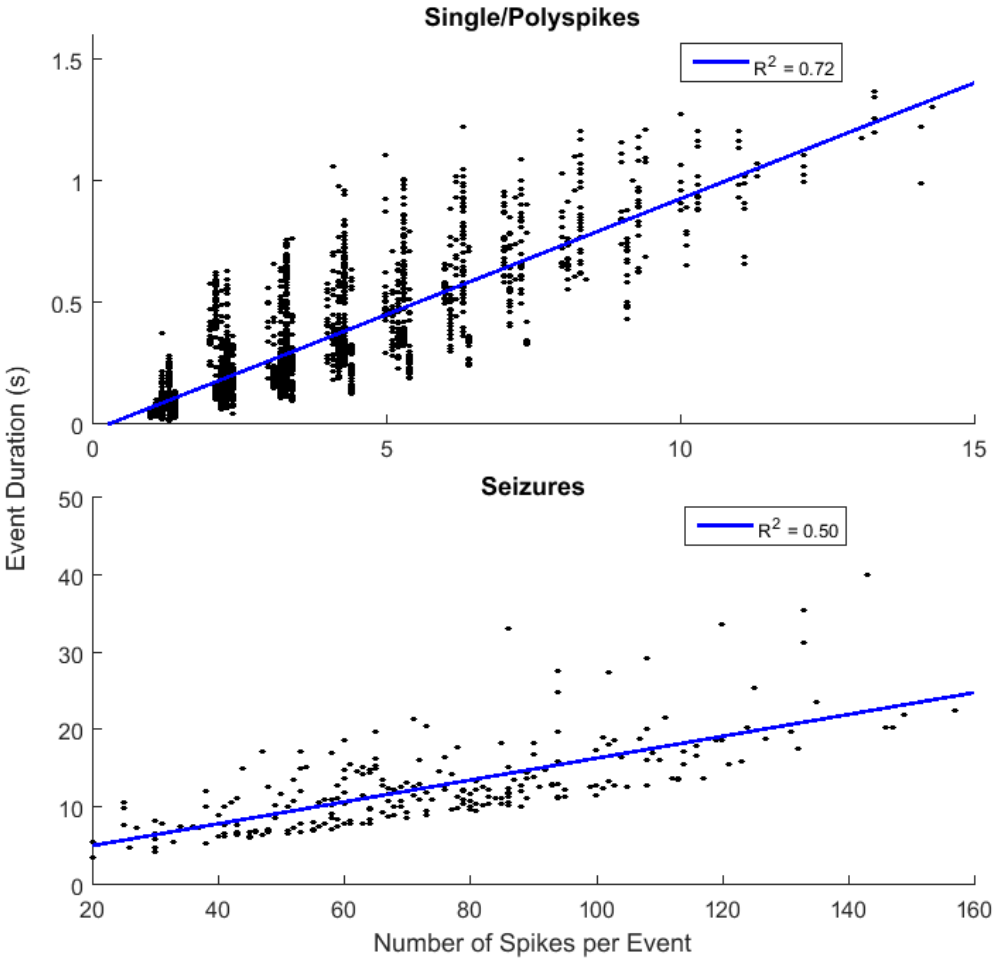

Figure 5.11 Event Duration vs Number of Spikes per Event The upper scatter plot shows the duration of all single/polyspikes under 1.5 s (99.9%) as a function of the number of spikes in each event. The lower plot shows the same for seizures, with events limited to 40 s (99.6%). The slopes of the fitted lines were 0.10 and 0.14 s/spike for the single/polyspikes and seizures, respectively. X-values for single/polyspikes from successive experiments were increased by 0.1 to more clearly show the events in the scatter plots. True integer values of number of spikes were used for the fit.

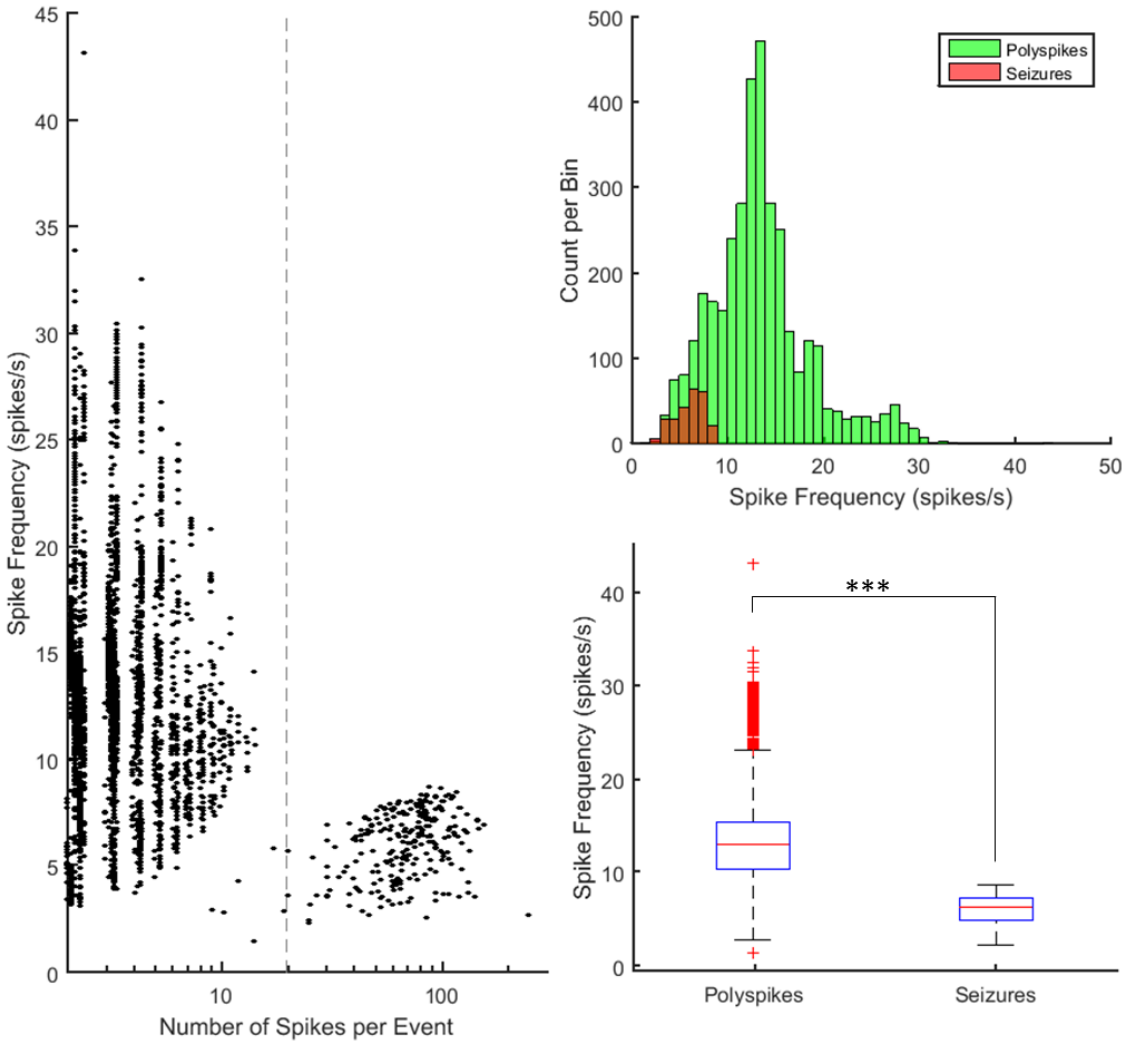

Figure 5.12 Event Spike Frequency The scatter plot on the left shows the frequency for all polyspikes and seizures across experiments, with a line dividing the two event types. The histogram and box plot on the right show the significantly different distributions, with medians of 13.0 and 6.4 spikes/s for polyspikes and seizures, respectively ($p<.001$). X-values from successive experiments were increased by 0.1 to more clearly show the events in the scatter plots.

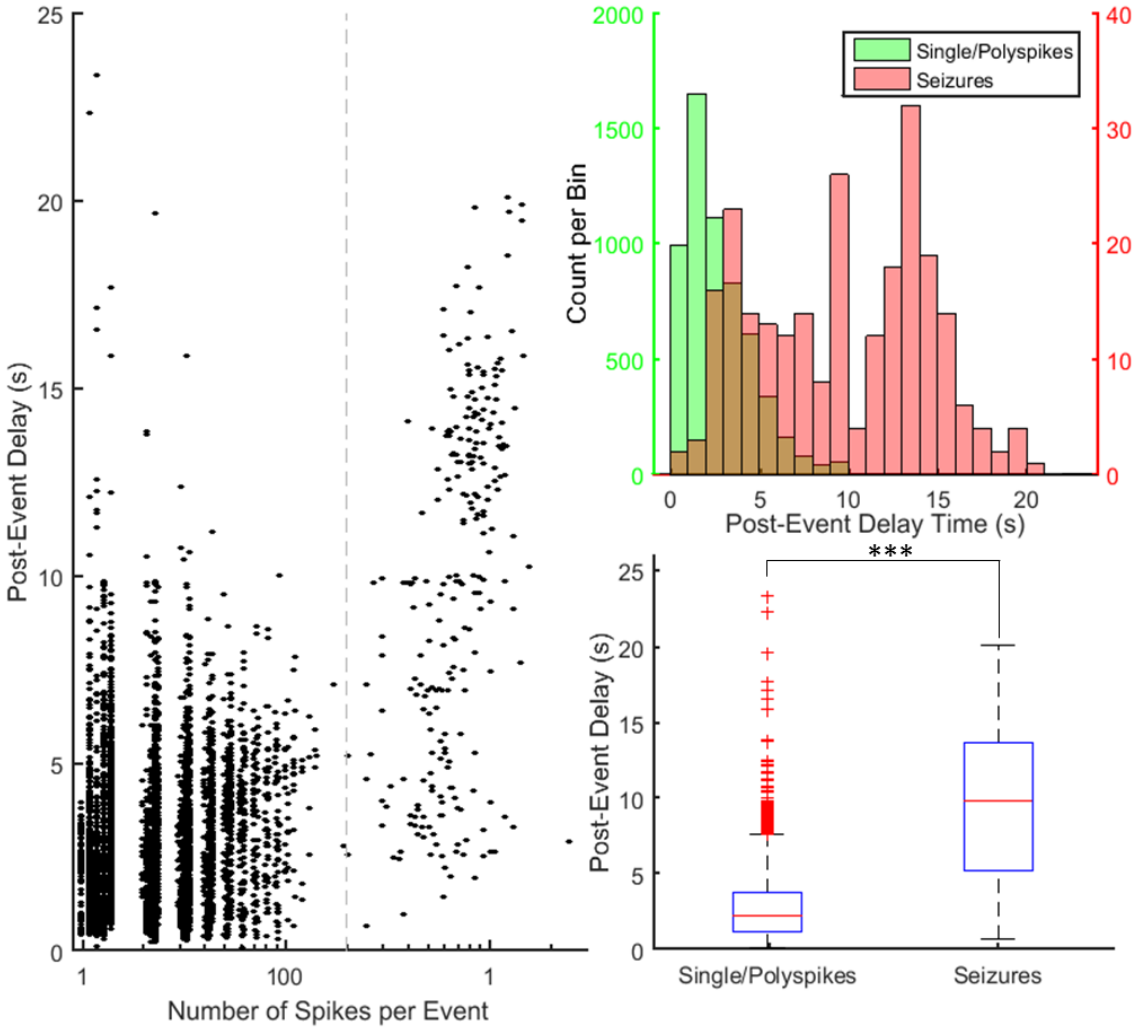

Figure 5.13 Post-Event Delay The scatter plot on the left shows the time after every event until the next event occurred, limited below 25 s to remove delays caused by breaks in the recording. The histograms and box plot on the right show the distributions with median delay times of 2.3 and 9.9 s for single/polyspikes and seizures respectively. The two distributions were significantly different. X-values from successive experiments were increased by 0.1 to more clearly show the events in the scatter plots.

There were significant changes in polyspikes depending on where they occurred relative to seizures. The top four plots in Figure 5.14 show that events immediately preceding seizures contained more spikes than those that immediately followed, with median values of 6 and 2 spikes/event, respectively ($p<0.001$). The scatter plots on the bottom of the figure are example periods from all five experiments that showed this phenomenon. There was a clear increase in the number of spikes for successive events leading up to a seizure, which caused them to reset back to shorter events before building up again. The number of events over which this increase occurred varied by experiment and, to a lesser degree, between seizure events within an experiment. This, along with the longer post-event delay, suggests that seizures put the brain into a state that is less susceptible to sustained epileptic events following their termination.

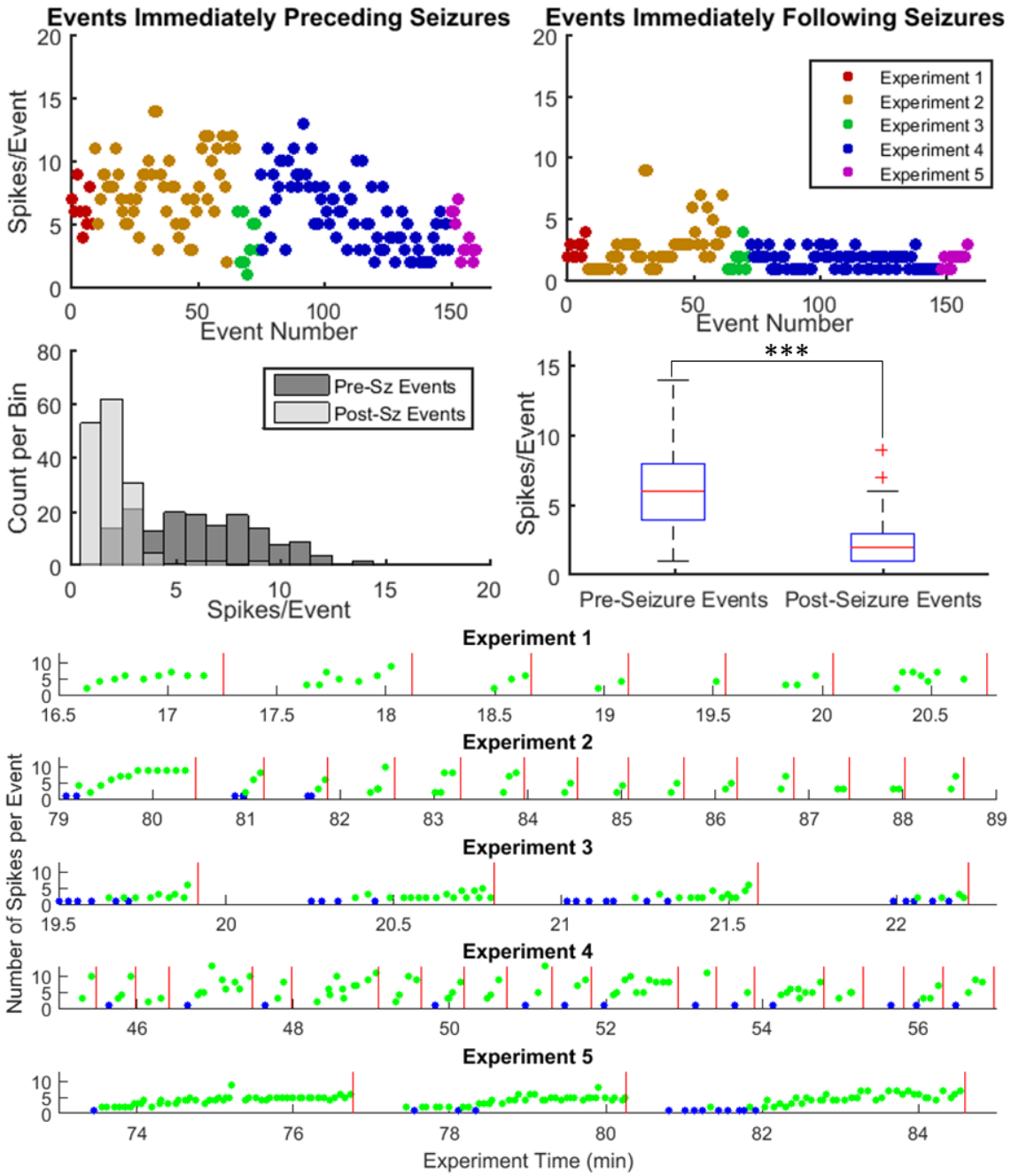

Figure 5.14 Number of Spikes for Events Preceding and Following Seizures The scatter plots on top show the number of spikes for every non-seizure event immediately preceding (left) and immediately following (right) every seizure. Single events between seizures were not counted. The histogram and box plot show the distinct distributions, with median values of 6 and 2 spikes/event before and after seizures, respectively. The bottom scatter plots show examples from each experiment showing events (blue for single spikes, green for polyspikes) with an increasing number of spikes between seizures, represented by red lines.

Properties of First Spikes in Events

The first spikes of events were more similar and detectable across an experiment than those that came later in polyspikes and seizures. For this reason, and the fact that many events only had one spike, first spike properties were quantified to see how they changed with the evolution of epileptic activity. The properties chosen were amplitude and duration. The duration of the first spike was calculated from the spike start and stop points found by the detector. Amplitude was calculated by taking the absolute value of the difference between most negative point during the first spike and the mean baseline voltage of a short time window just before the spike began.

In Figures 5.15 and 5.16 the calculated amplitude and duration of the first spike of every event is plotted against the time the event occurred. In both figures, blue, green and red dots represent single spikes, polyspikes and seizures, respectively. The first spike amplitude in experiments one, three and four increased slightly over the recording, but stayed relatively constant throughout. Experiment two had the range of the amplifiers set at 2 mV and 4 mV, causing most first spikes to saturate. First spike duration showed a more consistent increase over the course of the first four experiments, though it reached a plateau in all but the first. The acute effect of increased anesthesia in experiment 2 is evident, causing a drastic drop in duration around 70 min, before returning to previous levels.

The first spike amplitude and duration in experiment five showed a much different time course. The small injection of picrotoxin at the beginning of the experiment caused the appearance of single spikes that decreased in amplitude and duration over time. A subsequent injection quickly increased both properties, but they gradually fell again. Interestingly, as polyspikes appeared, the first spike duration bifurcated into two paths, one decreasing and the other slightly increasing. This could have been due to separate foci appearing from the multiple injections. Finally, a larger injection caused an increase in duration, though an overall decrease in amplitude.

To see if either of these properties exhibited a dependence on the length of an event from which they were measured, first spike amplitude and duration values were plotted against the number of spikes contained in the corresponding event. These plots are seen in Figure 5.17. There was no clear relationship between either property and number of spikes, with Pearson correlation coefficients of -0.05 and 0.13 for amplitude and duration, respectively.

These results show that first spikes in events do not cluster based on the type of event, but change slowly over time. Also, the first spikes have no predictive power of if the event will go on to be a seizure.

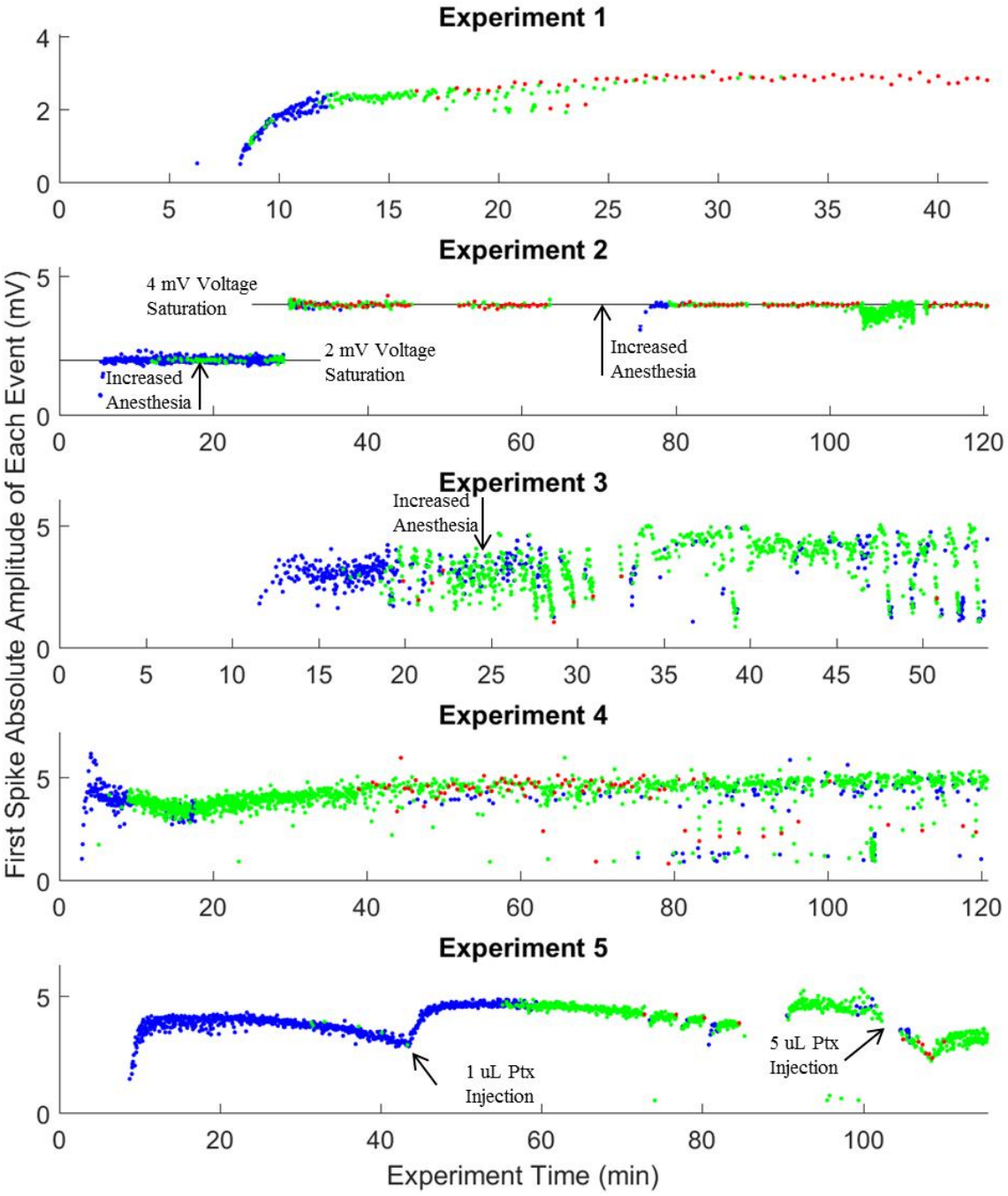

Figure 5.15 First Spike Amplitude over Experiments The absolute minimum amplitude of the first spike of every event is scattered against the time each event started. Blue, green and red points are single spikes, polyspikes and seizures, respectively. The amplitudes in experiment two were cut off at 2 mV early in the experiment and 4 mV later.

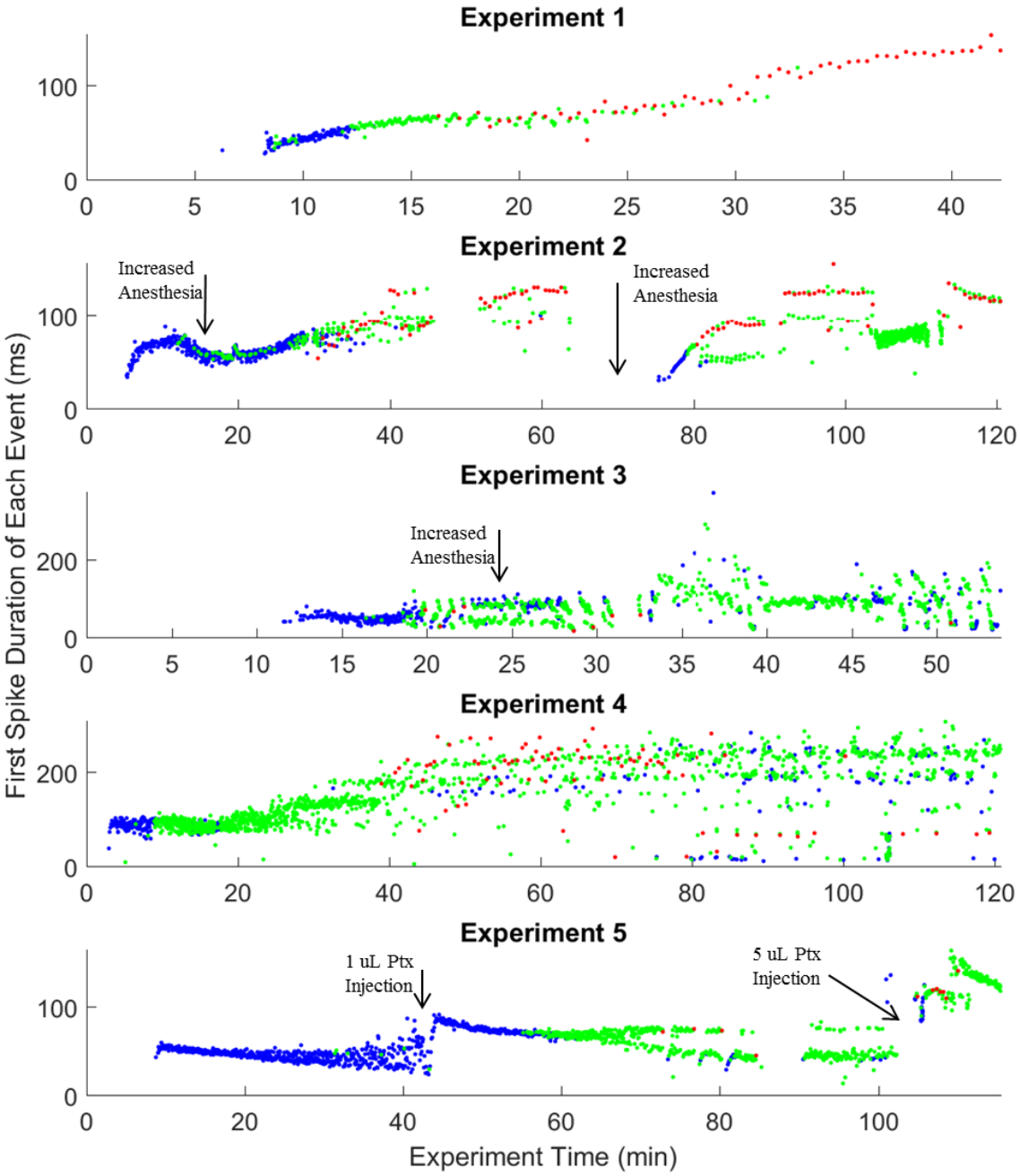

Figure 5.16 First Spike Duration over Experiments The duration of the first spike of every event is scattered against the time each event started. Blue, green and red points are single spikes, polyspikes and seizures, respectively.

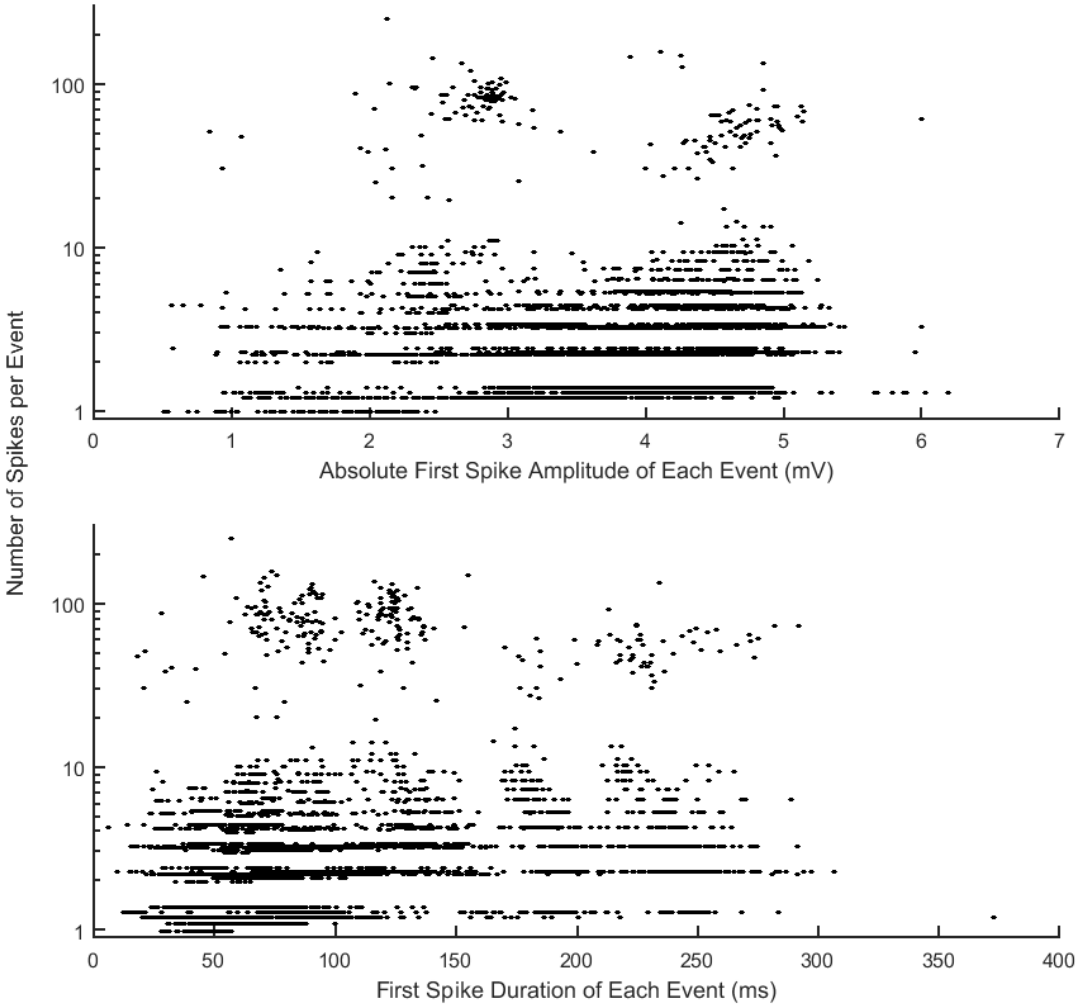

Figure 5.17 Number of Spikes vs First Spike Amplitude and Duration The upper and lower plots scatter the number of spikes per event against the first spike absolute minimum amplitude and duration of the first spike of each corresponding event. Pearson correlation coefficients were -0.05 and 0.13 for amplitude and duration vs. number of spikes, respectively. The second experiment was left out of the amplitude calculations due to saturation of the amplifiers. Y-values from successive experiments were increased by 0.1 to more clearly show the events in the scatter plots.

To see how the shape of first spikes evolved and how similar they were over the course of an experiment, a correlation analysis was performed. First, events were time-aligned to the point that each first spike crossed a negative threshold of ten times the average standard deviation of non-epileptic activity in a given experiment (described in Methods). Clips were taken of the 50 ms before and 100 ms after the threshold crossing in each event, in order to get equal-length signals of just the first spike. Next, correlation was performed between every pair of clips in each experiment. Figure 5.18 shows the upper triangle of the correlation matrix for each experiment on the left. Color represents the Pearson correlation coefficient between every two first spikes, with blue to yellow going from 0.5 to 1. There were very few correlations below 0.5, and those that were mainly came from experiment three. The highest correlations are seen close to the diagonal and drop away from it, indicating that first spikes from events nearer in time were more similar in shape than those further apart.

The median correlation coefficient of every pair of spikes that shared the same event separation was calculated and shown in the plots on the right in Figure 5.18. For instance, 0 is the diagonal from the correlation matrix, so it has a median value of 1. A separation of 1 represents the median correlation between events 1 and 2, 2 and 3, 3 and 4, and so on. The largest separation only contained the correlation of one pair of events: the first and last in each experiment. The plots show that overall, first spikes separated by fewer events were more highly correlated, and that correlation decreased as the temporal event separation increased. The dashed gray line in each plot represents a correlation value of 0.85. The five experiments reached this value at event separations of 202, 565, 138, 1153 and 1165. All of these values, except for the third experiment, were near or well over half of the events in the entire experiment.

Figure 5.19 gives a more detailed view on how the first spike shape changed. The plots on the left are expanded correlation matrices for five early events from each experiment, so each row in the plot gives the correlation coefficient of that event's first spike with the first pike of every other event in the experiment. The mean of the five chosen correlation vectors within each experiment was calculated and plotted in the graphs in the middle column. Six example first spikes from throughout each experiment are plotted on the right, with the events they represent marked in corresponding color on the middle plots. The increases in spike amplitude and duration appear to be the biggest contributors to decreasing correlation over time in experiments one and four. Over the course of experiments two and three, activity riding on the spikes appeared as they returned to baseline, causing a decreased correlation. The development of an early positive peak in experiment two also contributed. The quick, sharp drops in the mean correlation plots,

most apparent in experiments three and four, were caused by the detection of small spikes as first spikes of events. In experiment four, this was due to misclassification, as described in the Methods section. In experiment three though, many events did not seem to be part of seizures but were still low amplitude. Experiment five shows an increase in correlation corresponding to the second injection of picrotoxin, just as a jump in amplitude and duration of the first spike was seen in the previous analysis. This suggests that reapplication put the brain back into a state resembling that which followed the initial injection.

These results show that the first spikes of events were remarkably similar to one another throughout the course of each experiment. The shape changed slowly over time and was not affected by the type of event it was part of.

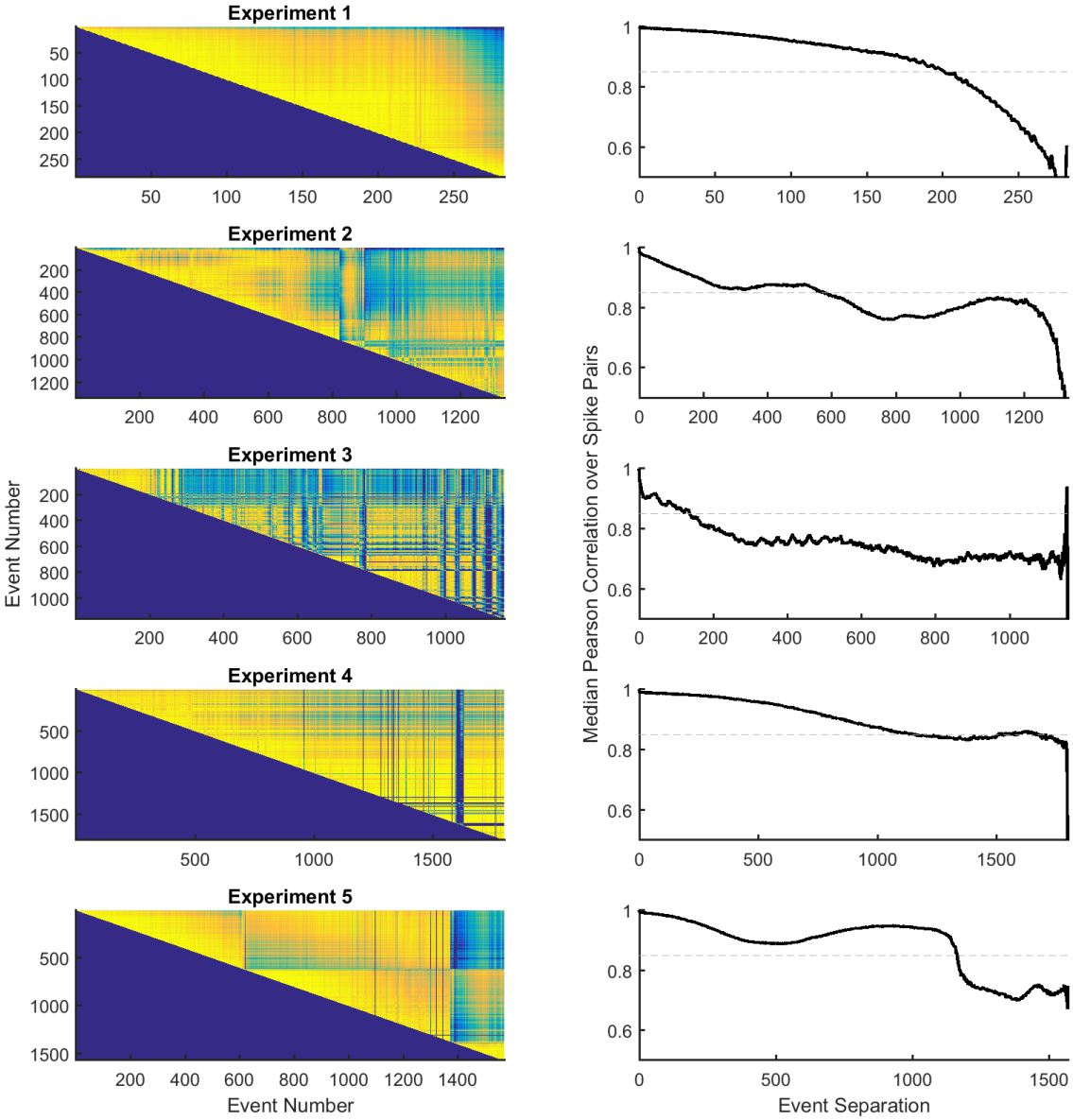

Figure 5.18 Correlation of First Spikes in Each Event over Entire Experiments The left column shows the correlation matrix for 150 ms clips of the first spike of every event detected and aligned with a 10SD threshold. The correlation values are 0.5 to 1 represented by dark blue to yellow. The right column shows the correlation between events as a function of the number of events between them in time. Each point is the median correlation value over all pairs of events with the same separation. The gray line is at a correlation value of 0.85.

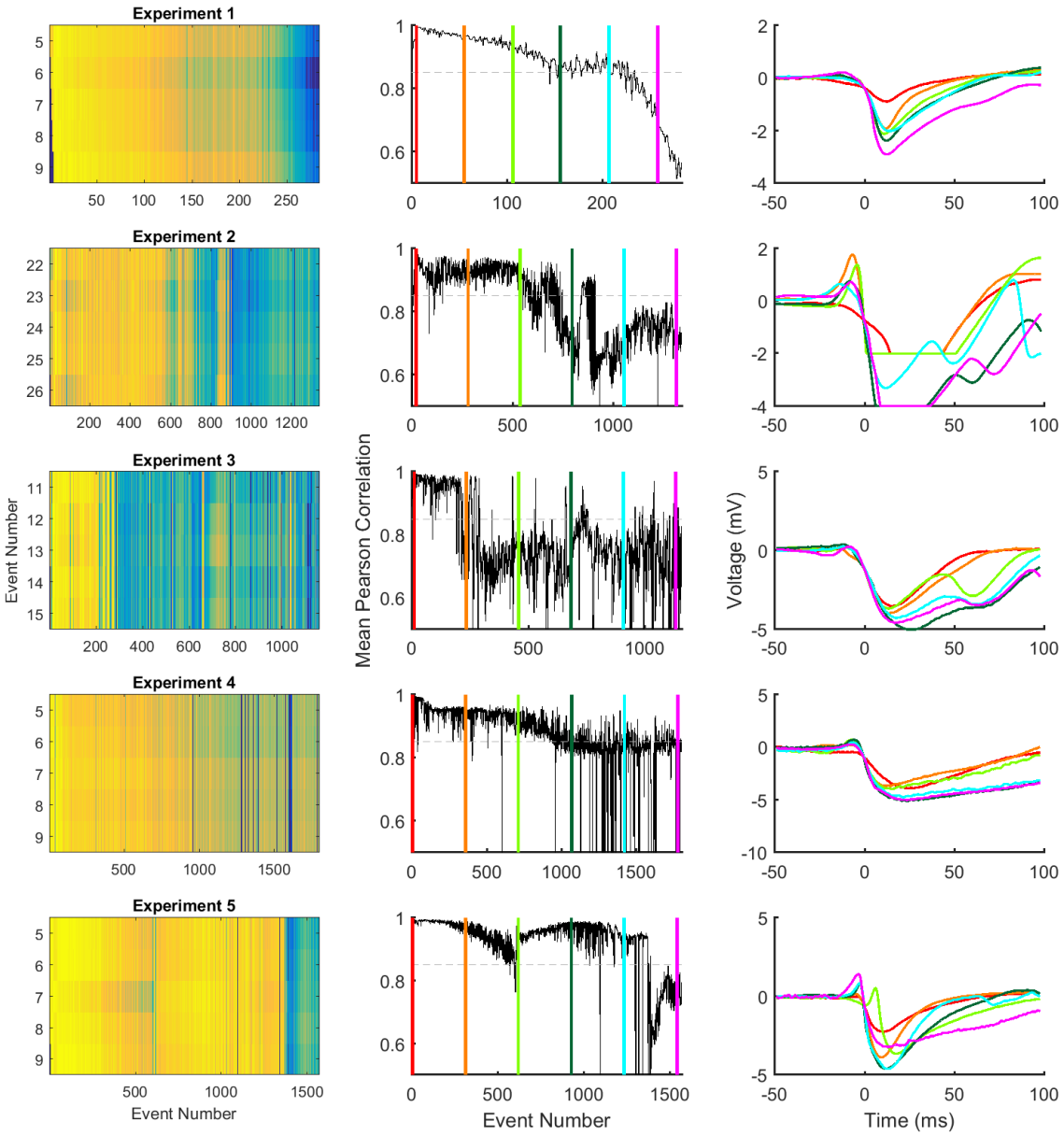

Figure 5.19 Correlation of Five Early First Spikes over Experiments The left column shows the correlation of the first spike of five early events (rows) with the first spike of all other events (columns). The mean of those five correlation vectors for each experiment is shown in the middle column. The first spike shape of earlier events was more similar to that of the five chosen near the beginning, and that similarity waned later in the experiment. Five example first spikes over the duration of each experiment are plotted in the right column to give examples of how the spike shape changed over time. The events plotted are marked with lines of corresponding color in the correlation plots in the center.

Subsequent Spike Properties

In every event, spikes were grouped into one of two categories: first spike or subsequent spike. The previous analyses explored the changes in first spike properties, but since most events contained multiple spikes, it is important to investigate the characteristics of subsequent spikes as well. The amplitude and duration all subsequent spikes were calculated in the same method as for first spikes, and the mean values were found over all subsequent spikes in each event. Figure 5.20 shows the distributions of first spike and subsequent spike amplitudes (top) and durations (bottom), broken down by experiment and event type. The height of the bars gives the median value and error bars are the first and third quartiles for the given grouping. In every category, both the mean subsequent spike amplitude and duration were significantly lower than those of the first spike, all with Wilcoxon rank sum p-values < 0.001. When all of the polyspikes are pooled across experiments, subsequent spikes were, on average, 2.64 mV smaller and 62 ms shorter than first spikes, as shown in Table 5.3. Similarly, in seizures, subsequent spikes were 2.22 mV smaller and 89.4 ms shorter than first spikes.

Figure 5.21 gives plots of the mean absolute negative amplitude and mean duration of the subsequent spikes in an event against the number of spikes it contained. The plots are very similar to those of the first spikes (Figure 5.17). The Pearson correlation coefficients were 0.15 and 0.12 for amplitude and duration vs. number of spikes, respectively. Just like first spikes, the shapes of the subsequent spikes were independent of event length.

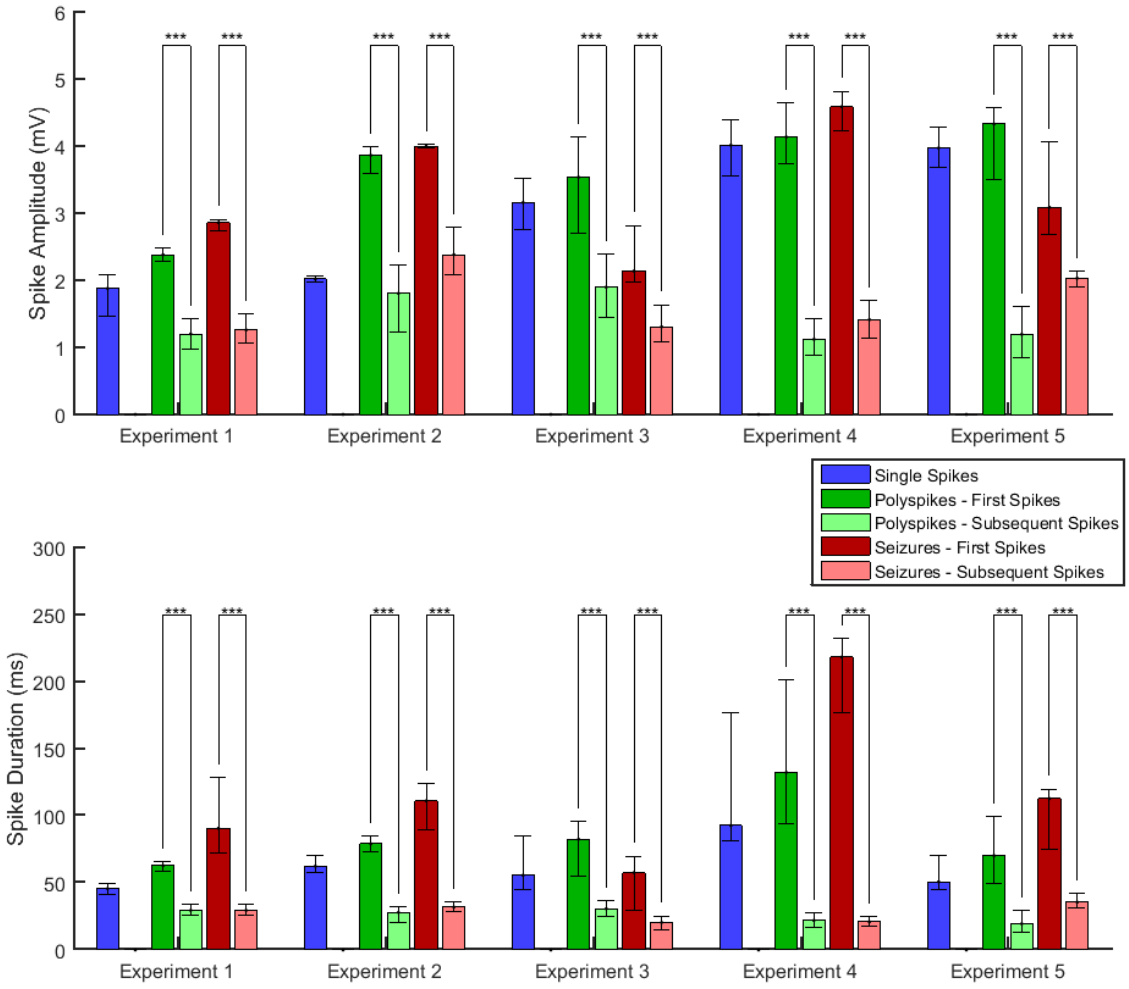

Figure 5.20 Amplitude and Duration of First and Subsequent Spikes in Events For each experiment, the median amplitude (upper) and duration (lower) of the first and subsequent spikes over event types and experiments are plotted. The error bars signify the first and third quartile of each distribution. The first and subsequent spikes in each event type and experiment had significantly different amplitude and duration distributions, with $p < 0.001$ using the Wilcoxon rank sum test. Note the amplitude values for experiment two were saturated, though the subsequent spikes are well below the saturation limit.

	Median Amplitude (mV)		Median Duration (ms)	
	First Spikes	Subsequent Spikes	First Spikes	Subsequent Spikes
Polyspikes	3.95	1.31	86.9	24.9
Seizures	3.98	1.76	119.4	30.0

Table 5.3 First and Subsequent Spike Amplitude and Duration over Experiments This table shows the median amplitude and duration of first and subsequent spikes taken from values pooled across experiments.

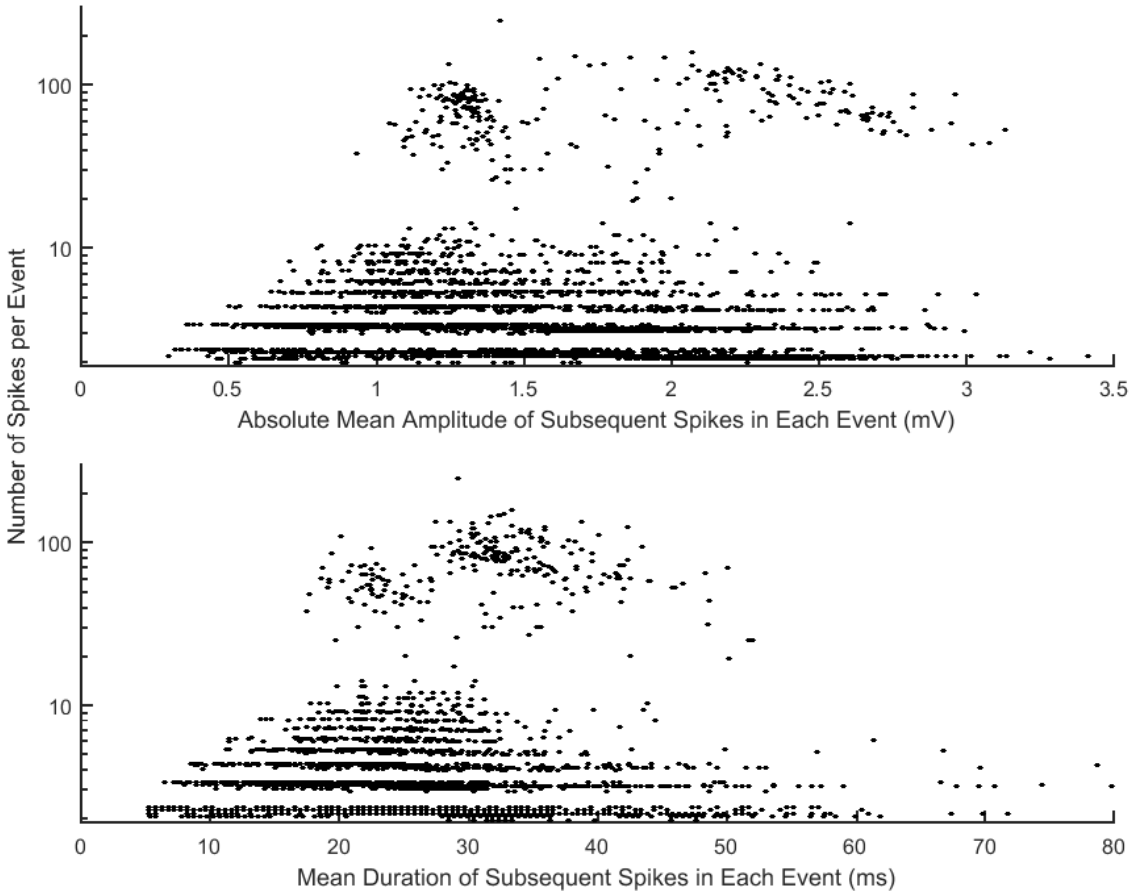

Figure 5.21 Number of Spikes vs Subsequent Spike Amplitude and Duration In the upper and lower scatter plots, the x-values represent the mean absolute negative amplitude and mean duration across all subsequent spikes within an event. Pearson correlation coefficients were 0.15 and 0.12 for amplitude and duration vs number of spikes, respectively. The second experiment was included since the amplitude of the subsequent spikes did not reach the cutoff range of the amplifier. Y-values from successive experiments were increased by 0.1 to more clearly show the events in the scatter plots.

Event Detection over Surface Array

In the previous section the event detector was only applied to a single electrode close to the site where picrotoxin was applied. The response of the cortex, however, changed across the surface array, markedly different farther from the convulsant. To explore the spatial response change, the event/spike detector was applied to the recordings from every electrode on the surface array. Figure 5.22 shows a 4x8 grid representing the array (configuration detailed in Figure 5.1) for each of the five experiments from top to bottom, separated into three columns by event type: single spikes, polyspikes, and seizures. The numbers on the grid are the number of detections on the corresponding electrode for a given experiment and event type. The colors represent the ratio of the number of detections on that electrode to the number of detections on the detector reference that was chosen for the previous analysis, marked with a black circle. Experiments two, three and four used electrode three, while experiments one and five used electrodes four and six, respectively.

Electrodes closer to the detector reference had a similar number of detected events and that number decreased on more distant electrodes. There were a few clear exceptions to this. The number of single/polyspikes in electrodes five and ten in the first experiment were much higher than those around them and even the detector reference. This was caused by many of the seizures being detected as individual spikes or polyspikes, which is reflected in the decreased number of seizures for those electrodes. This same occurrence was seen in experiment four, where many polyspikes and seizures were detected as single spikes resulting in much higher ratios outside of the reference. The fifth experiment shows an abnormally large increase in seizures for electrodes 10 and 29. This was due to high noise artifact on these channels that was detected as epileptic activity.

Across experiments, the number of electrodes on which events were detected was, at most, just over half of the array. Though we don't see all of the affected tissue due to picrotoxin placement on the edge of the array, if a similar spread in the opposite direction is assumed, the total area with detectable activity is around 6–10 mm in diameter. Commonly, clinical electrodes have 10 mm spacing with ~2 mm exposed contact diameter, making it possible to miss significant seizure activity that spreads no farther than 8 mm in diameter. Also, it is possible that interictal spikes picked up in human ECoG could be markers of smaller, focused seizures occurring between electrodes.

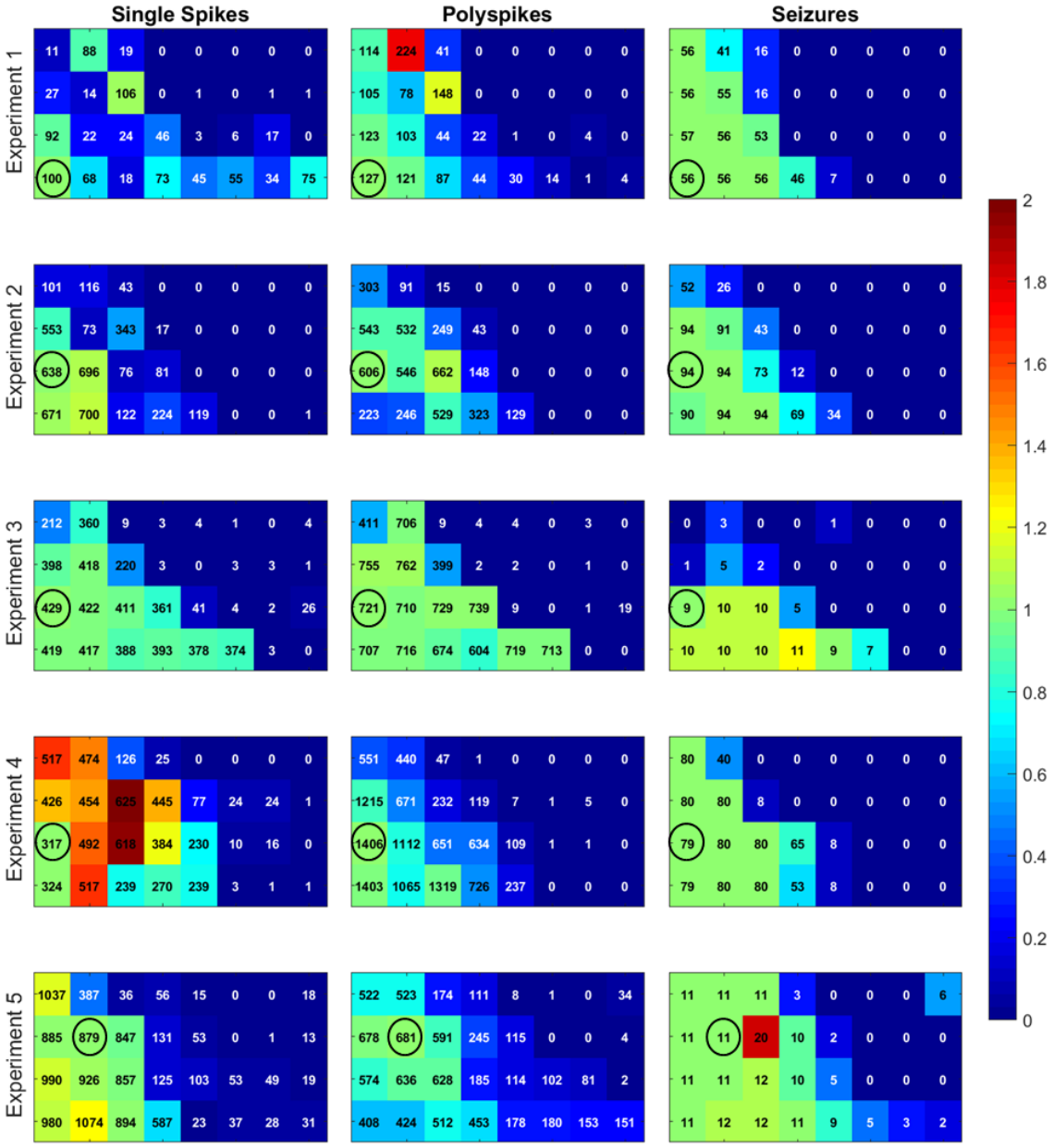

Figure 5.22 Event Detections over Surface Array Each 4x8 grid represents the surface ECoG array as shown in Figure 5.1, arranged in rows by experiment and columns by event type. The numbers on each point of the grids are the total detections for the corresponding event type on that electrode. Black circles indicate the detection reference electrodes from each experiment that were used for the analyses in the previous section. The color is the ratio of detected events on each electrode compared to the indicated focus electrodes, according to the color scale on the right.

Figure 5.23 gives an example from the first experiment of the detected events found over the surface array. The plots in (a) show, for each electrode, the number of spikes in each event as a function of time. It is clear that electrodes close to the detector reference (shaded) had very similar detections during the experiment, which changed greatly with distance. Many of the electrodes had no detections, or only a few single spikes. The raster plot in (b) gives a clearer picture of the different events detected at the same time across the array. Electrodes on the detection periphery (5, 9, 10, 15, 20) picked up many polyspikes and few seizures late in the experiment, during a time when the focus was detecting almost exclusively seizures. The most distant active electrodes (24, 28, 32), only saw occasional single spikes during this period. Interestingly, though the picrotoxin was applied caudolaterally near electrode one, the most distant electrodes with detections were on the medial side of the array, near the interhemispheric fissure. This could have been due to the shape of V1, extending farther in that direction versus V2, which was more caudal in the lateral portion of the lateral gyrus.

Figure 5.24 shows a similar example from experiment one, but plots the absolute first spike negative amplitude against the time each detected event occurred. Four electrodes on the bottom left of the array shared a similar increase in amplitude over time, but outside of that, the values were much lower and stayed relatively constant. The minor increases on the more distant electrodes did not depend on the event type, but on the time in the experiment. The more medial electrodes increased more in amplitude during the experiment than those that were most lateral (1, 5, 9). Upcoming analyses will shed more light on what caused those electrodes to have lower negative amplitudes on detected events. Amplitude and number of spike plots for the remaining four experiments can be found in the supplementary data section.

Finally, Figure 5.25 gives a summary of the amplitude of all detected events. At a given electrode, the color represents the absolute value of the average negative first spike amplitude for all events of the same type in an experiment. Experiments one, two and four exhibited an increase in the amplitude of events going from single spikes to polyspikes and seizures. Experiments three and five, however, show decreased amplitude in seizures compared to polyspikes. In the third experiment, spikes were very small around seizure events (possibly status epilepticus), and in the fifth experiment, most seizures appeared after a final, large picrotoxin injection that changed the seizure dynamics. In both amplitude figures, the amplitude values are not normalized, so caution must be taken comparing across electrodes. A voltage threshold based on the detector focus electrode was used in the detection, so normalizing could have caused many events to be missed.

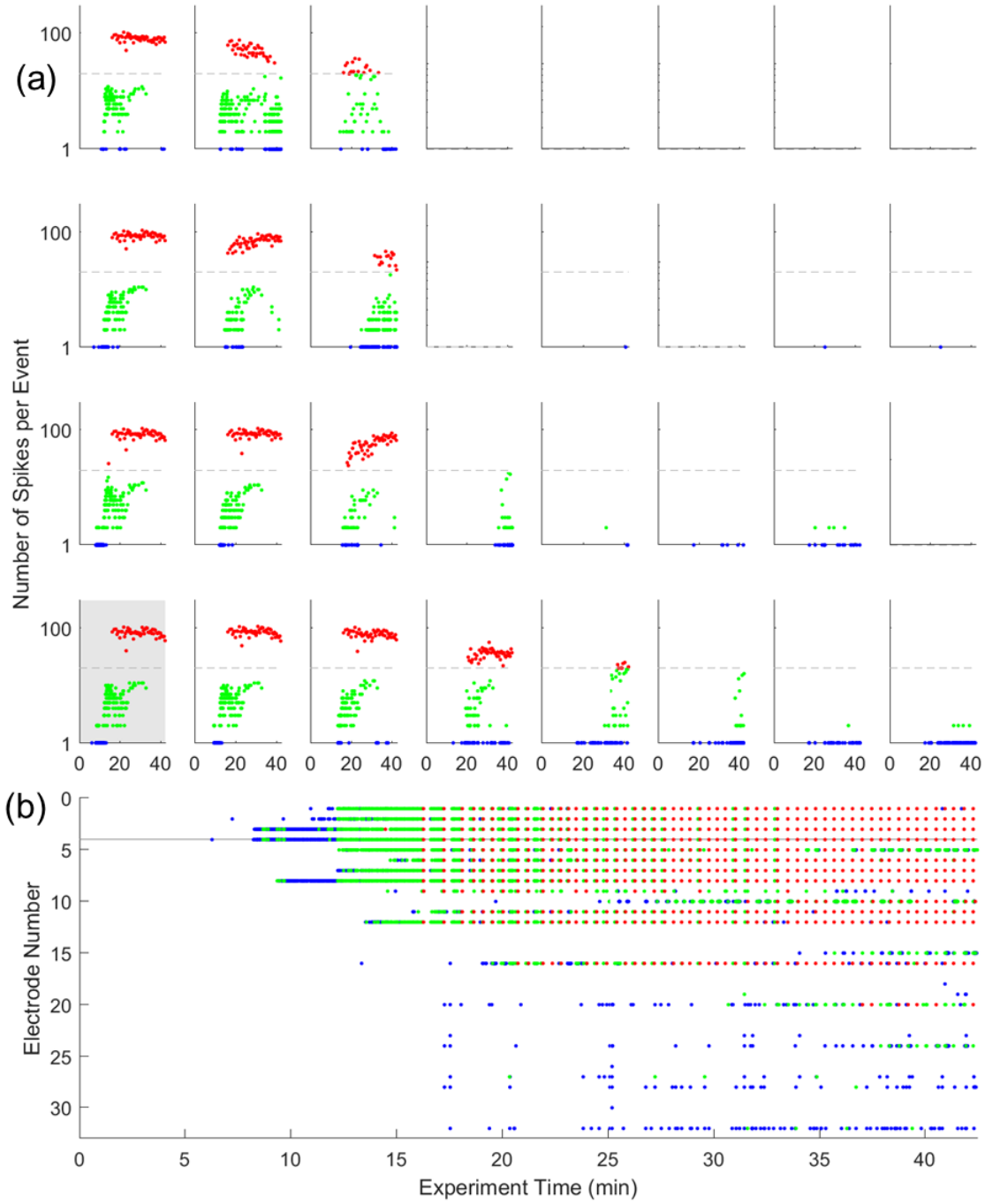

Figure 5.23 Number of Spikes Detected at Each Electrode - Experiment One The 4x8 set of plots shown in (a) gives the number of spikes (log scale) for every event detected at the corresponding electrode, with blue, green and red dots for single spikes, polyspikes, and seizures, respectively. The plot in (b) shows the same data but as a raster plot according to electrode number (Figure 5.1) to visualize simultaneous detections across the array. The line in (b) and the gray background (a) indicate the detection reference electrode. These plots for the remaining four experiments can be found in the supplementary data section.

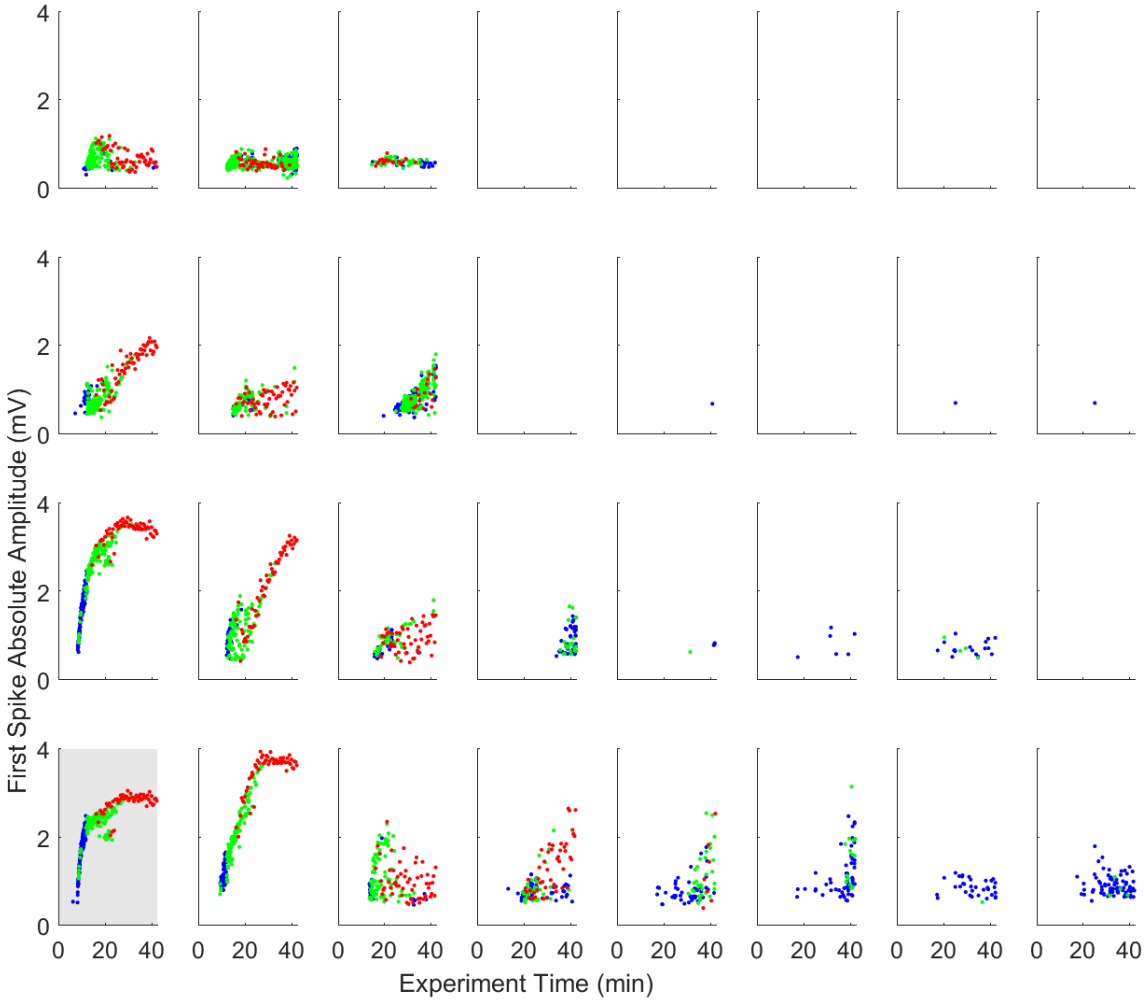

Figure 5.24 First Spike Amplitude of Detected Events at Each Electrode - Experiment One Each plot shows a scatter of absolute first spike negative amplitude vs. experiment time for all detected events on the corresponding electrode in the first experiment. Blue, green and red dots represent single spike, polyspike and seizure events, respectively. The shaded plot denotes the electrode used in the event evolution analyses. These plots for the remaining four experiments can be found in the supplementary data section.

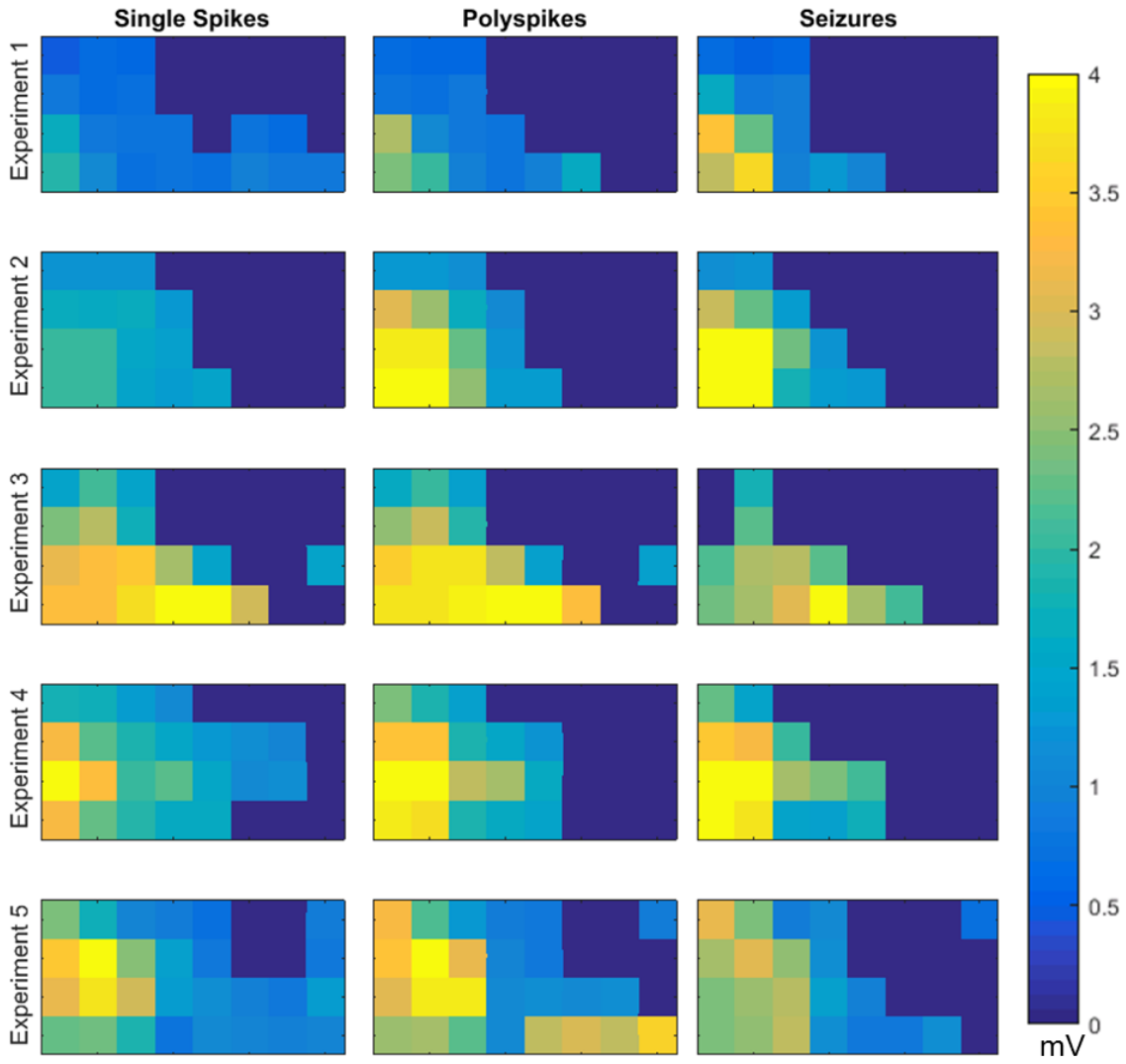

Figure 5.25 Average First Spike Amplitude of Detected Events at Each Electrode Each 4x8 grid represents the array for the corresponding experiment and event type. The color is the absolute value of the average first spike negative amplitude for all events of the same type detected at each electrode. Note the values are not normalized since the same detection threshold was used across all electrodes in the same experiment.

Spatial Properties of Focus-Detected Events

Applying the event detector to the entire ECoG array was used as a method of determining where events could be seen on the surface agnostic to the focus location, highlighting the importance of high spatial resolution arrays. Those detected events were not necessarily all occurring at the same time, and the detector did not reveal any information about the responses at electrodes without detections. This analysis will use the detections established in the first section, from one focus electrode close to the picrotoxin application, to investigate the corresponding activity across the array during those events. Figure 5.26 shows the first spike of a seizure recorded across the surface array during the first experiment. Responses on the bottom left of the array were mainly large negative spikes and easily detected. Farther away, near the middle of the grid, responses showed large positivity, which would not register as an event using the detector. There were also many responses that had some positive and some negative components. This spatial response was one of the common types seen over the five experiments.

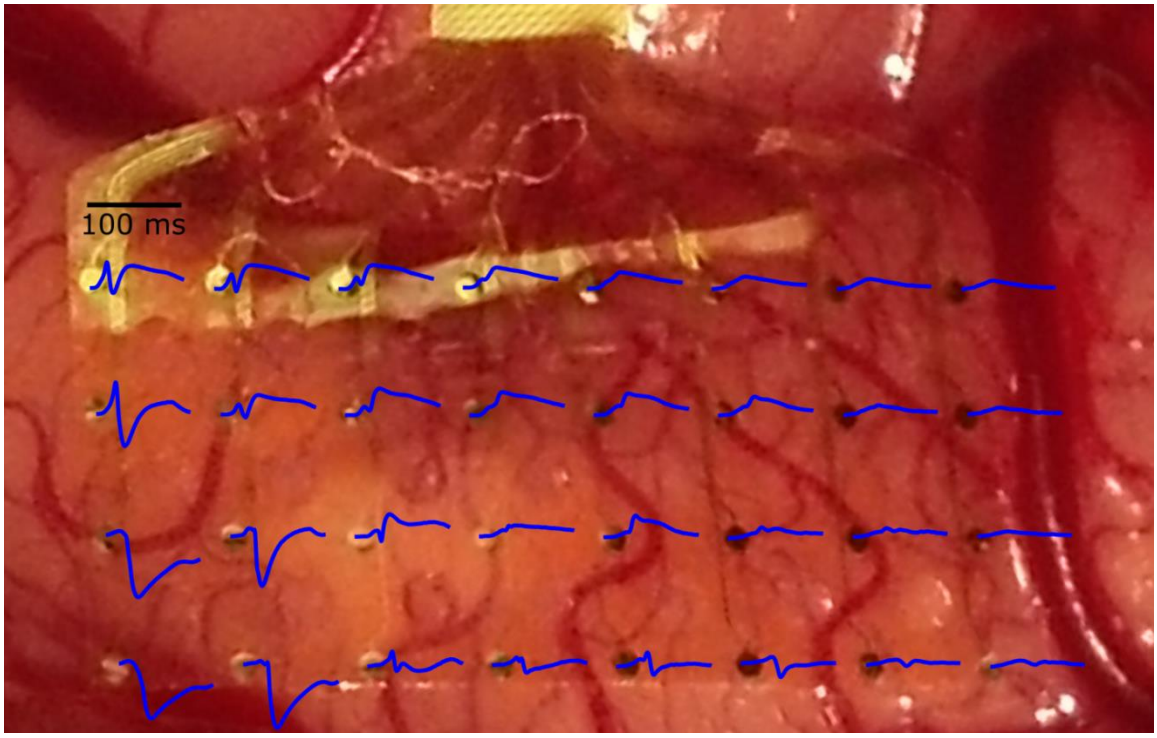

Figure 5.26 First Spike Example Across Surface Array Each trace is the activity recorded at the corresponding electrode during the first spike of a seizure near the end of the first experiment. Voltage is normalized to each electrode.

The first step in comparing the responses from different electrodes was to normalize the signals to account for differences in impedance, contact with the cortex and noise seen at different points in both space and time. Normalization was based off the baseline activity occurring in periods between epileptic events. The Methods section describes how the event detector calculated standard deviation on an electrode using a sliding window, and any windows above a set threshold for each experiment were considered part of an event. All windows that were below that threshold were considered baseline activity. For a given electrode, baseline windows were those under threshold both on that channel and on the detector reference electrode. Since electrode contact and other variables changed over the course of the experiment, each event on each electrode was normalized separately, using event timing from the detector reference. The pooled standard deviation of all baseline windows within one minute before and one minute after each event was calculated on every electrode. If fewer than 200 windows were in the ±1 min range, it was extended by 10 s increments until it included at least 200. The event at a given electrode was then normalized by dividing by the pooled baseline standard deviation around it.

Once normalization was performed, the thousands of detected events on every electrode had to be quantified to enable useful comparison across the array. First spikes of every event were used to carry out this investigation, since they were the largest and most consistent parts of every event and were seen on the largest number of electrodes. The previous figure showed that spikes in different areas varied between totally negative and totally positive, with many falling somehwere in between. Four different properties were utilized to explore the spatial spread of epileptic events: sum, absolute sum, minimum and maximum. Figure 5.27 shows these features calculated on given toy waveforms. Maximum and minimum were essential to quantify the positive and negative amplitude of the response spikes, but did not take duration into account. Waveforms (b) and (c) have the same minimum and maximum, but the majority of (c) is negative. This is where sum of the response is useful, as it shows that the negativity is dominant in the waveform. Sum can also be problematic, as both (a) and (b) have a sum of zero, but the former has very little response and the latter a significant response. Absolute sum can give an idea about the magnitude of a response, independent of polarity, as exemplified by the low value for (a). Finally, (d) shows a waveform with a low sum, implying near-equal positive and negative components. The clear difference in the amplitude of the polarities, though ignored by sum, is taken into account by the minimum and maximum values.

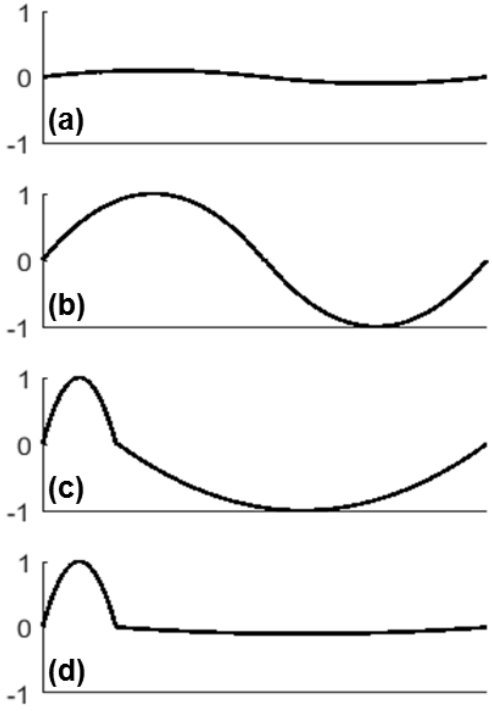

	Sum	Absolute Sum	Minimum	Maximum
(a)	0	27	-0.1	0.1
(b)	0	267	-1	1
(c)	-107	160	-1	1
(d)	13	40	-0.1	1

Figure 5.27 Spike Property Toy Examples Sum, absolute sum, minimum and maximum were the four features taken from first spikes of events at every electrode in order to quantify spatial spread. (a-d) are example spikes fabricated to describe the utility of each property.

A classifier was created to group each electrode into one of four categories: no detected response, focus, surround and border. The focus consisted of electrodes that had events with predominantly negative first spikes, the surround were predominantly positive, and the border were detectable first spikes with a relatively even mix of negativity and positivity. Since responses changed over the course of a recording, each experiment was broken up into three time periods – early, middle and late – with separate classification for each. The separation of the three periods was chosen to reflect the evolution of epileptic activity. Figure 5.28 shows the chosen times on a plot of the number of spikes in each event vs. experiment time. Clearly, experiments one and four were chosen to capture three periods dominated by single spikes, polyspikes and seizures. The points in experiment five lined up with the times at which additional picrotoxin was injected.

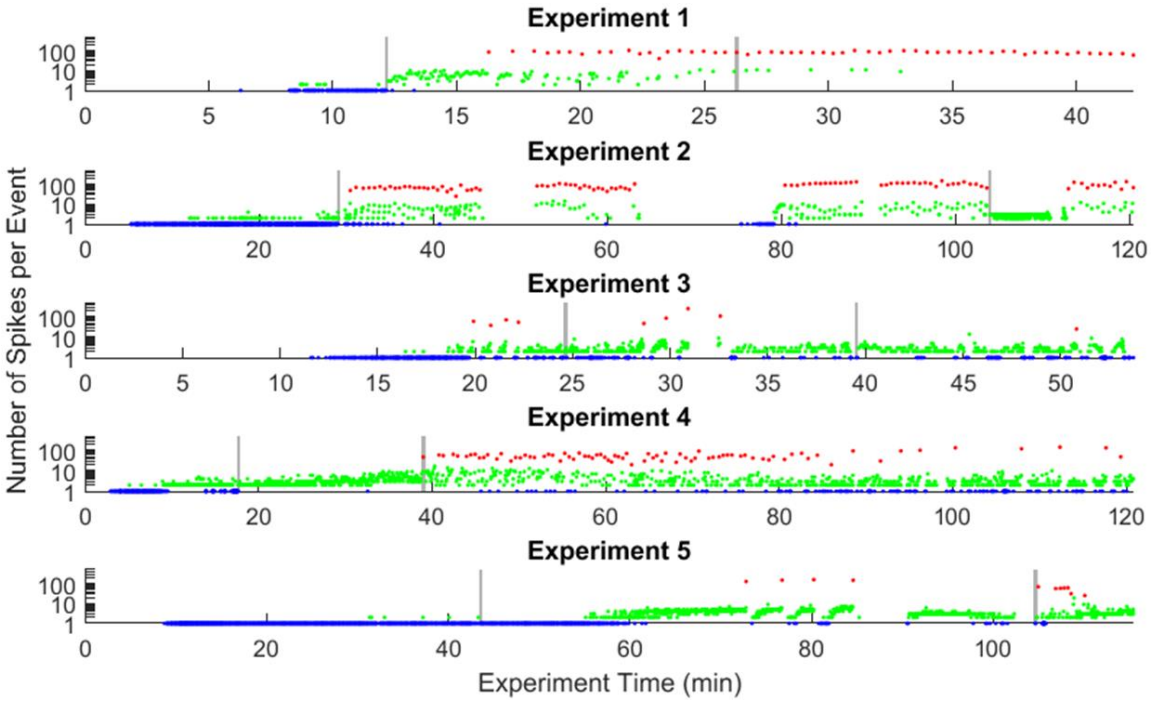

Figure 5.28 Time Period Separation for Each Experiment The scatter plot shows the number of spikes for every event by experiment, with blue, green and red dots representing single spikes, polyspikes and seizures, respectively. The gray lines indicate the time points used to separate each experiment into three time periods over which electrode classification and other analyses were performed.

To perform classification, 200-sample clips (~100 ms) were taken around the first spike of every event on each electrode, using timing determined by the detector focus electrode. Next, the sum and absolute sum of each clip were calculated and the median was found for every electrode over the three time periods. If the median absolute sum for a given electrode was below 200 (i.e. one standard deviation of baseline activity per sample), it was classified as no detectable response. Electrodes with absolute sum medians greater 200 were then categorized into:

i. Focus if the median sum was less than -200 (mostly negative)
ii. Surround if the median sum was greater than 200 (mostly positive)
iii. Border if the median sum was between the two values (mixed response)

Figure 5.29 gives the result of the classification for each experiment and time period. In all of the experiments, the focus showed some growth over the course of the experiment, but remained relatively well constrained. Experiments one, three and five all exhibited a strong surround throughout the experiment that gave little way to focus. There were few border electrodes in these experiments, mostly coming in five, which were eventually recruited into the focus after the final injection. Experiments two and four had almost no surround, and instead a sizeable area of the array saw no detectable response. They had more border than surround electrodes, outside of the final time period in experiment four. These border electrodes showed some positivity along with negativity, but simply grew smaller in total amplitude farther from the focus until there was no response seen, as opposed to a growing positive surround in the other experiments.

Example first spikes are shown in Figure 5.30 to give an idea how the responses on certain electrodes evolved in different experiments. Three electrodes were chosen per experiment with one each in the focus, border and surround (or no response) during the early time period. The colors show how that electrode was classified during each period. In all examples, the electrodes marked with a solid line started as focus and stayed that way the entire time, showing almost exclusively negative responses. The dashed lines all started as border electrodes, with some negativity and positivity, but were eventually fully negative responses as they were recruited into the focus. In the examples from the first and fifth experiments, the dotted electrodes were in the surround the whole time, increasing in positive amplitude throughout the experiments. The dotted electrode from experiment four started as a flat line, gained enough amplitude to be classified as a border, and eventually was predominantly positive in the surround in the late period. The positivity, however, was lower amplitude than the others, as experiment four did not have a strong surround.

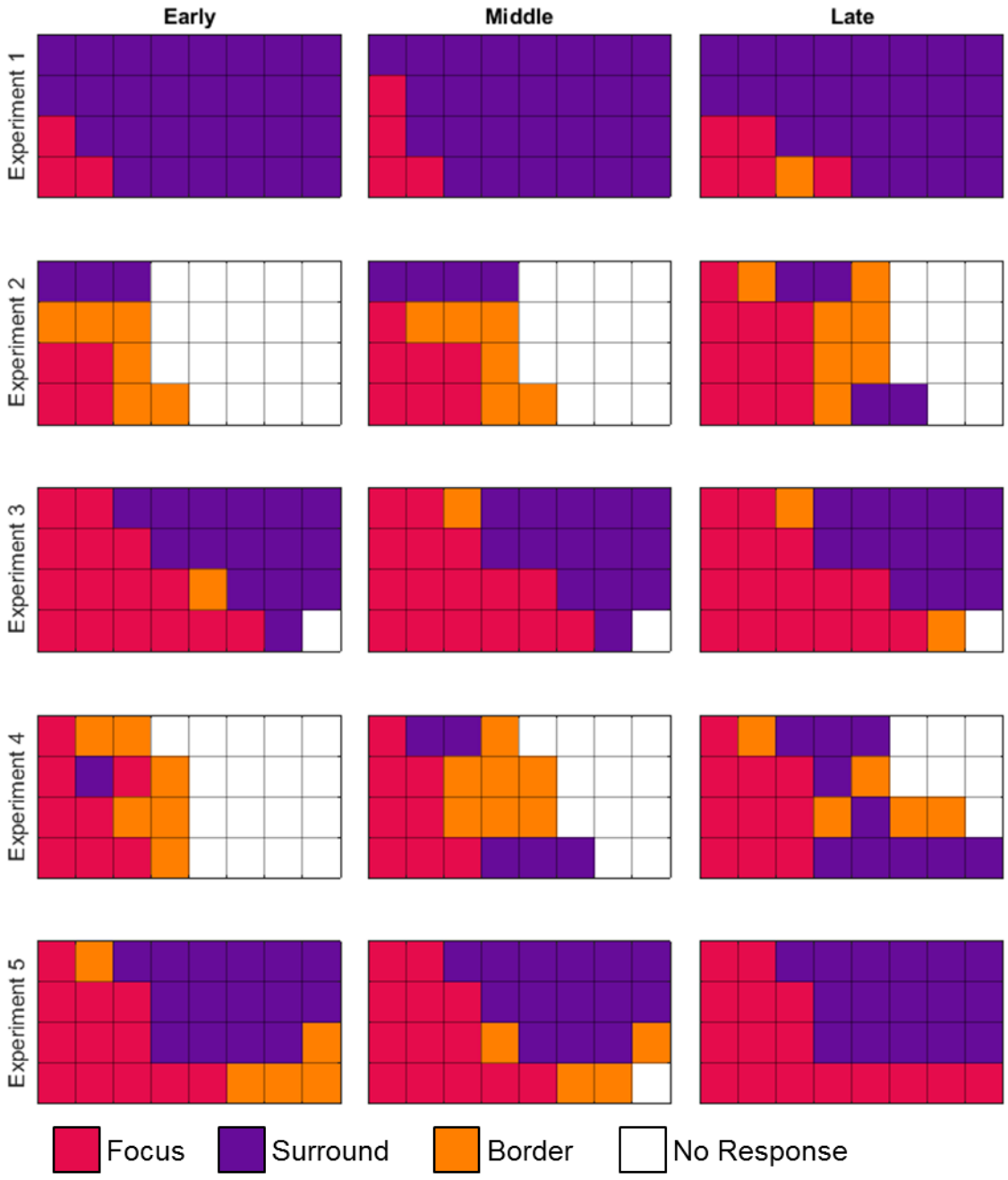

Figure 5.29 Focus, Surround and Border Classification by Electrode Each 4x8 grid represents the surface array for the experiment and time period denoted in the row and column labels. The color corresponds to the category the first spike responses fell into as shown by the color legend on the bottom. Focus electrodes had mainly negative first spikes, surround had mainly positive, and border had a mix of the two. There was some spatial growth of the focus over time, but it stayed relatively well constrained over each experiment.

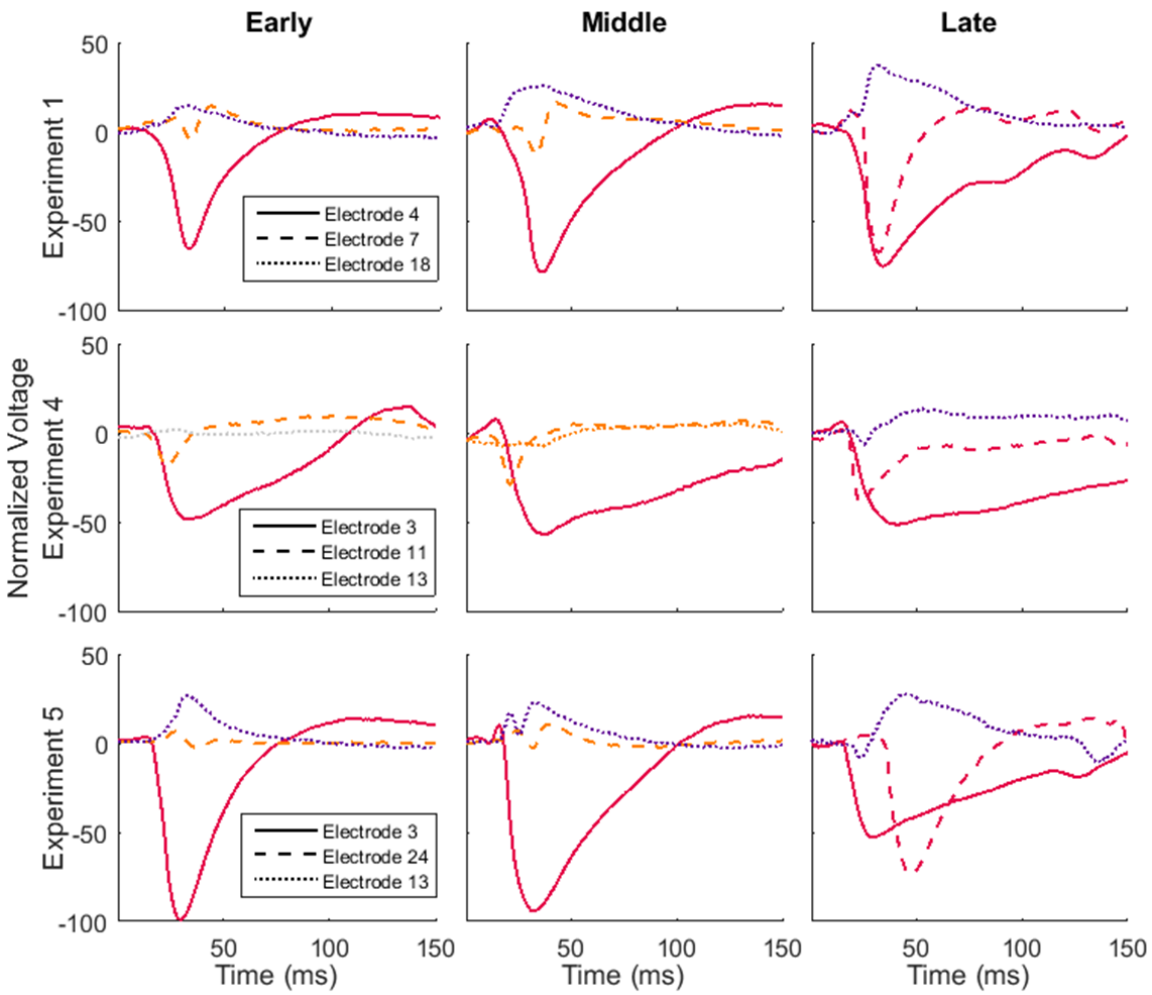

Figure 5.30 Example First Spike Response Evolution Three electrodes and three events, one from each time period from experiments one, four and five, were chosen. The first spikes of those events are plotted here, with solid, dashed and dotted lines corresponding to three different electrodes. Electrode numbering follows the scheme detailed in Figure 5.1. The color on each trace represents the classification of the electrode in the corresponding time period. The color scheme matches that used in Figure 5.29 for focus, border and surround. The solid line was in the focus from beginning to end and the dashed line was a border that got recruited into the focus. The dotted line was a surround by the end of all experiments, though very weak in the example from the fourth experiment.

To further explore the spatial spread of events, the minimum (most negative) and maximum (most positive) amplitudes of first spikes were calculated. Sum was useful for classifying the response as being mostly negative (focus) or positive (surround), but did not reveal how large responses were across electrodes. Figure 5.31 plots the first spike maximum and minimum for all events on each surface electrode during the first experiment. In the focus on the bottom left electrodes, there was a clear increase in negative amplitude, as was seen in Figure 5.15, along with a much smaller corresponding increase in positive amplitude. Electrodes just next to the focus increased in positive and negative amplitudes at similar rates. Even farther from the focus, large, increasing maxima and small, consistent minima were present, indicating strong surround that decayed with increasing distance. All electrodes outside of the focus were classified as surround, but this analysis shows that there were distinct differences in shape and evolution between those of the same type.

The median values of the minimum and maximum first spike amplitudes were calculated over events in the previously-defined early, middle and late time periods in each experiment and displayed in Figure 5.32. At each electrode, the colored upper right triangle represents the median maximum amplitude value, with green to red as increasing positivity. Likewise, the bottom left triangle in each square gives the median minimum amplitude values, with green to blue as increasing negativity. The responses from experiments one, three and five had many electrodes away from the focus with large maxima and minima close to zero. The positive area extended the width of the array, matching the surround electrodes seen in Figure 5.29 for those experiments. The electrodes with large minima and large maxima were relatively well separated with little overlap in those experiments. In the second and fourth experiments, however, the electrodes with large positive first spike amplitudes often also had strong negativity as well. Both polarities died out at a similar rate moving across the electrode away from the small, predominantly negative focus area. This aligns with the classification results for those two experiments, with a focus giving way to mainly border electrodes, and eventually no response. It is unclear what caused such different responses in these experiments, as one was surface application and one was depth, and there was nothing in the methodology specific to them.

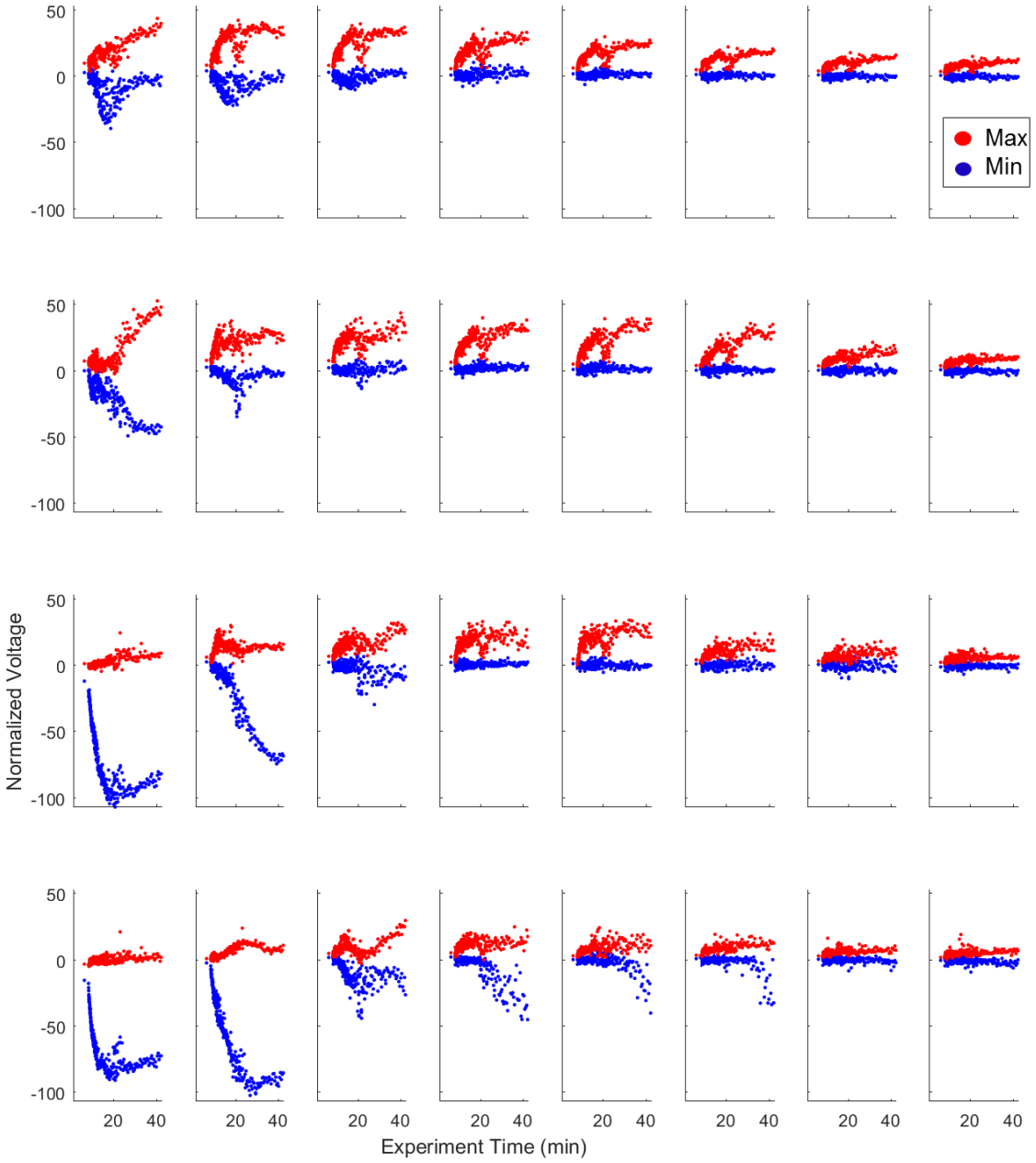

Figure 5.31 Maximum and Minimum Amplitude of First Spikes - Experiment One Each plot contains data from the corresponding electrode on the surface array in the first experiment. The red and blue dots are the maximum (most positive) and minimum (most negative) amplitudes from the first spike of every event in the experiment. The focus electrodes had very large negative values, while those near the focus had smaller minima that increased in negativity near the end of the experiment. The surround showed large, increasing maxima with smaller minima that remained constant. Amplitude plots for the remaining four experiments can be found in the supplementary data section.

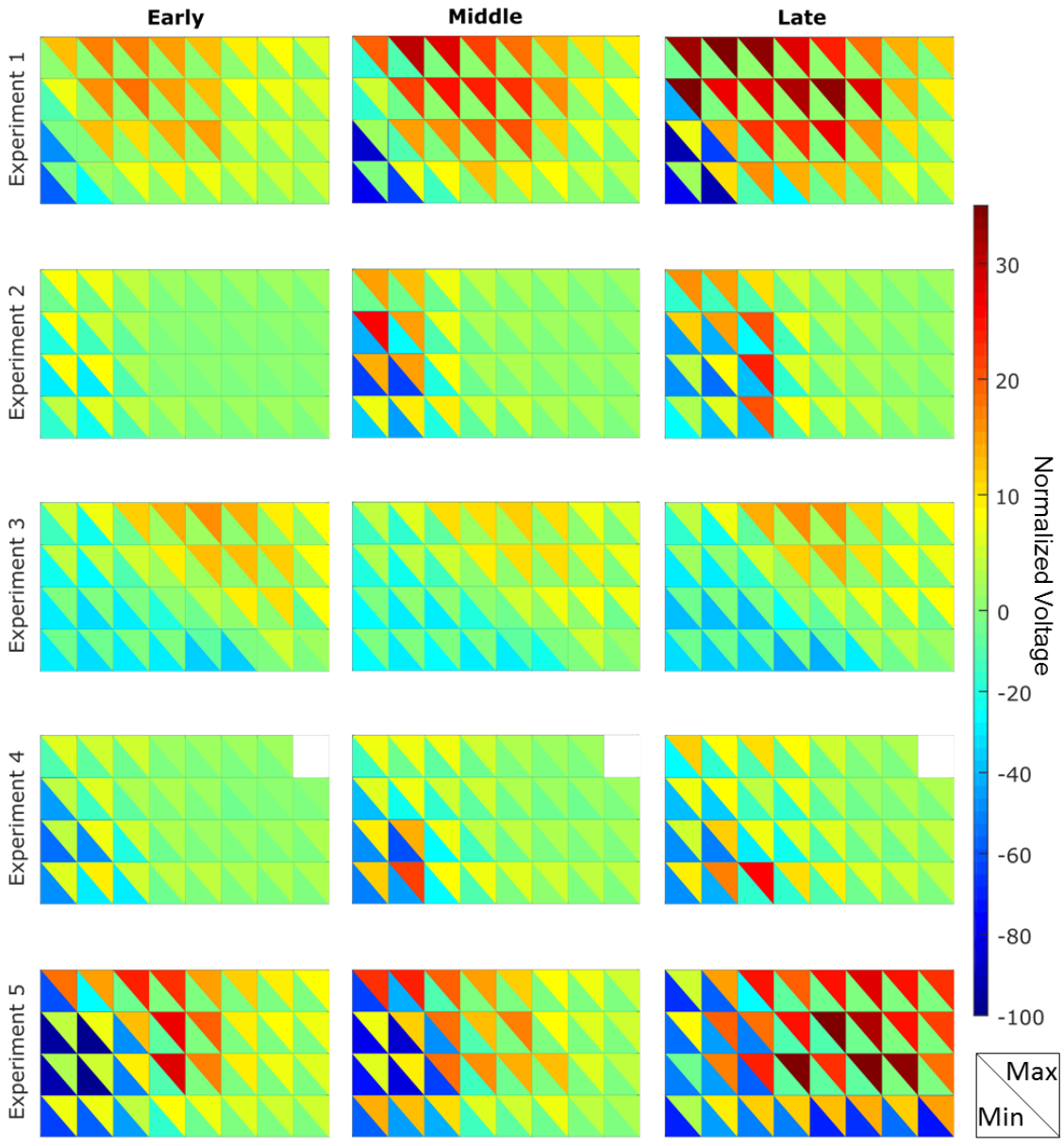

Figure 5.32 First Spike Maximum and Minimum Amplitude over All Experiments Each 4x8 grid represents the surface array, with different experiments arranged by row. Each electrode is split diagonally to represent two first spike values: maximum amplitude in the upper right and minimum amplitude in the bottom left. The color values are the median over all events in the time period of the corresponding column, with blue to green for the minima and green to red for the maxima. Note the color scale is not equal on both sides since the negativity was typically much higher amplitude. Experiments one, three and five had significant surround positivity away from the focus, but electrodes with the largest minimum and maximum amplitudes in the other experiments were in the same general area.

One interesting result from the preceding analyses was the presence of electrodes classified as surround, based on their predominantly positive first spikes, but with a large number of detected polyspikes and/or seizures using the detector designed for negative spiking activity. For example, in experiment one, electrodes 1, 5, 6, 10 and 11 fell in the surround category for all time periods, but hundreds of polyspikes and multiple seizures were detected on them. One explanation is that the subsequent spikes in those events were picked up by the detector, since the focus/surround classification was based on first spikes only. Figure 5.33 plots the first 800 ms of a polyspike from late in the first experiment over all surface electrodes. Looking just at the first spike, the focus and surround areas are evident. Electrodes near the bottom left had mainly negative first spikes and ones farther away, especially near the top of the grid, were positive. Many electrodes near the focus that began with a positive first spike, however, recorded subsequent spikes that were almost completely negative, signaling some form of recruitment in longer events.

In the example, it is clear that only some electrodes near the focus exhibited negative subsequent spikes, while many farther from the focus showed little activity of any sort after the first spike. To quantify the electrodes that had events with recruited subsequent spikes, the detections at every electrode were used. Since in many cases seizures at one site were picked up as polyspikes at others, the total number of spikes detected within the early, middle or late time period for each event was used in lieu of the number of events detected. Any non-focus electrode whose total number of detected spikes was at least 25% of that on the detector reference contact was classified as a recruited subsequent spike electrode. Figure 3.34 adds those as dotted pink squares on the previous classification maps. Experiments one and five, which had the strongest positivity around the focus, had the most recruited electrodes, most of which came from the surround. Experiments two and four, which showed little surround, had several recruited contacts, mostly coming from the border. Since border electrodes by definition had both positive and negative components, it could have been that the detector picked up the negative portions of those spikes, not a polarity reversal in subsequent activity seen in one and five. Finally, experiment three had no recruited electrodes; the surround maintained positivity throughout entire events. This was not the only result in which the third experiment was different from the rest. Table 5.4 summarizes the growth in both first spike focus and subsequent spike focus in each experiment.

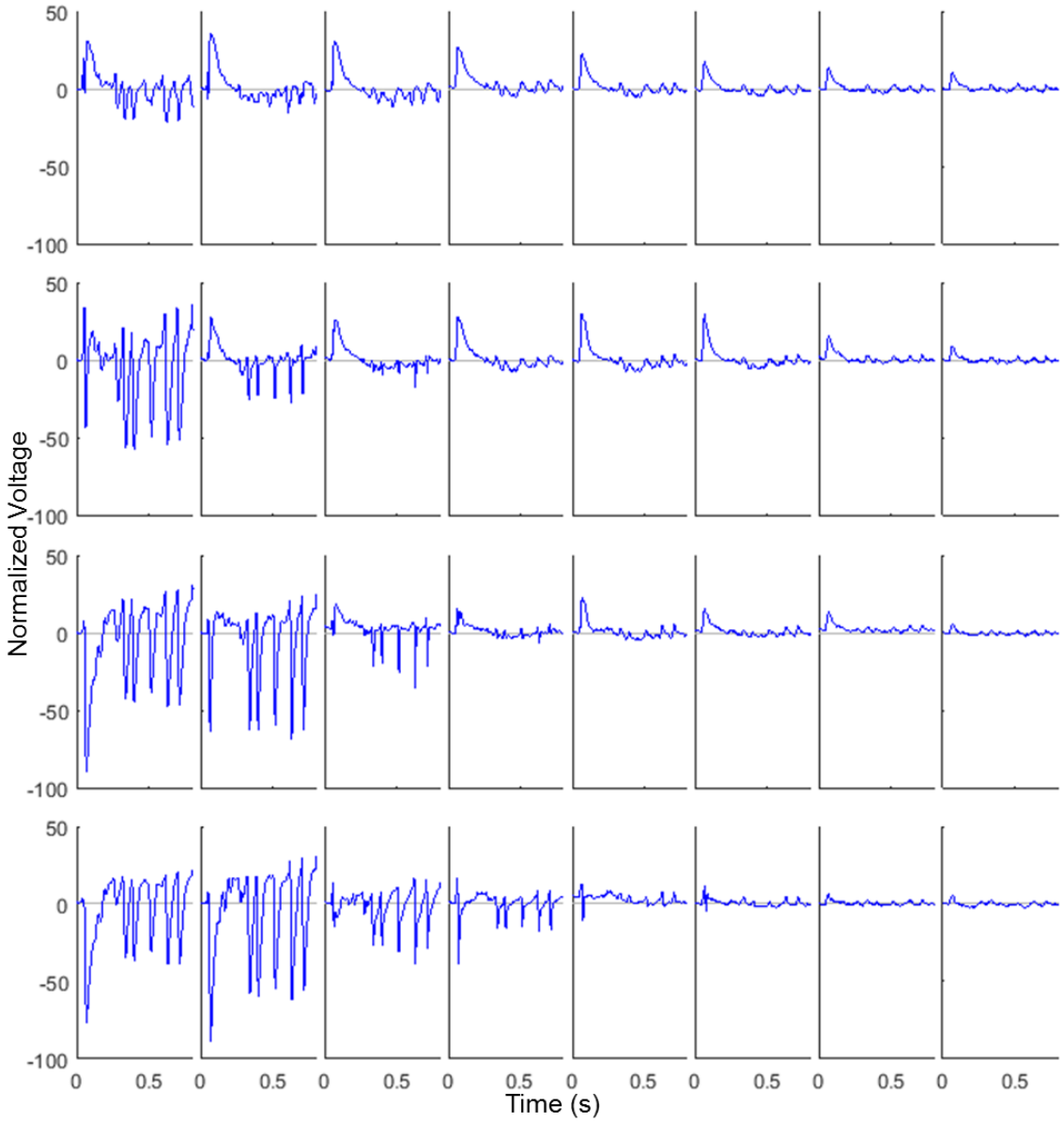

Figure 5.33 Example Polyspike across the Surface The first 800 ms of a late polyspike from experiment one is plotted on every surface electrode. Recordings near the focus had positive first spikes, which caused them to be classified as surround, but the subsequent activity was almost entirely negative.

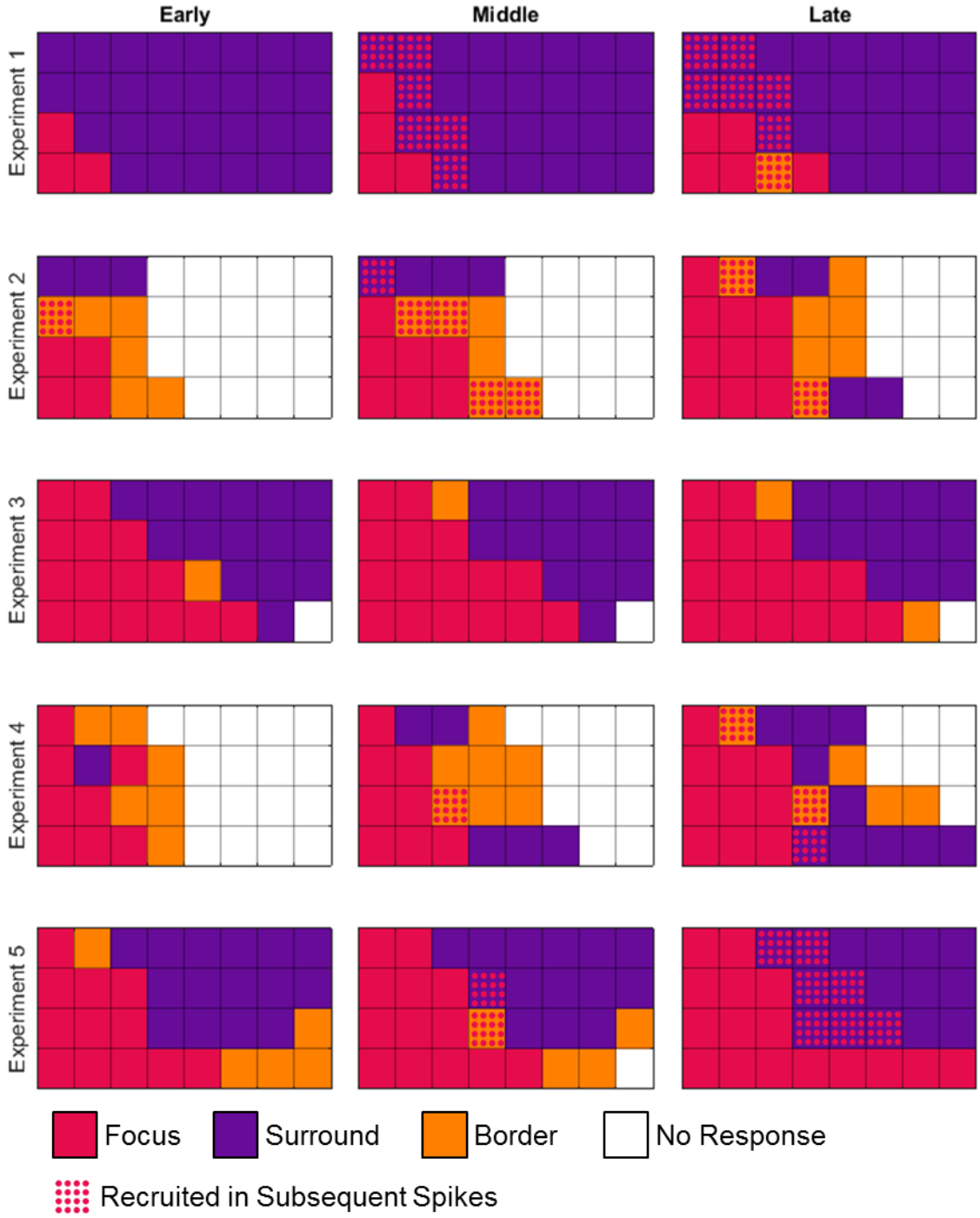

Figure 5.34 Classification by Area with Recruited Electrodes All properties of this graph are the same as Figure 5.29, except for the pink stippled squares, representing electrodes that exhibited events with recruited subsequent spikes. These were defined as non-focus contacts on which the number of spikes detected was at least 25% of that of the detector reference.

	First Spike Focus % Increase	Recruited Subsequent Spike Focus % Increase
Experiment 1	67%	300%
Experiment 2	150%	140%
Experiment 3	7%	7%
Experiment 4	25%	63%
Experiment 5	33%	92%

Table 5.4 Focus Area Growth The table gives the percent increase in the number of focus electrodes from the early time period to the late time period for each experiment. The left colum counts only first spike classified focus electrodes, and the right column includes those and subsequent spike recruited focus electrodes.

Propagation Velocity of Events

In addition to changing shape and amplitude across the surface array, there was a delay associated with the appearance of first spikes on different electrodes. This delay was determined by finding the threshold crossing of -20 normalized voltage units at each electrode in a time window around the start time of the first spike of every event on the focus detector electrode. Only focus electrode delays were used to calculate propagation velocity since border electrodes often had significant positive activity before crossing the negative threshold, resulting in long delays not due solely to propagation. For the same reason, only negative crossings were used, and the threshold was relatively high to avoid false detections. Any events with stimulation near the first spike were omitted from velocity analysis. To find propagation velocity for each event:

i. The electrodes in the focus with the earliest and latest crossings were found.
ii. The Cartesian distance between the two on the grid was calculated.
iii. The distance was divided by the delay time between their first spike threshold crossings.

Figure 5.35 shows the velocity for all events that fit the requirements plotted against experiment time. Overall, velocities were quite consistent within each experiment and even across experiments as well, with a median 0.32 m/s. There was no dependence on event type, nor was there a major shift over the course of each experiment. Figure 5.36 give a bar plot to describe the distribution of velocities over the early, middle and late time periods of every experiment. The largest outliers were the early and middle time periods of the fifth experiment, which were much faster than the others. They correspond to activity produced by a smaller amount of picrotoxin. The late time period came after a final, large injection, and exhibited slower propagation, on par with the other experiments. This suggests that the convulsant slowed down propagation in a concentration-dependent manner. The other experiments showed similar median velocities across the three time periods. Experiment three was the slowest, which could have been caused by the unique activity recorded during that event, as described previously, or its large focus size.

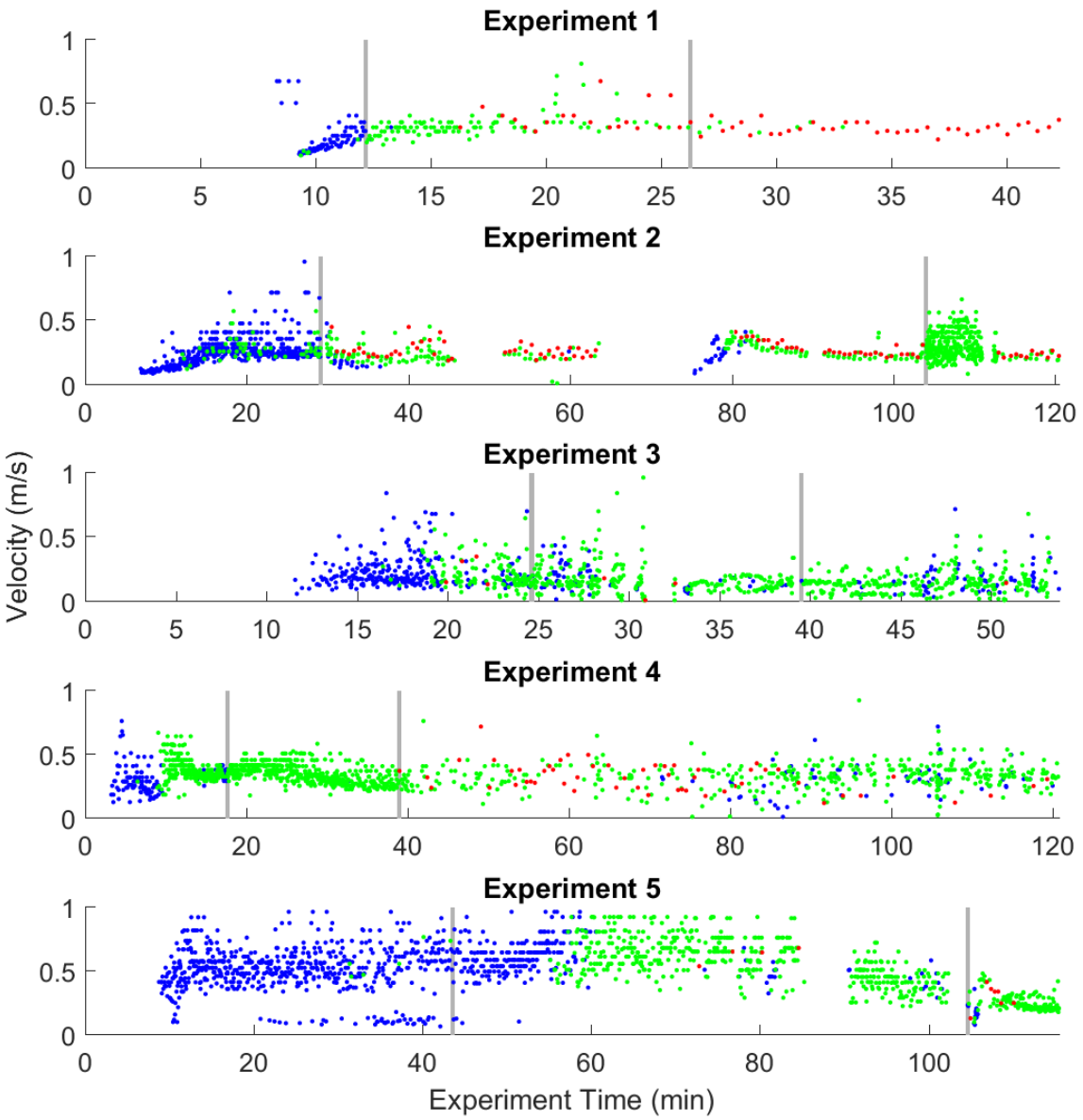

Figure 5.35 Propagation Velocity per Event For each experiment, the propagation velocity of each applicable event calculated on the surface electrodes in the focus is plotted against the start time of the event. The median velocity over all experiments was 0.32 m/s. Blue, green and red dots correspond to single spikes, polyspikes and seizures, respectively. Gray lines mark the three different time periods per event.

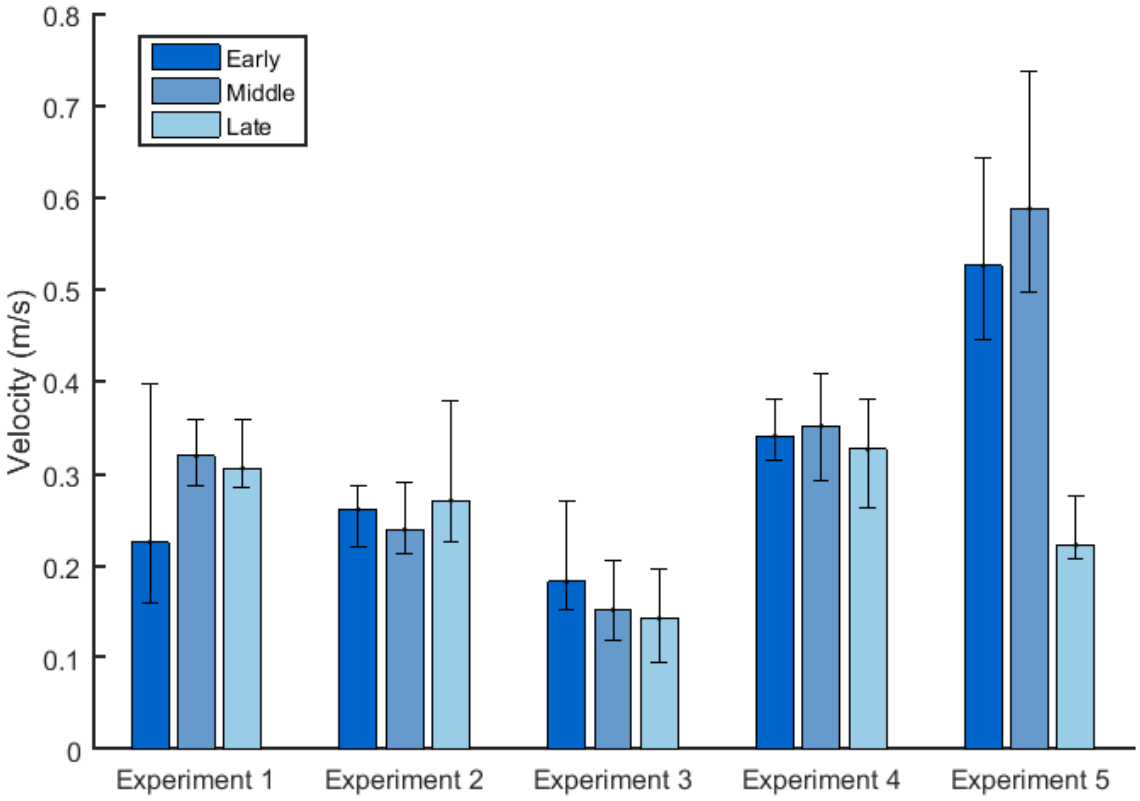

Figure 5.36 Propagation Velocity Distributions The height of each bar is the median propagation velocity of events in the focus during the noted time period in the corresponding experiment. The error bars represent the first and third quartile of each distribution.

Events in the Cortical Depth

In addition to μECoG grids on the cortical surface, every experiment had at least one depth array placed to explore the laminar activity causing epileptic events and how it related to the surface response. The depth LFPs required extra analysis because volume conduction added common signal to the higher-impedance, closely-spaced electrode recordings. This can be seen in the LFP example plotted on the left in Figure 5.37, showing the similarity between signals from contacts near each other. Bipolar montaging calculates the difference between every pair of channels to remove common signal, as seen in the middle plot of the figure. The bipolar channels with significant activity show the depths at which changes in electric field occurred. CSD analysis was performed by taking the negative second spatial derivative of the depth LFPs for each event, with the top and bottom traces duplicated to obtain CSD spanning the entire recorded depth. In experiment one, three channels had significant noise contamination and were replaced by the average of the two surrounding responses. The right plot in Figure 5.37 shows an example CSD profile, where blue represents current sinks and red represents current sources. Further details of CSD analysis can be found in Chapter 2.

The first quantification of depth activity consisted of calculating the standard deviation of each bipolar depth signal during the first spike of every event to find the locations of cortical generators. Standard deviation was chosen since it is a magnitude value, indifferent to the polarity of the bipolar channel, which could change depending on the direction of subtraction. Figure 5.38 plots the calculated first spike standard deviations for each bipolar channel, with dark blue to yellow as increasing voltage. It is clear that in every experiment, there were at least two distinct bands of activity that stayed at a constant depth or drifted slightly deeper as the experiments progressed. Experiments one and two both had two clear bands of activity that grew stronger over time, starting with the upper band. The other experiments saw activity lower in the depth much earlier, but with a similar spatial structure. These results showing clear striation suggests that the depth arrays detected the cortical generators of events, as the feline V1 has a well-established anatomical layering throughout the gray matter.

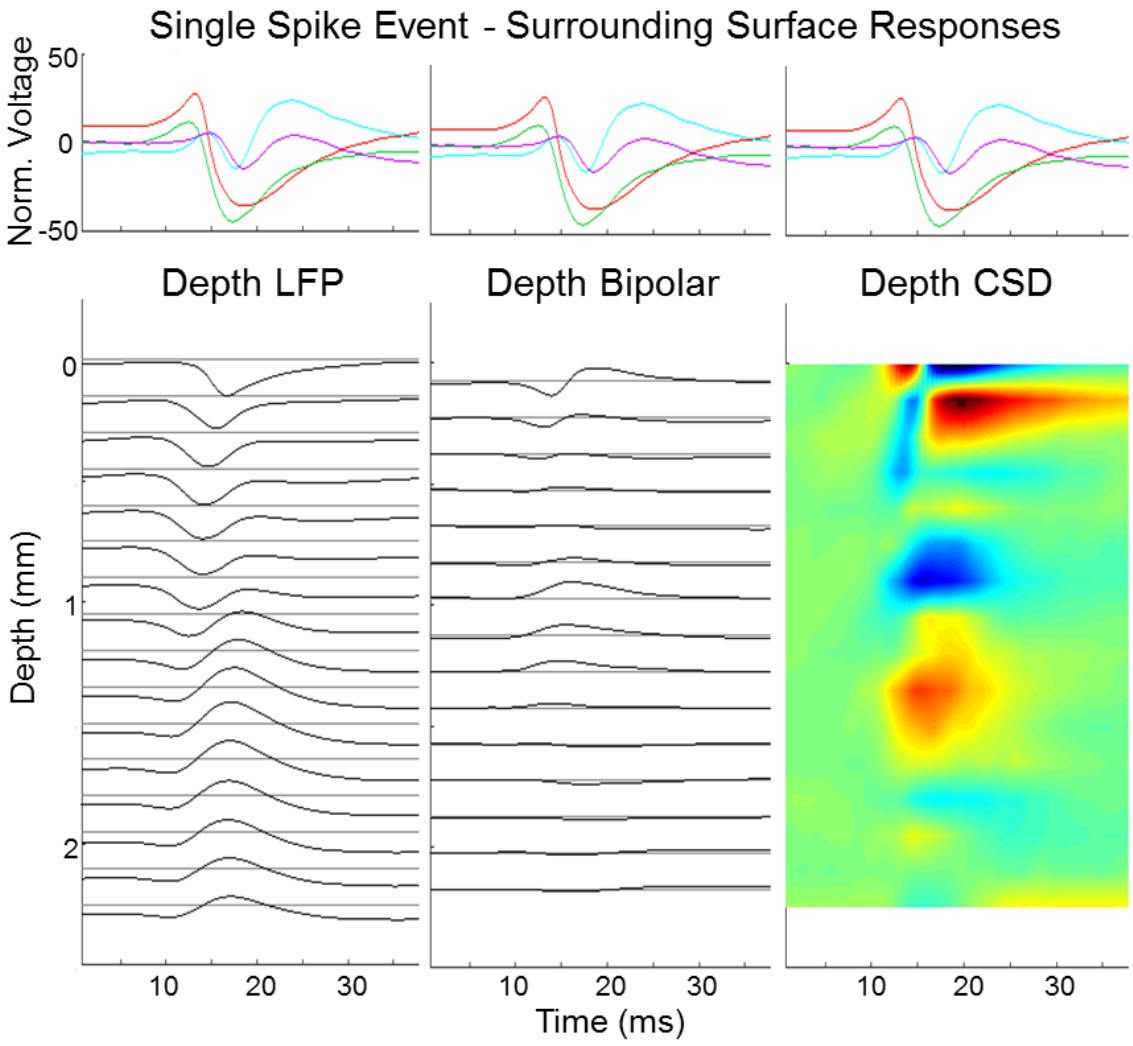

Figure 5.37 Example Depth Array Analyses A single spike from the fifth experiment is shown here. The upper plot on each column shows the spikes on the four surface electrodes around the depth shank. The left plot shows the LFP recorded on all 16 channels of the depth array. The center plot is the bipolar montage of the depth array, calculated by subtracting every pair of electrodes to remove common signal and show where activity is generated. The right plot is the current source density (CSD) of the traces, with blue and red representing current sinks and sources, respectively.

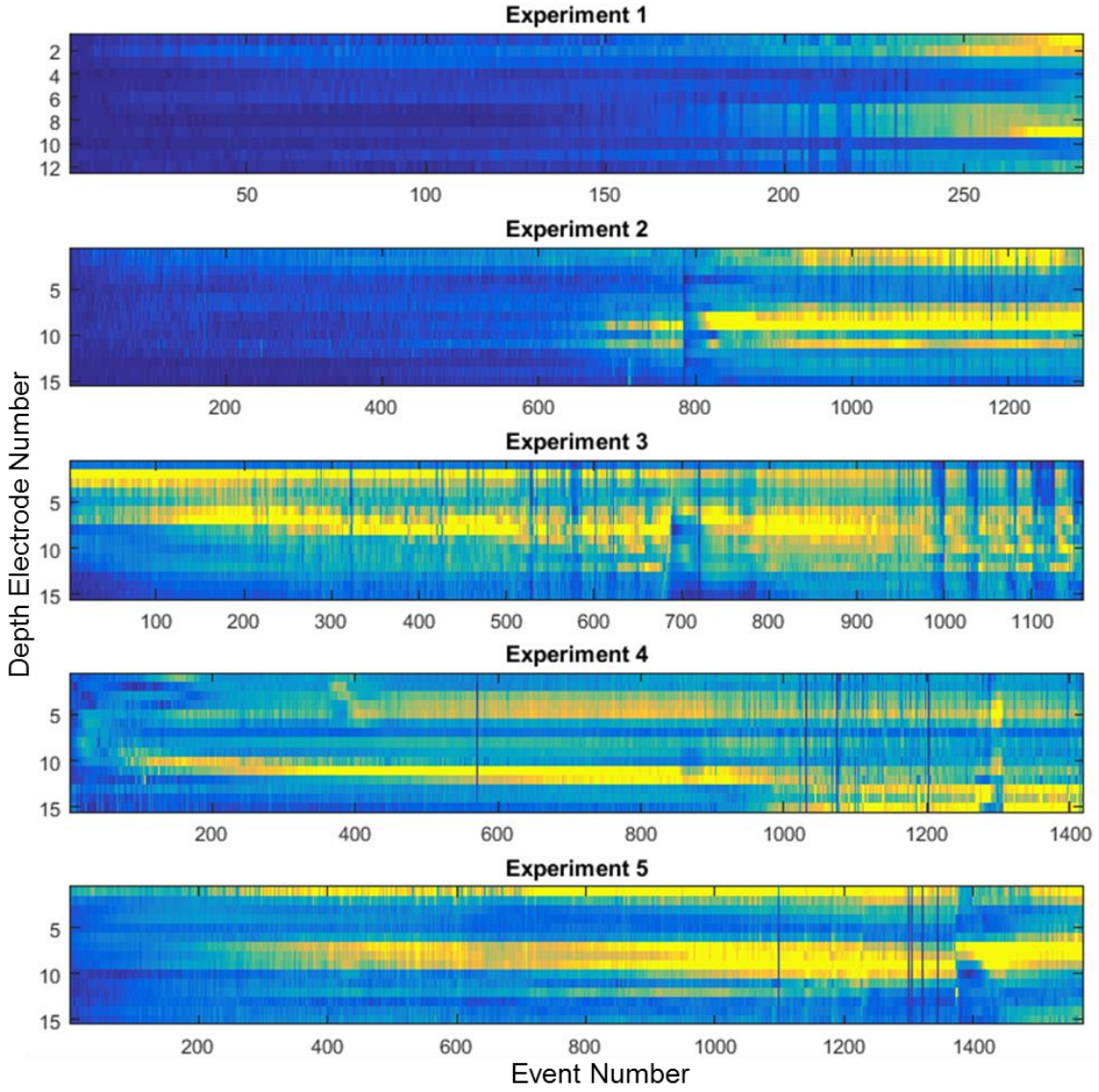

Figure 5.38 Depth Bipolar First Spike Standard Deviation Clips were taken of the bipolar-montaged depth recordings around the first spike of every event per experiment. The standard deviation within that clip on each channel was then calculated. The plots show this standard deviation value as a color from dark blue to yellow going from 0-400 μV. The y-axis has the bipolar channels 1-15 with increasing depth (3 electrodes removed from experiment one due to noise), and the x-axis is increasing event number over each experiment. The depths of activity were consistent and stratified in each experiment, matching the distinct layered structure of V1.

CSD analysis expands on the bipolar results by detailing where current flowed throughout the depth, caused by activity in the layers generating epileptic events. 60 ms clips around the first spike detection of each event were taken and the CSD was calculated on the depth response, as in the example from Figure 5.37. To investigate evolution over the course of the recordings, 200–300 evenly distributed clips from each experiment were appended sequentially. Plots of these clips are shown in 5.39, with a common color range across events within each experiment to highlight change in source/sink intensity over time. The CSD was left unitless as only the relative values between depths and time periods were of importance. Also plotted in the figure is the number of spikes per event as determined by the detector reference electrode and the first spike sum of every event on each of the four surface electrodes around the depth array. Each first spike sum is colored pink, purple or orange corresponding to focus, surround or border, respectively, using the classification described earlier. This was plotted to see how the CSD was affected by the location of the depth array relative to evolving focus and surround areas. Finally, the figure contains the classification grid for the late time period of each experiment, with the four surrounding electrodes marked, as well the location of the depth shank and detector reference electrode.

The depth arrays used to calculate the CSDs in Figure 5.39 were either in the focus or on the edge of it, with at least two of the neighboring surface electrodes classified as focus by the end of the experiment. The depth array in the fourth experiment was the closest to the picrotoxin application site, about 1 mm from the injection. Correspondingly, it was in the focus throughout most of the experiment, with only one of the adjacent surface electrodes showing positive surround response early in the recording. The CSD from that experiment had a sink around 0.6 mm in depth at the beginning that dropped in intensity quickly. A lower sink, around 1.3 mm, appeared shortly after the start of recording and grew in intensity over time. The time course of these sinks lined up with the increased negativity in the two nearby surface electrodes farther from the picrotoxin, signaling the recruitment of tissue into the focus. Eventually, the 1.3 mm sink dropped in intensity and an even deeper sink appeared, at a point when all surrounding surface electrodes were firmly in the focus. Experiment three shows a similar profile, since the four surface electrodes were in the focus the entire time. A strong superficial sink decreased in intensity over time, as a middle sink grew and a deep sink appeared. Experiment five had three of four adjacent surface electrodes exhibiting focus responses. It had a dominant middle sink, around 1 mm, and smaller upper and lower sinks.

Experiment two, which did not have a significant surround, started with very little activity of any sort on the surface around the depth array. This resulted in the absence of

any sinks or sources on the CSD. Once two of the neighboring surface electrodes showed focus first spikes, a large middle sink appeared around 1 mm, growing slightly but remaining quite consistent. There was evidence of sinks deeper and more superficial, though they were much lower intensity.

Experiment one was unique in that it started with predominantly positive activity around the depth array, indicating it was in the surround. The CSD showed a single superficial sink around 0.3 mm during that time, and it gradually increased in intensity. Once the negativity on the nearby surface electrodes increased and the focus grew, a sink around 1 mm appeared and got more intense. By the end, two surrounding surface electrodes exhibited strong focus spikes, one was border, and the third had strong surround positivity. At that time, the two sinks were at their strongest and a third deep sink on the very bottom of the array appeared. In this and the second experiment, seizures started simultaneous with the lower sinks. The other three experiments, which were in the focus throughout, saw deep activity well before seizures appeared.

These results show that the spatial growth of the seizure focus is related to the appearance of one or more strong sinks (and sources) at least 1 mm in depth. Activity more superficial than that was related to the presence of surround positivity near the depth shank (experiments one and four), though this was not consistent (experiment three). In cases where depth recruitment was seen (experiments one and two), growth of the focus into that area, and the corresponding appearance of deeper sources and sinks, occurred concomitant with the first seizures detected on the surface.

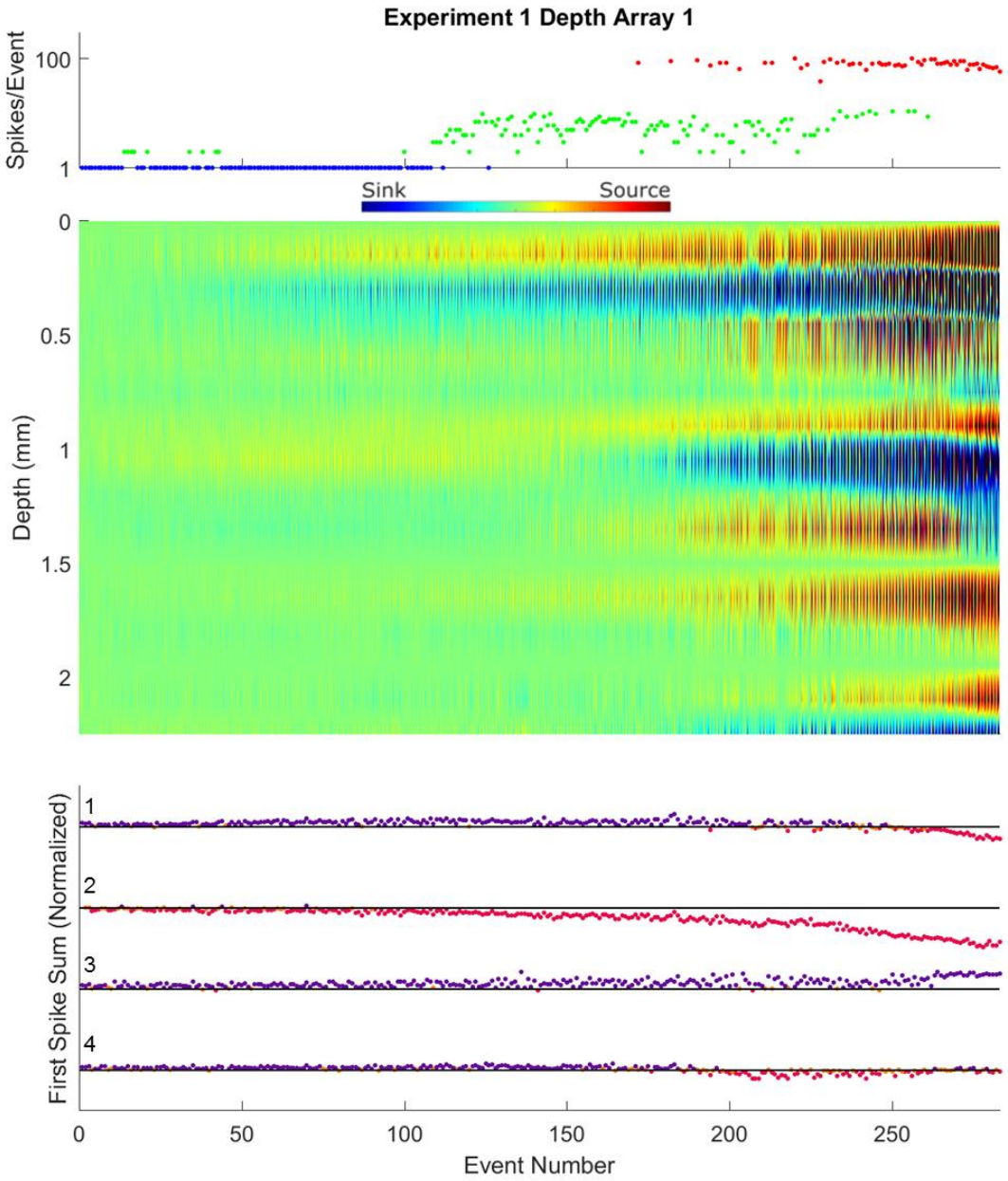

Figure 5.39 CSD Evolution - Experiment 1 The center plot shows the CSD calculated on clips around the first spike of events over the experiment, with blue as sink and red as source. The depth array location is marked with (X) on the grid on the bottom right. The top plot is the number of spikes per event on the detector reference electrode, denoted by a circle (O) in the grid. The bottom plot shows the first spike sum over all events for the four surface electrodes directly adjacent to the depth array, marked 1-4 in the plot and on the grid. The colors of the sums are pink, purple and orange corresponding to focus, surround and border classification. The grid has the same colors for the late time period of the experiment.

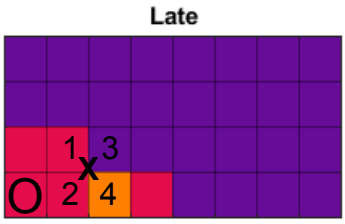

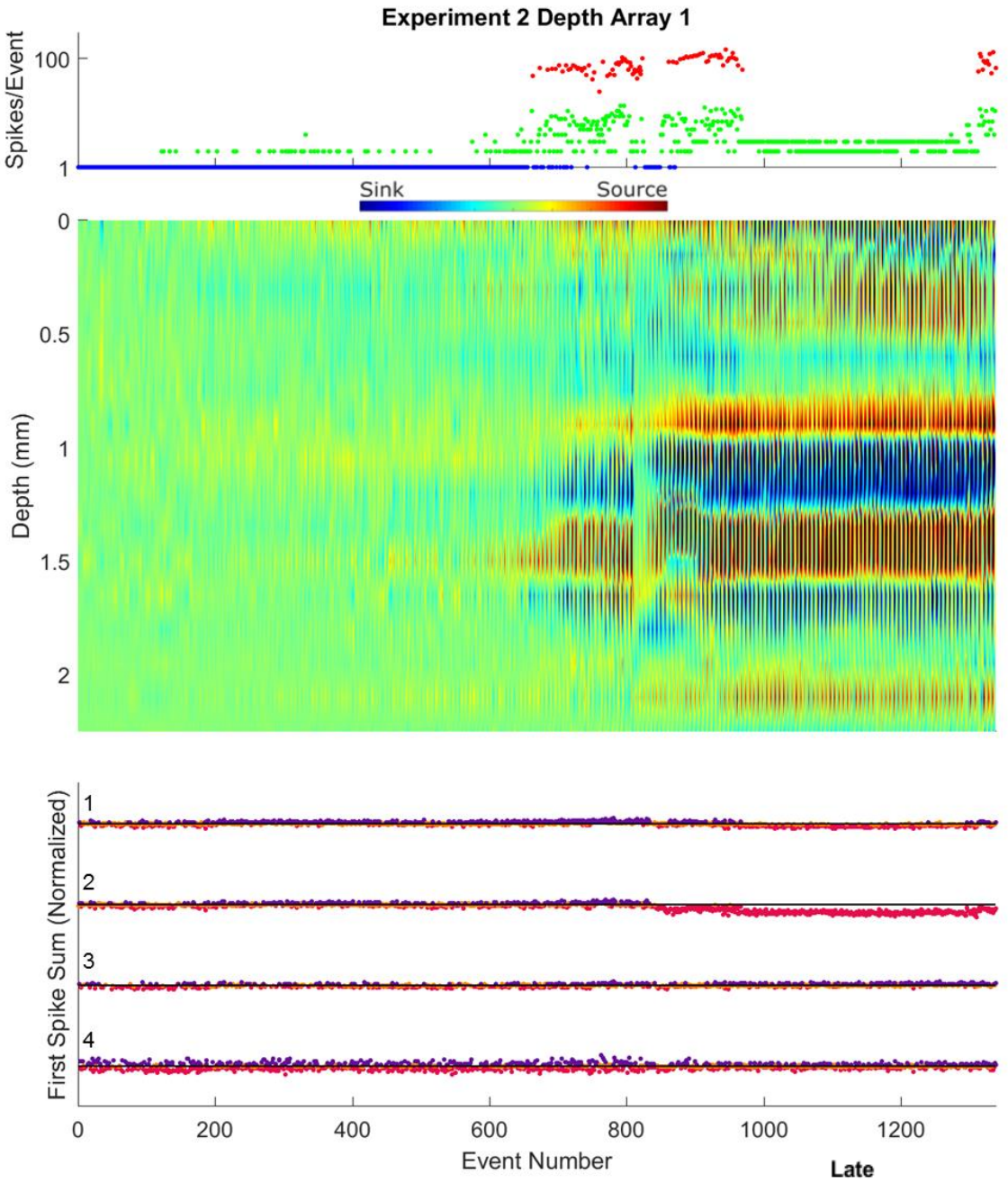

Figure 5.39 CSD Evolution (cont'd) - Experiment 2

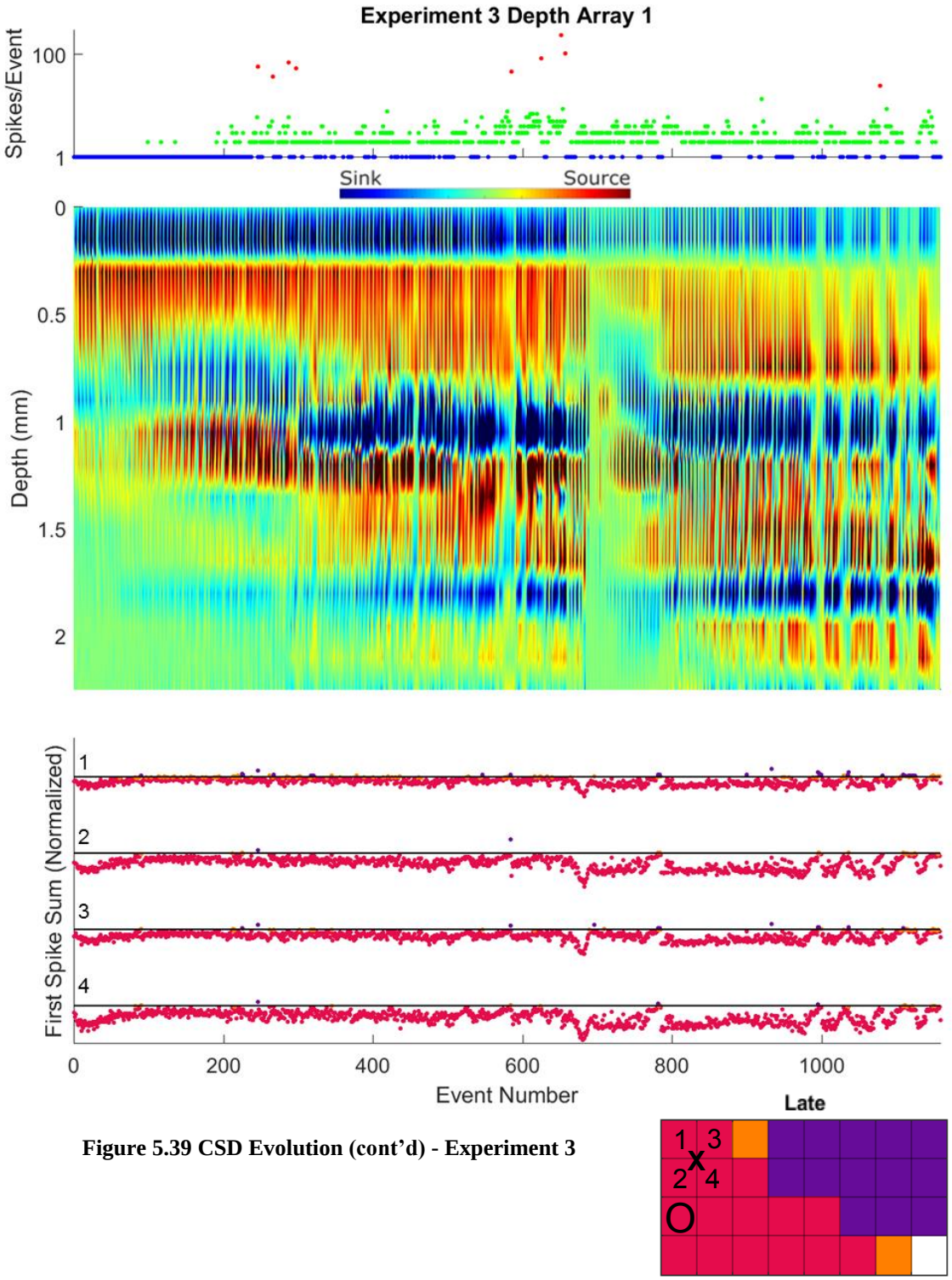

Figure 5.39 CSD Evolution (cont'd) - Experiment 3

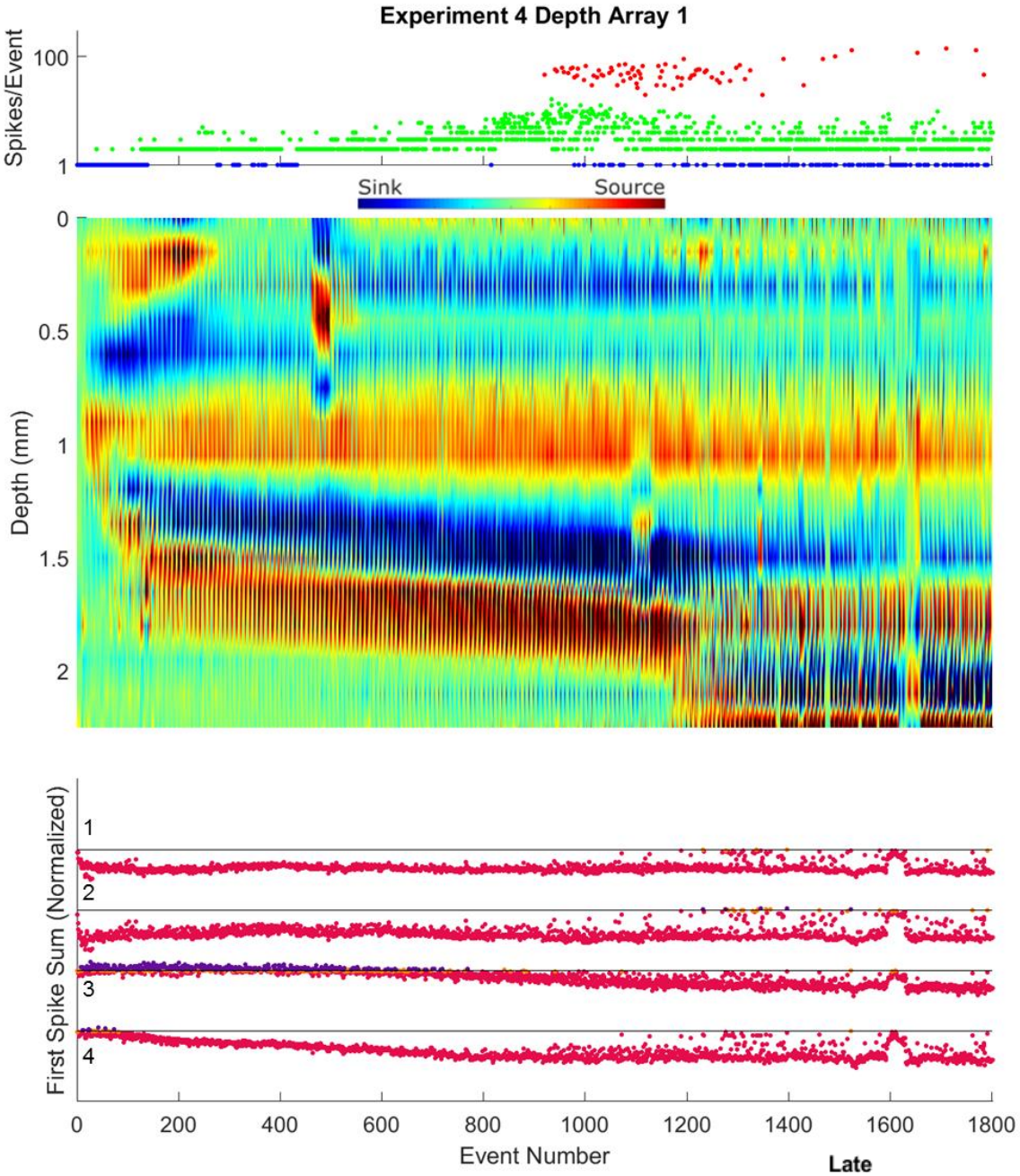

Figure 5.39 CSD Evolution (cont'd) - Experiment 4

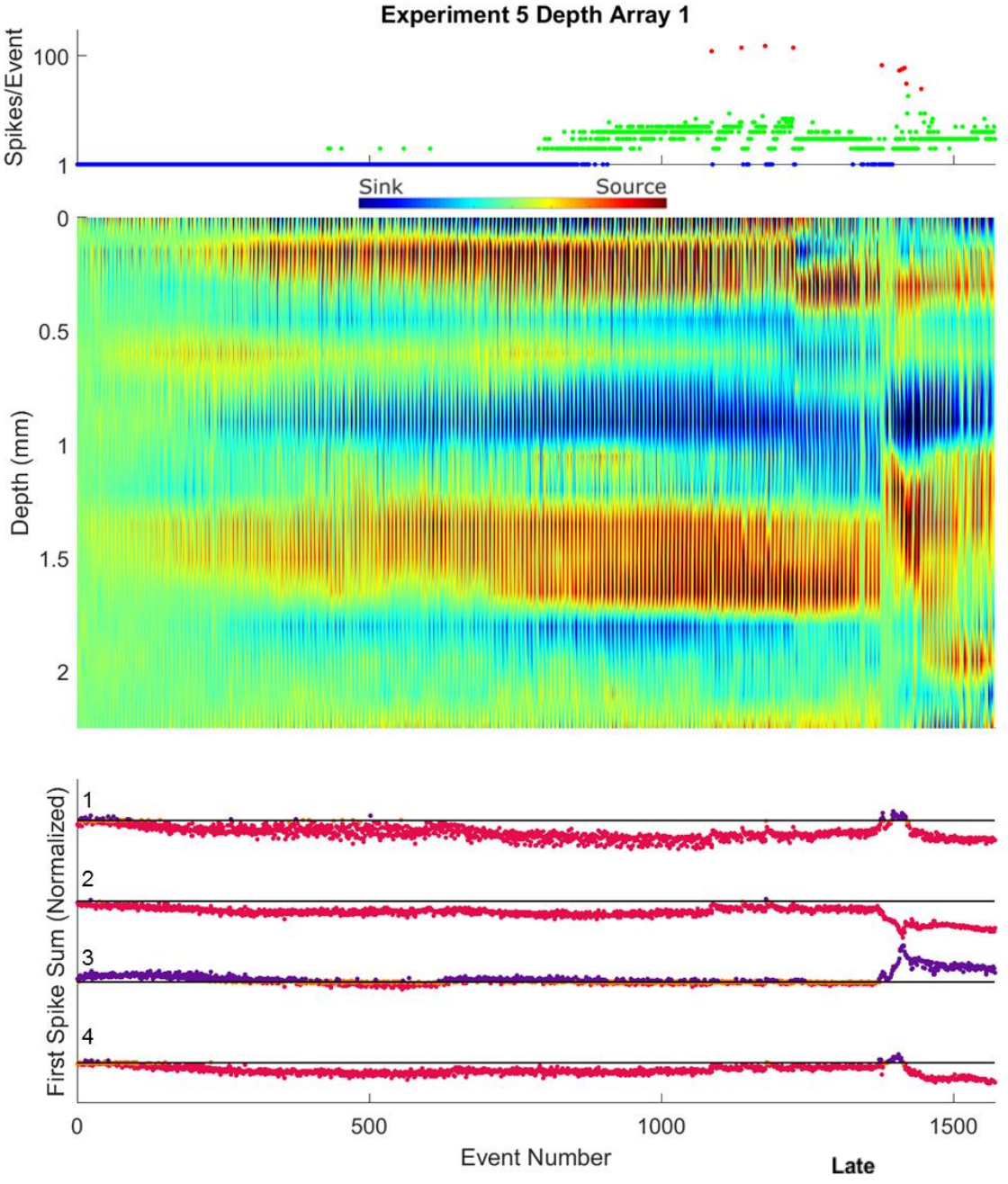

Figure 5.39 CSD Evolution (cont'd) - Experiment 5

The last three experiments had second depth arrays located farther from the focus. Only in the third experiment was there detectable activity over the course of the recording on that second shank. Figure 5.40 shows the CSD from the second depth array in the third experiment in the same fashion as those plotted in Figure 5.39. Overall, its signals were much smaller amplitude than those from the shank in the focus. Accordingly, the CSD was also lower intensity. At the beginning of the experiment, three of the neighboring surface electrodes were surround and the fourth was border. During this time, the most prominent activity was a sink around 0.6 mm with a source above it, similar to what was seen early in the CSD of experiments one and five shown previously. Over time, the border electrode became part of the focus, and the others, though still classified as boundary, saw smaller first spike sums. The decrease of surround strength occurred along the appearance of a consistent middle sink, around 1.2 mm, and a more volatile lower sink, closer to 2 mm. This lower activity matches with what was seen in the other experiments as the focus grew, even though this depth array was just on the very edge of it.

The location of the second depth array in the fourth experiment was far from the focus in an area where there was no detectable response from the nearby surface electrodes and thus nothing on the depth. In experiment five, the second electrode was in the surround, though the signal was too low to obtain useful CSD until after the final large picrotoxin injection. Figure 5.41 gives an example event from this time period, with the CSD profiles from both depth arrays as well as the response on the surface electrodes around each of them. The CSD from the surround had a very superficial sink, around 0.2 mm, with a source above it. The other depth array, mostly in the focus, had an upper, middle and lower sink, as was seen in Figure 5.39 for the fifth experiment. The sink/source arrangements for the subsequent spikes on the first depth array were very similar to that of the first spike; a characteristic common to depth arrays near the focus. The other depth shank, in the surround, saw the dipole orientation from the first spike reverse in the subsequent spikes, as the surface electrodes showed negativity replacing the initial positivity.

These results further suggest that positive surface surround responses were due to activity from superficial layers in the cortex, while negative focus responses required deeper layer engagement. Also, activity solely in the highest layers created different surface responses depending on the source/sink configuration, as was seen the subsequent spikes of events in the surround.

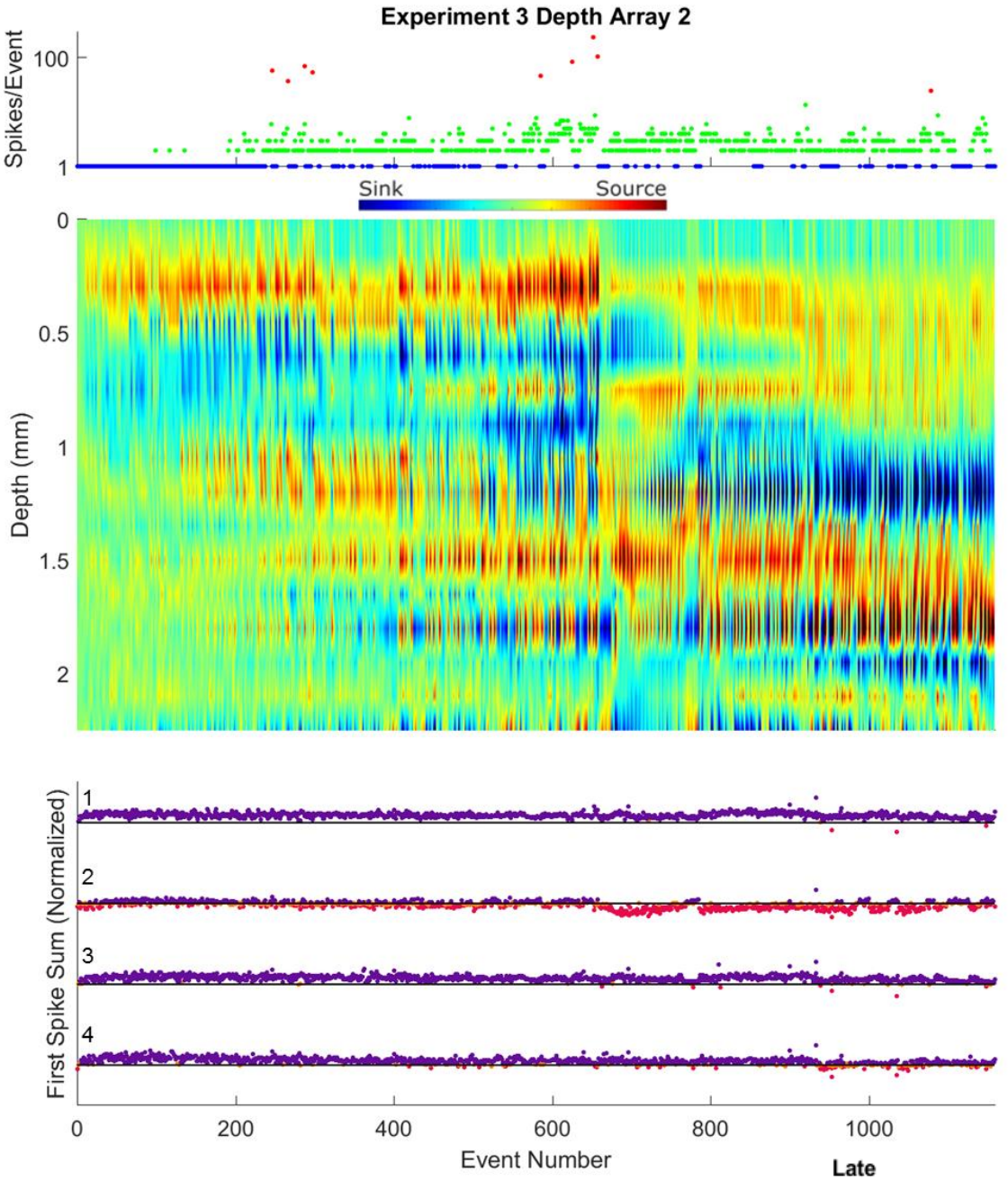

Figure 5.40 CSD Evolution - Experiment 3, Depth Array 2 The plots in this figure are the same as those described in Figure 5.40. The CSD is from the second depth array in the third experiment. The four adjacent surface electrodes were mostly in the surround during the experiment, though the first spikes became more negative over time.

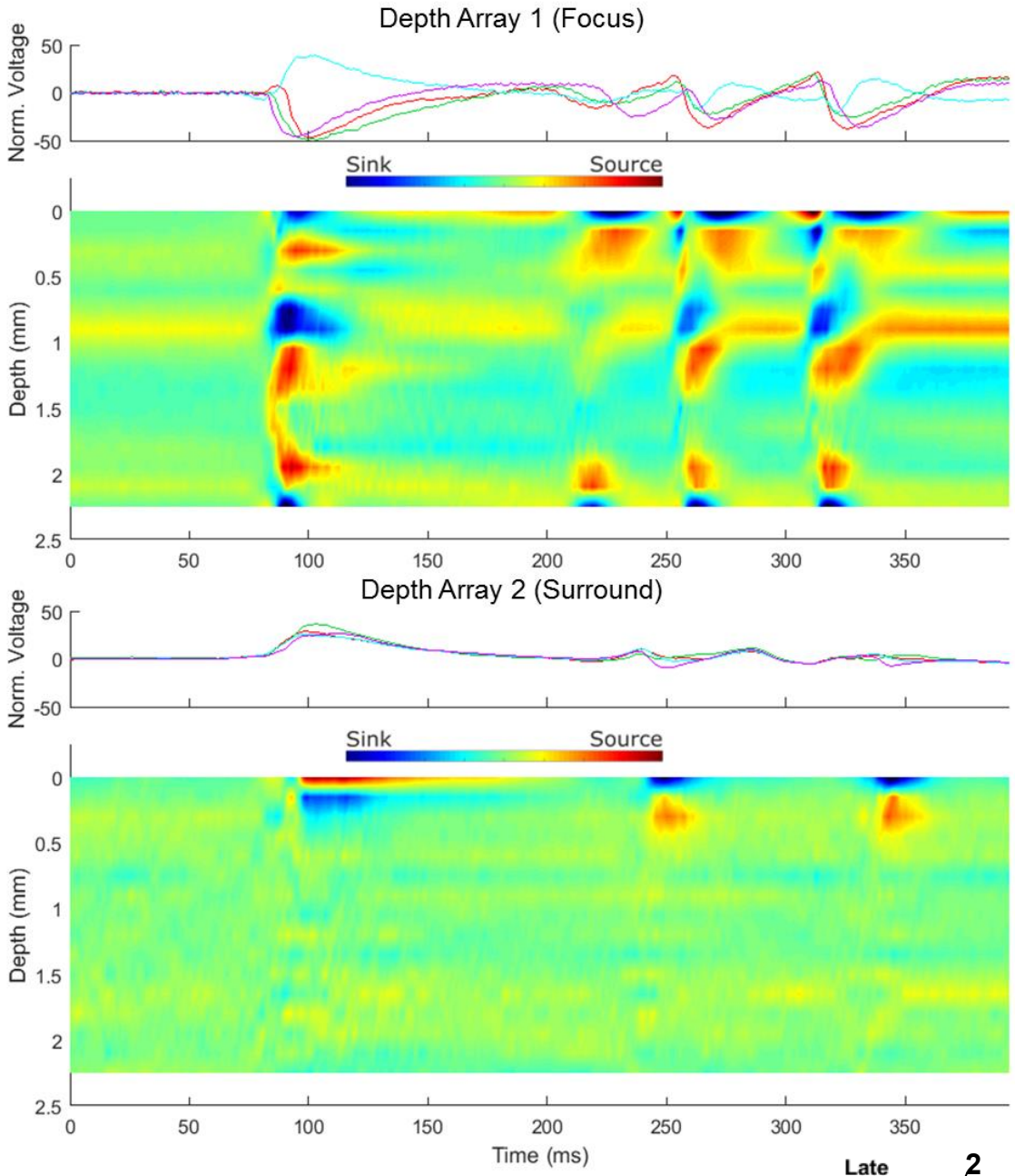

Figure 5.41 Focus and Surround Example CSD The figure shows the CSD profiles from both depth arrays used in experiment five during one polyspike event late in the recording. The location of the arrays relative to the surface are marked with (X) on the bottom right grid, with colors denoting focus and surround. Above both CSD profiles are the traces of the four surface electrodes directly around the corresponding depth shank.

Discussion

In the experiments detailed in this chapter, epileptic activity was induced in an isolated portion of healthy, anesthetized feline visual cortex. Across all subjects, the activity arose and evolved in a consistent, repeatable pattern. First, high amplitude, negative single spikes appeared as the sole event in the cortex. Over time, these turned into polyspikes as lower amplitude activity presented following the large spikes. Eventually, seizures appeared intermittently between polyspikes, with distinct timing and frequency characteristics. The spatial spread of the events was captured by a μECoG grid on the surface, revealing a small focus of strong negative activity near the chemoconvulsant that grew slightly over time. In three of the five experiments, the focus was surrounded by cortex that exhibited strong positive response to the large first spikes of events, but often died out or became negative over the duration of polyspikes and seizures. CSD calculated on linear depth arrays inserted into the cortex revealed the epileptic activity was marked by sinks in deeper layers that appeared as tissue was recruited into the focus. Many of these results are similar to those of previous seizure model studies and relate to common traits seen in human epilepsy.

Cellular Mechanisms

The large repetitive spikes at the beginning of all experiments are a hallmark of seizure models using GABA antagonists, as described in Chapter 2. They have been seen in many different species, in different brain regions, and in both *in vivo* and slice preparations (Dichter & Spencer 1969a; Dichter & Spencer 1969b; Miles et al. 1988; Prince & Wilder 1967; Chagnac-Amitai & Connors 1989). Studies at a cellular level have shown that the spikes are associated with a mass depolarization of neurons in the focus, caused by the lack of GABA-mediated inhibition. The inhibition in the focus was not completely wiped out, however, as evidenced by the long post-spike hyperpolarization and concurrent IPSPs. The studies also saw positive spiking in the area outside the focus, which became known as surround inhibition because it was associated with predominantly IPSPs in the underlying neurons (Prince & Wilder 1967). In tissue distant from the direct effects of the convulsant, the normally strong recurrent inhibition was still intact and extremely active due to the increased input from the focus. Areas in between the focus and surround inhibition exhibited a combination of the two, often with early IPSPs before the depolarizing spike and late hyperpolarization (Dichter & Spencer 1969a).

In previous work, spontaneous seizures were seen, but did not appear as consistently as single spikes, and often had to be elicited with electrical stimulation (Prince & Wilder 1967; Dichter & Spencer 1969a). The longer events had lower amplitude spikes that appeared after the first, caused by smaller, shorter depolarizations in pyramidal cells. The appearance of subsequent spikes coincided with the disappearance of the late hyperpolarization that followed single spikes in the focus, and the development of more prominent depolarization in the surround. The results we found reflected this change, as many events in the surround began with large positive spikes, but the secondary activity was negative, having been recruited into the focus. It was posited that a delay in the onset of post-spike inhibition in the focus, possibly due to excessive depolarization, allowed these secondary spikes to appear (Dichter & Spencer 1969b). This breakdown in inhibition must be spatially limited to areas within and just outside of the focus, as the entire grid was not recruited later in seizures. Additionally, two experiments showed no surround inhibition, but the evolution of seizure activity was not affected. Thus, in this model, it must be the inhibition remaining within the focus that is important in preventing spikes from turning into seizures, while the surround inhibition is merely a reflection of the focus.

The source of the large depolarizations that manifest as surface spikes have been shown to be large pyramidal neurons, which are located in layers II/III and V in cat visual cortex. Histology was not performed and the location and insertion angle of linear electrode arrays can greatly change the depths at which layers are found. However, in some experiments, visual stimulation was also performed, giving a CSD profile on the depth array with a known response. Figure 5.42 shows the CSD from the first spikes of three events spanning the course of the fifth experiment as well as the CSD profile of a visual evoked potential from the same experiment. As explained in Chapter 3, the lower sink is thought to correspond to layer IV, which is the primary target of projections from the thalamus in response to visual stimulation. Activity then travels polysynaptically to layers II/III, where the upper sink is believed to lie. The CSD from the seizure activity exhibits an opposite profile, with sinks in place of sources and vice versa. Studies in slices and deafferented brain regions have shown that seizure activity in this model can arise solely in intracortical networks (Dichter & Spencer 1969a; Miles et al. 1988; Chagnac-Amitai & Connors 1989; Zhang et al. 2014). Horizontal connections between regions in V1 are predominantly excitatory and mainly synapse on large pyramidal cells in layer V and layers II/III (Schmidt & Lowel 2002). Considering cellular recordings have shown the basis of the spikes to be the depolarization of pyramidal cells, it suggests that the major sinks in the focus are caused by intracortical excitatory connections to those layers, recurring in the disinhibited tissue. Additionally, the CSD results showed

that the spread of the focus was marked by the appearance of deeper sinks, which are believed to be in layer V. Previous work has shown that layer V is necessary for self-sustained horizontal propagation, and serves to amplify activity in layers II/III (Wester & Contreras 2012).

Finally, the propagation velocity calculated for epileptic events, 0.32 m/s, was slower than that of stimulation response, at 0.48 m/s. Previous studies have found these models to propagate even more slowly, closer to 0.1 m/s, though they were in slice preparations (Zhang et al. 2014). The slower velocity was thought to be caused by the recurrent synaptic activity between neurons that mediated the spread of synchrony (Miles et al. 1988). Early in the fifth experiment, when little picrotoxin was added, the velocity was higher around to 0.6 m/s, suggesting a dose-dependence on the recurrent excitation, seen previously in GABA antagonist models (Chagnac-Amitai & Connors 1989).

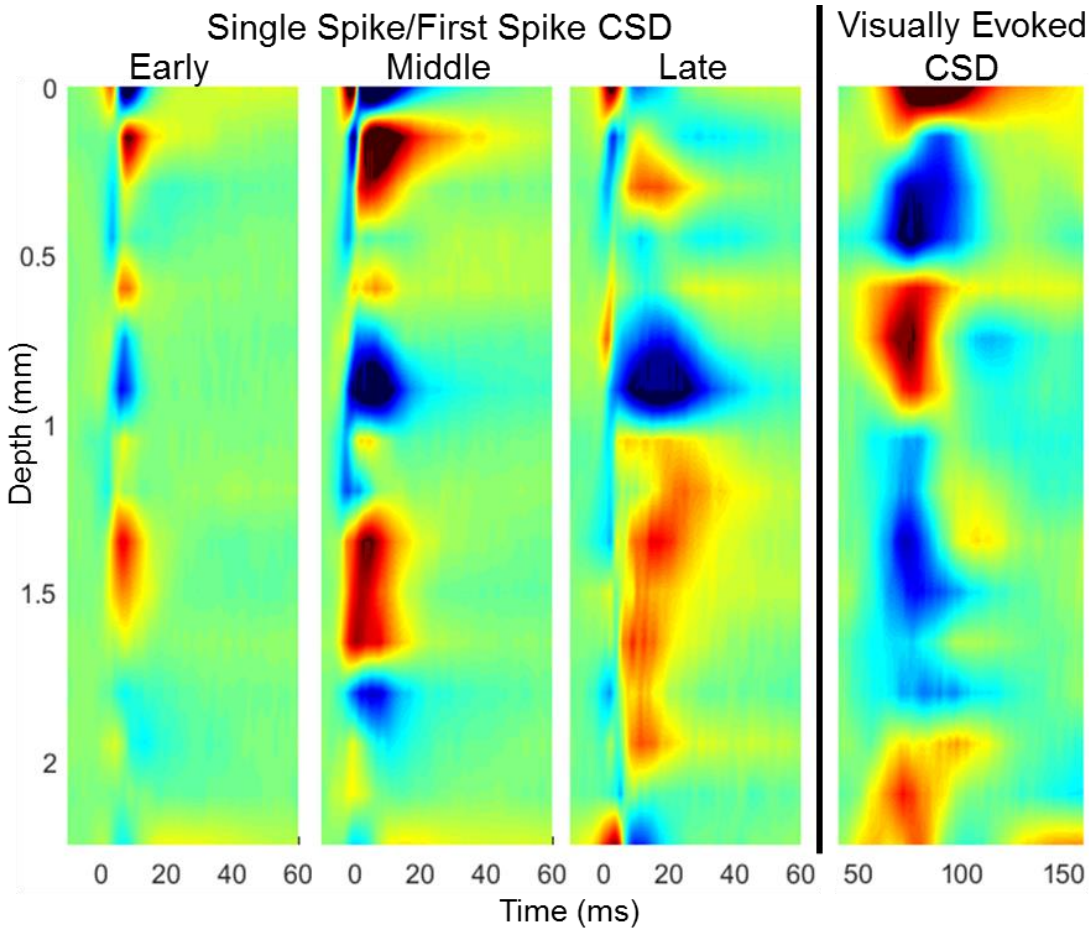

Figure 5.42 Epileptiform Spike and VEP CSD Comparison All CSDs shown above were from one animal, calculated on the same depth array in a constant location. The three on the left are from the first spikes of epileptic events taken from early, middle and late periods in the experiment. The profile on the right was calculated from visual evoked response to the appearance of a drifting grating, averaged over all orientations. The sinks in the visual CSD are thought to mark thalamacortical projections and postsynaptic targets known in the visual pathway. The sinks from seizure activity are in different layers, presumably those that contain large pyramidal cells that are the target of intracortical horizontal connections.

Similarity to Human Epilepsy

The appearance and progression of epileptiform activity in this model were much faster and more consistent than in human epilepsies, but there are many elements of similarity between the two. First, the single spike events are analogous to interictal spikes, both characterized by fast, synchronous discharge often followed by a slower wave. Correlation in humans has been seen between spikes and seizures both spatially and temporally, suggesting a common generator, though the mechanisms relating the two are far from clear (Staley & Dudek 2006; Hufnagel et al. 2000; Karoly et al. 2016). By the time monitoring is performed on patients, their epilepsy has progressed to the point of drug resistance. In order for these seizures to be recognizable on EEG or clinical ECoG electrodes, a comparatively large area of cortex must be involved. The area must then be comprised of either an initially large focus or one that entrained a sizeable network around it over time, enabling spikes to arise in a more diffuse area of cortex. In contrast, the picrotoxin model exhibits spikes solely in the seizure focus, possibly because it is very early in the epileptic process and the surrounding tissue remains predominantly non-epileptic with only limited focus growth.

In the model, polyspikes were very consistent in their shape and timing. In human epilepsy, interictal discharges can take on many morphologies, some of which share characteristics similar to the polyspikes seen in this work. For instance, multiple spike complexes are events that consist of two or more spikes appearing in bursts of variable duration (Niedermeyer 1999a). There has been some evidence that the presence of focal interictal rhythmic discharges like these arise directly from underlying epileptic tissue, such as cortical dysplasia (Gambardella et al. 1996; Noachtar et al. 2008). Periodic lateralized epileptiform discharges (PLEDs) are periodic complexes of spikes or sharp waves followed by a slow wave, typically around 1 Hz, and have a high association with seizures (Pohlmann-Eden et al. 1996). In some patients, these occur with low amplitude rhythmic discharges (PLEDs Plus), giving an appearance similar to polyspikes. PLEDs Plus have been found to have a higher correlation with seizures than those without rhythmic activity (Reiher et al. 1991). Additionally, the results showed that the number of spikes per polyspike typically increased leading up to seizure onset and dropped back down after termination. This pattern of activity buildup is often seen in clinical ECoG monitoring, as PLEDs evolve into PLEDs Plus with increasing duration and eventually a seizure (Litt et al. 1998). An example of this evolution compared to results from the picrotoxin model is shown in Figure 5.43.

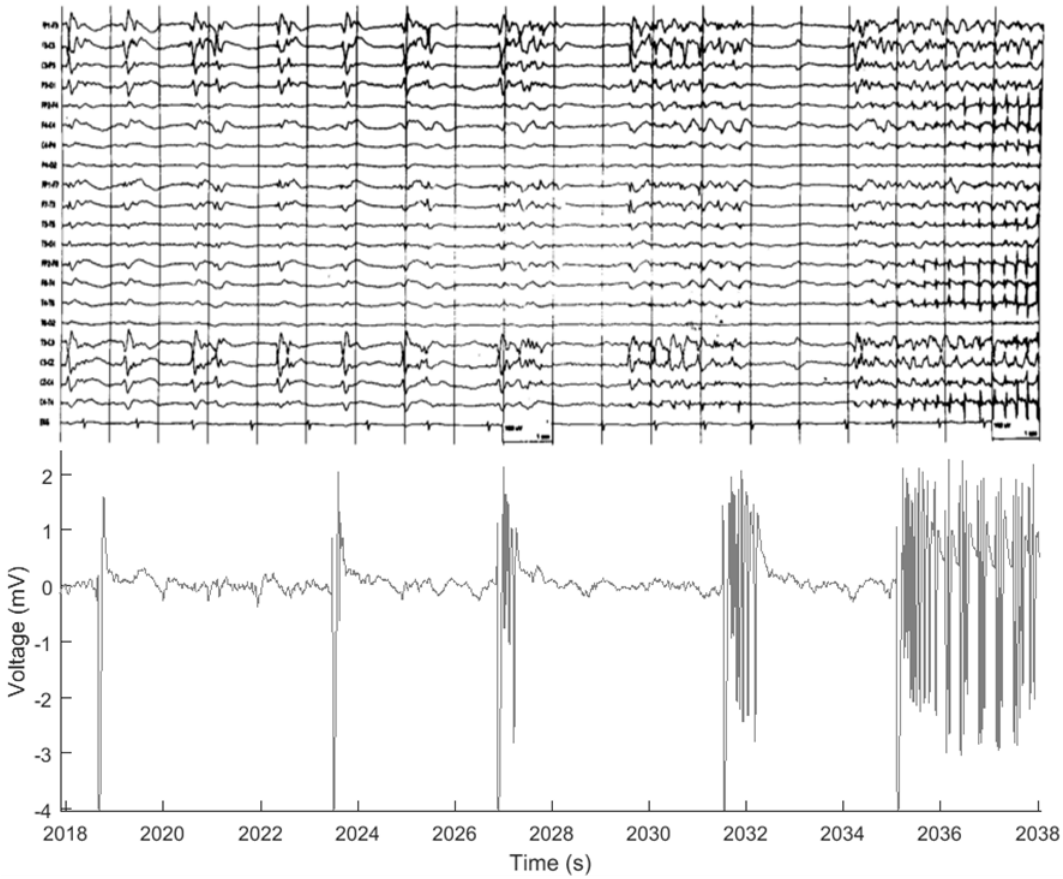

Figure 5.43 Polyspike Evolution to Seizure and Clinical Correlate The top traces are ECoG recordings from a patient with nonconvulsive status epilepticus, showing PLEDs evolve into more complicated PLEDs Plus and eventually a seizure. The bottom trace is from one electrode in the second experiment showing polyspikes with an increasing number of spikes leading to a seizure. The time period of both plots is 20 s. Adapted from (Litt et al. 1998).

The seizures caused by the application of picrotoxin had a very stereotypical response, consisting of rhythmic spiking that slowed down before turning into short bursts of spikes separated by slow wave activity. This electrographic pattern is commonly seen in seizures caused by many different forms of human epilepsies. One common seizure type with similar patterns are tonic-clonic seizures, marked by tonic contraction of muscles in the early phase that evolves into clonic convulsive movements during the late bursts, giving them their name (Dreifuss 1997). Tonic-clonic seizures often generalize, meaning they spread throughout the entire brain, but can occur focally as well (Hamer et al. 2003). An example of a focal tonic-clonic seizure compared to a seizure from the picrotoxin model with similar shape is shown in Figure 5.44. Additionally, our results showed that seizures had much longer post-event delays than single spikes or polyspikes. Clinically, tonic-clonic seizures typically end with a period of postictal electrical silence followed by slow activity (Niedermeyer 1999a). These similarities show that the seizure state is common across subjects and even species, and there are many different paths that can cause a network to fall into it.

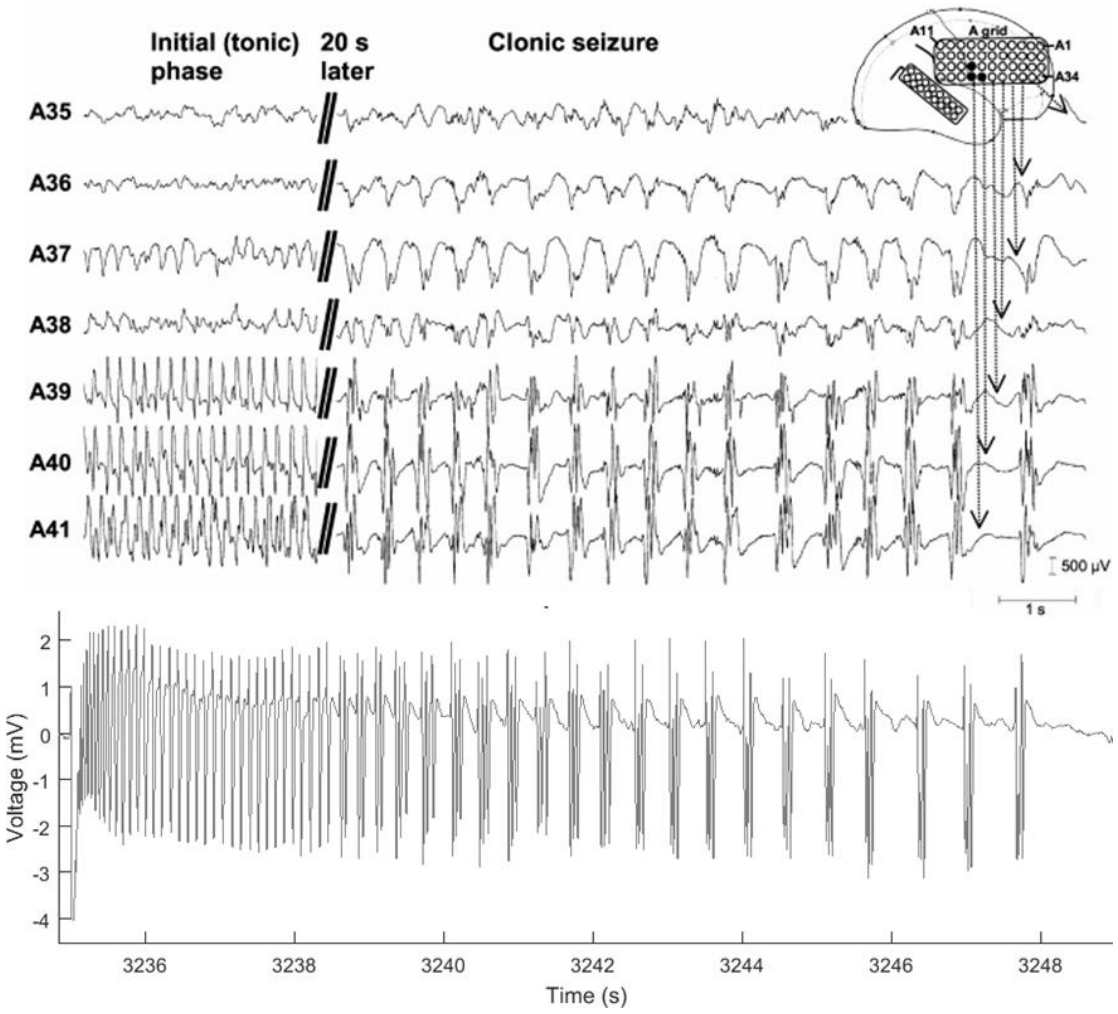

Figure 5.44 Human and Picrotoxin-Induced Seizure Examples The top traces are recordings from subdural clinical macroelectrodes, placed over the fronto-central region as shown in the top right. They show the clear evolution of a tonic-clonic seizure, but it does not generalize. The bottom plot is an example seizure from one electrode in experiment two that also remains focal. There is a similar transition from the fast-spiking tonic phase to slowing clonic bursts. Adapted from (Hamer et al. 2003).

Implications for Epilepsy Diagnosis and Treatment

When the event detector was run over the entire surface grid, at most half of the electrodes detected seizure activity, or a radius of activity of approximately 4 mm. Commonly, clinical macroelectrodes have 1 cm spacing and only ~2 mm exposed contact area (Ad-Tech Medical Instrument Corporation 2005). This spatial resolution could have easily missed full seizures that took place focally in the cortex. Submillimeter seizure-like events, or microseizures, have been seen in human epilepsy using research microelectrodes. They were not seen on the larger contacts and sporadically evolved into clinical seizures (Stead et al. 2010). Often, detections of spikes or polyspikes on the periphery of the focus corresponded to seizures occurring within it, suggesting that interictal events could signal stronger focal events nearby. Also, the low amplitude secondary spikes that built up to seizures could be easily missed with sparser sampling on larger electrodes. These findings suggest a benefit of including well-placed microelectrodes with higher spatial resolution in targeted areas along with current clinical ECoG electrodes. Subclinical seizures and other interictal discharges captured in the seizure onset zone may augment clinical decision-making and shorten the required recording time. Additionally, buildup of interictal spikes may prove to be more common than previously thought (due to low spatial sampling), shedding further light on the pathophysiology of seizure onset

Finding the focus in this model was trivial, as it was marked by large, negative spikes that were not seen elsewhere. In clinical settings, localizing the focus is not nearly as clear due to the spread of seizures over a large area of the cortex and the diffuse presence of spikes. Typically, epileptologists find the electrodes that show the earliest changes preceding a seizure as indicators of the seizure onset zone. The polarity of the signals is not commonly taken into account, possibly because differences between the focus and surround at the level seen in this model are not captured by large clinical grids. Utilizing denser arrays would help better understand the dynamics of seizure and spike generation within a patient, as evidence of inhibitory surround has been seen in humans very similar to that induced by chemoconvulsants in animal models (Schevon et al. 2012). A clearer picture of how epileptic events come about in a patient could both improve localization and reduce the unnecessary resection of healthy tissue.

One interesting observation from the results was that in many of the experiments the growth of the focus occurred preferentially on the medial side of the array, along the interhemispheric fissure. Specifically in experiment five, the picrotoxin injections were between the middle two rows, but the focus extended along the entire bottom (medial)

row and only two electrodes on the top (lateral) row, as seen in Figures 5.29. Electrical stimulation from the same experiment (experiment six in Chapter 4), exhibited similar directionality in response to current applied in the same spot as the picrotoxin injections. Figure 4.6 shows higher amplitude responses on the medial versus lateral edges. The reason for this asymmetrical spread could be due to the shape of the underlying functional areas. Visual stimulation was also performed in the same experiment (ORT4 in Chapter 4), and the differences in visual evoked potential are thought to indicate the underlying boundary between V1 and V2, as seen in Figure 4.4. From that, and the known physiology of the cat visual cortex, it seems the activity is constrained within V1, where the stimuli were applied. Horizontal connections within the cat visual cortex are known to connect neurons with similar response properties, and the properties of cells in V1 generally differ from those in V2. Thus, it makes sense that propagation is along paths with dense intracortical connections. If this is the case, it could add another tool to improve localization for resective surgery in human epilepsy. More rigorous methods would be required to fully map the underlying functional areas, such as functional mapping with higher spatial resolution grids and correlative histology.

Stimulation devices have recently become a viable alternative to resective surgery for the treatment of refractory epilepsy, as detailed in Chapter 2. One type of device directly stimulates the seizure onset zone with electrodes on the cortical surface, often in conjunction with targets in deeper brain structures, in response to detected seizure activity. The results from these devices have shown about a 40% reduction in seizure rate across patients (Morrell 2011). The findings from the picrotoxin model saw the spread of seizure activity in conjunction with deep sinks, presumably in layer V, which is known to be integral in horizontal propagation. The results from Chapter 4 showed that deeper stimulation elicited a stronger response in deep layers, though it was very dependent on the local network architecture. This suggests that direct stimulation of deeper layers could be more effective in disrupting the spread of epileptic events. Although at first glance this would seem more invasive, precision placement of several microelectrodes at millimeter depths could allow for more efficient stimulation with lower currents and less overall tissue contact. These small, targeted electrodes would thus lower the risk of tissue damage from chronic implantation and increase battery life. An alternative would be tailoring surface stimulation to target lower layers based on the underlying network, though more research is required to determine the feasibility of this approach.

Chapter 6 **Conclusions and Future Directions**

Contributions

Epilepsy continues to be a poorly understood disorder that affects millions of people. Patients whose seizures cannot be controlled by medication have a limited number of therapeutic options with relatively low success rates and significant adverse effects. One key to improving outcomes for patients suffering from medically refractory epilepsy is developing new technologies to better map and understand the dynamics of epileptic networks and to use that insight to improve methods to terminate seizures early in their generation. To help reach this goal, this thesis describes new devices created to record epileptiform activity with high spatial and temporal resolution and simultaneously stimulate to modulate these networks. It also analyzes high resolution recordings on the cortical surface and throughout the cortical laminae to elucidate the genesis and spread of seizure activity and how electrical stimulation can play a role in disrupting it.

Chapter 3 presents novel ECoG electrode arrays capable of sampling cortical LFPs with high spatial and temporal resolution. These arrays use flexible on-grid multiplexing and off-grid hardware to record from hundreds of electrodes with a small number of wires. Tests using these arrays in a constrained, *in vivo* seizure model reveal complex spatiotemporal patterns of epileptic activity on the cortical surface that inform and could substantially impact resective surgery. Newer iterations of the arrays and controlling hardware fabricated for this work enable patterned stimulation simultaneous with recording, for future use in responsive neurostimulation testing to terminate seizures. Early research on organic semiconductors as a naturally flexible, biocompatible, low-cost alternative to silicon demonstrates adequate amplification to buffer signals, but require additional improvements in bandwidth and patterning methods to be used in high channel count devices. Finally, the novel transparent graphene electrode arrays we fabricated are capable of recording low-noise electrical signals from the brain simultaneous with optical recording methods, which will allow epileptic networks to be investigated and controlled at cellular resolutions.

In Chapter 4, I performed experiments *in vivo* on healthy feline cortex to investigate the response to visual and electrical stimuli both on the cortical surface and throughout the laminae. The μECoG electrodes used had a high enough spatial resolution to discriminate between functional areas based on visual evoked responses and some could even detect orientation tuning from the surface. There were large differences between responses to the same electrical stimuli across subjects. Even within experiments, the surface response at different angles close to the stimulating electrode were variable, showing that the activation due to electrical stimulation is dependent on the local physiology and is not an isotropic response. Overall, the amplitude of responses on the surface was inversely proportional to the distance from the stimulating electrode, matching with the model of a point source in a conducting medium. This, combined with the fact that many areas that showed a response on the surface had no apparent CSD profile, leads to the conclusion that a large component of the recorded response to stimulation was volume-conducted signal. Additionally, there was a limit seen on the radius of activation caused by electrical stimulation independent of intensity and depth. This agrees with previous theories that electrical microstimulation directly affects a limited region of cortex with little synaptic activation, and increasing stimulation does not increase the area of activation but rather activates more neurons within the affected region.

In Chapter 5, *in vivo* experiments were performed in which a seizure focus was chemically induced in the visual cortex of an otherwise healthy cat and recorded with high density surface and depth electrode arrays. A consistent progression of epileptic events was seen across experiments, starting with single spikes, analogous to interictal spikes in human epilepsy, which evolved into polyspikes with an increasing duration, and finally intermittent seizures. This is a pattern of progression seen in human epilepsy, both in the intensive care unit in disease and in ECoG during seizure generation and status epilepticus. Quantitative characteristics of seizures were distinct from those of polyspikes, and electrographically resembled human seizures. Spatially, the seizure focus was contained within an area that could be missed on clinical macroelectrodes. The presence or lack of inhibitory surround in experiments had no effect on the event evolution, suggesting the breakdown of inhibition within the focus, not in the surrounding tissue, allowed single spikes to give way to polyspikes and seizures. The seizure focus grew slightly over time and was marked by the presence of deeper activity in the CSD, indicating that the recruitment of healthy tissue and subsequent propagation of seizures relies on deep pathways, presumably layer V. Thus, layer V is a promising target for seizure termination devices to stimulate in order to effectively disrupt epileptic spread in the network, either through penetrating electrodes or surface stimulation paradigms designed to modulate this cortical layer.

Future Directions

The results in this thesis yield many insights about the nature of cortical networks in healthy and seizure states, but also raise important questions about the physiology of epileptic networks and its clinical implications. From a clinical aspect, next steps should focus on employing our knowledge of seizure generation and progression from interictal bursts to sustained seizures, and developing the best stimulation paradigms for deterring seizure evolution at the focus site. This might entail mapping propagation pathways and tailoring stimulation to disable layer V neurons from spreading epileptiform activity. An important next experiment, one that would tie together the findings in this thesis, would use stimulation-enabled multiplexed arrays, as well as depth recording electrodes, to determine the optimal parameters and patterns of surface stimulation to reach deep layers. Depth response changes with parameter sweeps of stimulation intensity, pulse width, frequency, polarity and patterns on the surface need to be examined in healthy cortex, to assess its effects on various cortical layers. The results from these parameter sweeps will inform models of the underlying networks to better tailor stimulation to the local physiology. Seizures would then need to be induced to determine the effectiveness of the most promising stimulation parameters on epileptic activity. Depth stimulation would serve as a comparison against which the results from surface stimulation can be measured.

Another logical avenue for immediate future work is determining exactly what mechanisms are responsible for the propagation of seizures from a single focus. There are many experimental paradigms that could further elucidate this question. The most direct would be repeating the experiments performed in this thesis with better-positioned depth electrodes and picrotoxin injections. This would require online analysis of visual evoked potentials to map the functional areas and inject the convulsant near the boundary, testing the theory that the spread of epileptic activity obeys such borders. In these experiments, depth electrodes should be placed at multiple distances along the same path from the injection site, to more clearly analyze growth of discharge generating regions as seizures approach. Most important though, is performing histology on the tissue after the experiment to both verify the functional boundaries and determine the positioning of the depth electrodes in the laminae. Exquisite mapping of circuits with cellular resolution may initially be required to better understand the network neuroscience of seizure generation, which will inform new therapies. Future studies could use multi-unit recording electrodes to uncover cellular activity in the focus, surround or in the thalamus to see if it affects local seizure activity, given evidence of the important role it plays in propagating and terminating generalized seizures. Finally, the transparent graphene

electrodes presented in this work can be employed in conjunction with optical recording techniques, such as optogenetics, to gain a detailed view of the network activity in and around the focal substrate, be it functional, as in my experiments, or structural as well, as in many clinical cases.

My ultimate goal, in embarking on this thesis, was to develop new approaches to aid in the rational design of implantable neurostimulation devices for epilepsy. In that sense, I believe this work has been successful. My findings propose that rigorous, controlled experiments sampling cortical depth and surface *in vivo* will likely yield new implantation and stimulation strategies for seizure monitoring and control. There is a clear need for newer technologies capable of recording and stimulation, both in the depth and surface, to fully contain seizures. The work also suggests that these techniques may be quite useful in other brain-network disorders, with similar challenges. Rather than just being theoretical, the tools required for clinical translation are at hand, and I am hopeful that their application, building on my work, will improve the lives of patients with medically refractory epilepsy, and particularly those who are candidates for implantable, responsive therapeutic devices.

Supplementary Figures

Electrical Stimulation

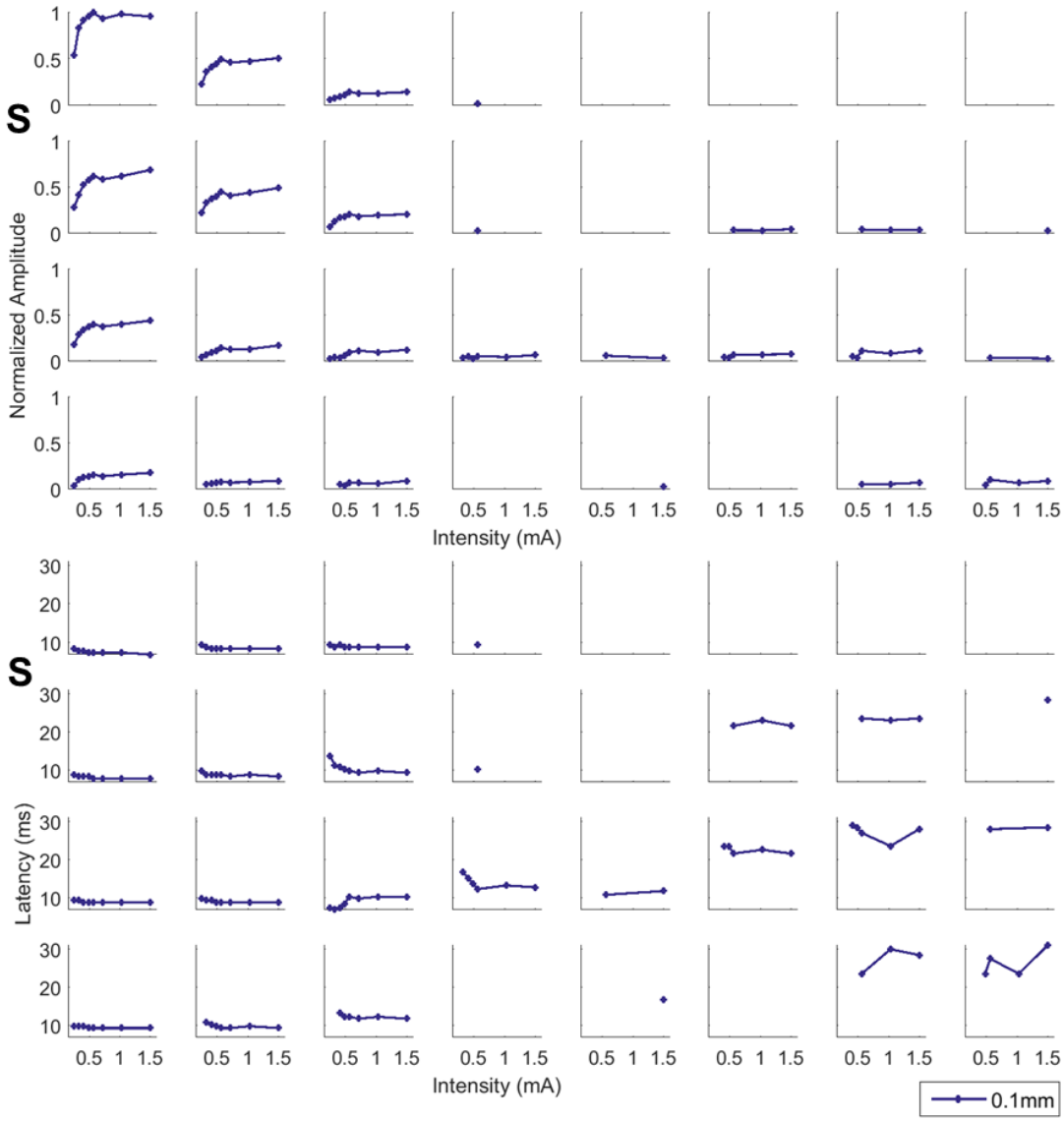

Figure S4.6 Surface Negative Peak Response to Stimulus Intensity Experiment One

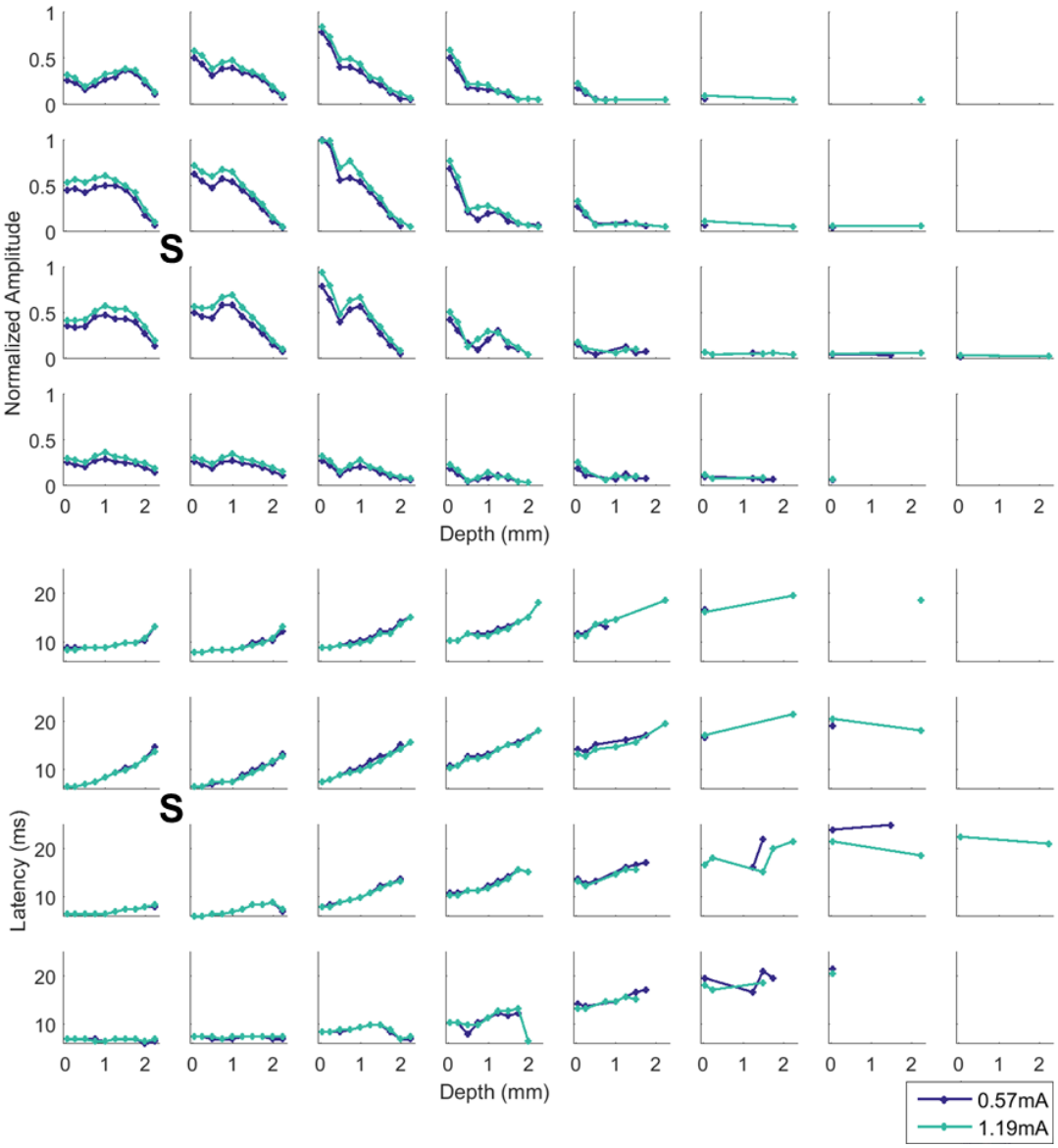

Figure S4.6 Surface Negative Peak Response to Stimulus Intensity and Depth Experiment Two

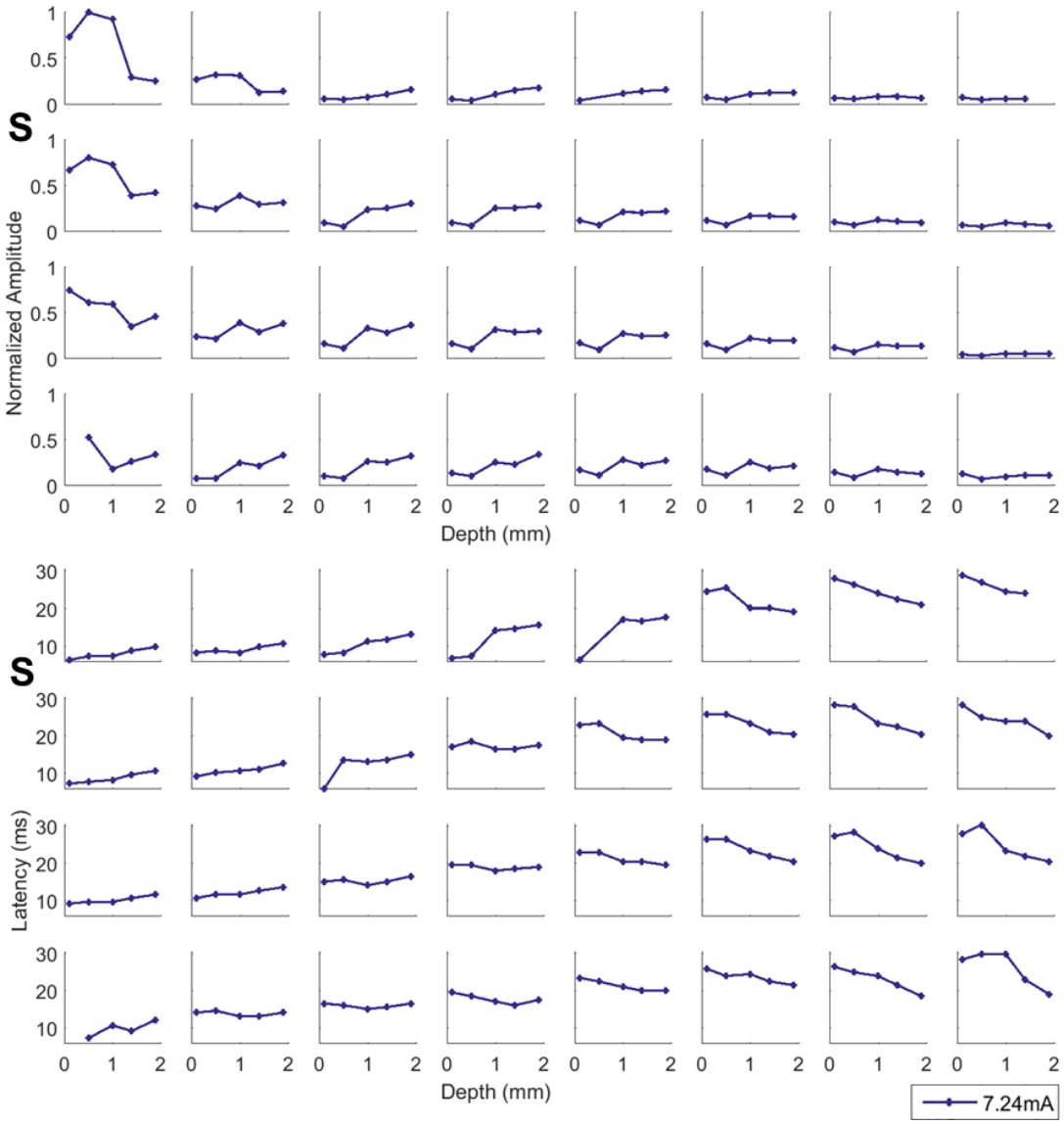

Figure S4.6 Surface Negative Peak Response to Stimulus Depth
Experiment Three

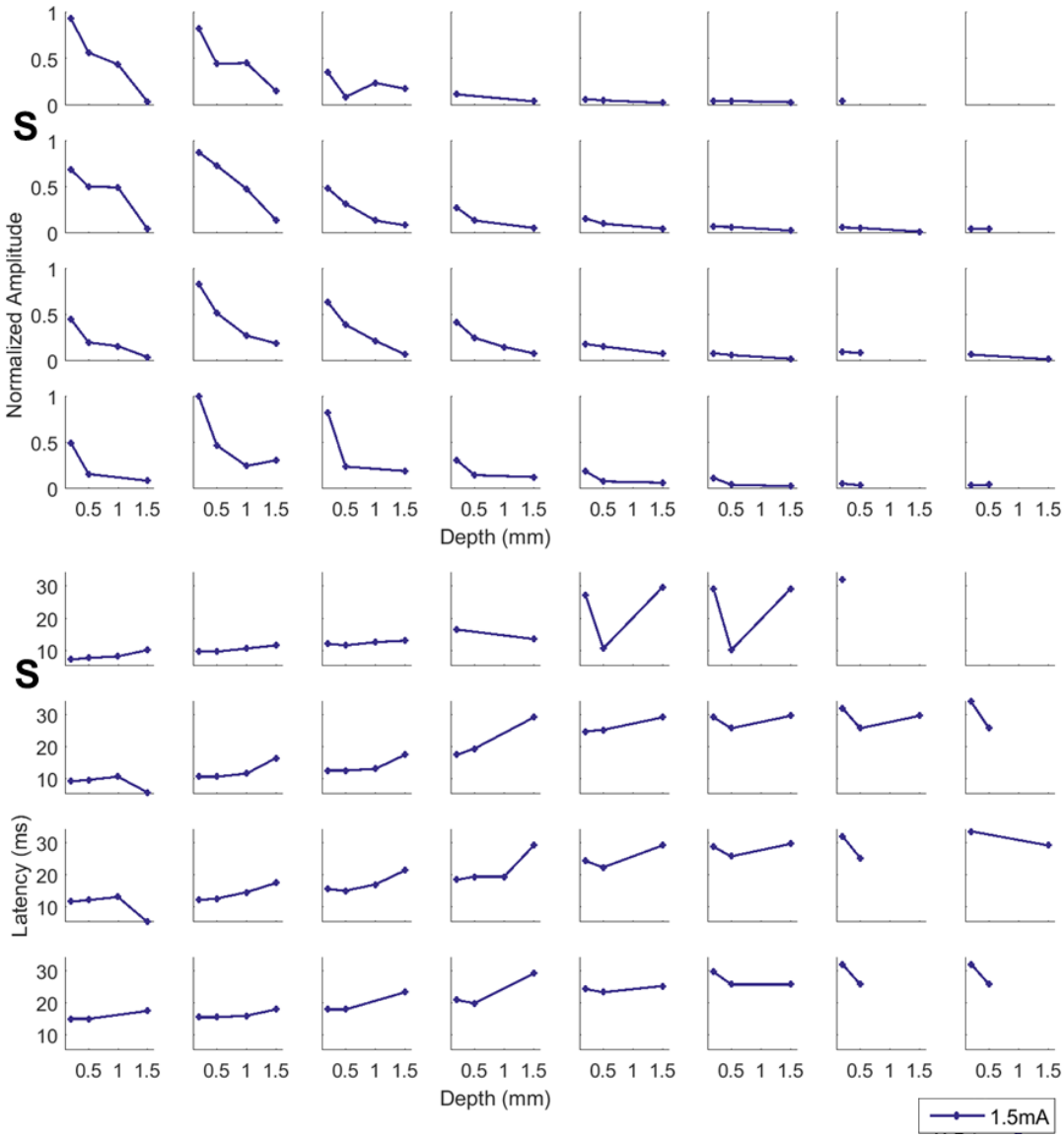

Figure S4.6 Surface Negative Peak Response to Stimulus Depth
Experiment Four

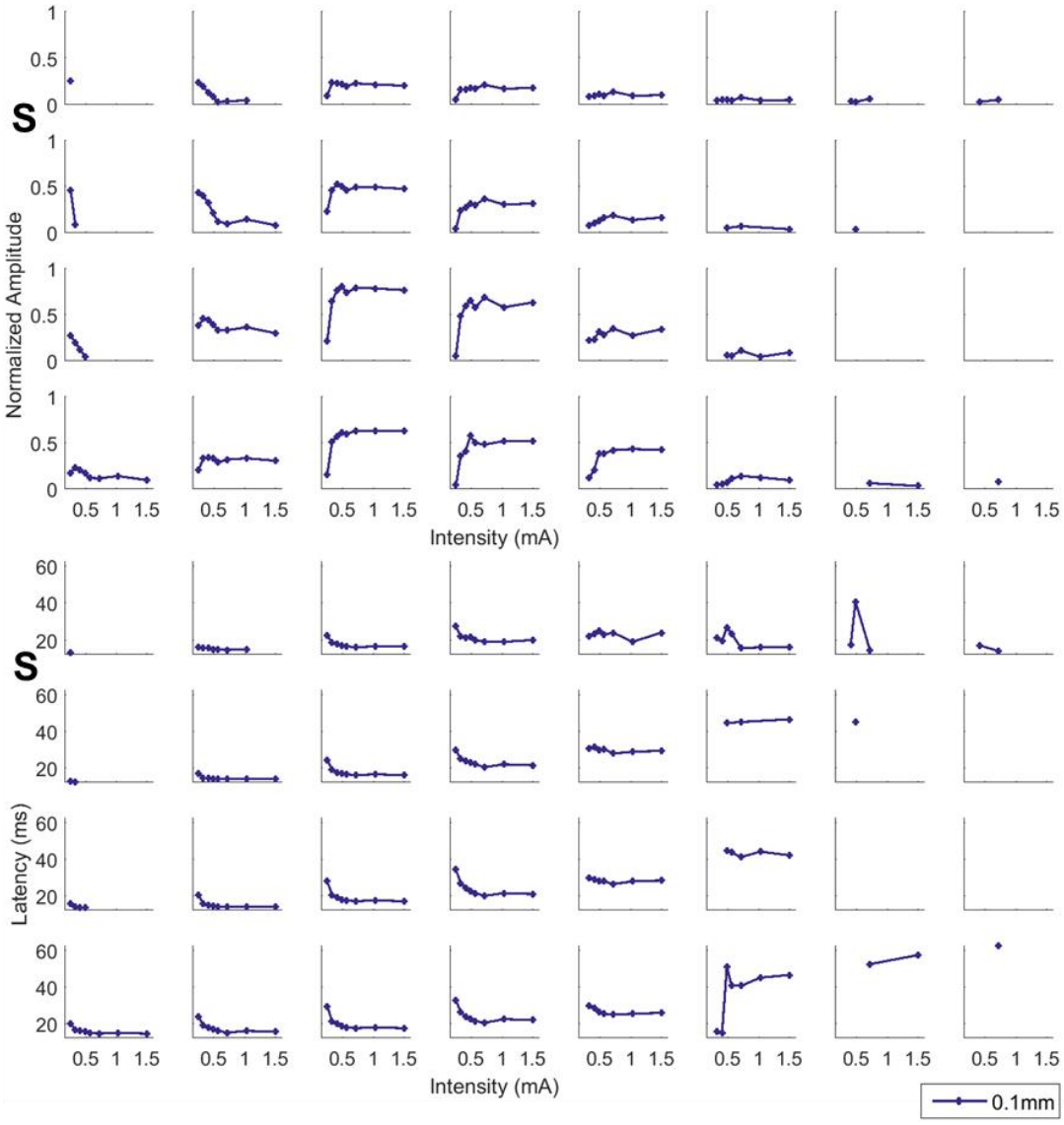

Figure S4.7 Surface Positive Peak Response to Stimulus Intensity
Experiment One

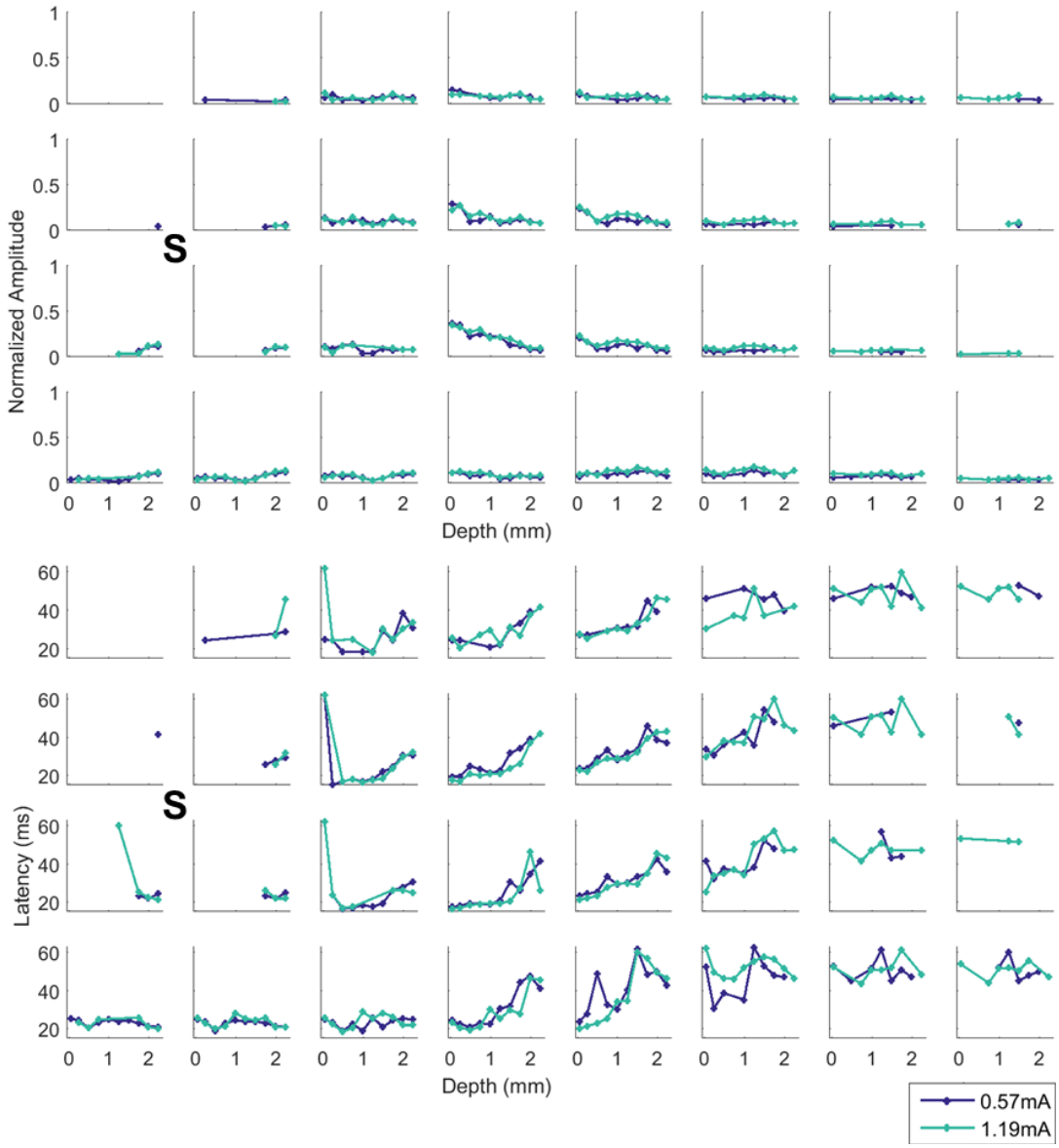

Figure S4.7 Surface Positive Peak Response to Stimulus Intensity and Depth Experiment Two

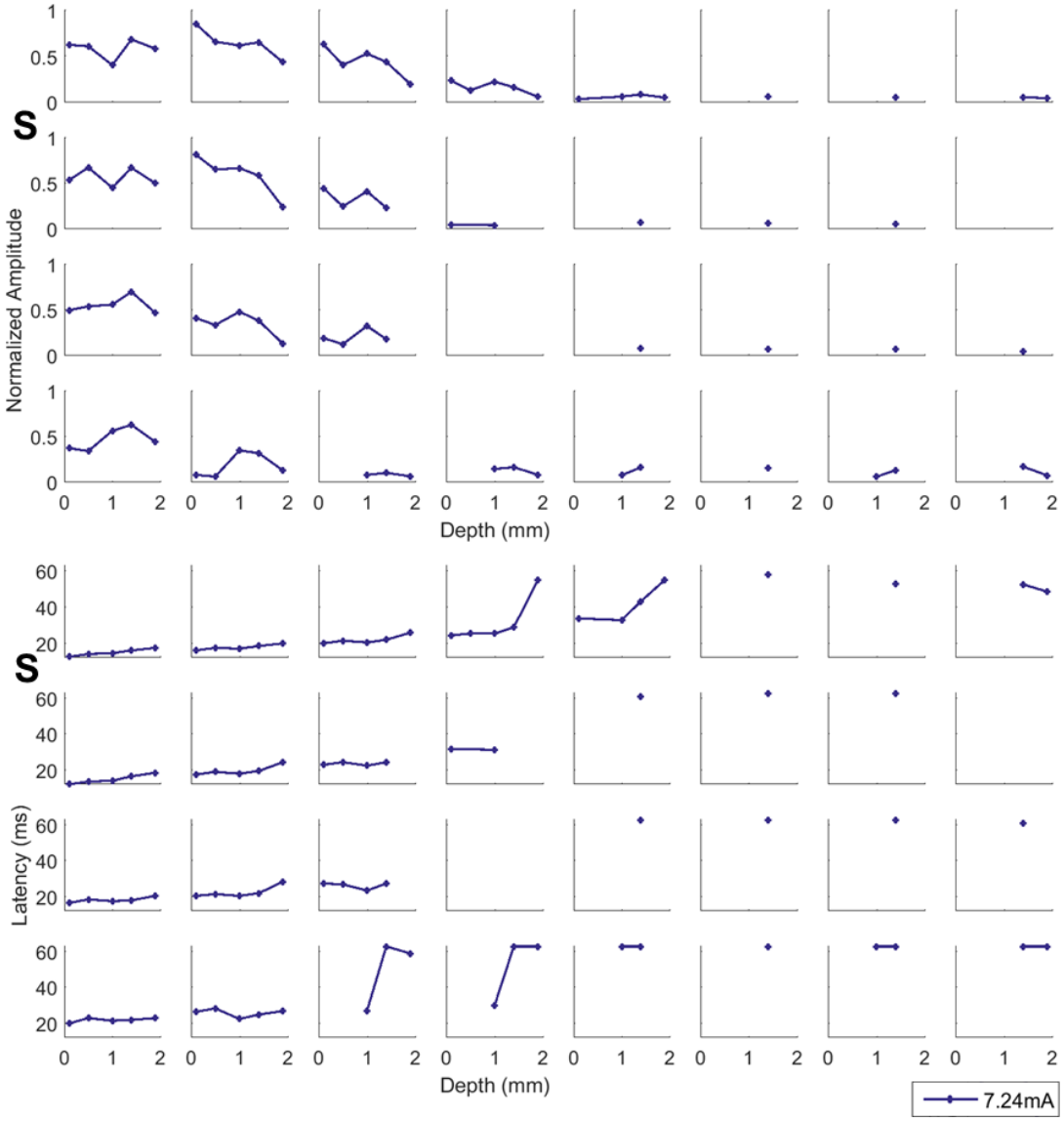

Figure S4.7 Surface Positive Peak Response to Stimulus Depth
Experiment Three

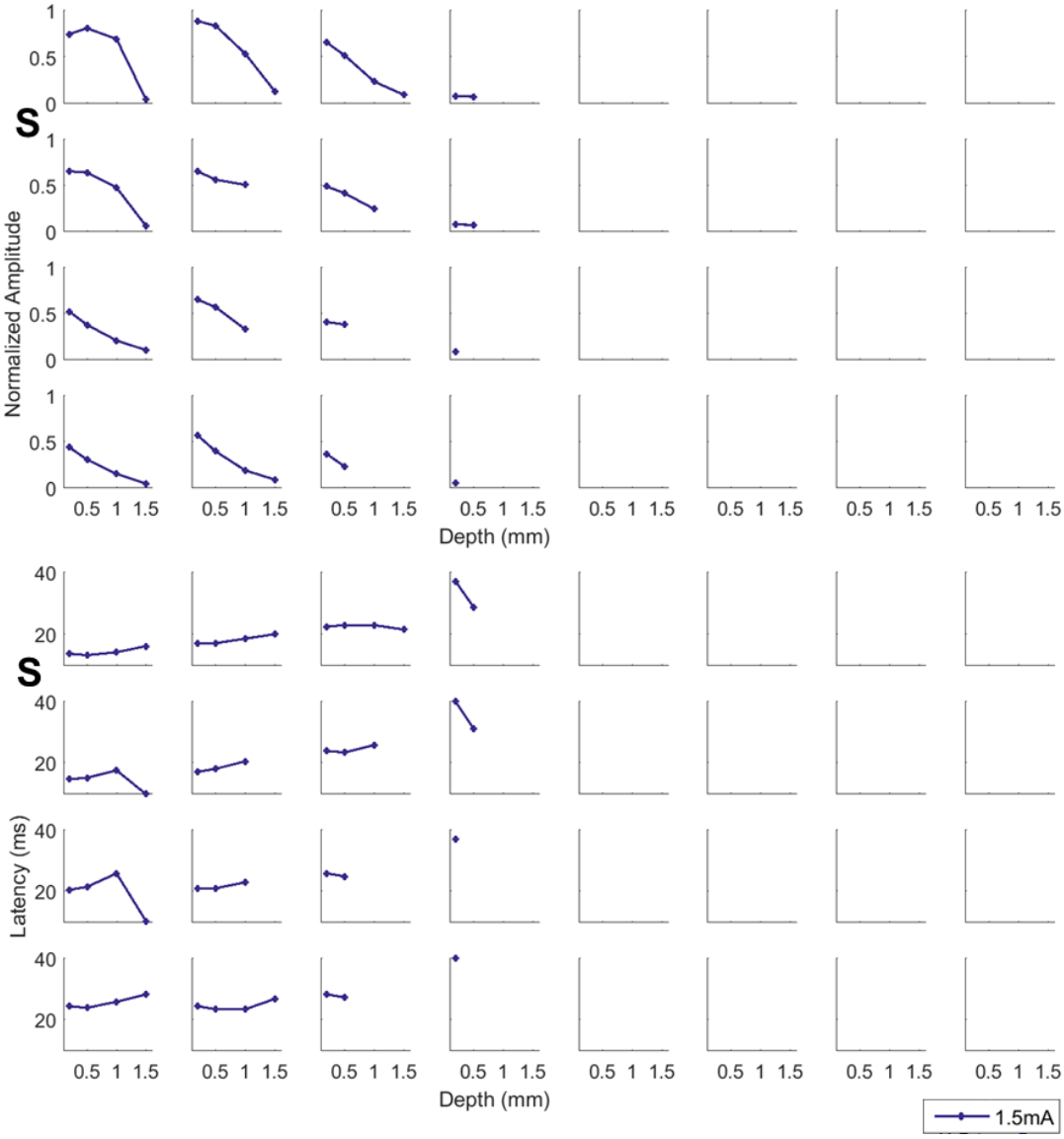

Figure S4.7 Surface Positive Peak Response to Stimulus Depth
Experiment Four

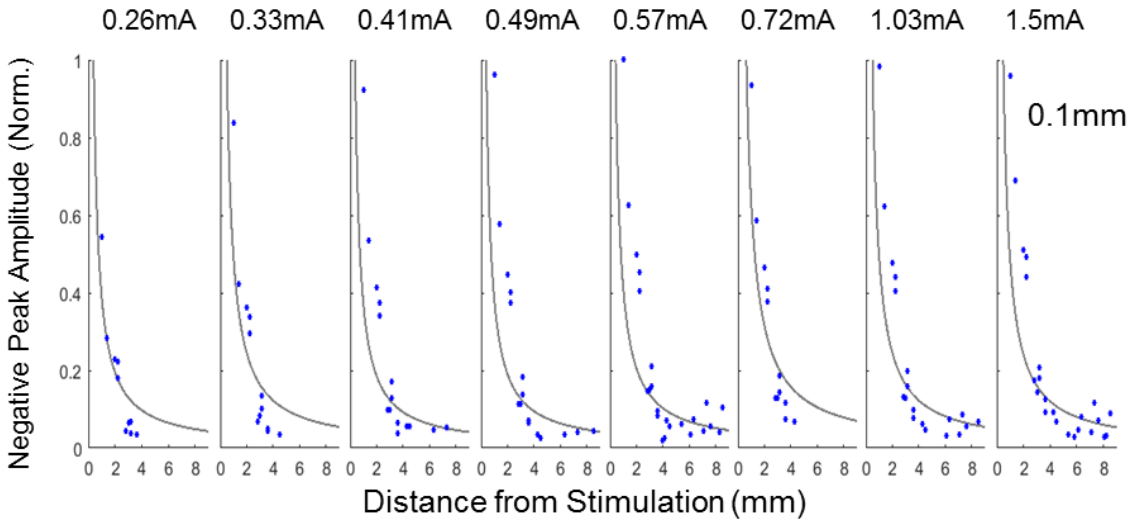

Figure S4.9 Surface Peak Voltage Change with Distance from Stimulation – Experiment One

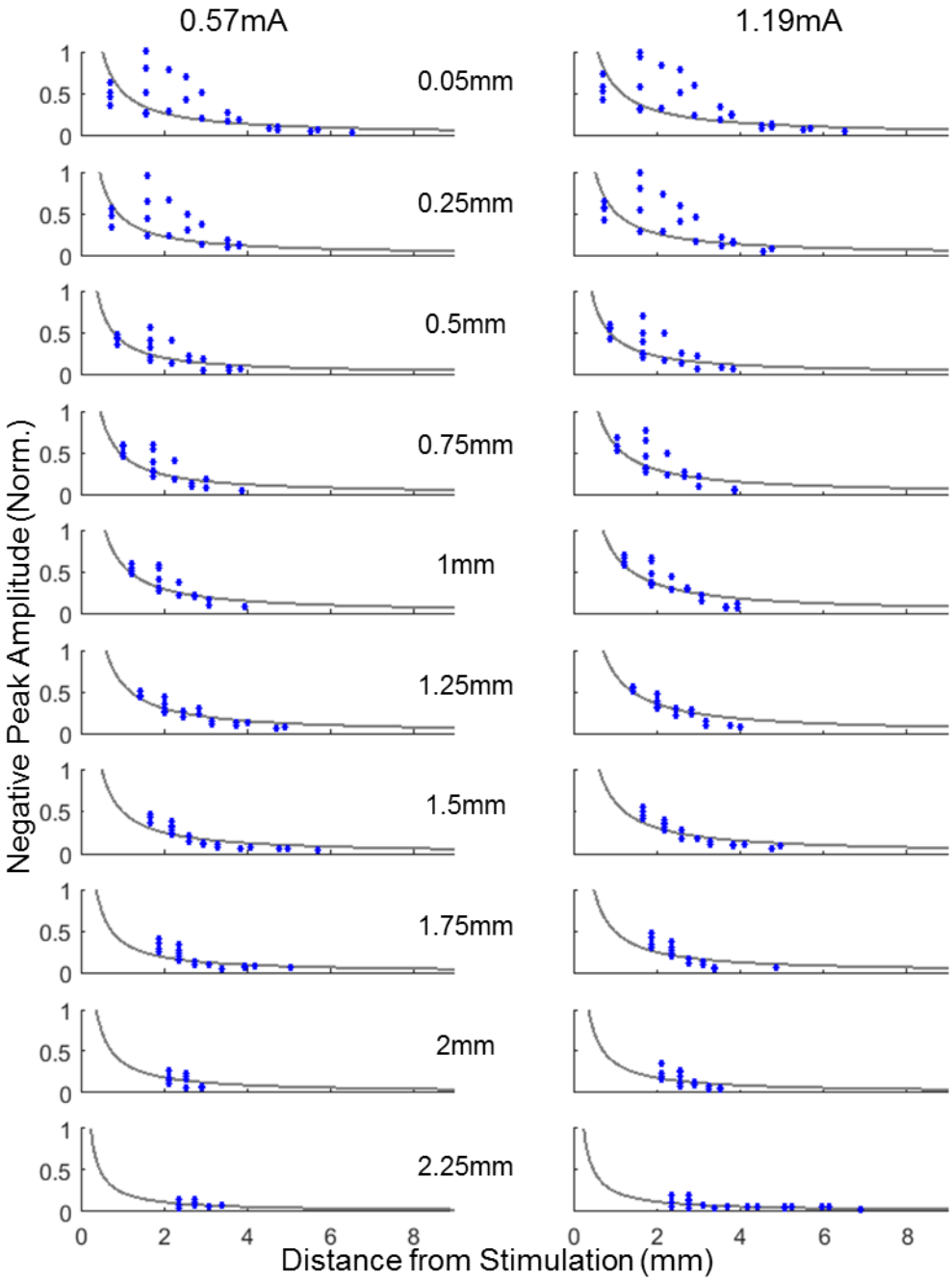

Figure S4.9 Surface Peak Voltage Change with Distance from Stimulation – Experiment Two

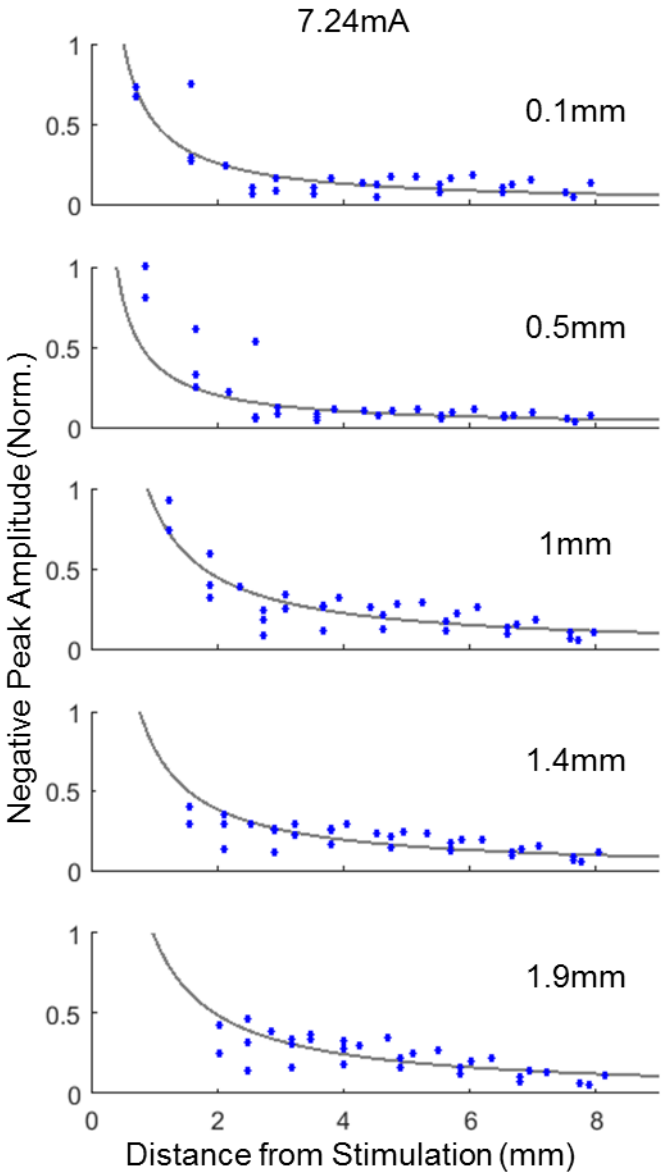

Figure S4.9 Surface Peak Voltage Change with Distance from Stimulation – Experiment Three

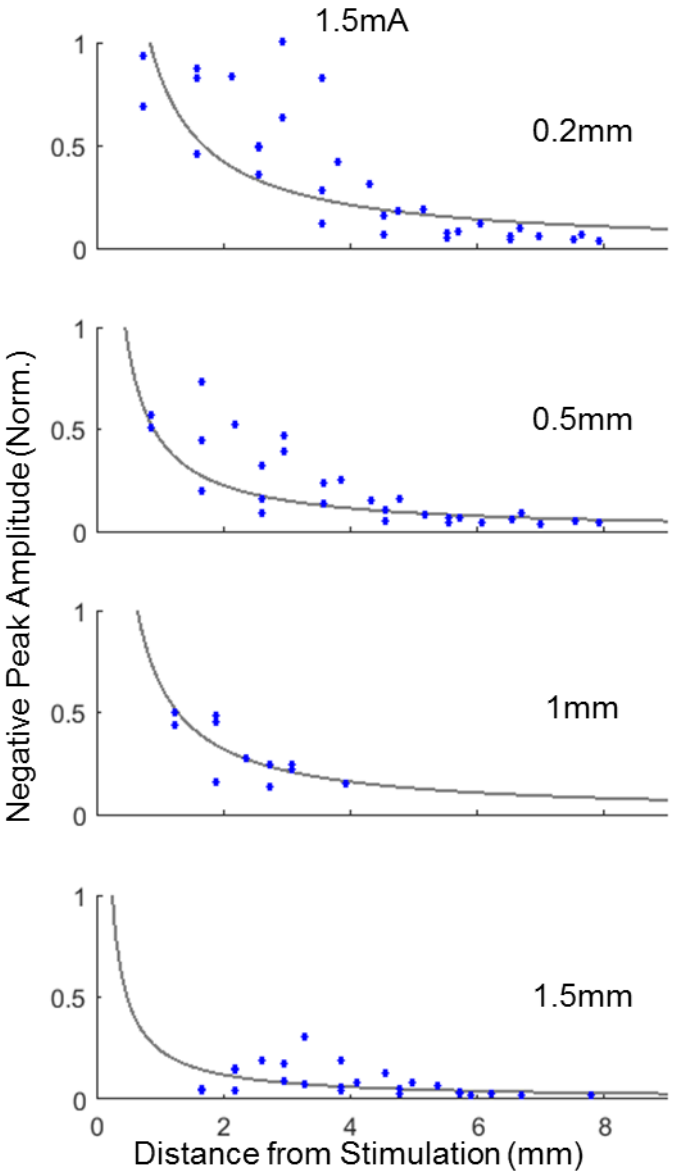

Figure S4.9 Surface Peak Voltage Change with Distance from Stimulation – Experiment Four

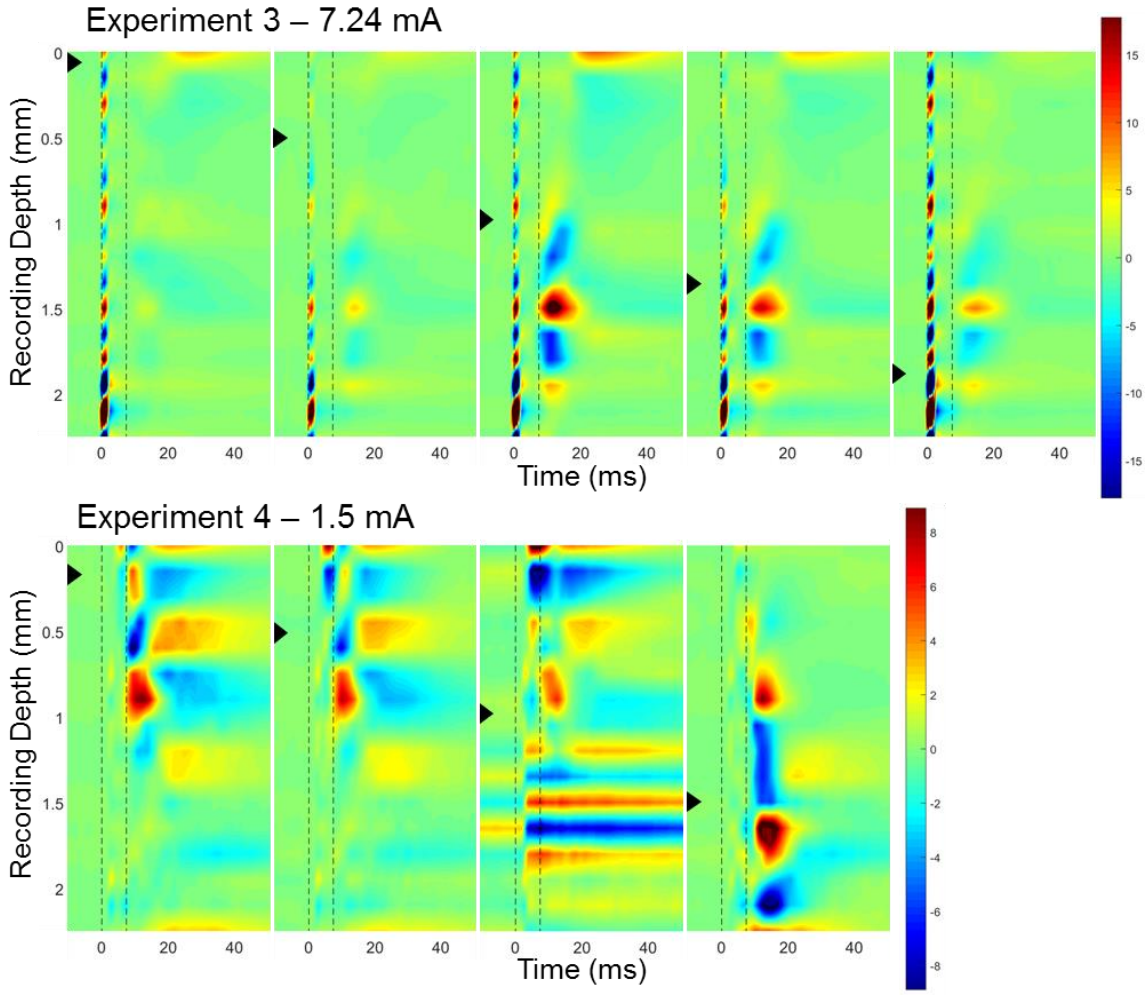

Figure S4.14 CSD Changes with Stimulation Depth – Experiments Three and Four

Seizure Activity

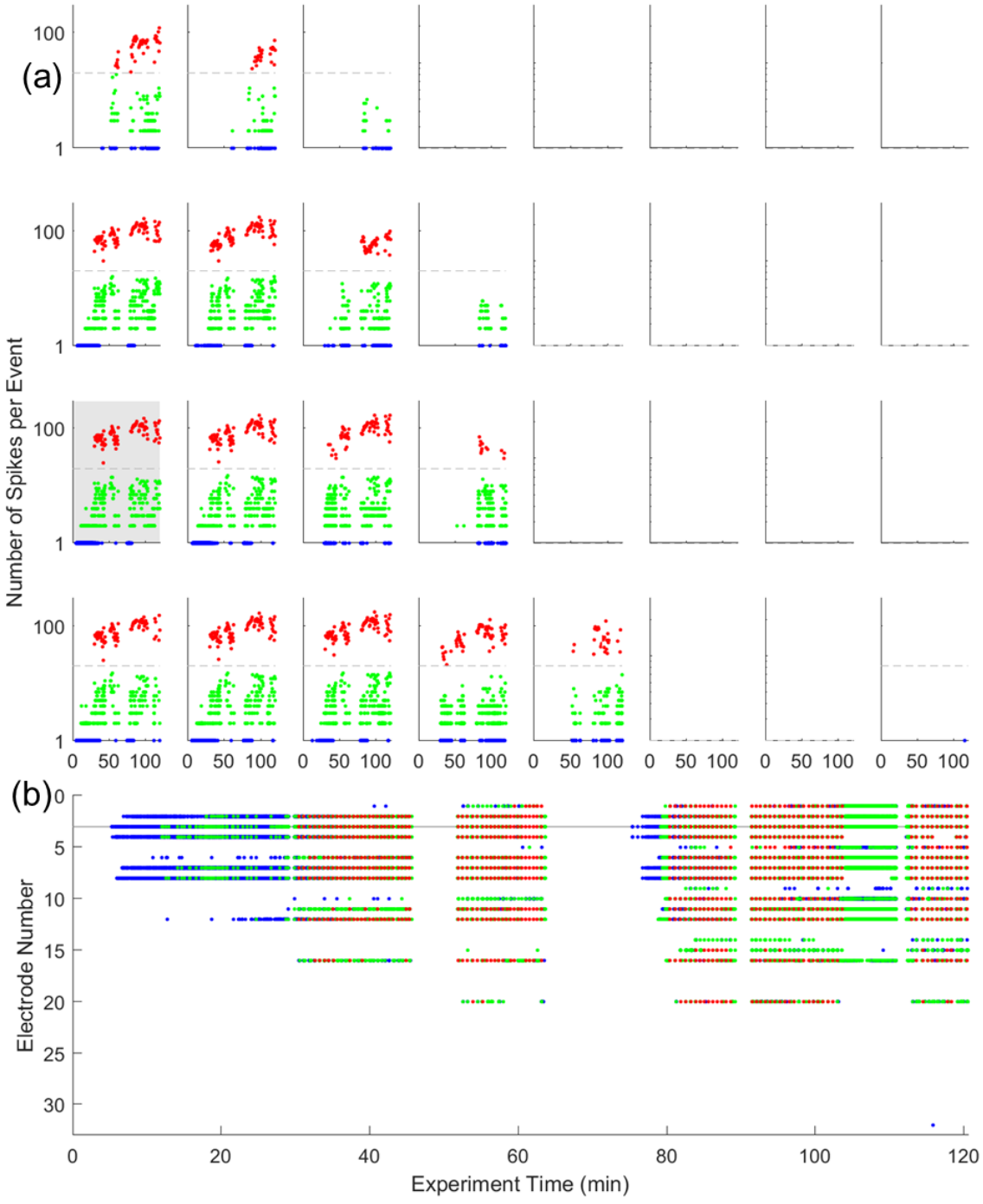

Figure S5.23 Number of Spikes Detected at Each Electrode - Experiment Two

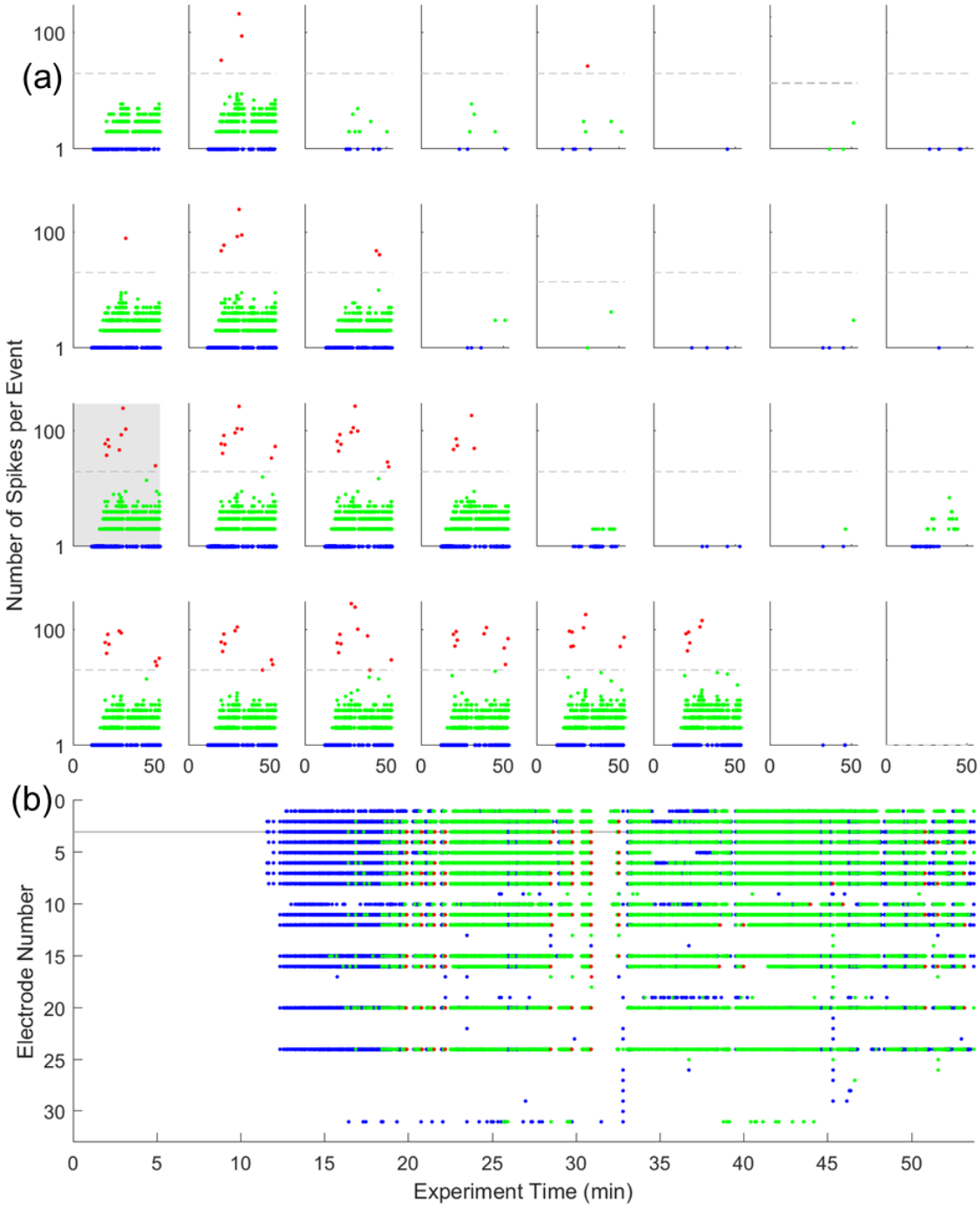

Figure S5.23 Number of Spikes Detected at Each Electrode - Experiment Three

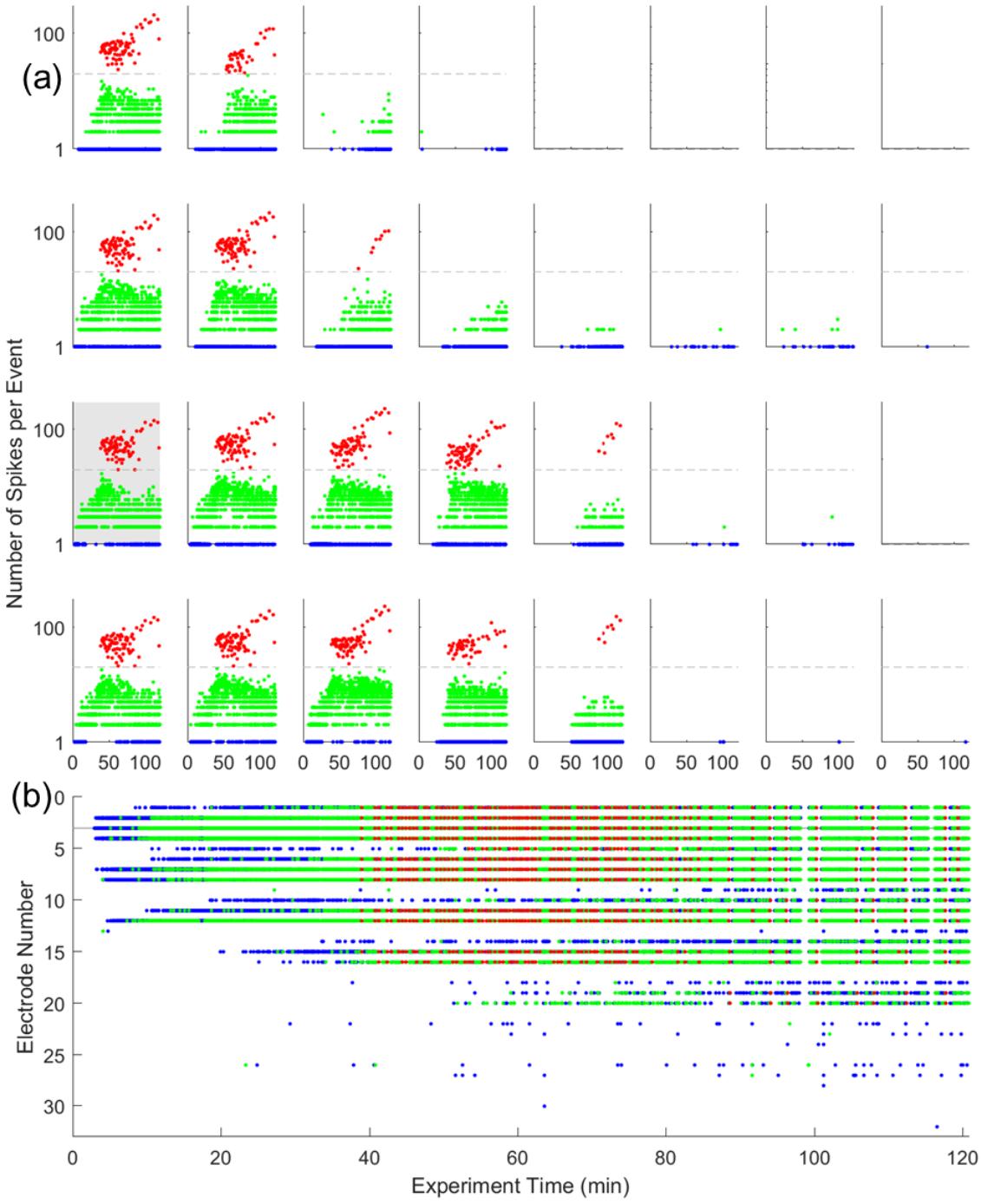

Figure S5.23 Number of Spikes Detected at Each Electrode - Experiment Four

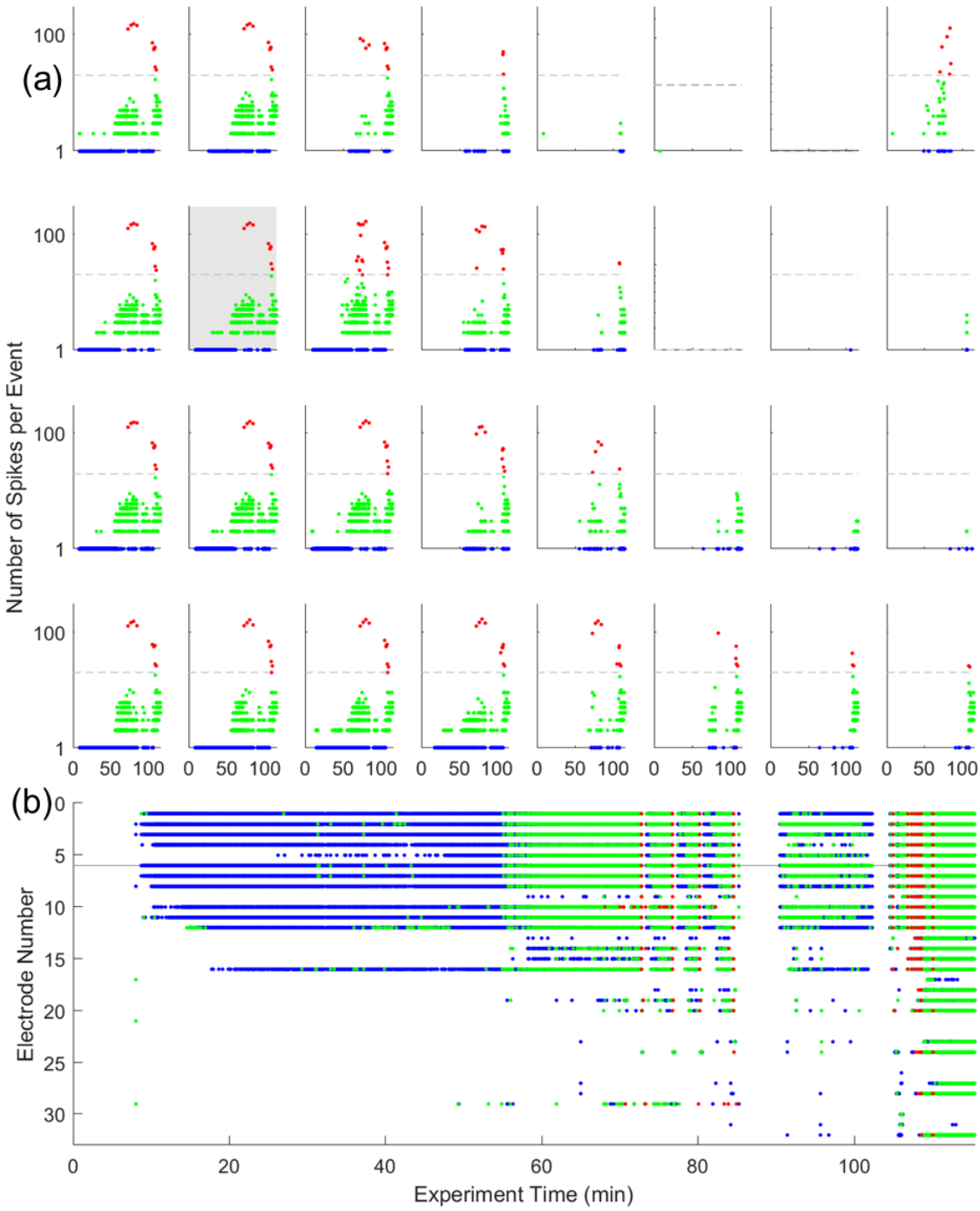

Figure S5.23 Number of Spikes Detected at Each Electrode - Experiment Five

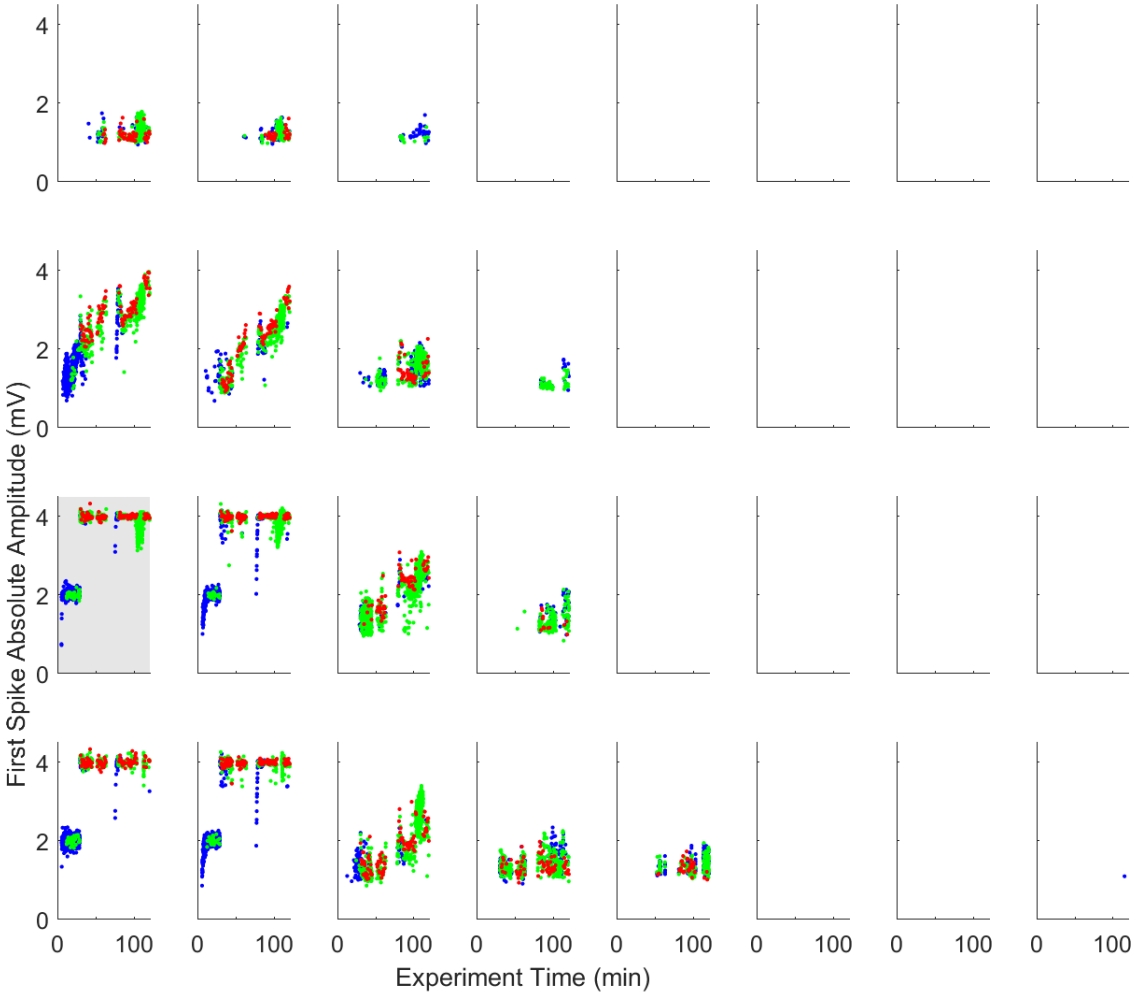

Figure S5.24 First Spike Amplitude of Detected Events at Each Electrode - Experiment Two

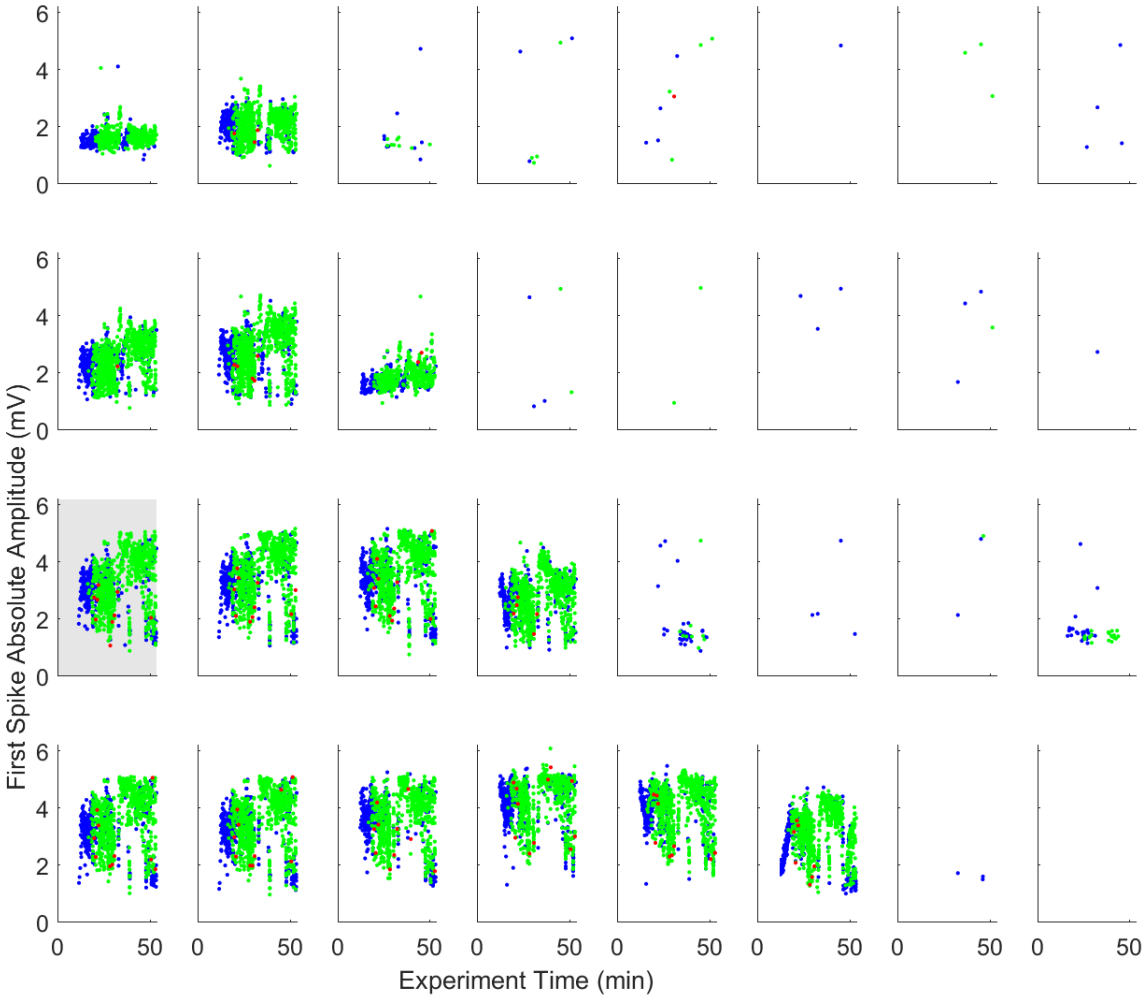

Figure S5.24 First Spike Amplitude of Detected Events at Each Electrode - Experiment Three

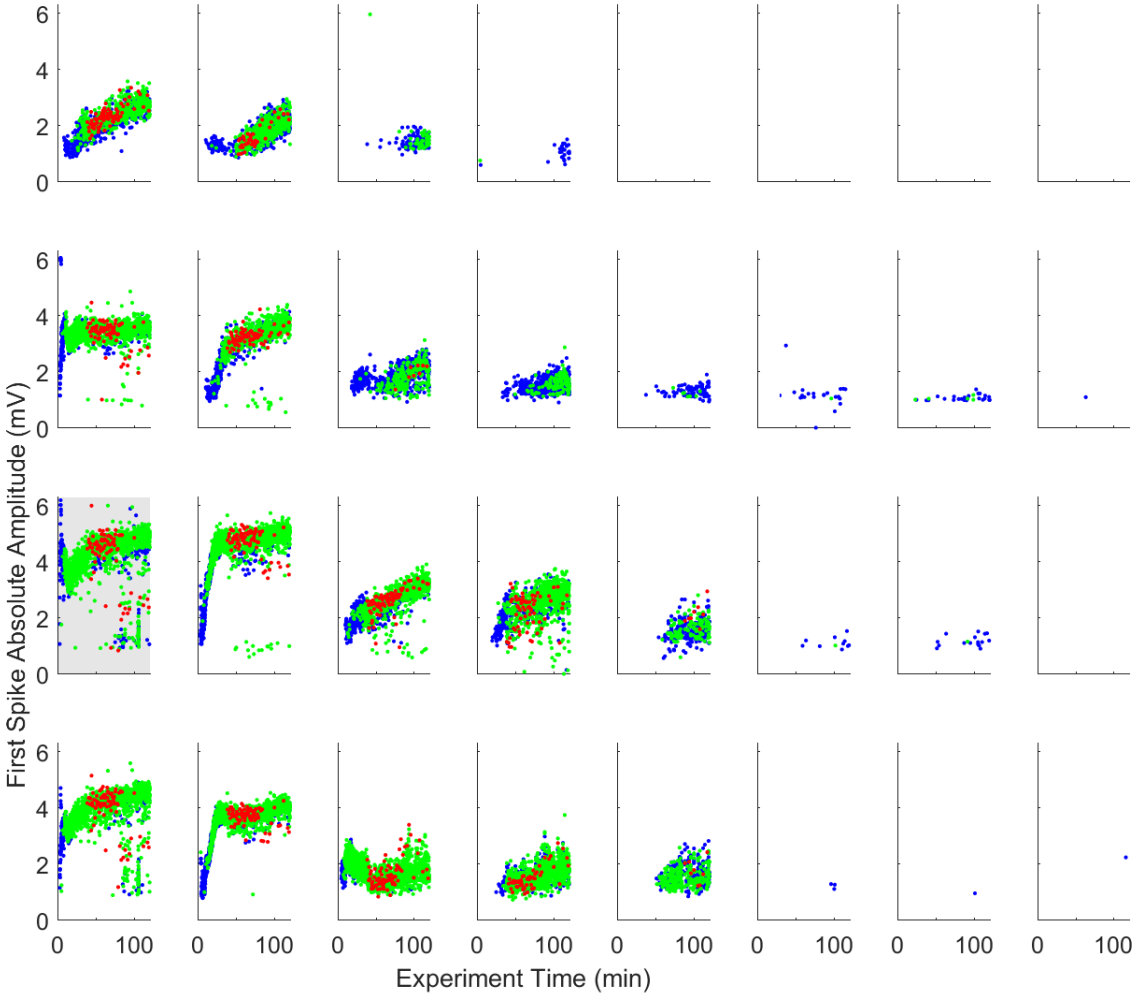

Figure S5.24 First Spike Amplitude of Detected Events at Each Electrode - Experiment Four

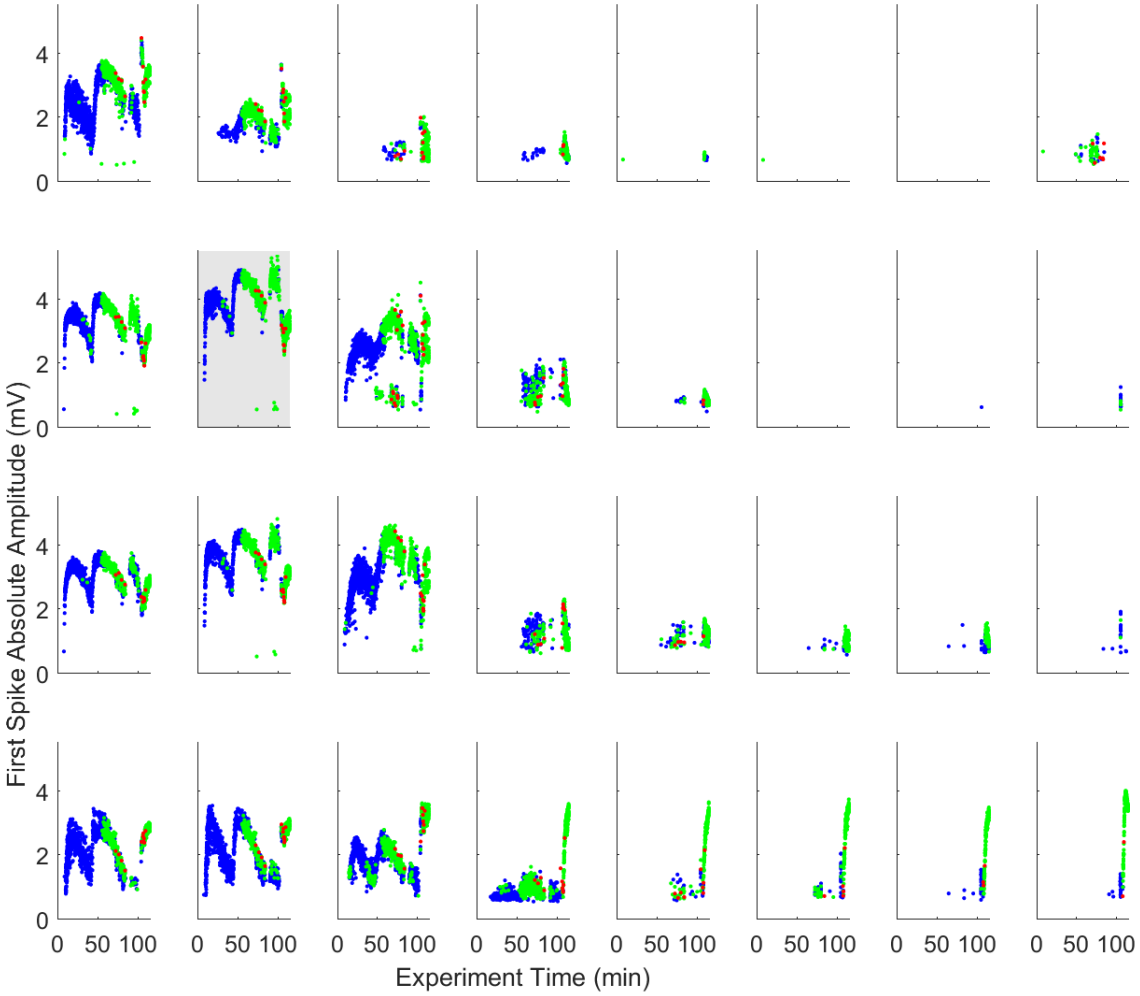

Figure S5.24 First Spike Amplitude of Detected Events at Each Electrode - Experiment Five

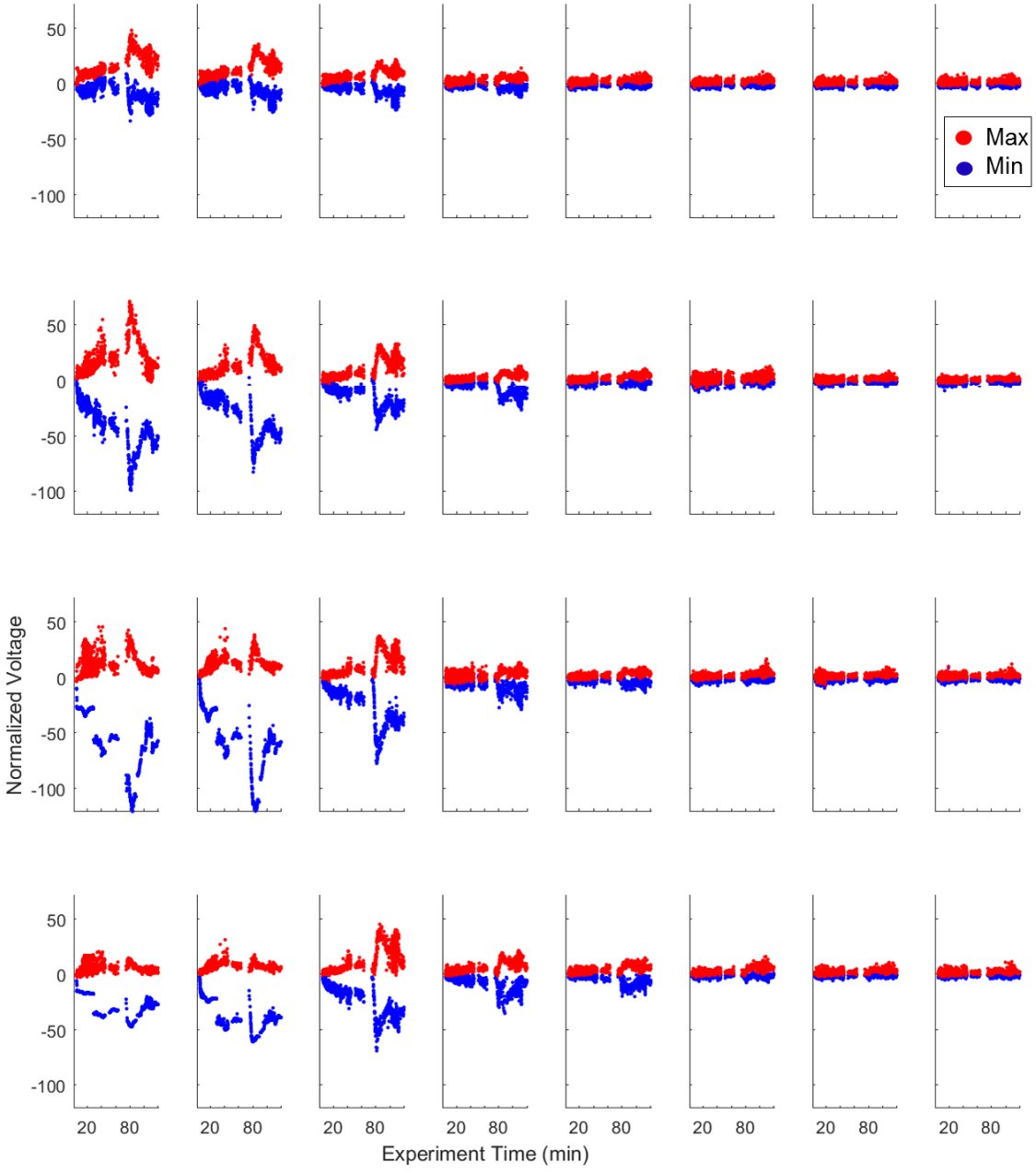

Figure S5.31 Maximum and Minimum Amplitude of First Spikes - Experiment Two

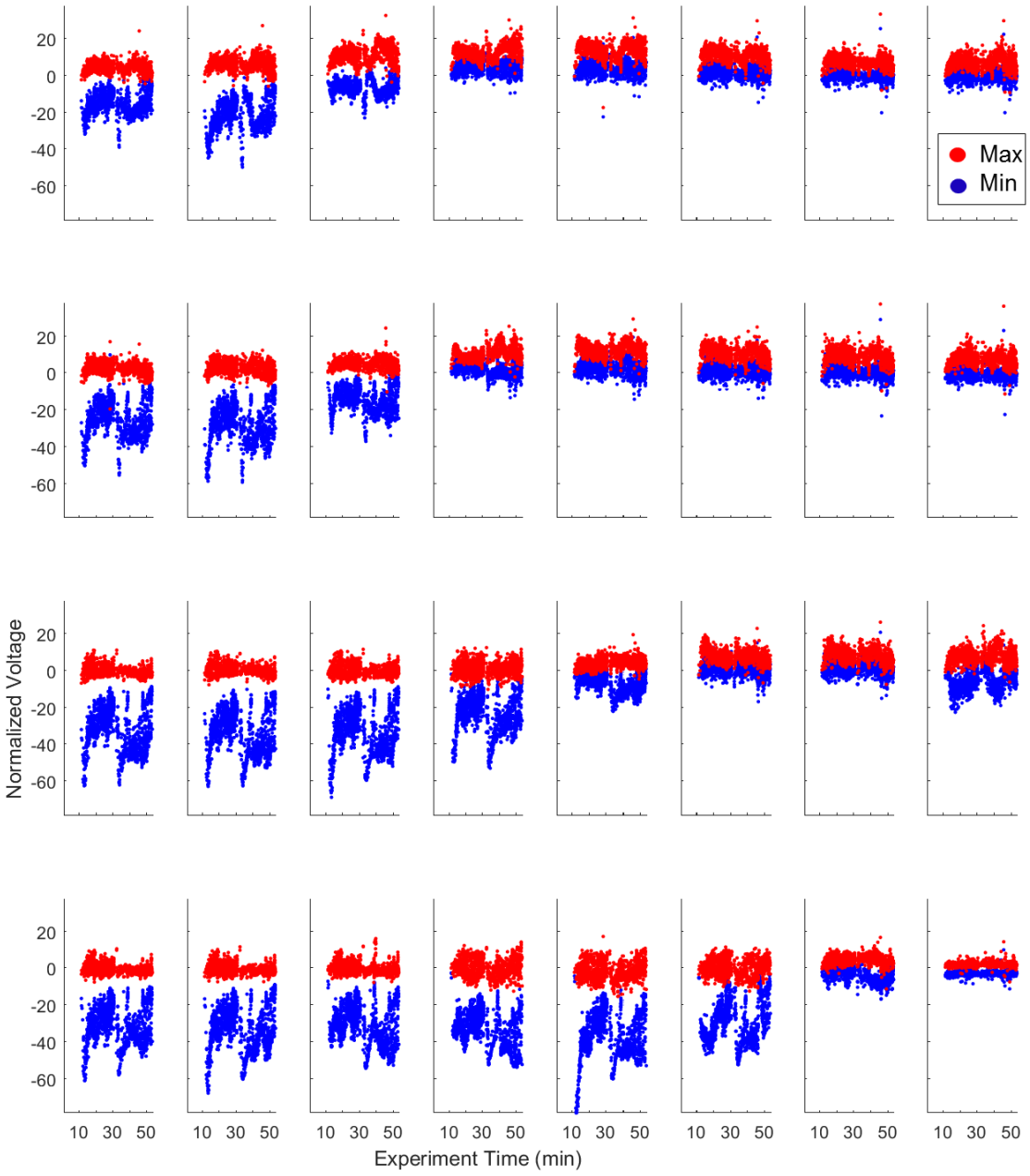

Figure S5.31 Maximum and Minimum Amplitude of First Spikes - Experiment Three

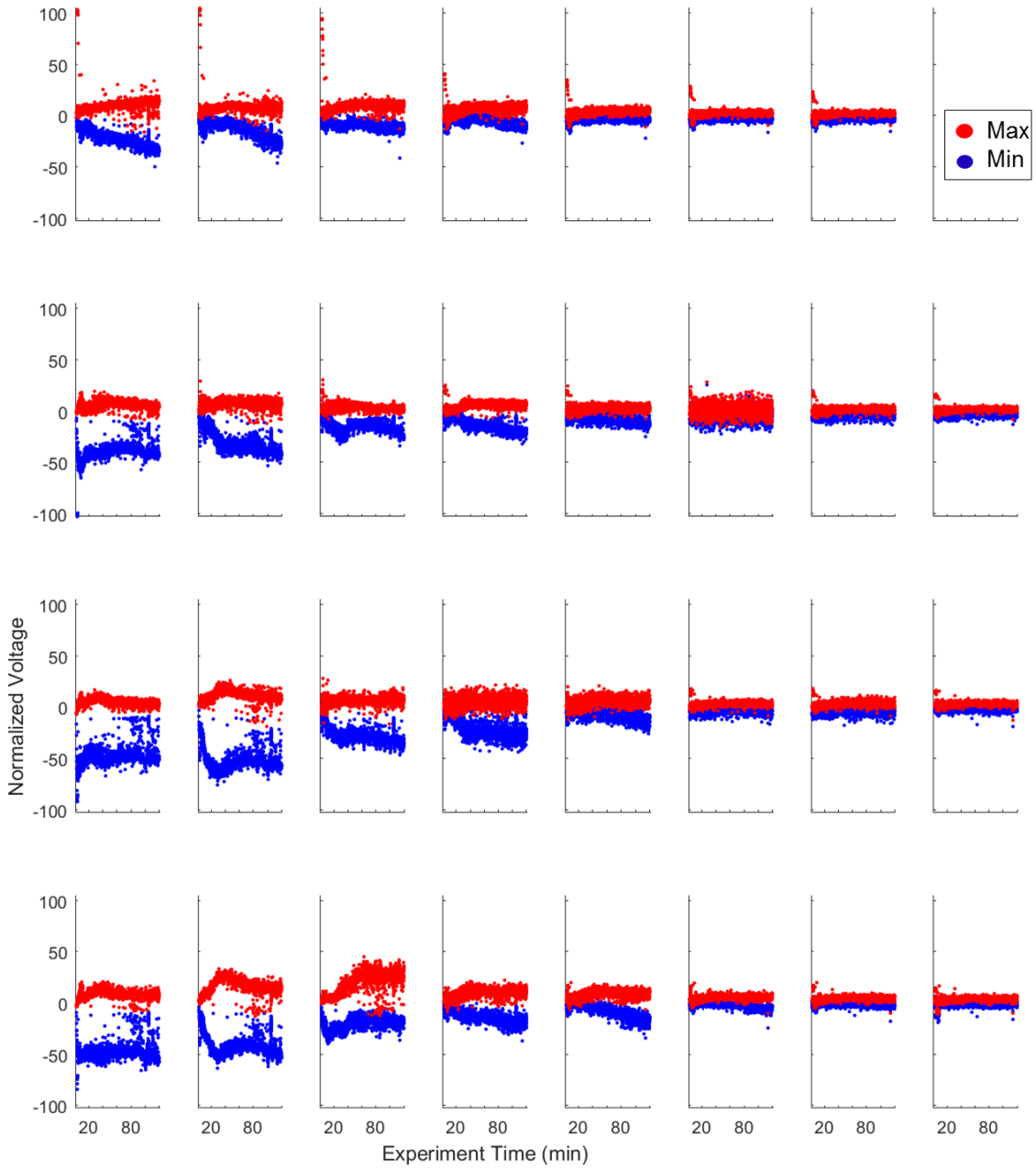

Figure S5.31 Maximum and Minimum Amplitude of First Spikes - Experiment Four

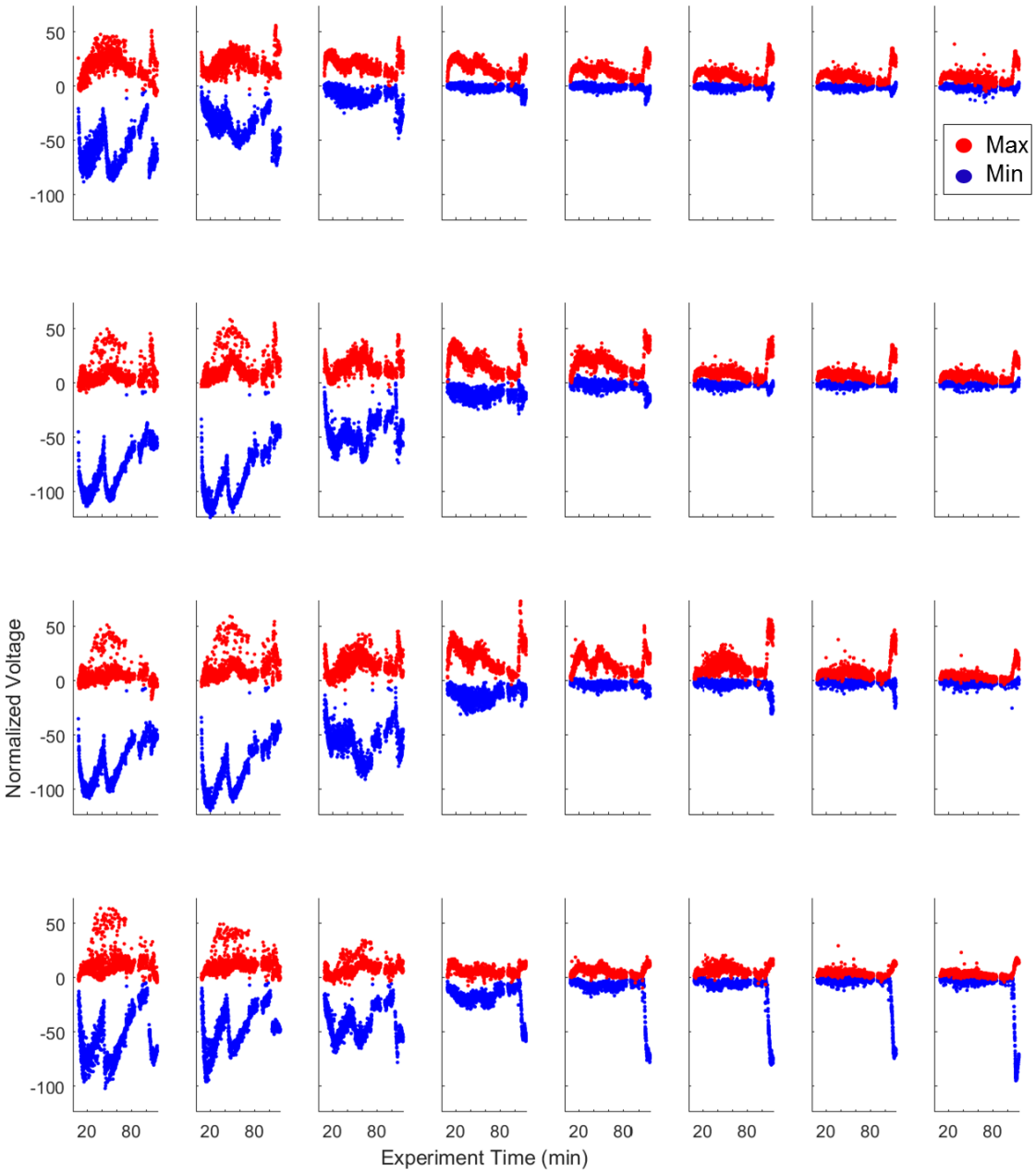

Figure S5.31 Maximum and Minimum Amplitude of First Spikes - Experiment Five

References

Ad-Tech Medical Instrument Corporation, 2005. Epilepsy & Neurosurgery Product Guide.

Afzali, A., Dimitrakopoulos, C.D. & Breen, T.L., 2002. High-performance, solution-processed organic thin film transistors from a novel pentacene precursor. *Journal of the American Chemical Society*, 124(30), pp.8812–3.

Anderson, W.S. et al., 2007. Studies of stimulus parameters for seizure disruption using neural network simulations. *Biological Cybernetics*, 97(2), pp.173–94.

Barth, D.S. & Sutherling, W., 1988. Current source-density and neuromagnetic analysis of the direct cortical response in rat cortex. *Brain Research*, 450(1-2), pp.280–94.

Berens, P. et al., 2008. Comparing the feature selectivity of the gamma-band of the local field potential and the underlying spiking activity in primate visual cortex. *Frontiers in Systems Neuroscience*, 2(2).

Berg, A.T. et al., 2008. Outcome measures. In J. Engel & T. A. Pedley, eds. *Epilepsy: A Comprehensive Textbook*. Philadelphia: Lippincott Williams & Wilkins, pp. 1929–1937.

Bergey, G.K. et al., 2015. Long-term treatment with responsive brain stimulation in adults with refractory partial seizures. *Neurology*, 84(8), pp.810–817.

Bink, H. et al., 2011. Flexible organic electronics for use in neural sensing. In *Engineering in Medicine and Biology Society, EMBC, 2011 Annual International Conference of the IEEE*. IEEE, pp. 5400–5403.

Bink, H., Wagenaar, J.B. & Viventi, J., 2013. Data acquisition system for high resolution, multiplexed electrode arrays. *International IEEE/EMBS Conference on Neural Engineering, NER*, pp.1001–1004.

Bishop, G.H. & Clare, M.H., 1953. Responses of cortex to direct electrical stimuli applied at different depths. *Journal of Neurophysiology*, 16(1), pp.1–19.

Blanche, T.J. et al., 2005. Polytrodes: High-density silicon electrode arrays for large-scale multiunit recording. *Journal of Neurophysiology*, 93, pp.2987–3000.

Bonhoeffer, T. & Grinvald, A., 1991. Iso-orientation domains in cat visual cortex are arranged in pinwheel-like patterns. *Nature*, 353(6343), pp.429–431.

Bonhoeffer, T. & Grinvald, A., 1993. The layout of iso-orientation domains in area 18 of cat visual cortex: Optical imaging reveals a pinwheel-like organization. *The Journal of Neuroscience*, 13(10), pp.4157–80.

Borchers, S. et al., 2012. Direct electrical stimulation of human cortex - the gold standard for mapping brain functions? *Nature Reviews. Neuroscience*, 13(1), pp.63–70.

Bronzino, J.D., 2014. Principles of electroencephalography. In J. D. Bronzino & D. R. Peterson, eds. *Biomedical Engineering Fundamentals*. CRC Press, pp. 47–1 – 47–12.

Butson, C. & McIntyre, C.C., 2008. Current steering to control the volume of tissue activated during deep brain stimulation. *Brain Stimulation*, 1(1), pp.7–15.

Butson, C.R. & McIntyre, C.C., 2006. Role of electrode design on the volume of tissue activated during deep brain stimulation. *Journal of Neural Engineering*, 3(1), pp.1–8.

Buzsáki, G., Anastassiou, C.A. & Koch, C., 2012. The origin of extracellular fields and currents - EEG, ECoG, LFP and spikes. *Nature Reviews. Neuroscience*, 13(6), pp.407–20.

Chagnac-Amitai, Y. & Connors, B.W., 1989. Horizontal spread of synchronized activity in neocortex and its control by GABA-mediated inhibition. *Journal of Neurophysiology*, 61(4), pp.747–758.

Chang, H.-T., 1951. Dendritic potential of cortical neurons produced by direct electrical stimulation of the cerebral cortex. *Journal of Neurophysiology*, 14(1), pp.1–21.

Chun, H., Lehmann, T. & Yang, Y., 2010. Implantable stimulator for bipolar stimulation without charge balancing circuits. *2010 Biomedical Circuits and Systems Conference (BioCAS)*, pp.202–205.

Constandinou, T. & Georgiou, J., 2008. A partial-current-steering biphasic stimulation driver for vestibular prostheses. *IEEE Transactions on Biomedical Circuits and Systems*, 2(2), pp.106–113.

Contreras, D. & Steriade, M., 1995. Cellular basis of EEG slow rhythms: A study of dynamic corticothalamic relationships. *The Journal of Neuroscience*, 15(1), pp.604–622.

De Curtis, M. & Avanzini, G., 2001. Interictal spikes in focal epileptogenesis. *Progress in Neurobiology*, 63(5), pp.541–567.

Dichter, M. & Spencer, W.A., 1969a. Penicillin-induced interictal discharges from the cat hippocampus. I. Characteristics and topographical features. *Journal of Neurophysiology*, 32(5), pp.649–662.

Dichter, M. & Spencer, W.A., 1969b. Penicillin-induced interictal discharges from the cat hippocampus. II. Mechanisms underlying origin and restriction. *Journal of Neurophysiology*, 32(5), pp.663–687.

Dreifuss, F.E., 1997. Classification of epileptic seizures. In J. Engel & T. Pedley, eds. *Epilepsy: A Comprehensive Textbook*. Lippincott -Raven, pp. 517–524.

Engel, A.K. et al., 2005. Invasive recordings from the human brain: clinical insights and beyond. *Nature Reviews. Neuroscience*, 6(1), pp.35–47.

Engel, J. & Pedley, T., 2008. Introduction: What is epilepsy? In J. Engel & T. Pedley, eds. *Epilepsy: A Comprehensive Textbook*. Philadelphia: Lippincott Williams & Wilkins, pp. 1–7.

Escabi, M.A. et al., 2014. A high-density, high-channel count, multiplexed ECoG array for auditory-cortex recordings. *Journal of Neurophysiology*, 112(6), pp.1566–1583.

Fisher, R. et al., 2010. Electrical stimulation of the anterior nucleus of thalamus for treatment of refractory epilepsy. *Epilepsia*, 51(5), pp.899–908.

Foutz, T.J. & McIntyre, C.C., 2010. Evaluation of novel stimulus waveforms for deep brain stimulation. *Journal of Neural Engineering*, 7(6), p.066008.

Fridley, J. et al., 2012. Brain stimulation for the treatment of epilepsy. *Neurosurgical Focus*, 32(3).

Gambardella, A. et al., 1996. Usefulness of focal rhythmic discharges on scalp EEG of patients with focal cortical dysplasia and intractable epilepsy. *Electroencephalography and Clinical Neurophysiology*, 98, pp.243–249.

Geim, A.K. & Novoselov, K.S., 2007. The rise of graphene. *Nature Materials*, 6, pp.183–191.

Girardin, C.C. & Martin, K.A.C., 2009. Inactivation of lateral connections in cat area 17. *The European Journal of Neuroscience*, 29(10), pp.2092–102.

Goldring, S. et al., 1961. Direct response of human cerebral cortex. *Archives of Neurology*, 4(6), pp.590–598.

Gray, C.M. & Singer, W., 1989. Stimulus-specific neuronal oscillations in orientation columns of cat visual cortex. *Proceedings of the National Academy of Sciences of the United States of America*, 86(5), pp.1698–702.

Greiner, H.M. et al., 2016. Preresection intraoperative electrocorticography (ECoG) abnormalities predict seizure-onset zone and outcome in pediatric epilepsy surgery. *Epilepsia*, 57(4), pp.582–589.

Griffith, R.W. & Humphrey, D.R., 2006. Long-term gliosis around chronically implanted platinum electrodes in the Rhesus macaque motor cortex. *Neuroscience Letters*, 406(1-2), pp.81–86.

Gwinn, R.P. et al., 2008. Local spatial effect of 50 Hz cortical stimulation in humans. *Epilepsia*, 49(9), pp.1602–1610.

Hamer, H.M. et al., 2003. Electrophysiology of focal clonic seizures in humans: A study using subdural and depth electrodes. *Brain*, 126(3), pp.547–555.

Henrie, J.A. & Shapley, R., 2005. LFP power spectra in V1 cortex: The graded effect of stimulus contrast. *Journal of Neurophysiology*, 94(1), pp.479–90.

Hirsch, J.A. & Gilbert, C.D., 1991. Synaptic physiology of horizontal connections in the cat's visual cortex. *The Journal of Neuroscience*, 11(6), pp.1800–9.

Histed, M.H., Bonin, V. & Reid, R.C., 2009. Direct activation of sparse, distributed populations of cortical neurons by electrical microstimulation. *Neuron*, 63, pp.508–522.

Hubel, D. & Wiesel, T., 1959. Receptive fields of single neurones in the cat's striate cortex. *The Journal of Physiology*, 148(3), pp.574–591.

Hubel, D.H. & Wiesel, T.N., 1963. Shape and arrangement of columns in cat's striate cortex. *The Journal of Physiology*, 165(3), pp.559–568.

Hufnagel, A. et al., 2000. Clinical relevance of quantified intracranial interictal spike activity in presurgical evaluation of epilepsy. *Epilepsia*, 41(4), pp.467–478.

Humphrey, A.L. et al., 1985. Termination patterns of individual X- and Y-cell axons in the visual cortex of the cat: Projections to area 18, to the 17/18 border region, and to both areas 17 and 18. *The Journal of Comparative Neurology*, 233, pp.190–212.

Ikeda, A., Miyamoto, S. & Shibasaki, H., 2002. Cortical motor mapping in epilepsy patients: Information from subdural electrodes in presurgical evaluation. *Epilepsia*, 43 Suppl 9(7), pp.56–60.

Kajikawa, Y. et al., 2011. How local is the local field potential? *Neuron*, 72(5), pp.847–858.

Kandratavicius, L. et al., 2014. Animal models of epilepsy: Use and limitations. *Neuropsychiatric Disease and Treatment*, 10, pp.1693–1705.

Karoly, P.J. et al., 2016. Interictal spikes and epileptic seizures: Their relationship and underlying rhythmicity. *Brain*, pp.1–13.

Katzner, S. et al., 2009. Local origin of field potentials in visual cortex. *Neuron*, 61(1), pp.35–41.

Klauk, H. et al., 2002. High-mobility polymer gate dielectric pentacene thin film transistors. *Journal of Applied Physics*, 92(9), p.5259.

Korshoej, A.R. et al., 2010. Kinetic analysis of evoked IPSCs discloses mechanism of antagonism of synaptic GABA-A receptors by picrotoxin. *British Journal of Pharmacology*, 159(3), pp.636–649.

Kuzum, D. et al., 2014. Transparent and flexible low noise graphene electrodes for simultaneous electrophysiology and neuroimaging. *Nature Communications*, 5.

Kwan, P. & Sander, J.W., 2004. The natural history of epilepsy: An epidemiological view. *Journal of Neurology, Neurosurgery, and Psychiatry*, 75(10), pp.1376–81.

Lee, C. et al., 2008. Measurement of the elastic properties and intrinsic strength of monolayer graphene. *Science*, 321, pp.385–388.

Lesser, R.P. et al., 1999. Brief bursts of pulse stimulation terminate afterdischarges caused by cortical stimulation. *Neurology*, 53(9).

Lesser, R.P., Crone, N.E. & Webber, W.R.S., 2010. Subdural electrodes. *Clinical Neurophysiology*, 121(9), pp.1376–92.

Lindén, H., Pettersen, K.H. & Einevoll, G.T., 2010. Intrinsic dendritic filtering gives low-pass power spectra of local field potentials. *Journal of Computational Neuroscience*, 29(3), pp.423–444.

Litt, B., 2003. Evaluating devices for treating epilepsy. *Epilepsia*, 44 Suppl 7, pp.30–7.

Litt, B. et al., 1998. Nonconvulsive status epilepticus in the critically ill elderly. *Epilepsia*, 39(11), pp.1194–1202.

Lopes da Silva, F.H. & Van Rotterdam, A., 1999. Biophysical aspects of EEG and magnetoencephalogram generation. In E. Niedermeyer & F. H. Lopes da Silva, eds. *Electroencephalography: Basic Principles, Clinical Applications, and Related Fields*. Lippincott Williams & Wilkins, pp. 93–109.

Maier, A. et al., 2010. Distinct superficial and deep laminar domains of activity in the visual cortex during rest and stimulation. *Frontiers in Systems Neuroscience*, 4(31), pp.1–11.

Maldonado, P.E., 1997. Orientation selectivity in pinwheel centers in cat striate cortex. *Science*, 276(5318), pp.1551–1555.

Malmivuo, J. & Plonsey, R., 1995. *Bioelectromagnetism - Principles and Applications of Bioelectric and Biomagnetic Fields*, New York: Oxford University Press.

Mazurek, M., Kager, M. & Van Hooser, S.D., 2014. Robust quantification of orientation selectivity and direction selectivity. *Frontiers in Neural Circuits*, 8(August), p.92.

Mccormick, D.A. & Contreras, D., 2001. On the cellular and network bases of epileptic

seizures. *Annual Review of Physiology*, 63, pp.815–846.

McIntyre, C.C. et al., 2004. Electric field and stimulating influence generated by deep brain stimulation of the subthalamic nucleus. *Clinical Neurophysiology*, 115(3), pp.589–95.

Miles, R., Traub, R.D. & Wong, K.S., 1988. Spread of Synchronous Firing in Longitudinal From the CA3 Region of the Hippocampus. *Journal of Neurophysiology*, 60(4), pp.1481–1496.

Miocinovic, S. et al., 2013. History, applications, and mechanisms of deep brain stimulation. *JAMA Neurology*, 70(2), pp.163–71.

Mitzdorf, U., 1985. Current source-density method and application in cat cerebral cortex: Investigation of evoked potentials and EEG phenomena. *Physiological Reviews*, 65(1), pp.37–100.

Mitzdorf, U. & Singer, W., 1978. Prominent excitatory pathways in the cat visual cortex (A 17 and A 18): A current source density analysis of electrically evoked potentials. *Experimental Brain Research*, 33, pp.371–394.

Morrell, M.J., 2011. Responsive cortical stimulation for the treatment of medically intractable partial epilepsy. *Neurology*, 77(13), pp.1295–1304.

Movshon, J.A., Thompson, I.D. & Tolhurst, D.J., 1978. Spatial and temporal contrast sensitivity of neurones in areas 17 and 18 of the cat's visual cortex. *The Journal of Physiology*, 283, pp.101–120.

Nair, D.R. et al., 2008. Chronic subdural electrodes in the management of epilepsy. *Clinical Neurophysiology*, 119(1), pp.11–28.

NeuroPace, 2015. *RNS System User Manual*, Mountain View, CA.

Nicholson, C. & Freeman, J.A., 1975. Theory of current source-density analysis and determination of conductivity tensor for anuran cerebellum. *Journal of Neurophysiology*, 38(2), pp.356–368.

Niedermeyer, E., 1999a. Abnormal EEG patterns: Epileptic and paroxysmal. In E. Niedermeyer & F. H. Lopes da Silva, eds. *Electroencephalography: Basic Principles, Clinical Applications, and Related Fields*. Lippincott Williams & Wilkins, pp. 235–260.

Niedermeyer, E., 1999b. Historical aspects. In E. Niedermeyer & F. H. Lopes da Silva, eds. *Electroencephalography: Basic Principles, Clinical Applications, and Related Fields*. Lippincott Williams & Wilkins, pp. 1–14.

Noachtar, S. et al., 2008. Interictal regional polyspikes in noninvasive EEG suggest

cortical dysplasia as etiology of focal epilepsies. *Epilepsia*, 49(6), pp.1011–1017.

Ojemann, G. et al., 1993. Cortical stimulation. In J. Engel, ed. *Surgical Treatment of the Epilepsies*. New York, New York, USA: Raven Press, pp. 399–414.

Padnick, L.B. & Linsenmeier, R.A., 1999. Properties of the flash visual evoked potential recorded in the cat primary visual cortex. *Vision Research*, 39(17), pp.2833–40.

Payne, B.R. & Peters, A., 2002. The concept of cat primary visual cortex. In B. R. Payne & A. Peters, eds. *The Cat Primary Visual cortex*. Academic Press, pp. 1–129.

Plummer, C., Harvey, A.S. & Cook, M., 2008. EEG source localization in focal epilepsy: Where are we now? *Epilepsia*, 49(2), pp.201–218.

Pohlmann-Eden, B. et al., 1996. Periodic lateralized epileptiform discharges — a critical review. *Journal of Clinical Neurophysiology*, 13(6), pp.519–530.

Polikov, V.S., Tresco, P.A. & Reichert, W.M., 2005. Response of brain tissue to chronically implanted neural electrodes. *Journal of Neuroscience Methods*, 148(1), pp.1–18.

Prince, D. a & Wilder, B.J., 1967. Control mechanisms in cortical epileptogenic foci: Surround inhibition. *Archives of Neurology*, 16, pp.194–202.

Reiher, J. et al., 1991. Periodic lateralized epileptiform discharges with transitional rhythmic discharges: association with seizures. *Electroencephalography and Clinical Neurophysiology*, 78, pp.12–17.

Rosenow, F. & Lüders, H., 2001. Presurgical evaluation of epilepsy. *Brain*, 124(9), pp.1683–1700.

Saudari, S.R. et al., 2010. Device configurations for ambipolar transport in flexible, pentacene transistors. *Advanced Materials*, 22(44), pp.5063–8.

Saudari, S.R., Frail, P.R. & Kagan, C.R., 2009. Ambipolar transport in solution-deposited pentacene transistors enhanced by molecular engineering of device contacts. *Applied Physics Letters*, 95(2), p.023301.

Schevon, C. a et al., 2012. Evidence of an inhibitory restraint of seizure activity in humans. *Nature Communications*, 3, p.1060.

Schmidt, K.E. & Lowel, S., 2002. Long-Range Intrinsic Connections in Cat Primary Visual Cortes. In B. R. Payne & A. Peters, eds. *The Cat Primary Visual cortex*. Academic Press, pp. 387–426.

Schroeder, C.E. et al., 1991. Striate cortical contribution to the surface-recorded pattern-reversal VEP in the alert monkey. *Vision Research*, 31(7-8), pp.1143–1157.

Schummers, J. et al., 2007. Dynamics of orientation tuning in cat V1 neurons depend on location within layers and orientation maps. *Frontiers in Neuroscience*, 1(1), pp.145–59.

Spira, M.E. & Hai, A., 2013. Multi-electrode array technologies for neuroscience and cardiology. *Nature Nanotechnology*, 8(2), pp.83–94.

Staley, K.J. & Dudek, F.E., 2006. Interictal spikes and epileptogenesis. *Epilepsy Currents*, 6(6), pp.199–202.

Stead, M. et al., 2010. Microseizures and the spatiotemporal scales of human partial epilepsy. *Brain*, 133(Pt 9), pp.2789–97.

Stepanyants, A. et al., 2009. The fractions of short- and long-range connections in the visual cortex. *Proceedings of the National Academy of Sciences of the United States of America*, 106(9), pp.3555–60.

Steriade, M. et al., 1998. Spike-wave complexes and fast components of cortically generated seizures. II. Extra- and intracellular patterns. *Journal of Neurophysiology*, 80(3), pp.1456–1479.

Steriade, M., Amzica, F. & Contreras, D., 1996. Synchronization of fast (30-40 Hz) spontaneous cortical rhythms during brain activation. *The Journal of Neuroscience*, 16(1), pp.392–417.

Sun, F.T. & Morrell, M.J., 2014. Closed-loop neurostimulation: The clinical experience. *Neurotherapeutics*, 11(3), pp.553–563.

Szelényi, A. et al., 2010. Intraoperative electrical stimulation in awake craniotomy: Methodological aspects of current practice. *Neurosurgical Focus*, 28(2), p.E7.

Tahon, K. et al., 2011. Current source density correlates of cerebellar Golgi and Purkinje cell responses to tactile input. *Journal of Neurophysiology*, 105(3), pp.1327–41.

Tao, J.X. et al., 2005. Intracranial EEG substrates of scalp EEG interictal spikes. *Epilepsia*, 46(5), pp.669–676.

Tehovnik, E.J. et al., 2006. Direct and indirect activation of cortical neurons by electrical microstimulation. *Journal of Neurophysiology*, 96(2), pp.512–21.

Téllez-Zenteno, J., Dhar, R. & Wiebe, S., 2005. Long-term seizure outcomes following epilepsy surgery: A systematic review and meta-analysis. *Brain*, 128(Pt 5), pp.1188–98.

Texas Instruments, 2008. *AN-1515: A Comprehensive Study of the Howland Current Pump*, Dallas, TX.

Theodore, W.H. & Fisher, R.S., 2004. Brain stimulation for epilepsy. *The Lancet*, 3(February), pp.111–118.

Tolias, A.S. et al., 2005. Mapping cortical activity elicited with electrical microstimulation using fMRI in the macaque. *Neuron*, 48(6), pp.901–911.

Trevelyan, A.J. & Schevon, C. a, 2013. How inhibition influences seizure propagation. *Neuropharmacology*, 69, pp.45–54.

Tusa, R.J., Palmer, L.A. & Rosenquist, A.C., 1978. The retinotopic organization of area 17 (striate cortex) in the cat. *Journal of Comparative Neurology*, 177(2), pp.213–35.

Vanleer, A.C. et al., 2016. Millimeter-scale epileptiform spike patterns and their relationship to seizures. *Journal of Neural Engineering*, 13(2).

Viventi, J. et al., 2010. A conformal, bio-interfaced class of silicon electronics for mapping cardiac electrophysiology. *Science Translational Medicine*, 2(24), p.24ra22.

Viventi, J. et al., 2011. Flexible, foldable, actively multiplexed, high-density electrode array for mapping brain activity in vivo. *Nature Neuroscience*, 14(12), pp.1599–605.

Westbrook, G.L., 2000. Seizures and epilepsy. In E. R. Kandel, J. H. Schwartz, & T. M. Jessell, eds. *Principles of Neural Science*. New York: McGraw-Hill, pp. 910–935.

Wester, J.C. & Contreras, D., 2012. Columnar interactions determine horizontal propagation of recurrent network activity in neocortex. *The Journal of Neuroscience*, 32(16), pp.5454–71.

World Health Organization, 2005. *Atlas: Epilepsy Care in the World*, Geneva: World Health Organization.

Worrell, G.A. et al., 2008. High-frequency oscillations in human temporal lobe: simultaneous microwire and clinical macroelectrode recordings. *Brain*, 131(Pt 4), pp.928–37.

Wurtz, R.H., 2009. Recounting the impact of Hubel and Wiesel. *The Journal of Physiology*, 587(12), pp.2817–2823.

Wurtz, R.H. & Kandel, E.R., 2000. Central visual pathways. In E. R. Kandel, J. H. Schwartz, & T. M. Jessell, eds. *Principles of Neural Science*. New York: McGraw-Hill, pp. 523–545.

Zhang, M. et al., 2014. Propagation of epileptiform activity can be independent of synaptic transmission, gap junctions, or diffusion and is consistent with electrical field transmission. *The Journal of Neuroscience*, 34(4), pp.1409–19.